DOCTORAL THESIS

DESIGN AND FABRICATION OF FUNCTIONAL HELIX-BASED METASURFACES

FANIAYEU IHAR

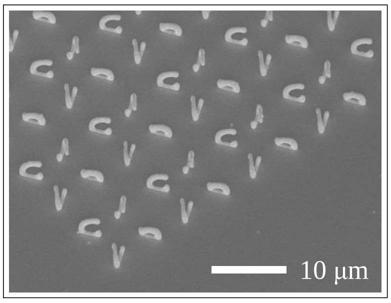

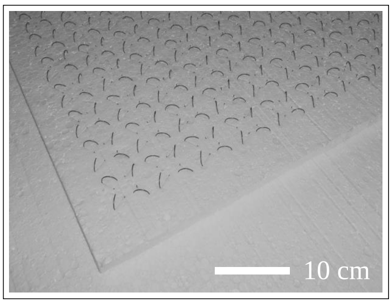

Universities:

Shizuoka University, Japan

Francisk Skorina Gomel State University, Belarus

Departments:

Nanovision Technology

Radiophysics and Electronics

Supervisors:

Professor Vygantas Mizeikis

Professor Igor Semchenko

September 2017

Acknowledgement

I would like to express my gratitude to all those who supported and helped me during my study at Shizuoka University in Japan. Many people have helped me in many ways, probably, without even realizing it. I am grateful to everyone for this.

Foremost, I would like to express my sincere appreciations to my supervisor Prof. Vygantas Mizeikis who provided to me the opportunity to work and contribute to the research of his group. From the very first days of my stay in Japan, he helped me with all occurring learning issues. He introduced to me various laser fabrication techniques, explained and helped me during other steps of post-processing for successful fabrication of functional metasurfaces. During many discussions and group meetings, I learned a lot from his profound knowledge. Moreover, Prof. Mizeikis gave me numerous comments and excellent ideas for high-level publications in scientific journals which have been reflected in this doctoral thesis. Besides the intellectual contribution, he took a great care of the financial support of my research, helped me with multiple presentations for international and domestic conferences. My respectful gratitude to you!

I want to express my gratitude to Prof. Igor V. Semchenko for the great ideas regarding the design and synthesis of helix-based metasurfaces. Thanks a lot for continuous support, kindness, and facilitation with my simultaneous study at Francisk Skorina Gomel State University in Belarus. Also, I would like to thank Prof. Sergei A. Khakhomov for encouragement and assistance with solving organizational issues concerning my study in Belarus. Thanks to Profs. I. V. Semchenko and S. A. Khakhomov, I have got an opportunity to study at Shizuoka University in Japan. Thank you so much!

I would like to express my special gratitude to my best friend, colleague, excellent specialist and just a wonderful person, Victor S. Asadchy. It is hard for me to appreciate his support and help with many issues throughout my study and daily life. Despite the fact that we study in different countries, we constantly cooperate and work together. I would like to note that some ideas outlined in this thesis were initiated by Victor and subsequently implemented by me. To a large extent, thanks to Victor's comments and suggestions, some important results on functional metasurfaces were obtained, which are a part of the current study. Thank you for everything!

I want to extend my thanks to all the members of the groups of Profs. Ono and Mizeikis for making me feel welcome and comfortable during my visit. Especially, I would like to thank my lab friends, two cheerful guys Atsutaka Miyamichi and Daichi Hayashi, who helped me a lot with a preparation of documents in Japanese and enjoyable conversations in the lab. Also, I would like to acknowledge my friends, Segrey Barsukov and Dmytro Gnatyuk, with whom I cheerfully spent my free time in Japan and with whom I shared so many awesome jokes. Separate thanks to my friends from Belarus, Vasily Velesnitsky and Alexander Krupeychenko, for their daily-life support. Thanks to my girlfriend for her care and amazing cooking. In addition to the above, I would like to thank all my friends from Belarus and Japan who might have no idea or interest in what I did here during the last 3 years and with whom I had pleasantly spent time.

I would like to express my gratitude to all my family for their support and love. My great gratitude to my brother for the long conversations and tremendous support in my life as well as in assisting with the preparation of official documents in Belarus. Finally, thanks to my mother and father who have always been with me whatever happen to me and wherever I am. I would not have got all of this far without your support and I hope, you are proud of me.

Thank you all for everything and have a nice reading!

Faniayeu Ihar
Hamamatsu, Japan, 2017

Abstract

Electromagnetic metamaterials and metasurfaces promise novel possibilities to control electromagnetic radiation using sub-wavelength scale structuring of materials instead of relying on their intrinsic optical properties. Helix-based metasurfaces can be tailored to exhibit a wide range of intriguing phenomena, such as perfect absorption, circular dichroism, and transformation of a polarization state of the incident electromagnetic radiation. An important advantage of helix-based metasurface architecture is the absence of opaque ground plane, which permits optical transparency at off-resonance frequencies. However, practical development of helix-based metasurfaces is impeded by their difficult fabrication, which requires three-dimensional structuring of periodic arrays of metallic helices. These difficulties become especially severe at optical frequencies when helical inclusions must be scaled to sub-micrometric size.

This thesis describes theoretical and experimental studies of helix-based metasurfaces for the microwave and infrared spectral ranges, with emphasis on practical realization of functional metasurfaces using Direct Laser Write lithography. Theoretical studies address basic physical principles and functionalities of helix-based metasurfaces by establishing relationship between parameters of the structures (size, shape, orientation and periodicity of helical inclusions comprising the metasurface, dielectric functions of the materials involved, and the intended operation spectral range), and individual polarizabilities of inclusions as well as collective optical response of the entire metasurface. This process was carried out using numerical Finite Element simulation of Maxwell's equations, and into account, the minimum feature size and spatial resolution of the fabrication techniques concerned. The theoretical design was strongly focused on metasurfaces with the perfect absorber and polarization rotator functionalities, that can be fabricated by mechanical machining and Direct Laser Write Lithography for the radio-frequency and infrared spectral ranges, respectively. Finally, a practically feasible design of cascaded 5-layer multifunctional wide-band metasurface for the microwave spectral range was proposed.

The suggested designs were tested practically by fabricating the metasurfaces and characterizing their optical properties. At microwave frequencies, metasurfaces with the perfect absorber and polarization rotator functionality were fabricated from metallic wire using mechanical machining. Transmittance, reflectance, and absorbance spectra of the fabricated samples have confirmed good perfect absorber performance with high absorbance of $A > 80\%$ and low reflectance $R < 7\%$ in the frequency range of 2.8-3.3 GHz, while cross-polarized transmittance $T_{\mathrm{cr}} > 90\%$ was confirmed for the polarization rotator. Metasurfaces for infra-red spectral range were realized using state-of-the-art Direct Laser Write lithography allowing to obtain feature sizes close to 100 nm using a non-linear exposure of photoresist by tightly focused pulses of femtosecond Ti: Sapphire laser. To obtain metallic response simple metallization by gold sputtering was used. All-metallic perfect absorbers based on vertical split-ring resonators possessing magnetic response and exhibit-

ing absorbance $A > 88\%$ in the $5 - 13$ μm wavelengths was demonstrated. The spectral tunability of these structures by tailoring their parameters, and possibility to obtain a plasmonic response in resonant mesh-type split-ring-based absorbers was demonstrated. Chiral-plate and compensated perfect absorbing metasurfaces fabricated using the same approach were found to exhibit perfect absorber resonance with absorbance $A > 80\%$ tunable in the $5 - 13$ μm spectral range by changing geometrical parameters of the structures. Practical steps to realize genuinely off-resonance transparent functional metasurfaces for infra-red spectral range using nanosecond-pulse laser ablation for selective metallization of the surface were undertaken and were found to show high potential to succeed in the near future.

These studies present an important step towards the practical realization of metasurfaces, especially at infra-red frequencies where traditional fabrication techniques cannot be applied. In the future, electromagnetic metasurfaces with helix-based architecture may be applied for spectral filtering, polarization transformation, and absorption enhancement of radio and optical waves. At infrared frequencies, they may help to enhance the detector sensitivity and to realize narrow-band thermal emitters and radiation coolers.

Organization of Thesis

Chapter 1 introduces the concept of metamaterial and its brief history. The classical theory of the electromagnetic wave interactions with a medium based on Maxwell's equations is presented, that leads to a definition of the macroscopic effective parameters for different media. Functionalities of metasurfaces in accordance with their applications and issues of practical scalability to shorter wavelengths are briefly mentioned.

Chapter 2 describes synthesis of the off-resonance transparent helix-based metasurfaces. At first, a novel method for determination of electric, magnetic, electromagnetic and magnetoelectric polarizability tensors of electrically small scatterer with arbitrary shape is proposed. Based on this method, helical resonators were tailored to the balance of their polarizabilities for synthesizing of transparent metasurfaces. As a result, polarization-insensitive off-resonance transparent helix-based metasurfaces in the microwave range are designed.

Chapter 3 is devoted to functionalities of the off-resonance transparent helix-based metasurfaces. As a starting point, analytical approach for determination of proper arrangement of helical resonators with balanced polarizabilities in the unit cell of metasurfaces are proposed. Based on this approach and numerical simulation, linearly polarized rotators and perfect absorbers based on double-turn helices for reflected and transmitted waves are designed. Due to off-resonance transparency in metasurfaces, a multifunctional multifrequency cascade metasurface in the microwave range is demonstrated.

Chapter 4 is dedicated to fabrication of functional off-resonance transparent helix-based metasurfaces for microwave range. Twist polarizer and absorbers based on helical resonators with balanced polarizabilities are realized.

Chapter 5 introduces a versatile maskless direct laser write lithography for fabrication of three-dimensional dielectric templates with high spatial resolution. Using this technique, a minimum feature size close to 120 nm by careful control of laser writing exposure conditions is found.

Chapter 6 shows practical realization by direct laser writing with subsequent metallization by gold sputtering of entire metal non-transparent absorbing metasurfaces for the infrared spectral range. As a result, absorbers based on vertical split-ring resonators and single-turn helical resonators were realized.

Chapter 7 presents numerically simulated results of functional off-resonance transparent helix-based metasurfaces in the infrared spectral range. Adapted for direct laser writing, linearly polarized rotators and perfect absorbers based on single-turn helices for reflected and transmitted waves are designed. Moreover, towards to realization of functional off-resonance transparent metasurfaces using laser ablation process was carried out.

Chapter 8 summarizes the obtained results and provide an outlook for this study.

Contents

Chapter 1

Introduction

Day by day, people diligently explore the electromagnetic phenomena and their mutual influence in the environment. Usually, all electromagnetic (EM) phenomena are the results of interactions between waves and materials. The researchers devote considerable interest to manipulating the EM properties of the material in the desired way, thereby obtaining the electromagnetic functionality of the material. This can be achieved by developing structures and geometry using existing natural materials. With a huge amount of material available in the world, the potential and diversity of EM devices are largely limited only by available materials that can be used to build them. Therefore, significant attention is paid to artificial materials capable of all-embracing manipulation of EM waves via structuring. In comparison with natural materials and their functionalities, artificial materials give tremendous freedom in the design and manipulation of EM waves leading to the new useful functionalities that have not been found in nature before.

1.1 Definition of metamaterials

In the last few decades, scientists and engineers have been actively using the approach to developing new materials exhibiting previously unseen, exotic electromagnetic properties. This approach consists of designing materials based on well-arranged functional inclusions with sub-wavelength dimensions with pre-assumed electromagnetic properties. This allows synthesizing new materials or composites based on sub-wavelength inclusions with the desired characteristics. As a rule, the dimensions of these inclusions exceed the atomic or molecular level of the ordinary material by several orders of magnitude. Consequently, the electromagnetic interaction of such an inclusion in the material can be expressed by the effective parameters of homogeneous media, since the inhomogeneity in these structures is much smaller than the operating wavelength. Typically, such materials are called "metamaterials". The prefix "meta" ($\mu\varepsilon\tau\alpha$ in Greek) means "beyond" of the conventional materials. The field of metamaterials was becoming popular with the appearance of a well-known article [1] (cited over 10951 times) that was published in 2000 by prof. J. Pendry. This work is devoted to the possibility of realization a perfect lens with simultaneously negative permeability and permittivity (well-known as a negative refractive index). Immediately, was carried out experimental verification of this phenomena at microwave frequencies and reported in [2]. It should be noted that the first theoretical background and the prerequisites for a medium with a negative refractive index were published in Veselago's work [3] a few decades ago, however, popularity has only been appearing since 2000. Subsequently, metamaterials were rapidly developed in other frequency ranges up to the visible range [4–7].

Many researchers associate the concept of metamaterials exclusively with their unique properties that were not observed in nature. However, during metamaterial development, the unique properties were found even in some natural materials. For example, negative refraction was observed in the complex eyes of some lobsters [8]. This situation is very similar to the development of the artificial photonic crystals, which is a significant achievement of many researchers. It turns out that similar structures with their properties actually existed a long time ago inside a gemstone opal and a wing of Morpho butterflies [9].

Interestingly, one of the first metamaterials was created probably two thousand years ago, long before the development of metamaterials. A famous example is a Lycurgus Cup that was made of ruby glass with a 5-50 nm size of gold nanoparticles inside [10]. These nanoparticles of gold surprisingly color the glass, specifically, in daylight the cup looks greenish, but it illuminates from the inside, and it glows with a ruby color [11, 12].

In fact, artificial electromagnetic metamaterials were studied long before using a word "metamaterial" in the scientific terminology. One of the examples of metamaterials with subwavelength inclusions was used to create a so-called "twisted jute" material, that was proposed by Bose in 1898 to achieve an artificial chiral effect [13]. Also, the periodic arrays of metal wires, dielectric spheres or plates, have been extensively studied in the microwave range more than half a century ago [14–16]. These artificial structures exhibit similar properties to electrical metamaterials in modern terminology. There are also other examples of structures similar to metamaterials, in which were used split-rings [17, 18], ordered frequency filters [19], bianisotropic and chiral materials [20], and others.

At the present stage of metamaterial development [21, 21–24], significant attention is paid to the improvement and optimization of existing structures comprising of diverse meta-atoms, as well as exploring the new functionality and their physical properties.

1.1.1 Maxwell's equations

The equations formulated by James Clerk Maxwell on the basis of the experimental results accumulated by the middle of the 19th century played a key role in the development of theoretical physics, electromagnetism, optics, electric circuits and even for all fields of physics directly or indirectly related to electromagnetism. A set of partial differential Maxwell's equations in SI-units are expressed in the following way [25]

$$\nabla \cdot \mathbf{D}(\mathbf{r}, t) = \rho(\mathbf{r}, t), \tag{1.1}$$

$$\nabla \cdot \mathbf{B}(\mathbf{r}, t) = 0, \tag{1.2}$$

$$\nabla \times \mathbf{E}(\mathbf{r}, t) = -\frac{\partial \mathbf{B}(\mathbf{r}, t)}{\partial t}, \tag{1.3}$$

$$\nabla \times \mathbf{H}(\mathbf{r}, t) = \mathbf{j}(\mathbf{r}, t) + \frac{\partial \mathbf{D}(\mathbf{r}, t)}{\partial t}, \tag{1.4}$$

with the dielectric displacement $\mathbf{D}(\mathbf{r}, t)$, the electric field $\mathbf{E}(\mathbf{r}, t)$, the magnetic field $\mathbf{H}(\mathbf{r}, t)$, the magnetic induction $\mathbf{B}(\mathbf{r}, t)$, the external charge density $\rho(\mathbf{r}, t)$, and the external current density $\mathbf{j}(\mathbf{r}, t)$. The equation (1.1) means the electric flux leaving a volume is proportional to the charge inside. In accordance with equation (1.2), there are no magnetic monopoles; the total magnetic flux through a closed surface is zero. Follows to equation (1.3), the voltage induced in a closed circuit is proportional to the rate of change of the magnetic flux it encloses. The last equation (1.3) shows the magnetic field induced around a closed loop and it is proportional to the electric current plus displacement current (rate of change of electric field) it encloses. However, the above Maxwell equations do not yet constitute a complete system of equations of the electromagnetic field, since they do not contain the properties of the medium in which the electromagnetic field is excited. Relations connecting the quantities of $\mathbf{E}(\mathbf{r}, t)$, $\mathbf{B}(\mathbf{r}, t)$, $\mathbf{D}(\mathbf{r}, t)$, $\mathbf{H}(\mathbf{r}, t)$, and $\mathbf{j}(\mathbf{r}, t)$ and taking into account the individual properties of the environment that are described well-known material equations.

It should be noted that the external charge density and the current density are connected through the conservation of charge in a relation known as the continuity equation:

$$\nabla \cdot \mathbf{j}(\mathbf{r}, t) + \frac{\partial \rho(\mathbf{r}, t)}{\partial t} = 0. \tag{1.5}$$

As well known, scientists actively develop and investigate the interaction of electromagnetic waves with metamaterials. In accordance with classical electromagnetic theory, the effects and interactions of EM fields with a media can be described by Maxwell's equations. This is a system of equations in differential or integral form describing the EM field and its relation to electric charges and currents in a vacuum and continuous media. Together with the expression for the Lorentz force, which determines the measure of the effect of the EM field on charged particles, form a complete system of equations of classical electrodynamics, sometimes called the Maxwell-Lorentz equations.

The material equations establish a connection between $\mathbf{D}(\mathbf{r}, t)$, $\mathbf{H}(\mathbf{r}, t)$, and $\mathbf{E}(\mathbf{r}, t)$, $\mathbf{B}(\mathbf{r}, t)$. This takes into account properties of the environment. In practice, material equations are espressed via experimentally determined parameters (depending, in general, on the frequency of the electromagnetic field) used, which are available in a handbook [26]. All charges and currents induced by the electromagnetic fields lead to a macroscopic electric polarization or dipole moment density $\mathbf{P}(\mathbf{r}, t)$ and a macroscopic magnetization $\mathbf{M}(\mathbf{r}, t)$ that influence to the wave propagation in media, respectively via the material equations:

$$\begin{aligned} \mathbf{D}(\mathbf{r}, t) &= \epsilon_0 \mathbf{E}(\mathbf{r}, t) + \mathbf{P}(\mathbf{r}, t), \\ \mathbf{B}(\mathbf{r}, t) &= \mu_0 \mathbf{H}(\mathbf{r}, t) + \mathbf{M}(\mathbf{r}, t). \end{aligned} \tag{1.6}$$

Here, we introduce the permittivity of free space $\epsilon_0 = 1/(c^2\mu_0) = 8.85 \times 10^{-12} F \cdot m^{-1}$, and the permeability of free space $\mu_0 = 4\pi \cdot 10^{-7} N/A^2$ the vacuum speed of light $c = 299,792,458$ m/s. Although for a wide class of substances the linear approximation for weak fields is performed with good accuracy, in the general case the relationship between $\mathbf{D}(\mathbf{r}, t)$, $\mathbf{H}(\mathbf{r}, t)$, and $\mathbf{E}(\mathbf{r}, t)$, $\mathbf{B}(\mathbf{r}, t)$ can be nonlinear. In addition, the more complex relationship is observed in media with spatial or temporal variances. In the case of spatial dispersion, the currents and charges at a given point in space depend on the field magnitudes not only at the same point, but also at neighboring points. In the case of time dispersion, the polarization and magnetization of the medium are not determined solely by the magnitude of the field at a given instant of time, but also depend on the magnitude of the fields at the preceding instants of time. In the most general case of nonlinear and inhomogeneous media with dispersion, the material equations take the integral form [25]

$$\begin{aligned}\mathbf{P}(\mathbf{r},t) &= \int_{\infty}^{-\infty}\int_{-\infty}^{t} \epsilon_0\chi_e(\mathbf{r}-\mathbf{r}',t-t')\mathbf{E}(\mathbf{r}',t')dt'd^3r',\\ \mathbf{M}(\mathbf{r},t) &= \int_{\infty}^{-\infty}\int_{-\infty}^{t} \mu_0\chi_m(\mathbf{r}-\mathbf{r}',t-t')\mathbf{H}(\mathbf{r}',t')dt'd^3r',\end{aligned} \tag{1.7}$$

with the electric $\chi_e(\mathbf{r}-\mathbf{r}',t-t')$ and magnetic susceptibilities $\chi_m(\mathbf{r}-\mathbf{r}',t-t')$, respectively. In the general case, both susceptibilities are second-rank tensors. Since most materials are isotropic and the susceptibility becomes scalar. Consequently, we can omit the integration over d^3r' and rewrite Eqs. (1.6) in frequency domain as:

$$\begin{aligned}\mathbf{D}(\mathbf{r},\omega) &= \epsilon_0\left[1+\chi_e(\omega)\right]\mathbf{E}(\mathbf{r},\omega) = \epsilon_0\epsilon(\omega)\mathbf{E}(\mathbf{r},\omega),\\ \mathbf{B}(\mathbf{r},\omega) &= \mu_0\left[1+\chi_m(\omega)\right]\mathbf{H}(\mathbf{r},\omega) = \mu_0\mu(\omega)\mathbf{H}(\mathbf{r},\omega).\end{aligned} \tag{1.8}$$

These equations describe how an applied electric field $\mathbf{E}$ interacts with the medium while it induces electric dipoles or orients the already existing electric dipoles with modification of the dielectric displacement $\mathbf{D}$. Magnetic field $\mathbf{H}$ induces or orients magnetic dipoles in medium respectively to the magnetic induction $\mathbf{B}$. In some special cases, an applied electric field leads to magnetic dipole moments and an applied magnetic field leads to electric dipole moments due to the electromagnetic cross-couplings that occur in bi-isotropic and bi-anisotropic media [27].

It is important to note that the effective material parameters, permittivity $\epsilon(\omega)$ and permeability $\mu(\omega)$, describe the linear interaction of the electromagnetic fields with isotropic and homogeneous materials. It is possible to analyze such a structured material with complicated geometries as an electromagnetically uniform medium which can be described through constitutive homogeneous parameters: electric permittivity $\epsilon(\omega)$ and magnetic permeability $\mu(\omega)$, respectively.

Thus, as follows from Maxwell's equations (1.1)–(1.4), the sign of $\epsilon(\omega)$ and $\mu(\omega)$ plays a fundamental role in the wave propagation behavior in natural materials and artificial metamaterials.

1.1.2 Wave equations

Maxwell's equations are the first-order differential equations in space and time. However, each equation includes both unknown vector functions $\mathbf{E}$ and $\mathbf{H}$. In the absence of charges and currents, one can pass to equations of the second order leading to the second order diffraction equations in space and time, the electric or magnetic fields that can be expressed by wave equations:

$$\nabla^2 \mathbf{E} + \mu_0\mu\epsilon_0\epsilon \frac{\partial^2 \mathbf{E}}{\partial t^2} = 0,$$
$$\nabla^2 \mathbf{H} + \mu_0\mu\epsilon_0\epsilon \frac{\partial^2 \mathbf{H}}{\partial t^2} = 0. \tag{1.9}$$

These equations describe electric or magnetic fields for homogeneous and isotropic media ϵ, $\mu = const$. A solution of equation (1.10) is given by

$$\mathbf{E}(\mathbf{r}, t) = \frac{1}{2}\left[\widetilde{\mathbf{E}}(\mathbf{r})e^{-i\omega t} + c.c.\right] = \Re\left[\widetilde{\mathbf{E}}(\mathbf{r})e^{-i\omega t}\right],$$
$$\mathbf{H}(\mathbf{r}, t) = \frac{1}{2}\left[\widetilde{\mathbf{H}}(\mathbf{r})e^{-i\omega t} + c.c.\right] = \Re\left[\widetilde{\mathbf{H}}(\mathbf{r})e^{-i\omega t}\right], \tag{1.10}$$

with the electric $\widetilde{\mathbf{E}}(\mathbf{r}) = \mathbf{E}_0 e^{i\mathbf{kr}}$ and magnetic $\widetilde{\mathbf{H}}(\mathbf{r}) = \mathbf{H}_0 e^{i\mathbf{kr}}$ fields that allows one focus on the coordinate dependence of the field. In some works, the coefficient 1/2 in the harmonic amplitude agreement is not used, which leads to a corresponding modification of all the expressions associated with this agreement. Thus, the Eqs. (1.10) represent plane waves oscillating in time with frequency ω and propagating in the direction of the wave vector $\mathbf{k}$.

For inhomogeneous wave equations the electric and magnetic fields have the following form [28]:

$$\nabla \times \nabla \times \mathbf{E} + \mu_0\epsilon_0 \frac{\partial^2 \mathbf{E}}{\partial t^2} = -\frac{\partial}{\partial t}\left(\mu_0 \mathbf{j} + \mu_0 \frac{\partial \mathbf{P}}{\partial t} + \nabla \times \mathbf{M}\right),$$
$$\nabla \times \nabla \times \mathbf{H} + \mu_0\epsilon_0 \frac{\partial^2 \mathbf{H}}{\partial t^2} = \nabla \times \mathbf{j} + \nabla \times \frac{\partial \mathbf{P}}{\partial t} + \frac{\partial \mathbf{M}}{\partial t}. \tag{1.11}$$

Conditions on the right-hand sides of both wave equations express the initial terms. There are two types of initial terms of the Eqs. (1.11), at first, the current density of the external source $\mathbf{j}$ and, the second, $\partial\mathbf{P}/\partial t$ and $\nabla \times \mathbf{M}$ as the current density of polarization and magnetization, respectively. The latter one describes the interaction of electromagnetic radiation with matter.

Substituting the plane wave solution into the wave equation (1.9) leads to the dispersion relation:

$$\frac{\omega^2}{|\mathbf{k}|^2} = \frac{c^2}{\epsilon\mu}. \tag{1.12}$$

Using dispersion relation, the refractive index has the following form:

$$n = \pm\sqrt{\epsilon\mu}. \tag{1.13}$$

The decision which sign of the refractive index we have to choose, can be easily deduced from the continuity conditions for fields at interfaces when both permittivity and permeability are real numbers. If one or both of them are complex numbers, we can use a lengthy formula to deduce the sign of n for given complex values of ϵ and μ from Ref. [29]. As it is well known, the refractive index possesses the positive branch for natural materials but it can be opposite for metamaterials.

1.1.3 Macroscopic effective parameters

As mentioned above, electromagnetic properties of materials are determined by two parameters: permittivity ϵ and permeability μ, respectively. These parameters describe interaction and coupling of electromagnetic waves with materials. Together with refractive index $n = \sqrt{\epsilon\mu}$ and impedance $Z = \sqrt{\mu/\epsilon}$, it can be used to describe the overall average response in a whole material. Essentially, parameters n and Z are also the macroscopic effective parameters since on the macroscopic level, the electromagnetic responses of the inhomogeneous structure are averaged.

In the case of metamaterials, the scale of inhomogeneity is much smaller than the operating wavelength. This corresponds to lattice constant of artificial periodic structures. Although interaction between electromagnetic fields and meta-atoms is quite difficult on the scale of inhomogeneities, the wave feels a homogeneous medium macroscopically. In addition, electromagnetic metamaterial response to external fields are similar to traditional materials and can be described by effective parameters, namely, permittivity, permeability, refractive index, and impedance. From the standpoint of Maxwell's equations, the materials described by ϵ and μ are a collection of sub-wavelength units with electric and magnetic properties. Due to the special design of meta-atoms, which is usually a thin metal-dielectric structure, it allows adapting the electromagnetic response of medium in unprecedented and desired way from metamaterials. Thus, material response to external fields is largely determined only by two parameters ϵ and μ, we can conveniently characterize most electromagnetic materials in an electromagnetic parameter space based on the two values [30].

Figure 1.1 shows the quadrant of material parameter space characterized by the real part of permittivity ϵ_{r} and the real part of permeability μ_{r}, respectively. This corresponds to the following cases:

$\underline{\epsilon > 0,\ \mu > 0}$: Medium with both positive values of permittivity and permeability include most common transparent materials such as dielectric materials and it is called Double Positive Medium (DPM). The electromagnetic waves that are propagated in this medium have a right-handed triad of the vectors $\mathbf{E}$, $\mathbf{H}$, and $\mathbf{k}$.

$\underline{\epsilon < 0,\ \mu > 0}$: Medium with permittivity less than zero and permeability greater than zero is called as Epsilon Negative (ENG) medium. An electrical plasma is a common example of this medium. Plasma is one of the four fundamental states of matter, the others being solid, liquid, and gas. Electromagnetic waves do not interact inside the plasma at frequencies below the plasma frequency that it can be directly obtained from the dispersion relation. Moreover, there are no real solutions for the wave vector in ENG media.

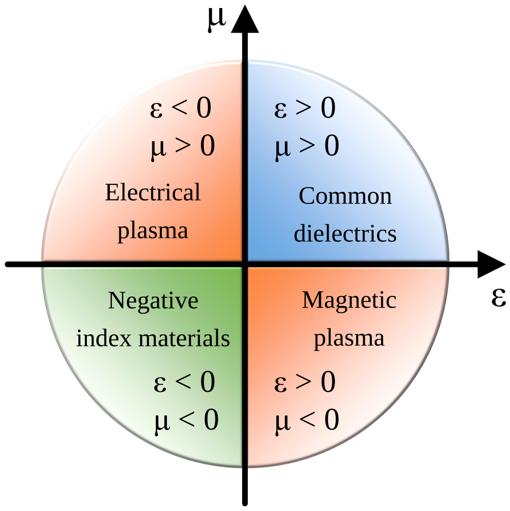

Figure 1.1: Material parameter space characterized by electric permittivity (ϵ) and magnetic permeability (μ). The two axes correspond to the real parts of permittivity and permeability, respectively.

$\epsilon > 0,\ \mu < 0$: Medium with permittivity greater than zero and permeability less than zero called as μ-negative (MNG) medium. A typical example of such medium is magnetic plasma. The natural materials of magnetic plasma are some antiferromagnetic and ferrimagnetic materials that exhibit $\Re(\mu) < 0$ within a frequency band above the resonance frequency. In this case, the wave incident on the medium of this family damps slowly in the medium, and no propagating modes can be stable. It should be mentioned that there is no exact analog of an electric plasma due to the absence of magnetic monopoles.

$\epsilon < 0,\ \mu < 0$: Medium with simultaneously negative values of permittivity and permeability is called as Double Negative (DNG) medium. Artificial materials well-known as metamaterials can exhibit a negative refraction. It is also termed as left-handed media that may exhibit the phenomenon of backward wave propagation sometimes. Negative index of refraction derives mathematically from the vector triplet **E**, **H**, and **k** forming a left-handed triad.

Thus, electromagnetic materials with all possible combinations of ϵ_{r} and μ_{r} can be expressed in the parameter space [22]. It is well known, that the dielectric permittivity function $\epsilon(\omega)$ satisfies Kramers-Kronig relations [25]. Consequently, $\epsilon(\omega)$ has an imaginary part, which characterizes the dissipation of energy in the medium.

The field vectors **E** and **D** are not necessarily parallel to each other in an anisotropic medium. Therefore, the permittivity should be in the form of a tensor, rather than a scalar value. In most metamaterials studied to date, anisotropic and highly dispersive media exhibit such properties. For this reason, it is necessary to indicate frequency and direction that addressing to effective parameters of metamaterials. Likewise, for some bianisotropic media, EM properties are not clearly described by tensors ϵ and μ due to the complexity of meta-atoms. Such structures possess additional material parameters, such as magnetoelectric coefficients, which are connected to electric and magnetic fields.

In the studies of metamaterials, a significant attention must be payed to an innovative use of EM parameter space ϵ and μ. The main focus of metamaterial studies lies in the design of artificial materials with exotic electromagnetic properties that are not prohibited by Maxwell's equations but are not observed in traditional media. It allows expanding the parameter space for better control of electromagnetic waves. For example, negative index metamaterials complete the quadrant of material parameter space, which previously was not available. Given current and projected advances in computer technology and manufacturing techniques, other areas of the parameter space will be investigated for the additional and unprecedented EM properties.

1.2 Electromagnetic metasurfaces

Thanks to rapid development and improvement of metamaterials, two-dimensional (2D) or planar metamaterials have been widely explored. These structures allow a full control over reflected and transmitted waves and offer opportunities for a new generation of microwave and optical devices. Since a few years ago, such planar metamaterials were categorized as metasurfaces. Below, we will provide a definition of metasurfaces and their practical scalability in the electromagnetic spectrum, as well as functionalities and applications.

1.2.1 Introduction to metasurfaces

Metamaterials are generally understood as three-dimensional (3D) structures that exhibit desirable electromagnetic behavior. 3D metamaterials can be modified by placing electrically small scatterers or holes in a 2D pattern on their surfaces or interfaces. This allows to significantly reduce the thickness of metamaterials and achieve new electromagnetic properties. Moreover, practical realization such thin materials are more easier and expedient for fabrication technologies. This surface version of the metamaterial is called metasurface, which essentially replaces metamaterials in many aspects and applications.

Metasurface is a 2D version of 3D bulk metamaterial, defined as optically thin and dense array of structural elements possessing the extraordinary properties provided by their constituent elements. Metasurfaces usually have an arbitrarily shaped surface consisting of subwavelength-size resonant inclusions. A behavior of metasurfaces (or metamaterials) can be characterized by effective polarizabilities of the unit cell comprising of subwavelength inclusions. The periodicity of metasurface also corresponds to subwavelength dimensions that exhibit as nearly homogeneous polarizable sheets in contrast to diffraction gratings, since they can be tightly arranged into the array. This allows to control EM waves and create the fields with more higher spatial resolution. In general, metasurfaces can provide complete control over the reflected and transmitted waves in a wide range of EM devices [31–35]. It should be noted that if a planar array consisting of subwavelength elements has a periodicity comparable to or greater than the wavelength, then such structures can not be defined as metasurfaces. Moreover, if inclusions are located in the array with an optically small spacing but their height (the thickness of the metasurface) is large, such an array should be called as a bulk material. Examples of such materials are moth-eye antireflection coatings designed for solar cells, thick layers consisting of essentially long metal nanorods or carbon nanotubes, etc. [36]

Artificial 2D periodic structures with EM waves controlling were studied long before the appearance of the term "metasurface". Intensive studies of wire dense arrays or so-called inductive mesh led to the appearance of lightweight reflectors, polarizers and other devices [37–39]. As a result, the averaged boundary conditions and a homogenization theory of artificial EM surfaces were explored. Thereby, the development of metasurfaces opens up new possibilities and functionality to control and transform electromagnetic fields.

1.2.2 Functionalities

We mentioned earlier that metamaterials exhibit the exotic electromagnetic properties which are not readily available in nature. They have many great functionalities that also can be realized using metasurfaces and in some cases, they are more preferable using metamaterials. There are at least three reasons in favor of the use of metasurfaces:

- bulk periodic arrays or multilayered structures are very difficult to realize for optical wavelengths since it requires to use very complex and expensive technologies.

- electromagnetic waves have to propagate the considerable distances in bulk metamaterials, which accompanied by high losses, especially at the resonance. The undesirable absorption in the volume of metamaterials reduces many of their proposed practical applications, such as ideal lensing [21]. Metasurfaces demonstrate much better ability to form light streams compare to bulk metamaterials, since they have lower absorption levels, or even exhibit lossless behaviour [34, 35, 40].

- since metasurfaces are electrically thin layers (much smaller than the wavelength of interest), they can be easily integrated into nanophotonic systems or can significantly reduce the dimensions of the antenna arrays or other radio devices at the microwave range [22, 23, 41].

Thus, using metasurfaces for full-wave control, especially in the optical spectrum range are more preferred. At the moment, a large number of functionalities have been obtained using metasurfaces. Several review articles describing their principle of work, functionality and some applications of metasurfaces [42, 55–57] were published. Here, we pay attention especially to two review papers [42, 57]. The first paper is a survey in the form of a general theory, design, and implementation of optically thin absorbing metasurfaces, and the second one is a functional classification of metasurfaces based on bianisotropic inclusions and their applications.

Bianisotropic metasurfaces are oriented to many applications from frequency-selective absorption to polarization tailoring. They possess bianisotropic properties using chiral-based [58–60] and omega-based [61] inclusions. Applying external electric or magnetic fields, polarized chiral inclusions simultaneously exhibit a derivation of parallel electric and magnetic dipole moments, while in omega-based inclusions both electric and magnetic

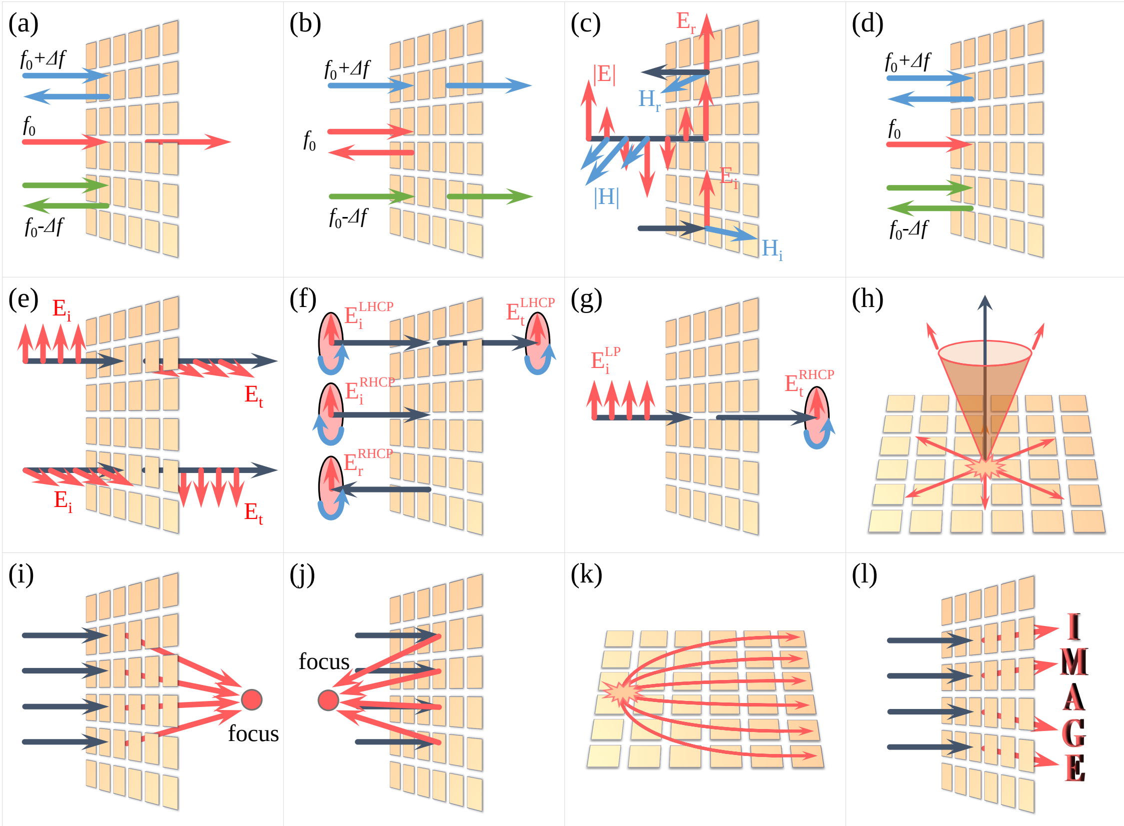

Figure 1.2: Functionalities of metasurfaces: (a) bandpass frequency selective surface [43], (b) bandstop frequency selective surface [44], (c) high impedance surface [45], (d) narrow-band perfect absorber [46], (e) twist polarizer [47], (f) right-handed circular-polarization frequency selective surface [48], (g) linear-to-circular polarization converter [49], (h) two-dimensional leaky-wave antenna with a conical-beam pattern [50], (i) focusing transmitarray [51], (j) focusing reflectarray [52], (k) flat Luneburg lens [53], and (l) hologram [54].

dipole moments are orthogonal to each other due to only electric or magnetic external field [62, 63]. Consequently, metasurfaces with or without bianisotropy exhibit multiple functionalities which are summarized in the Figure 1.2.

As seen from Fig. 1.2, manipulation of polarization, amplitude, phase and other characteristics consists of their functionalities, as well as makes it possible to multiple application for EM devices. Metasurfaces are compatible with simple planar fabrication technologies which in turn leads to ultra-thin devices with unprecedented functionalities. It can be expected, that a progress in the design and implementation of metasurfaces will lead to new functionalities and improved their performance. Therefore, it might lead to the development of new designs for optically thin metasurfaces with increased bandwidth and reduced losses.

1.2.3 Practical scalability of metasurfaces

Metasurfaces with their remarkable EM properties can work in a wide electromagnetic spectrum as seen from Figure 1.3. However, there is a problem of practical scalability of designs for the considered frequency range. As it is well known, scalability is the

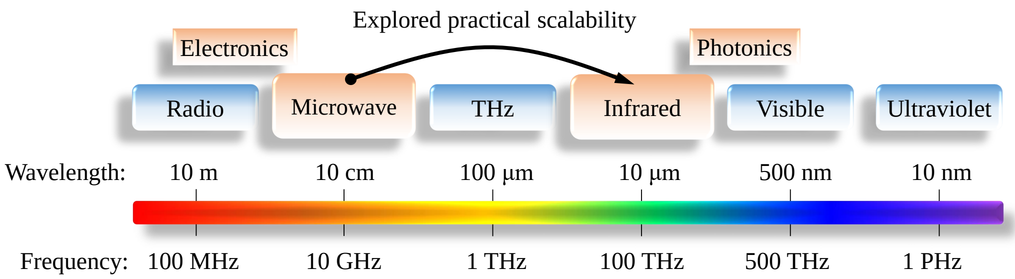

Figure 1.3: The electromagnetic spectrum of metasurface research.

capacity to be changed in size or scale. In order to increase the operational frequency of metasurface, the unit cell size has to be decreased proportionally. Consequently, there are significant difficulties and limitations in the implementation of functional metasurfaces at higher frequencies, since this requires the use of micro- and nano-technologies, which in turn have limitations in the resolution of the fabrication as well as materials properties have to be taken into account. It worth to notice that for natural materials this problem is very acute since the EM properties strictly depend on the properties of the material, and do not on its structural parameters.

The first known artificial homogeneous media that have dispersion properties of reflection or transmission modes were realized for radio frequency range [64, 65] based on the technological capabilities of the time. Not so long ago, even the first experimental demonstration of a negative refractive medium was realized in the microwave frequency range 4.2–4.6 GHz [2]. Hence, the realization of metastructures with macroscale size is easier and less expensive too. Development of micro and nanofabrication give us possibilities in practical downscaling of m-scale metastructures to μm-scaling or even nm-scaling size. The development of metasurfaces came at that time when fabrication technologies have allowed to create the nanoscale artificial structures for the operation at the visible wavelength range. Therefore, practical realization of functional metasurfaces almost simultaneously from radio frequency to visible spectral ranges has been demonstrated. Nevertheless, a huge amount of metasurfaces were implemented in the microwave range for the first time and later there is realized for the shorter wavelengths by proportional downscaling of structural parameters with taking into account dispersion properties of used materials. One of such examples are the mushroom-type metasurfaces. The first fabrication demonstration has been done in the microwave range [45] and later it was shown for IR spectral range [66]. Another famous example of practical scalability of metasurfaces is the patch-based array antennas that at first was realized for operation microwave frequency of 3 GHz [67] and later experimentally tested at 200 THz frequency range [68]. On more example is the metasurface based on split-ring resonators that usually possesses a magnetic response. Such properties were shown for THz range [69] and, hereinafter, the magnetic response was achieved even for the visible wavelengths [70]. Thus, all of these examples demonstrate some possibilities of practical scalability and capabilities of metasurfaces which have striking advantages in comparison with natural materials.

Nevertheless, metasurfaces based on 3D resonant inclusions are problematic to realize even for the microwave range, and it is very laborious to fabricate them for IR and visible ranges. To some extent, we address this issue this to realization of metasurfaces based on 3D helical inclusions that can exhibit advantageous EM properties for wide EM spectrum [71–74]. Using Direct Laser Writing technique, it is possible to fabricate metasurfaces consisting of 3D metallic microscale helical resonators was reported in Refs. [75–78] that give us a good direction for solving of problem for practical scalability and fabrication of 3D functional helix-based metasurfaces.

1.2.4 Applications

Almost practical applications of metasurfaces still have only potential possibilities, since metamaterials are a relatively recent research area and the horizon of possibilities has to be explored. Nevertheless, EM metasurfaces open up new opportunities for applications in many fields of technology, from electronics to photonics. The first experimental realization of negative refractive media has a significant contribution to science since it could be used to create a perfect flat lens, which would overcome the diffraction limits of existing materials. Such lenses are very useful for biomedical purposes. In the microwave frequency range, metastructures are used for antenna applications. More generally, the concept of metamaterials is used to create various high-impedance surfaces, artificial magnetic conductors for flat low-profile antennas, etc. [79–81]. Potential applications could be found in medicine for effective detection of cancer with a safer and less painful experience, and 3D imaging of teeth that works more accurate than conventional X-Ray imaging, also specifically for security checking situation in airports and other places by using THz radiation. Most potential applications of metastructures are optical filters, medical devices, remote aerospace applications, sensor detection and infrastructure monitoring, smart solar power management, crowd control, radomes, high-frequency battlefield communication and lenses for high-gain antennas, improving ultrasonic sensors, and even shielding structures from earthquakes. Especially, metasurfaces open up new possibilities in the design of cloaking devices, imaging and sensing, data storage and quantum information processing, and also in light harvesting [31, 32, 82].

As an example, some practical application and commercialization of metamaterial devices were shown on "10th International Congress on Advanced Electromagnetic Materials in Microwaves and Optics, 2016". Unfortunately, there was only two reports supporting an antenna application and metamaterial-based liquid crystal display manufacturing [83, 84]. This indicates that metamaterials are still young scientific field and actual applications in life are simply limited by our imagination.

It is worth mentioning one example from history. Physicist Heinrich Rudolf Hertz has experimentally verified the existence of electromagnetic waves in 1887, and when people asked him where it could be used, he answered: "It's of no use whatsoever. This is just an experiment that proves Maestro Maxwell was right – we just have these mysterious electromagnetic waves that we cannot see with the naked eye. But they are there." Today people even can not imagine their life without using electromagnetic waves!

Chapter 2

Synthesis of helix-based metasurfaces

The method how to synthesize off-resonance transparent metasurfaces based on helical resonators possessing equivalent EM response to external excitation owing to the tailoring of structural parameters of resonators to the balance of their polarizabilities is described (Section 2.1). Towards to synthesis of metasurfaces, a novel method for determination of polarizability tensor components of electrically small inclusions with an arbitrary shape is proposed (Section 2.2). This method based on the scattering response is measured using numerical simulation in the far-field zone and in two opposite directions that significantly simplify the way to find all polarizability components. Further, helical resonators were chosen as the preferable EM polarizable resonant inclusions by finding their individual polarizabilities to create the off-resonance transparent metasurfaces in accordance with desired EM properties. Structural parameters of helical resonators were optimized in such a way as to satisfy the condition for balancing the induced dipole moments (so-called balance of polarizabilities) in the helices by the excitation of linearly polarized plane waves at normal incidence (Section 2.3). Using proposed analytical approach and numerical simulation, polarization-insensitive off-resonance transparent metasurfaces based on helices with balanced polarizabilities were demonstrated (Section 2.4).

2.1 Reflection, transmission, and absorption from metasurface

The main EM characteristics of metasurfaces are usually described by the reflection (R), transmission (T), and absorption (A) coefficients. In physics, the reflection coefficient is a parameter that describes how much of an electromagnetic wave is reflected by an impedance discontinuity in the transmission medium. It is equal to the ratio of the amplitude of the reflected wave to the incident wave. The reflection coefficient is closely related to the transmission coefficient. The transmission coefficient is used when wave propagation in a medium containing discontinuities is considered. A transmission coefficient describes the amplitude, intensity, or total power of a transmitted wave relative to an incident wave. Absorption of electromagnetic radiation is the way in which the energy of a photon is taken up by matter, typically the electrons of an atom. Thus, the electromagnetic energy is transformed into internal energy of the absorber, for example, thermal energy. All these coefficients can be expressed as follows:

$$R = \frac{\mathbf{E}_{\mathrm{r}}}{\mathbf{E}_{\mathrm{inc}}}, \qquad T = \frac{\mathbf{E}_{\mathrm{t}}}{\mathbf{E}_{\mathrm{inc}}}, \qquad A = 1 - R - T, \tag{2.1}$$

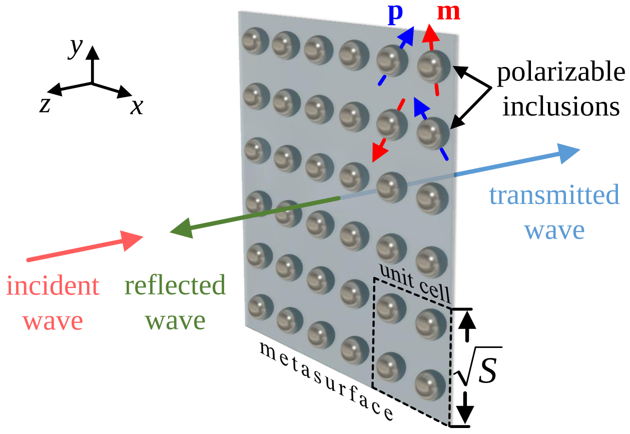

Figure 2.1: A schematic illustration of electrically thin metasurface excited by incident waves.

where $\mathbf{E}_{\mathrm{inc}}$, $\mathbf{E}_{\mathrm{r}}$, and $\mathbf{E}_{\mathrm{t}}$ are amplitude of incident, reflected, and transmitted fields, respectively. In optics and electromagnetics in general, "reflection, transmission, and absorption coefficients" can refer to either the amplitude reflection, transmission, and absorption coefficients described here, or the reflectance, transmittance, and absorbance depending on context. It should be mentioned that we speak about regular reflection (or specular reflection) and regular transmission (or direct transmission) when no diffusion occurs, reflection or transmission of unidirectional waves results in an unidirectional waves according to the laws of geometrical optics. However, reflection and transmission can be accompanied by diffusion (also called scattering), which is the process of deflecting unidirectional waves into many directions. We do not consider diffuse reflection and transmission processes.

As a starting point, we consider a plane EM wave incident onto a infinite metasurface comprising of sub-wavelength resonant inclusions with arbitrary shape arranged on a periodic 2D lattice with the unit cell of the area S. These inclusions should be polarizable to the external excitation that lead to inducing of electric ($\mathbf{p}$) and magnetic dipole ($\mathbf{m}$) moments, respectively. By assuming infinite metasurface, the reflected and transmitted fields can be expressed as follows [85]:

$$\mathbf{E}_{\mathrm{r}} = -\frac{j\omega}{2S}\left(\eta_0\mathbf{p} - \mathbf{n}\times\mathbf{m}\right), \tag{2.2}$$

$$\mathbf{E}_{\mathrm{t}} = \mathbf{E}_{\mathrm{inc}} - \frac{j\omega}{2S}\left(\eta_0\mathbf{p} + \mathbf{n}\times\mathbf{m}\right), \tag{2.3}$$

where ω is the angular frequency, $\mathbf{E}_{\mathrm{inc}}$ is incident electric field, η_0 is the free-space impedance. Since, inclusions in metasurface have sub-wavelength size their induced electric and magnetic moments can be characterised by effective polarizabilities (ability to form dipoles) of inclusions as [86]:

$$\mathbf{p} = \overline{\overline{\alpha}}_{\mathrm{ee}}\cdot\mathbf{E}_{\mathrm{inc}} + \overline{\overline{\alpha}}_{\mathrm{em}}\cdot\mathbf{H}_{\mathrm{inc}}, \tag{2.4}$$

$$\mathbf{m} = \overline{\overline{\alpha}}_{\mathrm{me}}\cdot\mathbf{E}_{\mathrm{inc}} + \overline{\overline{\alpha}}_{\mathrm{mm}}\cdot\mathbf{H}_{\mathrm{inc}}, \tag{2.5}$$

where $\overline{\overline{\widehat{\alpha}}}_{\rm ee}$, $\overline{\overline{\widehat{\alpha}}}_{\rm mm}$, $\overline{\overline{\widehat{\alpha}}}_{\rm em}$ and $\overline{\overline{\widehat{\alpha}}}_{\rm me}$ are an effective electric, magnetic and magnetoelectric polarizability tensors of the unit cell. The effective polarizabilities include the effects of electromagnetic interactions between inclusions within the metasurface and their determination represents a difficult task since it requires consideration of the complex interaction in the metasurface. However, the resonant inclusions are density-packed ($\lambda_{\rm r} < \sqrt{S}$) in the metasurface that cannot create new dipole moments with neighboring inclusions.

Thus, effective polarizabilities have the same components as the individual ones and can be written as follows [87]:

$$\begin{aligned}
\overline{\overline{\widehat{\alpha}}}_{\rm ee} &= \widehat{\alpha}_{\rm ee}^{\rm xx}\mathbf{x}_0\mathbf{x}_0 + \widehat{\alpha}_{\rm ee}^{\rm xy}\mathbf{x}_0\mathbf{y}_0 + \widehat{\alpha}_{\rm ee}^{\rm yx}\mathbf{y}_0\mathbf{x}_0 + \widehat{\alpha}_{\rm ee}^{\rm yy}\mathbf{y}_0\mathbf{y}_0,\\
\overline{\overline{\widehat{\alpha}}}_{\rm em} &= \widehat{\alpha}_{\rm em}^{\rm xx}\mathbf{x}_0\mathbf{x}_0 + \widehat{\alpha}_{\rm em}^{\rm xy}\mathbf{x}_0\mathbf{y}_0 + \widehat{\alpha}_{\rm em}^{\rm yx}\mathbf{y}_0\mathbf{x}_0 + \widehat{\alpha}_{\rm em}^{\rm yy}\mathbf{y}_0\mathbf{y}_0,\\
\overline{\overline{\widehat{\alpha}}}_{\rm me} &= \widehat{\alpha}_{\rm me}^{\rm xx}\mathbf{x}_0\mathbf{x}_0 + \widehat{\alpha}_{\rm me}^{\rm xy}\mathbf{x}_0\mathbf{y}_0 + \widehat{\alpha}_{\rm me}^{\rm yx}\mathbf{y}_0\mathbf{x}_0 + \widehat{\alpha}_{\rm me}^{\rm yy}\mathbf{y}_0\mathbf{y}_0,\\
\overline{\overline{\widehat{\alpha}}}_{\rm mm} &= \widehat{\alpha}_{\rm mm}^{\rm xx}\mathbf{x}_0\mathbf{x}_0 + \widehat{\alpha}_{\rm mm}^{\rm xy}\mathbf{x}_0\mathbf{y}_0 + \widehat{\alpha}_{\rm mm}^{\rm yx}\mathbf{y}_0\mathbf{x}_0 + \widehat{\alpha}_{\rm mm}^{\rm yy}\mathbf{y}_0\mathbf{y}_0,
\end{aligned} \tag{2.6}$$

where $\mathbf{x}_0, \mathbf{y}_0$ are the unit vectors of the Cartesian coordinate system and, as example, $\widehat{\alpha}_{\rm ee}^{\rm xx}$ is component of electric effective polarizability tensor defined in x-axis direction.

Then, by substituting the effective polarizabilities from (2.6) to equation for electric and magnetic dipolar moments (2.4) and(2.5), respectively, and ultimately substituting to (2.2) and (2.3) with re-arranging the terms, we can get expressions for reflected and transmitted fields. The reflected electric field can be represented in the follows:

$$\begin{aligned}
\mathbf{E}_{\rm r} = -\frac{j\omega}{2S}\Bigg\{&\left[\eta_0\widehat{\alpha}_{\rm ee}^{\rm xx} - \widehat{\alpha}_{\rm em}^{\rm xy} + \widehat{\alpha}_{\rm me}^{\rm yx} - \frac{1}{\eta_0}\widehat{\alpha}_{\rm mm}^{\rm yy}\right]\mathbf{x}_0\mathbf{x}_0\\
&+\left[\eta_0\widehat{\alpha}_{\rm ee}^{\rm xy} + \widehat{\alpha}_{\rm em}^{\rm xx} + \widehat{\alpha}_{\rm me}^{\rm yy} + \frac{1}{\eta_0}\widehat{\alpha}_{\rm mm}^{\rm yx}\right]\mathbf{x}_0\mathbf{y}_0\\
&+\left[\eta_0\widehat{\alpha}_{\rm ee}^{\rm yx} - \widehat{\alpha}_{\rm em}^{\rm yy} - \widehat{\alpha}_{\rm me}^{\rm xx} + \frac{1}{\eta_0}\widehat{\alpha}_{\rm mm}^{\rm xy}\right]\mathbf{y}_0\mathbf{x}_0\\
&+\left[\eta_0\widehat{\alpha}_{\rm ee}^{\rm yy} + \widehat{\alpha}_{\rm em}^{\rm yx} - \widehat{\alpha}_{\rm me}^{\rm xy} - \frac{1}{\eta_0}\widehat{\alpha}_{\rm mm}^{\rm xx}\right]\mathbf{y}_0\mathbf{y}_0\Bigg\}\cdot\mathbf{E}_{\rm inc}.
\end{aligned} \tag{2.7}$$

Similarly, we can write the transmitted electric field as:

$$\begin{aligned}
\mathbf{E}_{\rm t} = \Bigg\{&\left[1 - \frac{j\omega}{2S}\left(\eta_0\widehat{\alpha}_{\rm ee}^{\rm xx} - \widehat{\alpha}_{\rm em}^{\rm xy} - \widehat{\alpha}_{\rm me}^{\rm yx} + \frac{1}{\eta_0}\widehat{\alpha}_{\rm mm}^{\rm yy}\right)\right]\mathbf{x}_0\mathbf{x}_0\\
&+\left[1 - \frac{j\omega}{2S}\left(\eta_0\widehat{\alpha}_{\rm ee}^{\rm yy} + \widehat{\alpha}_{\rm em}^{\rm yx} + \widehat{\alpha}_{\rm me}^{\rm xy} + \frac{1}{\eta_0}\widehat{\alpha}_{\rm mm}^{\rm xx}\right)\right]\mathbf{y}_0\mathbf{y}_0\\
&-\frac{j\omega}{2S}\left(\eta_0\widehat{\alpha}_{\rm ee}^{\rm yx} - \widehat{\alpha}_{\rm em}^{\rm yy} + \widehat{\alpha}_{\rm me}^{\rm xx} - \frac{1}{\eta_0}\widehat{\alpha}_{\rm mm}^{\rm xy}\right)\mathbf{y}_0\mathbf{x}_0\\
&-\frac{j\omega}{2S}\left(\eta_0\widehat{\alpha}_{\rm ee}^{\rm xy} + \widehat{\alpha}_{\rm em}^{\rm xx} - \widehat{\alpha}_{\rm me}^{\rm yy} - \frac{1}{\eta_0}\widehat{\alpha}_{\rm mm}^{\rm yx}\right)\mathbf{x}_0\mathbf{y}_0\Bigg\}\cdot\mathbf{E}_{\rm inc}.
\end{aligned} \tag{2.8}$$

Based on Eqns. (2.7) and (2.8) can be found reflection, transmission and absorption coefficients from metasurface consisting of density-packed resonant polarizable inclusions.

This approach for the definition of the reflected and transmitted fields from metasurface through effective polarizabilities has been reported in literature [88]. Therefore, if we know the effective polarizability tensors of the resonant inclusions, the main EM characteristics of metasurface can be found. Moreover, the definition of polarizabilities gives more useful information than an only determination of R, T, and A. Polarizabilities determine the property of matter and the dynamical response of a bound system to external fields and provide insight into an inclusion's internal structure. Consequently, there is an urgent need for calculation of all components of polarizability tensors of arbitrary shape inclusions.

2.2 Calculation of all components of polarizability tensors

Here, we present a novel method for determination of all components of individual polarizability tensors of a polarizable single inclusion with an arbitrary shape. This approach is based on the determination of scattered electric field in a far-field zone by the excitation of an incident plane wave from two opposite side with different polarization states. This approach comes from the first attempt to obtain polarizability tensors based on the dipole approximation theory and using numerical simulation for the far-field scattering response was considered in our litherature [89]. Here, we improved and simplified this polarizability retrieval method so that it can be utilized for arbitrary shaped small inclusions. This method was published in our article [8-A].

2.2.1 Definition of dipole moments

In order to determine the individual polarizabilities of an arbitrary inclusion, we analyze the far-field response of the inclusion to incident plane waves. We start from writing the relations for the polarizabilities of the inclusion in terms of the dipole moments induced by a set of probing fields. In the most general case, assuming that the induced dipole moments in the inclusion depend linearly on the applied fields, the dipolar moments induced in the inclusion relate to the incident fields (at the location of the inclusion) by the polarizability tensors as:

$$\begin{bmatrix} \mathbf{p} \\ \mathbf{m} \end{bmatrix} = \begin{bmatrix} \overline{\overline{\alpha}}_{\rm ee} & \overline{\overline{\alpha}}_{\rm em} \\ \overline{\overline{\alpha}}_{\rm me} & \overline{\overline{\alpha}}_{\rm mm} \end{bmatrix} \cdot \begin{bmatrix} \mathbf{E}_{\rm inc} \\ \mathbf{H}_{\rm inc} \end{bmatrix}. \tag{2.9}$$

An important issue is the choice of the alignment of the inclusion with respect to the center of the coordinate system from which the far-field response of the inclusion is determined (see Fig. 2.2). The proper choice is that when the induced electric and magnetic dipole moments of the inclusion are located at the coordinate origin. If this condition is not satisfied, the higher order multiple moments start to gain importance and one should take them into account, otherwise, the accuracy of the polarizability retrieval method will decrease. Usually, since electrically small size of the inclusion is assumed, setting the origin to the geometrical center of the inclusion is the proper choice. As an example, here we write the formulas for the case when the incident plane waves illuminating the inclusion propagate along the z-axis. It will be shown that the directions can be chosen arbitrarily. Obviously, choosing the z-directed incident waves, one can find only the components of

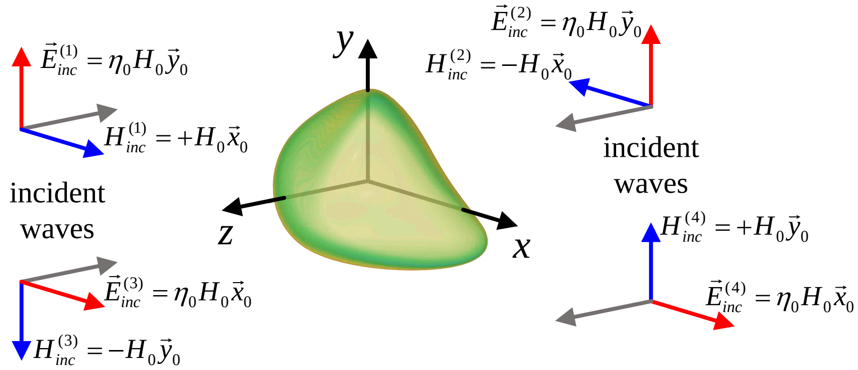

Figure 2.2: An arbitrary shape inclusion in the center of a Cartesian coordinate system which is excited by incident linearly polarized wave with different polarization states.

the polarizability tensors in the x, y-plane. The other components can be determined similarly using incident waves propagating along the x and y-axes. Taking into account that the incident plane waves are transverse and propagate along the z-axis, equations (2.9) simplify to:

$$\begin{bmatrix} \mathbf{p}_{\rm x} \\ \mathbf{p}_{\rm y} \end{bmatrix} = \begin{bmatrix} \alpha_{\rm ee}^{\rm xx} & \alpha_{\rm ee}^{\rm xy} \\ \alpha_{\rm ee}^{\rm yx} & \alpha_{\rm ee}^{\rm yy} \end{bmatrix} \cdot \begin{bmatrix} E_{\rm inc}^{x} \\ E_{\rm inc}^{y} \end{bmatrix} + \begin{bmatrix} \alpha_{\rm em}^{\rm xx} & \alpha_{\rm em}^{\rm xy} \\ \alpha_{\rm em}^{\rm yx} & \alpha_{\rm em}^{\rm yy} \end{bmatrix} \cdot \begin{bmatrix} H_{\rm inc}^{x} \\ H_{\rm inc}^{y} \end{bmatrix},$$
$$\begin{bmatrix} \mathbf{m}_{\rm x} \\ \mathbf{m}_{\rm y} \end{bmatrix} = \begin{bmatrix} \alpha_{\rm me}^{\rm xx} & \alpha_{\rm me}^{\rm xy} \\ \alpha_{\rm me}^{\rm yx} & \alpha_{\rm me}^{\rm yy} \end{bmatrix} \cdot \begin{bmatrix} E_{\rm inc}^{x} \\ E_{\rm inc}^{y} \end{bmatrix} + \begin{bmatrix} \alpha_{\rm mm}^{\rm xx} & \alpha_{\rm mm}^{\rm xy} \\ \alpha_{\rm mm}^{\rm yx} & \alpha_{\rm mm}^{\rm yy} \end{bmatrix} \cdot \begin{bmatrix} H_{\rm inc}^{x} \\ H_{\rm inc}^{y} \end{bmatrix}. \tag{2.10}$$

Hereafter we use numerical indices x, y, z, representing the $\mathbf{x}_0$, $\mathbf{y}_0$ and $\mathbf{z}_0$ projections of vectors, respectively. It can be seen from (2.10) that to determine any polarizability component, it is insufficient to know the response of the inclusion to only one incident wave. The simplest way to find the component is an illumination of the inclusion by two incident plane waves $\mathbf{E}_{\rm inc}^{(3)}$ and $\mathbf{E}_{\rm inc}^{(4)}$ (see Fig. 2.2) with the following polarization states:

$$\mathbf{E}_{\rm inc} = \eta_0 H_0 \mathbf{x}_0, \qquad \mathbf{H}_{\rm inc} = \pm H_0 \mathbf{y}_0, \tag{2.11}$$

in which the $\pm$ sign corresponds to waves propagating in $+\mathbf{z}_0$ and $-\mathbf{z}_0$ directions, respectively, and H_0 is the magnitude of the incident magnetic field. The inclusion is situated in free space with the characteristic impedance η_0. Here, for simplicity, we assume that the two incident waves have equal amplitudes and phases at the location of the inclusion. Although in inclusion it is difficult to generate two incident waves with precisely equal phases, the problem can be solved similarly with the assumption that the waves in (2.11) have not only different propagation directions but also different amplitudes and phases, meaning that this assumption is not limiting. Substituting (2.11) in (2.10), we get:

$$\begin{aligned}
p_{\rm x}^{\pm} &= \alpha_{\rm ee}^{\rm xx}\eta H_0 \pm \alpha_{\rm em}^{\rm xy} H_0,\\
p_{\rm y}^{\pm} &= \alpha_{\rm ee}^{\rm yx}\eta H_0 \pm \alpha_{\rm em}^{\rm yy} H_0,\\
m_{\rm x}^{\pm} &= \alpha_{\rm me}^{\rm xx}\eta H_0 \pm \alpha_{\rm mm}^{\rm xy} H_0,\\
m_{\rm y}^{\pm} &= \alpha_{\rm me}^{\rm yx}\eta H_0 \pm \alpha_{\rm mm}^{\rm yy} H_0,
\end{aligned} \tag{2.12}$$

where the double signs correspond to the double signs in (2.11). Next, the simple solution of the equations with regard to the polarizability components reads:

$$\begin{aligned}
\alpha_{\rm ee}^{\rm xx} &= \frac{1}{2\eta H_0}(p_{\rm x}^{+} + p_{\rm x}^{-}), \quad & \alpha_{\rm em}^{\rm xy} &= \frac{1}{2H_0}(p_{\rm x}^{+} - p_{\rm x}^{-}),\\
\alpha_{\rm ee}^{\rm yx} &= \frac{1}{2\eta H_0}(p_{\rm y}^{+} + p_{\rm y}^{-}), \quad & \alpha_{\rm em}^{\rm yy} &= \frac{1}{2H_0}(p_{\rm y}^{+} - p_{\rm y}^{-}),\\
\alpha_{\rm me}^{\rm xx} &= \frac{1}{2\eta H_0}(m_{\rm x}^{+} + m_{\rm x}^{-}), \quad & \alpha_{\rm mm}^{\rm xy} &= \frac{1}{2H_0}(m_{\rm x}^{+} - m_{\rm x}^{-}),\\
\alpha_{\rm me}^{\rm yx} &= \frac{1}{2\eta H_0}(m_{\rm y}^{+} + m_{\rm y}^{-}), \quad & \alpha_{\rm mm}^{\rm yy} &= \frac{1}{2H_0}(m_{\rm y}^{+} - m_{\rm y}^{-}).
\end{aligned} \tag{2.13}$$

In order to derive the other 8 polarizability components in the x, y-plane, we choose the incidence in the form with $\mathbf{E}_{\rm inc}^{(1)}$ and $\mathbf{E}_{\rm inc}^{(2)}$ as:

$$\mathbf{E}_{\rm inc} = \eta_0 H_0 \mathbf{y}_0, \qquad \mathbf{H}_{\rm inc} = \pm H_0 \mathbf{x}_0. \tag{2.14}$$

Likewise, for these two different incident waves, electric and magnetic dipole moments can written in according to (2.7) as:

$$\begin{aligned}
\bar{p}_{\rm x}^{\pm} &= \alpha_{\rm ee}^{\rm xy}\eta H_0 \pm \alpha_{\rm em}^{\rm xx} H_0,\\
\bar{p}_{\rm y}^{\pm} &= \alpha_{\rm ee}^{\rm yy}\eta H_0 \pm \alpha_{\rm em}^{\rm yx} H_0,\\
\bar{m}_{\rm x}^{\pm} &= \alpha_{\rm me}^{\rm xy}\eta H_0 \pm \alpha_{\rm mm}^{\rm xx} H_0,\\
\bar{m}_{\rm y}^{\pm} &= \alpha_{\rm me}^{\rm yy}\eta H_0 \pm \alpha_{\rm mm}^{\rm yx} H_0,
\end{aligned} \tag{2.15}$$

where we use notations with bars in order to distinguish the induced dipole moments for different polarization states in (2.11) and (2.14). The double sign in (2.15) corresponds to the double sign in (2.14). Similarly, we can derive expressions for the polarizability components:

$$\begin{aligned}
\alpha_{\rm ee}^{\rm xy} &= \frac{1}{2\eta H_0}(\bar{p}_{\rm x}^{+} + \bar{p}_{\rm x}^{-}), \quad & \alpha_{\rm em}^{\rm xx} &= \frac{1}{2H_0}(\bar{p}_{\rm x}^{+} - \bar{p}_{\rm x}^{-}),\\
\alpha_{\rm ee}^{\rm yy} &= \frac{1}{2\eta H_0}(\bar{p}_{\rm y}^{+} + \bar{p}_{\rm y}^{-}), \quad & \alpha_{\rm em}^{\rm yx} &= \frac{1}{2H_0}(\bar{p}_{\rm y}^{+} - \bar{p}_{\rm y}^{-}),\\
\alpha_{\rm me}^{\rm xy} &= \frac{1}{2\eta H_0}(\bar{m}_{\rm x}^{+} + \bar{m}_{\rm x}^{-}), \quad & \alpha_{\rm mm}^{\rm xx} &= \frac{1}{2H_0}(\bar{m}_{\rm x}^{+} - \bar{m}_{\rm x}^{-}),\\
\alpha_{\rm me}^{\rm yy} &= \frac{1}{2\eta H_0}(\bar{m}_{\rm y}^{+} + \bar{m}_{\rm y}^{-}), \quad & \alpha_{\rm mm}^{\rm yx} &= \frac{1}{2H_0}(\bar{m}_{\rm y}^{+} - \bar{m}_{\rm y}^{-}).
\end{aligned} \tag{2.16}$$

Thus, we have determined 16 polarizability components of the inclusion in terms of the induced dipole moments by probing plane waves. The other 20 components one can derive in the same way illuminating the inclusion by waves propagating along the x and y-axes. Further, we will determine 16 components of individual polarizability tensors from the far-zone scattered fields.

2.2.2 Calculation of all polarizabilities for electrically small inclusions

A scatterer with induced oscillating electric and magnetic multipoles radiates energy in all directions. Here, we study the case of an electrically small inclusion (the size of the inclusion is small compared to the wavelength of the incident waves) that allows us to take into account only the lowest multipoles, i.e. the electric and magnetic dipoles. The scattered far fields from an electrically small inclusion are defined by the induced dipole moments in the form [90]:

$$\begin{aligned} \mathbf{E}_{\rm sc} &= \frac{k^2}{4\pi\epsilon_0 r}e^{-jkr}\left[(\mathbf{n}\times\mathbf{p})\times\mathbf{n}-\frac{1}{c\mu_0}\mathbf{n}\times\mathbf{m}\right], \\ \mathbf{H}_{\rm sc} &= \frac{1}{\eta_0}\mathbf{n}\times\mathbf{E}_{\rm sc}, \end{aligned} \tag{2.17}$$

where $\mathbf{n}$ is the unit vector in the direction of observation, r is the distance between the inclusion and the observation point, $k=\omega/c$ is the wave number in surrounding space, and the time-dependence $e^{j\omega t}$ is understood. Since it is required to find only the $\mathbf{x}_0$ and $\mathbf{y}_0$ projections of the electric and magnetic dipole moments (according to (2.10) and (2.16)), we choose the observation direction to be along $+z$ and $-z$ (however, this choice is not compulsory). Taking this into account, we can rewrite the scattered electric field in (2.17) as:

$$\begin{aligned} {}_{\rm z}\mathbf{E}_{\rm sc} &= \gamma\left[(\mathbf{p}_{\rm x}+\frac{1}{\eta_0}\mathbf{m}_{\rm y})\mathbf{x}_0+(\mathbf{p}_{\rm y}-\frac{1}{\eta_0}\mathbf{m}_{\rm x})\mathbf{y}_0\right], \\ {}_{-\rm z}\mathbf{E}_{\rm sc} &= \gamma\left[(\mathbf{p}_{\rm x}-\frac{1}{\eta_0}m_{\rm y})\mathbf{x}_0+(\mathbf{p}_{\rm y}+\frac{1}{\eta_0}\mathbf{m}_{\rm x})\mathbf{y}_0\right], \end{aligned} \tag{2.18}$$

where $\gamma=\dfrac{k^2}{4\pi\epsilon_0 r}e^{-jkr}$ is a parameter introduced for convenience. Although these formulas are for the case of the incidence (2.11), similar formulas can be written also (with notations in bars) for the incidence defined in (2.14). Combining equations (2.18), we find formulas for calculation of electric and magnetic dipole moments:

$$\begin{aligned} p_{\rm x}^{\pm} &= \frac{1}{2\gamma}({}_{\rm z}E_{\rm sc_x}^{\pm}+{}_{-\rm z}E_{\rm sc_x}^{\pm}), \\ p_{\rm y}^{\pm} &= \frac{1}{2\gamma}({}_{\rm z}E_{\rm sc_y}^{\pm}+{}_{-\rm z}E_{\rm sc_y}^{\pm}), \\ m_{\rm x}^{\pm} &= \frac{\eta_0}{2\gamma}({}_{-\rm z}E_{\rm sc_y}^{\pm}-{}_{\rm z}E_{\rm sc_y}^{\pm}), \\ m_{\rm y}^{\pm} &= \frac{\eta_0}{2\gamma}({}_{\rm z}E_{\rm sc_x}^{\pm}-{}_{-\rm z}E_{\rm sc_x}^{\pm}). \end{aligned} \tag{2.19}$$

At this step, we are ready to write general formulas for calculating all the polarizability components in the x, y-plane. First, we consider the case when the incident fields equal $\mathbf{E}_{\rm inc} = \eta_0 H_0 \mathbf{x_0}$, $\mathbf{H}_{\rm inc} = \pm H_0 \mathbf{y_0}$. Then, substituting (2.19) in (2.13), we write the expressions for the polarizability components:

$$
\begin{aligned}
\alpha_{\rm ee}^{\rm xx} &= \frac{1}{4\gamma\eta H_0}\left({}_{\rm z}E_{\rm sc_x}^{+} + {}_{-\rm z}E_{\rm sc_x}^{+} + {}_{\rm z}E_{\rm sc_x}^{-} + {}_{-\rm z}E_{\rm sc_x}^{-}\right), \\
\alpha_{\rm em}^{\rm xy} &= \frac{1}{4\gamma H_0}\left({}_{\rm z}E_{\rm sc_x}^{+} + {}_{-\rm z}E_{\rm sc_x}^{+} - {}_{\rm z}E_{\rm sc_x}^{-} - {}_{-\rm z}E_{\rm sc_x}^{-}\right), \\
\alpha_{\rm ee}^{\rm yx} &= \frac{1}{4\gamma\eta H_0}\left({}_{\rm z}E_{\rm sc_y}^{+} + {}_{-\rm z}E_{\rm sc_y}^{+} + {}_{\rm z}E_{\rm sc_y}^{-} + {}_{-\rm z}E_{\rm sc_y}^{-}\right), \\
\alpha_{\rm em}^{\rm yy} &= \frac{1}{4\gamma H_0}\left({}_{\rm z}E_{\rm sc_y}^{+} + {}_{-\rm z}E_{\rm sc_y}^{+} - {}_{\rm z}E_{\rm sc_y}^{-} - {}_{-\rm z}E_{\rm sc_y}^{-}\right), \\
\alpha_{\rm me}^{\rm xx} &= \frac{1}{4\gamma H_0}\left({}_{-\rm z}E_{\rm sc_y}^{+} - {}_{\rm z}E_{\rm sc_y}^{+} + {}_{-\rm z}E_{\rm sc_y}^{-} - {}_{\rm z}E_{\rm sc_y}^{-}\right), \\
\alpha_{\rm mm}^{\rm xy} &= \frac{\eta_0}{4\gamma H_0}\left({}_{-\rm z}E_{\rm sc_y}^{+} - {}_{\rm z}E_{\rm sc_y}^{+} - {}_{-\rm z}E_{\rm sc_y}^{-} + {}_{\rm z}E_{\rm sc_y}^{-}\right), \\
\alpha_{\rm me}^{\rm yx} &= \frac{1}{4\gamma H_0}\left({}_{\rm z}E_{\rm sc_x}^{+} - {}_{-\rm z}E_{\rm sc_x}^{+} + {}_{\rm z}E_{\rm sc_x}^{-} - {}_{-\rm z}E_{\rm sc_x}^{-}\right), \\
\alpha_{\rm mm}^{\rm yy} &= \frac{\eta_0}{4\gamma H_0}\left({}_{\rm z}E_{\rm sc_x}^{+} - {}_{-\rm z}E_{\rm sc_x}^{+} - {}_{\rm z}E_{\rm sc_x}^{-} + {}_{-\rm z}E_{\rm sc_x}^{-}\right).
\end{aligned}
\tag{2.20}
$$

To clarify the notation here we can use an example, ${}_{-\rm z}E_{\rm sc_x}^{+}$ denotes the $\mathbf{x}_0$ projection of the scattered electric field in the $-z$-direction if the inclusion is illuminated by the incident wave $\mathbf{E}_{\rm inc} = \eta_0 H_0 \mathbf{x}_0$, $\mathbf{H}_{\rm inc} = +H_0 \mathbf{y}_0$.

Next, we study the case when the incident fields are defined as $\mathbf{E}_{\rm inc} = \eta_0 H_0 \mathbf{y}_0$, $\mathbf{H}_{\rm inc} = \pm H_0 \mathbf{x}_0$. Likewise, the expressions for the other 8 polarizability components can be found:

$$
\begin{aligned}
\alpha_{\rm ee}^{\rm xy} &= \frac{1}{4\gamma\eta H_0}\left({}_{\rm z}\bar{E}_{\rm sc_x}^{+} + {}_{-\rm z}\bar{E}_{\rm sc_x}^{+} + {}_{\rm z}\bar{E}_{\rm sc_x}^{-} + {}_{-\rm z}\bar{E}_{\rm sc_x}^{-}\right), \\
\alpha_{\rm em}^{\rm xx} &= \frac{1}{4\gamma H_0}\left({}_{\rm z}\bar{E}_{\rm sc_x}^{+} + {}_{-\rm z}\bar{E}_{\rm sc_x}^{+} - {}_{\rm z}\bar{E}_{\rm sc_x}^{-} - {}_{-\rm z}\bar{E}_{\rm sc_x}^{-}\right), \\
\alpha_{\rm ee}^{\rm yy} &= \frac{1}{4\gamma\eta H_0}\left({}_{\rm z}\bar{E}_{\rm sc_y}^{+} + {}_{-\rm z}\bar{E}_{\rm sc_y}^{+} + {}_{\rm z}\bar{E}_{\rm sc_y}^{-} + {}_{-\rm z}\bar{E}_{\rm sc_y}^{-}\right), \\
\alpha_{\rm em}^{\rm yx} &= \frac{1}{4\gamma H_0}\left({}_{\rm z}\bar{E}_{\rm sc_y}^{+} + {}_{-\rm z}\bar{E}_{\rm sc_y}^{+} - {}_{\rm z}\bar{E}_{\rm sc_y}^{-} - {}_{-\rm z}\bar{E}_{\rm sc_y}^{-}\right), \\
\alpha_{\rm me}^{\rm xy} &= \frac{1}{4\gamma H_0}\left({}_{-\rm z}\bar{E}_{\rm sc_y}^{+} - {}_{\rm z}\bar{E}_{\rm sc_y}^{+} + {}_{-\rm z}\bar{E}_{\rm sc_y}^{-} - {}_{\rm z}\bar{E}_{\rm sc_y}^{-}\right), \\
\alpha_{\rm mm}^{\rm xx} &= \frac{\eta_0}{4\gamma H_0}\left({}_{-\rm z}\bar{E}_{\rm sc_y}^{+} - {}_{\rm z}\bar{E}_{\rm sc_y}^{+} - {}_{-\rm z}\bar{E}_{\rm sc_y}^{-} + {}_{\rm z}\bar{E}_{\rm sc_y}^{-}\right), \\
\alpha_{\rm me}^{\rm yy} &= \frac{1}{4\gamma H_0}\left({}_{\rm z}\bar{E}_{\rm sc_x}^{+} - {}_{-\rm z}\bar{E}_{\rm sc_x}^{+} + {}_{\rm z}\bar{E}_{\rm sc_x}^{-} - {}_{-\rm z}\bar{E}_{\rm sc_x}^{-}\right), \\
\alpha_{\rm mm}^{\rm yx} &= \frac{\eta_0}{4\gamma H_0}\left({}_{\rm z}\bar{E}_{\rm sc_x}^{+} - {}_{-\rm z}\bar{E}_{\rm sc_x}^{+} - {}_{\rm z}\bar{E}_{\rm sc_x}^{-} + {}_{-\rm z}\bar{E}_{\rm sc_x}^{-}\right).
\end{aligned}
\tag{2.21}
$$

It is seen from (2.20) and (2.21) that to calculate a polarizability component, both the amplitudes and phases of the incident and scattered waves are required. This is, in fact, an inevitable property of all scattering-based polarizability retrieval methods (e.g. [91, 92]).

Although it does not complicate the use of the method in numerical calculations, it can imply certain difficulties for experimental measurements.

From (2.20) and (2.21) one can see that to extract one specific polarizability component of the inclusion by this method, we need to probe (or measure) the scattered fields only in two directions (at any arbitrary point in far-field). In order to find all 16 polarizability components, it is sufficient to know the scattered fields in two directions and to use only four different plane-wave illuminations.

Summarizing, we have reported a method for determination of all components of individual polarizability tensors for the electrically small inclusion with the arbitrary shape which can be found from Eqns. (2.20) and (2.21), respectively. Basic of proposed approach is a scattering response measured in the far-field zone and in two opposite directions with the different polarization state of incident linearly polarized waves. This method requires less complicated calculations and due to its simplicity can be utilized also experimentally. Further, we will test our method for determination of well-known metallic resonators and will address attention to the choice of more useful resonators for the synthesis of functional off-resonance transparent metasurfaces.

2.2.3 Polarizabilities of resonant inclusions

As it was mentioned before, the definition of polarizabilities gives an important information about the reaction of polarizable inclusion to external excitation and its EM properties. Moreover, it helps us to chose what kind of inclusions can be preferable for the synthesis of functional off-resonance transparent metasurfaces. First of all, we focus on the metallic resonant inclusions, since they are more sensitive and polarizable to the excitation by incident waves as well as are the best candidates for manipulation of reflected, transmitted, and absorbed waves. Thus, we utilize the method for extracting polarizabilities of metallic resonators for the synthesis of functional off-resonance metasurfaces.

As a starting point, we calculate the scattered fields (for example ${}_{-\mathrm{z}}\bar{E}^{+}_{\mathrm{sc}_\mathrm{x}}$) from the resonant inclusion by full-wave numerical simulation using ANSYS HFSS based on finite element method (FEM). It is possible to calculate the scattered fields using other approaches, e.g., based on the method of moments (MoM), finite-difference-time-domain (FDTD) method or measure the far-fields experimentally. As it is seen from (2.13), we can find all these components using two incident waves with the polarization states defined by (2.11). In order to determine the electric and magnetic dipolar moments in (2.13), we probe the fields scattered by the inclusion in the $+\mathbf{z}_0$ and $-\mathbf{z}_0$ directions, as it is dictated by (2.19). Next, using the final formulas (2.20) and (2.21), we calculate the components of polarizability tensors of resonant inclusions in the considered electromagnetic spectrum.

Based on knowledge of classical electrodynamics [25], we consider the typical metallic resonant inclusions as electric and magnetic dipolar resonators. Typical electric and magnetic dipole resonators are a straight and split ring perfect conductors (lossless). Here, we consider the only case of the main resonance where the length of resonators (L) is equal to half resonant wavelength ($L = \lambda_{res}/2$), respectively. All resonators are excited by the incident linearly polarized plane wave at normal incidence in the microwave spectral

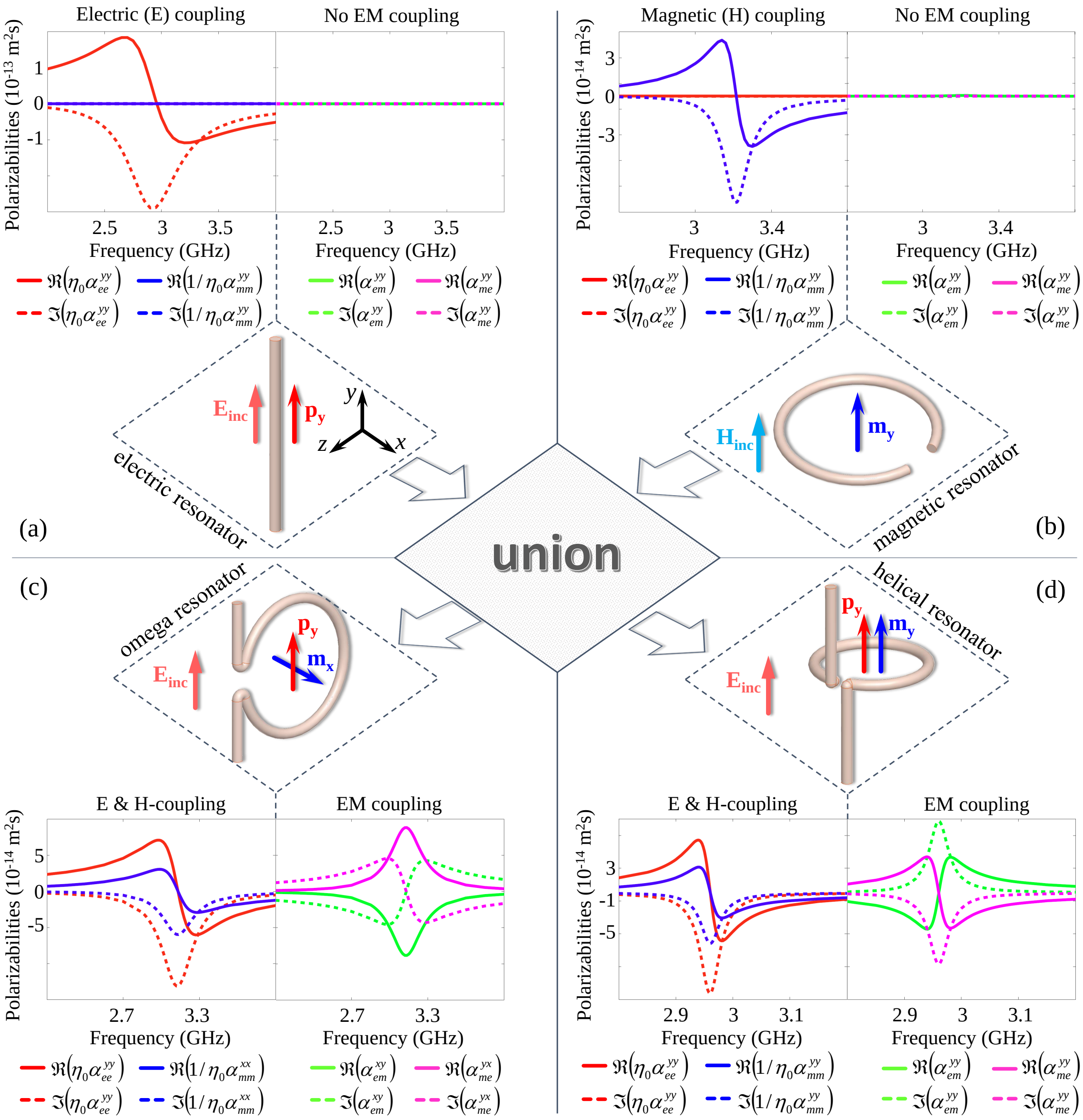

Figure 2.3: (a) Illustration of electric dipole resonator and its polarizability components in the microwave frequency band. (b) Design of magnetic dipole resonator and plots of polarizability components versus frequencies. (c) Ω-shape resonator with indicated dipolar moments and its the main polarizabilities, respectively. (d) Design of canonical helical resonator with the main polarizability tensor components in microwave band. Resonators induce the electric **p** and magnetic **m** dipole moments that are indicated in the designs. Each resonator was chosen to the excitation of the main resonance mode with the length of about $\lambda_{\text{res}}/2$ with a wire diameter of 1 mm. The type of electromagnetic couplings are indicated above the plots.

range.

Figure 2.3(a) shows an electric dipole resonator and its the electric, magnetic, electromagnetic and magnetoelectric axial components of polarizability tensors in the range of $2-4$ GHz calculated based on Eqns. (2.20) and (2.21) and using numerical simulation. As can be seen, electric resonator induces only an electric dipole moment $\mathbf{p} = \alpha_{\text{ee}}^{\text{yy}}\mathbf{E}_{\text{inc}}$

owing to excitation of incident plane wave ($\mathbf{E}_{\rm inc} = E_0\mathbf{y}_0\|$ y-axis) at normal incidence. The magnetic, electromagnetic and magnetoelectric polarizabilities are equal zero as it was expected. Therefore, electric resonator interacts only with incident electric field and, as a result, any EM couplings do not occur in half wavelength electric resonator.

Figure 2.3(b) shows a magnetic resonator or well-known as a split-ring resonator (SRR) and its polarizability in the microwave range. The resonator is excited by incident magnetic field. SRR possess only magnetic moment $\mathbf{m} = \alpha_{\rm mm}^{\rm yy}\mathbf{H}_{\rm inc}$ at normal incidence of plane wave ($\mathbf{H}_{\rm inc} = H_0\mathbf{y}_0\|$ y-axis). As seen from calculated polarizabilities, the axial components of electric, electromagnetic, and magnetoelectric polarizabilities are equal zero in accordance with a theoretical basis. Similar to the case of the electric resonator, usually magnetic resonator interacts with incident magnetic field and has not any EM couplings too.

Further, we can use electric and magnetic resonators for the realization of off-resonance transparent metasurfaces. However, the using of these resonators gives us less functionality since each resonator operates only with electric or magnetic fields. A sequential combination of these resonators is a bad solution since each resonator will be excited at a certain frequency, which ultimately results in a shift in the resonance frequencies between the electric and magnetic responses. Moreover, the adjustment of electrical and magnetic resonances to the same frequency is very difficult and requires both time and resources to achieve a single-frequency resonant response. Therefore, we are aiming to find electromagnetic resonators for the synthesis of off-resonance transparent metasurfaces.

One of the simple ways is to unite the electric and magnetic resonators into a single electromagnetic resonator that must possess electric, magnetic and electromagnetic response to external excitation. The union of straight resonator and SRR leads to the creation of new two types of electromagnetic resonators well-known as omega-resonators and chiral resonators. These resonators correspond to the class of reciprocal bi-anisotropic medium [27]. Reciprocity means that the relationship between an oscillating current and the resulting electric field is unchanged where the current is placed and where the field is measured. Reciprocal and non-reciprocal bianisotropic media were actively investigated in the electrodynamic community due to their EM properties and capabilities to the excitation by electric and/or magnetic fields independently [87]. The most common to use omega-type [20,93] and helix-type resonators [94,95] to create the reciprocal bianisotropic medium with unique EM properties. Here, we determined polarizabilities of omega-type and helix-type resonators by usage of our approach.

Figure 2.3(c) shows the design of Omega resonator (Ω-resonator) and its calculated components of polarizability tensors in the microwave range. Ω-resonator is excited by incident electric field with polarization state of $\mathbf{E}_{\rm inc} = E_0\mathbf{y}_0\|$ y-axis, where Ω-resonator induces the electric ($\mathbf{p}\|$ y-axis) and magnetic ($\mathbf{m}\|$ x-axis) moments simultaneously. As can be seen, only four polarizability components of Ω-resonator make a significant contribution to the radiation in the defined coordinate system: $\alpha_{\rm ee}^{\rm yy}$, $\alpha_{\rm mm}^{\rm xx}$, $\alpha_{\rm em}^{\rm xy}$, and $\alpha_{\rm me}^{\rm yx}$. Thus, Ω-resonator possesses electric and magnetic couplings as well as electromagnetic and magnetoelectric couplings or Ω-coupling from the interaction with incident electric and/or magnetic fields. Moreover, the electric and magnetic polarizabilities of resonator become purely imaginary while the electromagnetic polarizabilities are real at the resonance. It should be mentioned that metasurfaces based on Ω-type resonators possessing an advantageous EM properties have been previously reported in litherature [52, 96].

Another type of electromagnetic resonator is depicted in Figure 2.3(d), where a typical design of chiral resonator (used a canonical helix) with its polarizabilities in the microwave frequency band were shown. Chiral resonator is excited by incident linearly polarized plane waves with polarization state as $\mathbf{E}_{\rm inc} = E_0\mathbf{y}_0 \|$ y-axis. As seen, resonator possesses electromagnetic and magnetoelectric couplings (chiral-coupling) in accordance with the axial components of polarizability tensors $\alpha_{\rm ee}^{\rm yy}$, $\alpha_{\rm mm}^{\rm yy}$, $\alpha_{\rm em}^{\rm yy}$, and $\alpha_{\rm me}^{\rm yy}$. In comparison with Ω-resonator, canonical helix induces the electric and magnetic dipolar moments directed along y-axis simultaneously. Thus, metasurfaces consist of omega-type or helix-type resonators have different EM couplings, properties, and functionalities. As an example, chiral metasurfaces comprising of helical resonators were reported in [71, 88, 97].

To the best of our knowledge, it is preferable to use the chiral resonators (in particular, smooth helices) for the realization of functional off-resonance transparent metasurfaces since helical resonators have more functionalities and capabilities for manipulation of reflected and transmitted waves at the resonance. Moreover, simple geometry of smooth helical resonator makes it as a good candidate in the fabrication process for the high frequencies. Thus, using the theoretical approach described early and numerical simulation, we have found the main components of polarizability tensors well-known metallic dipole resonators. Calculated polarizabilities qualitatively describe the EM properties and features each half-wavelength resonators, which can contribute to the consciousness of off-resonance transparent metasurfaces with given functionalities.

2.3 Balance of polarizabilities

On the way to the synthesis of functional off-resonance transparent metasurfaces based on helical resonators, it is necessary to know the conditions when metasurface does not reflect incident plane waves away from the resonance or even at the operational resonant frequency. In other words, it is necessary to know the condition that the impedance of the metasurface is matched with the impedance of free space to obtain a zero reflection even at the resonance. This condition can be easily obtained according to the Eqn. (2.2) and require zero reflected fields ($\mathbf{E}_{\rm r} = 0$) from metasurface. Therefore, condition for impedance matching with free-space of metasurface (zero reflection) can be written in the following form:

$$\eta_0\mathbf{p} = \frac{1}{\eta_0}\mathbf{m}. \tag{2.22}$$

According to conditions (2.22), reflectionless metasurface must have and induce the equivalent electric and magnetic dipolar moments that should possess to equivalent electromagnetic response from metasurface. This condition for balancing the induced dipole moments both in metastructures and resonators to achieve various functionalities was described in the works of [25, 71, 95]. In order to satisfy the condition (2.22), it is necessary to the determinate dipolar moment of inclusion comprising metasurface. However, this is a very difficult task and might be impossible, since, for example, we cannot calculate electric and magnetic moments of inclusions directly from Eqn. (2.4) and (2.5). We have to know the scattered electric fields from inclusion or metasurface to find all polarizabilities for the subsequent expressions of dipole moments through these defined polarizabilities. Therefore, it is better and easy to work in term of polarizabilities of inclusions on the basis of which the off-resonance transparent metasurfaces will be synthesized.

2.3.1 Conditions for impedance matching of metasurfaces

In advance, we consider the metasurface with components of effective polarizability tensors of the unit cell. Later, we will move from the effective polarizabilities $\overline{\overline{\widehat{\alpha}}}$ of the unit cell to the individual polarizabilities ($\overline{\overline{\alpha}}$) of the resonance inclusions. The definition of the condition for matching the impedance with free space or other words for obtaining zero reflection from the metasurface through effective polarizabilities can be found from Eqn. (2.7) in the following way [98]:

$$\begin{aligned}
\eta_0\widehat{\alpha}_{\rm ee}^{\rm xx} - \widehat{\alpha}_{\rm em}^{\rm xy} + \widehat{\alpha}_{\rm me}^{\rm yx} - \frac{1}{\eta_0}\widehat{\alpha}_{\rm mm}^{\rm yy} &= 0,\\
\eta_0\widehat{\alpha}_{\rm ee}^{\rm xy} + \widehat{\alpha}_{\rm em}^{\rm xx} + \widehat{\alpha}_{\rm me}^{\rm yy} + \frac{1}{\eta_0}\widehat{\alpha}_{\rm mm}^{\rm yx} &= 0,\\
\eta_0\widehat{\alpha}_{\rm ee}^{\rm yx} - \widehat{\alpha}_{\rm em}^{\rm yy} - \widehat{\alpha}_{\rm me}^{\rm xx} + \frac{1}{\eta_0}\widehat{\alpha}_{\rm mm}^{\rm xy} &= 0,\\
\eta_0\widehat{\alpha}_{\rm ee}^{\rm yy} + \widehat{\alpha}_{\rm em}^{\rm yx} - \widehat{\alpha}_{\rm me}^{\rm xy} - \frac{1}{\eta_0}\widehat{\alpha}_{\rm mm}^{\rm xx} &= 0.
\end{aligned} \tag{2.23}$$

As it was mentioned before, we choose chiral-type resonators and consider only bi-anisotropic chiral medium. In this case, conditions (2.22) are significant simplified since the all cross-polarizabilities of electric, meagnetic, electromagnetic, and magnetoelectric polarizabilities are equal zero [95]:

$$\widehat{\alpha}_{\rm ee}^{\rm xy} = \widehat{\alpha}_{\rm ee}^{\rm yx} = \widehat{\alpha}_{\rm mm}^{\rm xy} = \widehat{\alpha}_{\rm mm}^{\rm yx} = \widehat{\alpha}_{\rm em}^{\rm xy} = \widehat{\alpha}_{\rm em}^{\rm yx} = \widehat{\alpha}_{\rm me}^{\rm xy} = \widehat{\alpha}_{\rm me}^{\rm yx} = 0. \tag{2.24}$$

Therefore, conditions (2.2) can be re-written as:

$$\begin{aligned}
\eta_0\widehat{\alpha}_{\rm ee}^{\rm xx} &= \frac{1}{\eta_0}\widehat{\alpha}_{\rm mm}^{\rm yy},\\
\widehat{\alpha}_{\rm em}^{\rm xx} &= -\widehat{\alpha}_{\rm me}^{\rm yy},\\
\widehat{\alpha}_{\rm em}^{\rm yy} &= -\widehat{\alpha}_{\rm me}^{\rm xx},\\
\eta_0\widehat{\alpha}_{\rm ee}^{\rm yy} &= \frac{1}{\eta_0}\widehat{\alpha}_{\rm mm}^{\rm xx}.
\end{aligned} \tag{2.25}$$

Equations in (2.25) are conditions for the balance of effective polarizabilities for chiral medium or conditions for the free-space impedance matching of chiral metasurface. These conditions have been used for the realization of different functional metasurfaces in [95, 98, 99]. The balance of polarizabilities denotes equality of the electric, magnetic, and magnetoelectric coupling and response from inclusion. This leads to very strong interaction with electromagnetic fields [100].

2.3.2 Helical resonators with balanced polarizabilities

To the best of our knowledge, different classes of bi-anisotropic inclusions (reciprocal and non-reciprocal inclusions) were tuned to achive the balance of their individual polarizabilities and can be found in [89, 101–103]. Here, we focus on achieving the balance of polarizabilities of electromagnetic helical resonators, specifically a smooth conductive helical resonators, since they have a simple and flexible shape that can be easily realized for the different spectral ranges. Before synthesizing the metasurface with balanced effective polarizabilities based on chiral elements (helical resonators), it is necessary to adjust the helical resonators to the condition of balancing their individual polarizabilities. However, it is easy to do since the balanced effective polarizabilities have the same form as balanced individual polarizabilities [104].

As it was in the previous case, it is not necessary to calculate all the components of individual polarizability tensors of the helical resonators, since only the axial components contribute to the radiation of the electromagnetic wave. From this it follows that cross-polarizabilities are equal to zero ($\alpha_{\rm ee}^{\rm xy} = \alpha_{\rm ee}^{\rm yx} = \alpha_{\rm em}^{\rm xy} = \alpha_{\rm em}^{\rm yx} = \alpha_{\rm me}^{\rm xy} = \alpha_{\rm me}^{\rm yx} = \alpha_{\rm mm}^{\rm xy} = \alpha_{\rm mm}^{\rm yx} = 0$). Moreover, the condition holds for the helical inclusions, as it must be in accordance with the Onsager-Casimir principle in the theory of bi-anisotropic media [105]. Thus, the conditions for the balance of individual polarizabilities for helical inclusions have the follows form [71, 95]:

$$\eta_0 \alpha_{\rm ee}^{\rm yy} = \frac{1}{\eta_0} \alpha_{\rm mm}^{\rm yy} = \pm \alpha_{\rm em}^{\rm yy} = \mp \alpha_{\rm me}^{\rm yy}, \tag{2.26}$$

$$\eta_0 \alpha_{\rm ee}^{\rm xx} = \frac{1}{\eta_0} \alpha_{\rm mm}^{\rm xx} = \pm \alpha_{\rm em}^{\rm xx} = \mp \alpha_{\rm me}^{\rm xx}, \tag{2.27}$$

where, for example, $\alpha_{\rm ee}^{\rm xx}$ or $\alpha_{\rm ee}^{\rm yy}$ means axial components of electric polarizability tensors depending on the orientation (along with x-axis or y-axis) of the helical resonator in a coordinate system. Signs "±" or "∓" depend on the handedness of helical resonators but in any case, these signs will be opposite as it follows from the principle of Onsager-Casimir. As seen, axial individual polarizability is normalized to the impedance of free-space. As a result, helical resonators with balanced polarizabilities have an equivalent electromagnetic response to the excitation of the incident linearly polarized plane waves. Other words, balances helical resonators possess independent polarization excitation.

Further, we focus on using smooth metallic helical resonators with different numbers of turns (N_t), since a geometry of such resonators is simple and can be easily fabricated by modern technologies. Moreover, helical resonators possess electromagnetic response to the external excitation that makes them as a good candidate for our purposes. Then, we are aiming to find the balance of polarizabilities appears in helical resonators by tailoring of structural parameters. It should be noted that analytical method to define the optimal parameters of N-turn helices can be found in literature [71].

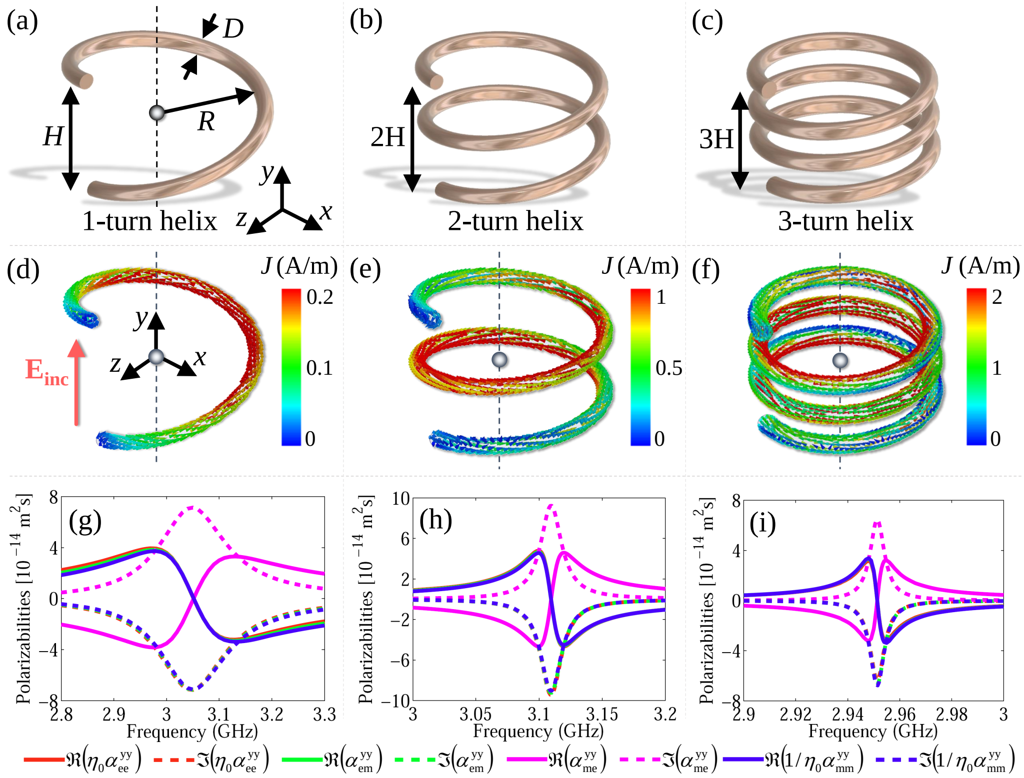

Figure 2.4: (a-c) Geometry of single, double, and triple-turn helices with indicated structural parameters. (d-f) Distribution of the current density of 1,2,3-turn helices at the resonances of 3.05, 3.11, 2.95 GHz, respectively. (g-i) Axial components of polarizability tensors in the microwave range. The length of helices is equal to the half operational wavelength.

Here, we use the method for determination of all components of electric, magnetic, electromagnetic and magnetoelectric polarizability tensors described before. First of all, we found polarizabilities of half-wavelength single-turn (1-turn), double-turn (2-turn), and triple-turn (3-turn) helical resonators with arbitrary parameters (see Figures 2.4(a-c)) using our approach and numerical simulation. Then, by tailoring of radius (R) and pitch (H) of 1,2,3-turn helices but with fixed diameter of the wire (D) we found the balance of axial polarizability components in the microwave range. A material of helices was chosen as a copper.

Figures 2.4(d-f) shows a current density distribution of 1,2,3-turn helices at the resonances of 3.05, 3.11, 2.95 GHz, respectively. As seen, maximum of excitation occurs at the central part of the helical curve and minimums exist on the arm ends. This corresponds to the excitation of helical resonators at the main resonance, where the length of the helix is equal to the half-wavelength resonance condition of $\lambda_{res}/2$. Also, the amplitude of current density increases with the turn numbers of helices that lead to the proportional increase of resistive loss in metal.

Figures 2.4(g-i) shows axial components of electric ($\alpha_{\rm ee}$), magnetic ($\alpha_{\rm mm}$), electromagnetic ($\alpha_{\rm em}$) and magnetoelectric ($\alpha_{\rm me}$) individual polarizabilities of helical resonators in the microwave range. By tailoring of structural parameters of 1,2,3-turn helical resonators, we

	H, mm	R, mm	D, mm	f_{res}, GHz
1-turn helix	11.3	7.2	1	3.05
2-turn helix	2.3	3.3	0.5	3.11
3-turn helix	0.8	2	0.4	2.95

Table 2.1: Structural parameters of helical resonators with balanced polarizabilities.

found the balance of individual polarizabilities which are satisfied to the conditions (2.26). All structural parameters of the copper helices that have balanced polarizability components are shown in Table 2.1. As seen, the resonance band becomes more narrow with increasing turns of the helix that corresponds to the narrowband frequency resonant selectivity. Thus, these helical resonators with balanced polarizabilities are a perfect candidate for realization of functional off-resonance transparent metasurfaces.

It should be noted one more time that the practical implementation of considered smooth helices in comparison, for example, canonical helices should be much easy in the microwave frequency band and for more high frequencies too. However, further increasing of the helical turns (even to 4-turns) leads to significant difficulties for practical fabrication since the distance between loop wires becomes critical small.

2.4 Polarization-insensitive helix-based metasurfaces

Towards to realization of functional off-resonance metasurfaces, already we know the conditions (2.25) to achieve zero reflection from metasurface and which polarizable inclusions (smooth helical resonators) we can you use for that. Moreover, we can achieve equivalent EM response from 1,2,3-turn helical resonators which have to be tuned to the balance of their polarizabilities. Here, we synthesize of helix-based metasurfaces to achieve the equivalent EM response to the linearly polarized incident waves.

As well known, macroscale metasurfaces based on helical resonators with balanced polarizabilities have been utilized for realization of such functionalities as circular polarization transformation [71, 97, 106] and low-reflection covering [72]. Interestingly, that metasurfaces consisting of canonical, single-turn, and double-turn helical resonators with balanced polarizabilities were studied analytically and by numerical simulation to achieve equivalent EM response by excitation at normal incidence already were reported in [106]. However, proposed helix-based metasurfaces demonstrated not perfect equivalent response, since reflection and transmission spectra were not the same by excitation at different polarization state at normal incidence. Therefore, some inaccuracy in the analytic model or in simulation results were admitted. Here, we demonstrate absolutely polarization-invariant electromagnetic response from metasurfaces based on 1,2,3-turn helical resonators with balanced polarizabilities in the microwave range by usage of our approach and numerical simulation.

Figure 2.5 shows a schematic illustration of metasurface consisting of helical resonators which were tailored to the balance of their polarizabilities in accordance to condition (2.26) and arranged on a periodic 2D lattice with a sub-wavelength period of $p = 30$ mm. Helical

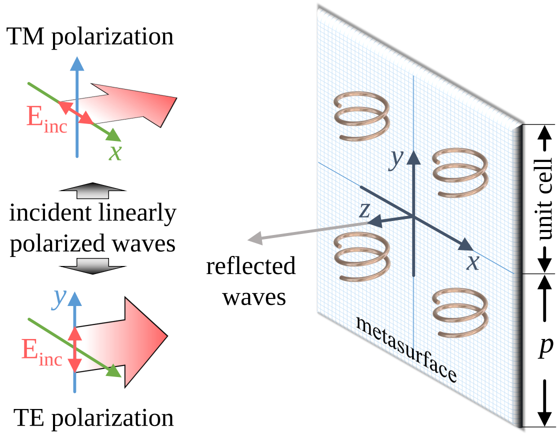

Figure 2.5: Schematic illustration of helix-based metasurface with respect to TE and TM polarization states at normal incidence.

resonators are located in the lattice in such a way that the axis of each helix is directed in one direction along the y-axis. The unit cell of metasurface consists of the single copper helical resonator. Structural parameters of helices were taken from Table 2.1. Helix-based metasurfaces are excited by the incident linearly polarized plane waves with transverse electric (TE) and transverse magnetic (TM) polarizations, respectively.

Figure 2.6(a-c) shows numerically simulated reflection spectra of metasurfaces based on 1,2,3-turn helices for TE and TM polarizations at normal incidence. As seen from simulated results, 1,2,3-turn helix-based metasurfaces exhibit resonance reflection peak over of 27% at resonant frequencies of 2.99, 2.96, and 2.98 GHz, respectively. It is clear to see that reflection spectra exhibit absolutely polarization-invariant behavior to the incident plane wave. Therefore, helical resonators comprising of metasurfaces exhibit the equivalent EM response to external excitation. Moreover, helix-based metasurfaces possess 100% transparency away from the resonance frequency. In a case of single-turn helix-based metasurface, reflection spectrum exhibits more wide resonance behavior since a volume of the resonator is a bigger than other helices.

Thus, we synthesized off-resonance transparent metasurfaces based on 1,2,3-turn helical resonators which structural parameters were tailored to achieve the balance of their axial individual polarizabilities in accordance with condition (2.26). As a result, we demonstrated polarization-insensitive helix-based metasurfaces in the microwave range.

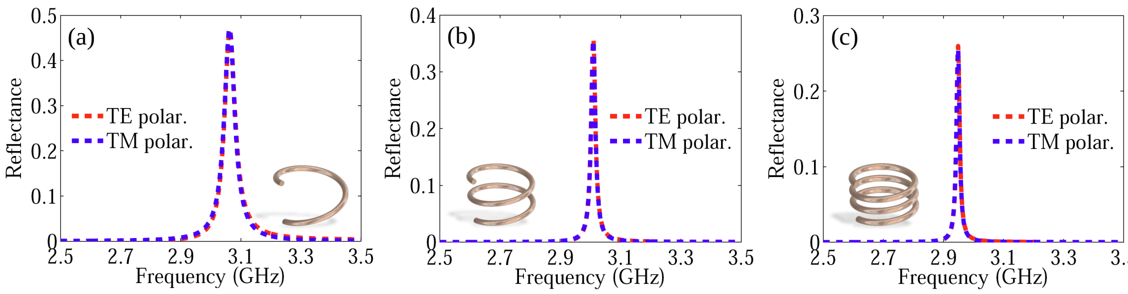

Figure 2.6: Reflection spectra of metasurfaces based on (a) 1-turn, (b) 2-turn, and (c) 3-turn helical resonators for TE and TM polarizations at normal incidence.

2.5 Conclusions

- Simple method for determination of all components of electric, magnetic, electromagnetic, and magnetoelectric polarizability tensors of electrically small inclusions with arbitrary shape has been proposed. Due to the determination of scattered electric fields in the far-field zone and numerical simulation based on FEM we have performed the calculation of polarizabilities for electric and magnetic resonators. Thus, we have tested our method in accordance with well-known resonators and their EM properties.

- Chiral helical resonators were chosen for the synthesis of functional off-resonance transparent metasurfaces owing to their chiral bi-anisotropic coupling and EM response to the excitation both electric and magnetic fields independently. Determination of axial components of electric ($\overline{\overline{\alpha}}_{\rm ee}$), magnetic ($\overline{\overline{\alpha}}_{\rm mm}$), electromagnetic ($\overline{\overline{\alpha}}_{\rm em}$), and magnetoelectric ($\overline{\overline{\alpha}}_{\rm me}$) individual polarizability tensors was performed for the microwave range. As a result, helical resonator exhibits the electromagnetic behavior by excitation of linearly polarized incident waves.

- Conditions for impedance matching or zero reflection of chiral-based metasurfaces with free-space was reported. Thus, helical resonators can be used for the realization of metasurfaces which can exhibit zero reflection even at the resonance.

- Structural parameters of helical resonators with different numbers of turns (single, double, and triple) were tailored to their balance of polarizabilities in accordance with conditions (2.26) or (2.27). Helical resonators possessing the balance of polarizabilities must have equivalent EM response and balance of inducing (see Eqn. (2.22)) to the external excitation by EM waves.

- Using numerical simulation, we have shown that metasurfaces based on 1,2,3-turn helical resonators with balanced polarizabilities exhibit absolutely polarization-insensitive EM response in the range of 2.5-3.5 GHz to excitation of the incident linearly polarized wave with TE and TM polarizations, respectively.

Chapter 3

Functionalities of helix-based metasurfaces

The analytical approach for determination of proper arrangement of metallic helical resonators in a 2D periodic lattice with balanced polarizabilities to create the off-resonance transparent metasurfaces depending on desired functionalities has been reported (Section 3.1). If the proper arrangement of helical resonators in a 2D array is known, it allows us to create functional metasurfaces with advantageous EM properties. Using our approach and numerical simulation, off-resonance transparent linearly polarized rotators (co-reflector and cross-reflector) based on double-turn helices for reflected waves in the microwave range have been synthesized (Section 3.2). Similar to the previous case, off-resonance transparent helix-based rotators for transmitted waves (co-transmit and cross-transmit) in the microwave range were reported (Section 3.3). Following the conditions for total absorption of EM waves in metasurfaces, reflectionless perfect absorbers based on double-turn helices have been demonstrated using numerical simulation (Section 3.4). By combining of the proposed off-resonance transparent rotators and perfect absorbers, multifunctional multifrequency helix-based cascaded metamaterial was synthesized and tested by numerical simulation (Section 3.5).

3.1 The arrangement of helical resonators in metasurface

Before, off-resonance transparent metasurfaces comprising of 1,2,3-turn helical resonators with tailored structural parameters to the balance of individual polarizabilities have been reported. As a result, helix-based metasurfaces exhibit the equivalent EM response to the excitation by linearly polarized plane waves at normal incidence. In other words, EM properties of proposed helix-based metasurfaces do not depend on the polarization orientation of the incident linearly polarized plane waves. This property is very useful and is one of the advantages of helix-based metasurfaces in comparison with polarization-sensitive metasurfaces. However, the realization of off-resonance transparent metasurfaces with great functionalities which, for example, would be capable of manipulation of amplitude, polarization, phase, wavefront shaping, and anomalous refraction for reflected and transmitted waves is more advantageous and useful. Nevertheless, there is a problem with the proper arrangement of polarizable inclusions in periodic lattice arises in the way of synthesizing metasurfaces with desired functionalities. Here, we will show an analytical method for determination of required arrangement of helical resonators in 2D periodic lattice depending on the desired functionalities. Next, we will synthesize the off-resonance transparent metasurfaces based on double-turn metallic helices with balanced polariz-

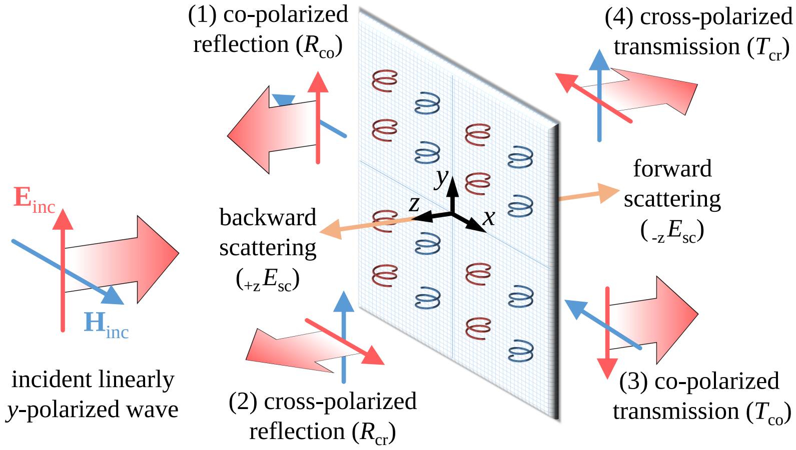

Figure 3.1: A schematic illustration of functional helix-based metasurface. By excitation of incident linearly y-polarized plane waves, functionalities of metasurface correspond to polarization transformations of reflected and transmitted waves to co- and cross-polarizations, respectively.

abilities by usage of proposed analytical approach and numerical simulation. We focus on achievement such functionalities as the rotation of polarization plane for reflected and transmitted waves (see Figure 3.1) as well as to obtain a total absorption in the microwave range.

First of all, we are aiming to find the analytical approach for determination of proper arrangement of helical resonators in 2D periodic lattice depending on their desired properties. To the best of our knowledge, several works have paid attention to the problem of the location of resonant inclusions in the lattice using fundamental principles of dipole-dipole interactions in the electrostatic regime [107–109]. Coupling effects in metamaterials between resonant inclusions comprising of them play a dominant role for the desired EM properties. Due to the fact that the size of the unit cells of metasurfaces is much smaller than the operating wavelength, it leads to strong interaction between the neighboring inclusions in the unit cells [110–113]. As a result, functionalities of metasurfaces can be changed substantially in comparison with their individual properties of the resonant inclusions [111, 113]. This case is in analogy to solid state physics, where the electronic properties of solids can dramatically different from those of individual atoms [114]. Summing up it should be noted, that the understanding of the fundamental coupling mechanisms between resonant inclusions as well as their arrangement will provide significant insight into designing and optimizing metasurfaces with desirable EM properties.

As a starting point, we consider a case of scattering electric far-fields in backward ($_{+z}\mathbf{E}_{sc}$) and forward ($_{-z}\mathbf{E}_{sc}$) directions from electrically thin chiral metasurface that is given in Figure 3.1. Infinite metasurface in xy-plane consists of helical resonators (for example, double-turn helices) which are arbitrarily located in the unit cell that have electrically small size in comparison to the incident wavelength. It allows to take into account only the lowest multipoles, i.e. the electric and magnetic dipoles. Total scattered fields in far-field from an electrically small polarizable inclusions are defined by the induced dipole moments in the form [90]. The scattered electric field from metasurface in backward direction ($\mathbf{n} = \mathbf{z}_0$) can be expressed as:

$$_{+\mathrm{z}}\mathbf{E}_{\mathrm{sc}} = \frac{k^2}{4\pi\epsilon_0 r}e^{-jkr}\left(\mathbf{p} - \frac{1}{\eta_0}\mathbf{z}_0 \times \mathbf{m}\right), \tag{3.1}$$

and in forward direction ($\mathbf{n} = -\mathbf{z}_0$):

$$_{-\mathrm{z}}\mathbf{E}_{\mathrm{sc}} = \frac{k^2}{4\pi\epsilon_0 r}e^{-jkr}\left(\mathbf{p} - \frac{1}{\eta_0}\mathbf{m} \times \mathbf{z}_0\right). \tag{3.2}$$

As folows from Eqns. (2.4) and (2.5), induced electric and magnetic dipole moments can be expressed through electric ($\overline{\overline{\widehat{\alpha}}}_{\mathrm{ee}}$), magnetic ($\overline{\overline{\widehat{\alpha}}}_{\mathrm{mm}}$), electromagnetic ($\overline{\overline{\widehat{\alpha}}}_{\mathrm{em}}$), and magneto-electric ($\overline{\overline{\widehat{\alpha}}}_{\mathrm{me}}$) effective polarizability tensors of bi-anisotropic polarizable inclusion (helical resonators). Similar equations are derived for the uniaxial symmetry that allows only isotropic response and rotation around the z-axis, therefore, all polarizability components in (2.3) can be expressed in terms of *co* and *cross* definitions respect to the polarization plane of incident wave [104]. In general case, effective polarizabilities are given in Eqs. (2.3) have the new forms:

$$\begin{aligned} \overline{\overline{\widehat{\alpha}}}_{\mathrm{ee}} &= \widehat{\alpha}_{\mathrm{ee}}^{\mathrm{co}}\overline{\overline{I}}_{\mathrm{t}} + \widehat{\alpha}_{\mathrm{ee}}^{\mathrm{cr}}\overline{\overline{J}}_{\mathrm{t}}, &\quad \overline{\overline{\widehat{\alpha}}}_{\mathrm{mm}} &= \widehat{\alpha}_{\mathrm{mm}}^{\mathrm{co}}\overline{\overline{I}}_{\mathrm{t}} + \widehat{\alpha}_{\mathrm{mm}}^{\mathrm{cr}}\overline{\overline{J}}_{\mathrm{t}} \\ \overline{\overline{\widehat{\alpha}}}_{\mathrm{em}} &= \widehat{\alpha}_{\mathrm{em}}^{\mathrm{co}}\overline{\overline{I}}_{\mathrm{t}} + \widehat{\alpha}_{\mathrm{em}}^{\mathrm{cr}}\overline{\overline{J}}_{\mathrm{t}}, &\quad \overline{\overline{\widehat{\alpha}}}_{\mathrm{me}} &= \widehat{\alpha}_{\mathrm{me}}^{\mathrm{co}}\overline{\overline{I}}_{\mathrm{t}} + \widehat{\alpha}_{\mathrm{me}}^{\mathrm{cr}}\overline{\overline{J}}_{\mathrm{t}}, \end{aligned} \tag{3.3}$$

where indexes *co* and *cr* are referred to the symmetric and antisymmetric parts of the corresponding dyadic, respectively. Tensor $\overline{\overline{I}}_{\mathrm{t}} = \overline{\overline{I}} - \mathbf{z}_0\mathbf{z}_0$ and $\overline{\overline{J}}_{\mathrm{t}} = \mathbf{z}_0 \times \overline{\overline{I}}_{\mathrm{t}}$ are the transverse unit dyadic and the vector-product operator, respectively. Polarizabilities with co-polarized components in new designations can be easily expressed through old one as follows:

$$\begin{aligned} \widehat{\alpha}_{\mathrm{ee}}^{\mathrm{co}}\overline{\overline{I}}_{\mathrm{t}} &= \widehat{\alpha}_{\mathrm{ee}}^{\mathrm{xx}}\mathbf{x}_0\mathbf{x}_0 + \widehat{\alpha}_{\mathrm{ee}}^{\mathrm{yy}}\mathbf{y}_0\mathbf{y}_0, \\ \widehat{\alpha}_{\mathrm{em}}^{\mathrm{co}}\overline{\overline{I}}_{\mathrm{t}} &= \widehat{\alpha}_{\mathrm{em}}^{\mathrm{xx}}\mathbf{x}_0\mathbf{x}_0 + \widehat{\alpha}_{\mathrm{em}}^{\mathrm{yy}}\mathbf{y}_0\mathbf{y}_0, \\ \widehat{\alpha}_{\mathrm{me}}^{\mathrm{co}}\overline{\overline{I}}_{\mathrm{t}} &= \widehat{\alpha}_{\mathrm{me}}^{\mathrm{xx}}\mathbf{x}_0\mathbf{x}_0 + \widehat{\alpha}_{\mathrm{me}}^{\mathrm{yy}}\mathbf{y}_0\mathbf{y}_0, \\ \widehat{\alpha}_{\mathrm{mm}}^{\mathrm{co}}\overline{\overline{I}}_{\mathrm{t}} &= \widehat{\alpha}_{\mathrm{mm}}^{\mathrm{xx}}\mathbf{x}_0\mathbf{x}_0 + \widehat{\alpha}_{\mathrm{mm}}^{\mathrm{yy}}\mathbf{y}_0\mathbf{y}_0, \end{aligned} \tag{3.4}$$

and cross-components are

$$\begin{aligned} \widehat{\alpha}_{\mathrm{ee}}^{\mathrm{cr}}\overline{\overline{J}}_{\mathrm{t}} &= \widehat{\alpha}_{\mathrm{ee}}^{\mathrm{xy}}\mathbf{x}_0\mathbf{y}_0 + \widehat{\alpha}_{\mathrm{ee}}^{\mathrm{yx}}\mathbf{y}_0\mathbf{x}_0, \\ \widehat{\alpha}_{\mathrm{em}}^{\mathrm{cr}}\overline{\overline{J}}_{\mathrm{t}} &= \widehat{\alpha}_{\mathrm{em}}^{\mathrm{xy}}\mathbf{x}_0\mathbf{y}_0 + \widehat{\alpha}_{\mathrm{em}}^{\mathrm{yx}}\mathbf{y}_0\mathbf{x}_0, \\ \widehat{\alpha}_{\mathrm{me}}^{\mathrm{cr}}\overline{\overline{J}}_{\mathrm{t}} &= \widehat{\alpha}_{\mathrm{me}}^{\mathrm{xy}}\mathbf{x}_0\mathbf{y}_0 + \widehat{\alpha}_{\mathrm{me}}^{\mathrm{yx}}\mathbf{y}_0\mathbf{x}_0, \\ \widehat{\alpha}_{\mathrm{mm}}^{\mathrm{cr}}\overline{\overline{J}}_{\mathrm{t}} &= \widehat{\alpha}_{\mathrm{mm}}^{\mathrm{xy}}\mathbf{x}_0\mathbf{y}_0 + \widehat{\alpha}_{\mathrm{mm}}^{\mathrm{yx}}\mathbf{y}_0\mathbf{x}_0. \end{aligned} \tag{3.5}$$

As it was mentioned before, we consider bi-anisotropic chiral metasurfaces for which all cross-components of polarizability tensors are equal to zero [95]. Therefore, only *co*-components contribute to the radiation from chiral metasurfaces consisting of helical resonators [96]. That leads to the simplification of expressions (3.4) and (3.5) and can be re-written as follows:

$$\begin{aligned} \overline{\overline{\widehat{\alpha}}}_{\mathrm{ee}} &= \widehat{\alpha}_{\mathrm{ee}}^{\mathrm{co}}\overline{\overline{I}}_{\mathrm{t}}, \qquad \overline{\overline{\widehat{\alpha}}}_{\mathrm{mm}} = \widehat{\alpha}_{\mathrm{mm}}^{\mathrm{co}}\overline{\overline{I}}_{\mathrm{t}} \\ \overline{\overline{\widehat{\alpha}}}_{\mathrm{em}} &= \widehat{\alpha}_{\mathrm{em}}^{\mathrm{co}}\overline{\overline{I}}_{\mathrm{t}}, \qquad \overline{\overline{\widehat{\alpha}}}_{\mathrm{me}} = \widehat{\alpha}_{\mathrm{me}}^{\mathrm{co}}\overline{\overline{I}}_{\mathrm{t}}. \end{aligned} \tag{3.6}$$

Next, helix-based metasurface is illuminated by a normally incident plane waves propagating along the $-\mathbf{z}_0$ direction as shown in Figure 3.1 with the following polarization states:

$$\mathbf{E}_{\mathrm{inc}} = E_0\mathbf{y}_0, \qquad \mathbf{H}_{\mathrm{inc}} = \frac{E_0}{\eta_0}\mathbf{x}_0. \tag{3.7}$$

By substituting (3.6) and (3.7) into (2.4) and (2.5), the induced electric and magnetic moments in metasurface can be expressed as follows:

$$\begin{aligned} \mathbf{p} &= \widehat{\alpha}_{\mathrm{ee}}^{\mathrm{co}}E_0\mathbf{y}_0 + \widehat{\alpha}_{\mathrm{em}}^{\mathrm{co}}\frac{E_0}{\eta_0}\mathbf{x}_0, \\ \mathbf{m} &= \widehat{\alpha}_{\mathrm{me}}^{\mathrm{co}}E_0\mathbf{y}_0 + \widehat{\alpha}_{\mathrm{mm}}^{\mathrm{co}}\frac{E_0}{\eta_0}\mathbf{x}_0. \end{aligned} \tag{3.8}$$

where E_0 is the amplitude of incident electric field. However, it is better to work in term of individual polarizabilities since the method for determination them was described. Thus, effective polarizabilities of unit cell can be expressed in terms of individual polarizabilities of the resonators though interaction constants in the following way [104]:

$$\widehat{\alpha}_{\mathrm{ee}}^{\mathrm{co}} = \frac{\alpha_{\mathrm{ee}}^{\mathrm{co}}}{1-\overline{\overline{\beta}}_{\mathrm{e}}\alpha_{\mathrm{ee}}^{\mathrm{co}}}, \ \ \widehat{\alpha}_{\mathrm{mm}}^{\mathrm{co}} = \frac{\alpha_{\mathrm{mm}}^{\mathrm{co}}}{1-\overline{\overline{\beta}}_{\mathrm{m}}\alpha_{\mathrm{mm}}^{\mathrm{co}}}, \tag{3.9}$$

where explicit analytical expressions for the interaction constants can be found in [115]:

$$\begin{aligned} \overline{\overline{\beta}}_{\mathrm{e}} &= -\left(\Re\left[\frac{j\omega\eta_0}{4S}\left(1-\frac{1}{jkR}\right)e^{-jkR}\right] + j\left[\frac{k^3}{6\pi\epsilon_0} - \frac{\eta_0\omega}{2S}\right]\right)\overline{\overline{I}}_{\mathrm{t}}, \\ \overline{\overline{\beta}}_{\mathrm{e}} &= \eta_0^2\overline{\overline{\beta}}_{\mathrm{m}}, \quad R = \frac{a}{1.438}. \end{aligned} \tag{3.10}$$

In accordance to the conditions for impedance matching (2.25), co-polarized components of effective polarizability tensors can be written in the following way:

$$\widehat{\alpha}_{\mathrm{ee}}^{\mathrm{co}} = \frac{1}{\eta_0^2}\widehat{\alpha}_{\mathrm{mm}}^{\mathrm{co}}, \quad \widehat{\alpha}_{\mathrm{em}}^{\mathrm{co}} = -\widehat{\alpha}_{\mathrm{me}}^{\mathrm{co}}. \tag{3.11}$$

Thus, by substituting (3.11) in (3.9), conditions for impedance matching of metasurface through the individual polarizabilities of helical resonators we can express as follows:

$$\alpha_{\mathrm{ee}}^{\mathrm{co}} = \frac{1}{\eta_0^2}\alpha_{\mathrm{mm}}^{\mathrm{co}}, \ \ \alpha_{\mathrm{em}}^{\mathrm{co}} = -\alpha_{\mathrm{me}}^{\mathrm{co}}, \tag{3.12}$$

where individual polarizabilities of helical resonators satisfy to the balance of their co-polarizabilities and have identical symmetry properties as effective co-polarizabilities of the unit cell in metasurface.

Follows to above, metasurface consisting of helical resonators with balanced co-polarizabilities is excited by linearly y-polarized incident wave and induces the equivalent electric and magnetic moments simultaneously. These dipole moments can oscillate only in the direction of the helix axis. However, regardless of the helices arrangement in the unit cell, each helix will be excited only one of the electric ($\mathbf{E}_{\mathrm{inc}}$) or magnetic ($\mathbf{H}_{\mathrm{inc}}$) components of the incident plane wave, respectively. Therefore, helices arranged along the y-axis (helix axis is directed along the y-axis) will be excited only by the electric field, while helices arranged along the x-axis will be excited by the magnetic field, respectively. Consequently, induced electric and magnetic moments of helices arranged helices along x-axis have the next form:

$$\mathbf{p}_{\mathrm{x}} = \alpha_{\mathrm{em}}^{\mathrm{co}} \frac{E_0}{\eta_0} \mathbf{x}_0, \;\; \mathbf{m}_{\mathrm{x}} = \alpha_{\mathrm{mm}}^{\mathrm{co}} \frac{E_0}{\eta_0} \mathbf{x}_0, \tag{3.13}$$

and for helices arranged along the y-axis

$$\mathbf{p}_{\mathrm{y}} = \alpha_{\mathrm{ee}}^{\mathrm{co}} E_0 \mathbf{y}_0, \;\; \mathbf{m}_{\mathrm{y}} = \alpha_{\mathrm{me}}^{\mathrm{co}} E_0 \mathbf{y}_0. \tag{3.14}$$

Next, it is necessary to find polarizabilities of the helical resonators. Here, we do not use our method for determination of polarizabilities since it requires to use numerical simulation. We would like to find the arrangement of helical resonators purely analytically. In this case, we can use the special approach for determination of individual polarizabilities only for canonical helical resonators (see Figure 2.3(d)) which was given in literature [95]. Using this approach, we defined the analytical expressions for determination of polarizabilities for smooth helical resonators. It can be assumed in the following form:

$$\begin{aligned} \alpha_{\mathrm{ee}}^{\mathrm{co}} &= \frac{L^2}{j\omega} \cdot \frac{1}{Z_{\mathrm{h}}}, \;\; \alpha_{\mathrm{mm}}^{\mathrm{co}} = -\mu_0^2 \cdot \frac{j\omega S_h^2}{Z_{\mathrm{h}}}, \\ \alpha_{\mathrm{em}}^{\mathrm{co}} &= \mp\mu_0 \cdot \frac{SL}{Z_{\mathrm{h}}}, \;\; \alpha_{\mathrm{me}}^{\mathrm{co}} = \pm\mu_0 \cdot \frac{SL}{Z_{\mathrm{h}}}, \\ L &= \frac{2\pi R}{\cos\varphi} N_{\mathrm{h}}, \;\; S_{\mathrm{h}} = \frac{4\pi R^2}{\cos^2\varphi} N_{\mathrm{h}}, \end{aligned} \tag{3.15}$$

where L is the total length of the helix, S is the occupied area, R is the radius of the helix, N_{h} is the number of turns, φ is the pitch angle, and Z_{h} is impedance of the helix. The plus-minus sign corresponds to right-handed and left-handed helices, respectively. Next, we introduce a new parameter α for the simplicity of decision:

$$\alpha = \mu_0 \frac{SL}{Z_{\mathrm{h}}}. \tag{3.16}$$

Then, *co-* and *cross*-polarizabilities of helices can be expressed thought α in the following way:

$$\begin{aligned} \alpha_{\mathrm{ee}}^{\mathrm{co}} &= \alpha \frac{L^2}{j\omega\mu_0 S_{\mathrm{h}} L} = -\alpha \frac{j}{\eta_0}, \\ \alpha_{\mathrm{mm}}^{\mathrm{co}} &= -\alpha \frac{j\mu_0^2 \omega S_{\mathrm{h}}}{L} = -\alpha j \eta_0, \\ \alpha_{\mathrm{me}}^{\mathrm{co}} &= \pm\alpha, \quad \alpha_{\mathrm{em}}^{\mathrm{co}} = \mp\alpha. \end{aligned} \tag{3.17}$$

At polarization state: $\mathbf{E}_{\text{inc}} = E_0\mathbf{x}_0$, $\mathbf{H}_{\text{inc}} = -E_0/\eta_0\mathbf{y}_0$		
Backscattering	Handedness	Orientation
${}_{+z}\mathbf{E}^{\text{x}}_{\text{sc}_1} = \zeta(j\mathbf{x}_0 + \mathbf{y}_0)$	right-handed	horizontally
${}_{+z}\mathbf{E}^{\text{y}}_{\text{sc}_2} = \zeta(-j\mathbf{x}_0 - \mathbf{y}_0)$	right-handed	vertically
${}_{+z}\mathbf{E}^{\text{x}}_{\text{sc}_3} = \zeta(j\mathbf{x}_0 - \mathbf{y}_0)$	left-handed	horizontally
${}_{+z}\mathbf{E}^{\text{y}}_{\text{sc}_4} = \zeta(-j\mathbf{x}_0 + \mathbf{y}_0)$	left-handed	vertically
At polarization state: $\mathbf{E}_{\text{inc}} = E_0\mathbf{y}_0$, $\mathbf{H}_{\text{inc}} = E_0/\eta_0\mathbf{x}_0$		
Backscattering	Handedness	Orientation
${}_{+z}\mathbf{E}^{\text{x}}_{\text{sc}_5} = \zeta(-\mathbf{x}_0 + j\mathbf{y}_0)$	right-handed	horizontally
${}_{+z}\mathbf{E}^{\text{y}}_{\text{sc}_6} = \zeta(\mathbf{x}_0 - j\mathbf{y}_0)$	right-handed	vertically
${}_{+z}\mathbf{E}^{\text{x}}_{\text{sc}_7} = \zeta(\mathbf{x}_0 + j\mathbf{y}_0)$	left-handed	horizontally
${}_{+z}\mathbf{E}^{\text{y}}_{\text{sc}_8} = \zeta(-\mathbf{x}_0 - j\mathbf{y}_0)$	left-handed	vertically

Table 3.1: Backward scattering fields for left- and right-handed helices oriented horizontally or vertically in the unit cell of metasurface.

As a result, electric and magnetic moments in (3.13) and (3.14) can be re-written to the simple form as:

$$\begin{aligned} \mathbf{p}_{\text{x}} &= \mp\alpha\frac{E_0}{\eta_0}\mathbf{x}_0, \quad \mathbf{m}_{\text{x}} = -\alpha j E_0\mathbf{x}_0, \\ \mathbf{p}_{\text{y}} &= -\alpha j\frac{E_0}{\eta_0}\mathbf{y}_0, \quad \mathbf{m}_{\text{y}} = \pm\alpha E_0\mathbf{y}_0. \end{aligned} \tag{3.18}$$

Further, we can define the total scattered fields in backward and forward directions from metasurfaces consisting of helical resonators that are arranged along x-axis (horizontally) and y-axis (vertically), respectively. For example, scattered fields in the backward direction (${}_{+z}\mathbf{E}^{\text{x}}_{\text{sc}}$) from right-handed helices arranged vertically in the unit cell can be found as:

$${}_{+z}\mathbf{E}^{\text{y}}_{\text{sc}} = \frac{k^2}{4\pi\epsilon_0 r}e^{-jkr}\left(\alpha\frac{E_0}{\eta_0}\mathbf{x}_0 - \alpha j\frac{E_0}{\eta_0}\mathbf{y}_0\right) = \gamma\frac{\alpha E_0}{\eta_0}\left(\mathbf{x}_0 - j\mathbf{y}_0\right). \tag{3.19}$$

For simplicity and clarity, we rename the parameter of $\gamma\alpha E_0/\eta_0$ to ζ, so that the equation (3.19) is re-written in the following form:

$${}_{+z}\mathbf{E}^{\text{y}}_{\text{sc}} = \zeta\left(\mathbf{x}_0 - j\mathbf{y}_0\right). \tag{3.20}$$

Thus, total reflected fields (${}_{+\text{z}}\mathbf{E}^{total}_{\text{sc}} = {}_{+z}\mathbf{E}^{\text{y}}_{\text{sc}}$) from metasurface consisting of helical resonators arranged only along y-axis will be expressed by the equation (3.20). Using the same way, we can define the backward and forward scattered fields depending on the orientation of helices in the unit cell of metasurface and as a result, reflected and transmitted fields. Table 3.1 shows scattered fields in the backward direction respect to the incident polarization states for right-/left-handed helical resonators and their orientations in the unit cell of metasurface.

In order to find scattered fields in the forward direction, it is necessary to substitute

At polarization state: $\mathbf{E}_{\text{inc}} = E_0\mathbf{x}_0$, $\mathbf{H}_{\text{inc}} = -E_0/\eta_0\mathbf{y}_0$		
Forward scattering	Handedness	Orientation
${}_{-z}\mathbf{E}^{\text{x}}_{\text{sc}_1} = \zeta(-j\mathbf{x}_0 + \mathbf{y}_0)$	right-handed	horizontally
${}_{-z}\mathbf{E}^{\text{y}}_{\text{sc}_2} = \zeta(-j\mathbf{x}_0 + \mathbf{y}_0)$	right-handed	vertically
${}_{-z}\mathbf{E}^{\text{x}}_{\text{sc}_3} = \zeta(-j\mathbf{x}_0 - \mathbf{y}_0)$	left-handed	horizontally
${}_{-z}\mathbf{E}^{\text{y}}_{\text{sc}_4} = \zeta(-j\mathbf{x}_0 - \mathbf{y}_0)$	left-handed	vertically
At polarization state: $\mathbf{E}_{\text{inc}} = E_0\mathbf{y}_0$, $\mathbf{H}_{\text{inc}} = E_0/\eta_0\mathbf{x}_0$		
Forward scattering	Handedness	Orientation
${}_{-z}\mathbf{E}^{\text{x}}_{\text{sc}_5} = \zeta(\mathbf{x}_0 - j\mathbf{y}_0)$	right-handed	horizontally
${}_{-z}\mathbf{E}^{\text{y}}_{\text{sc}_6} = \zeta(\mathbf{x}_0 - j\mathbf{y}_0)$	right-handed	vertically
${}_{-z}\mathbf{E}^{\text{x}}_{\text{sc}_7} = \zeta(-\mathbf{x}_0 - j\mathbf{y}_0)$	left-handed	horizontally
${}_{-z}\mathbf{E}^{\text{y}}_{\text{sc}_8} = \zeta(-\mathbf{x}_0 - j\mathbf{y}_0)$	left-handed	vertically

Table 3.2: The forward scattering fields for left- and right-handed helices oriented horizontally or vertically in the unit cell of metasurface.

the equation (3.18) in (3.2) and express the total field (${}_{-\text{z}}\mathbf{E}^{total}_{\text{sc}}$). For example, forward scattered field (${}_{-z}\mathbf{E}^{\text{y}}_{\text{sc}}$) from metasurface consist of right-handed helices that are arranged only along y-axis (vertically) can be expressed as:

$$ {}_{-z}\mathbf{E}^{\text{y}}_{\text{sc}} = \zeta\left(\mathbf{x}_0 - j\mathbf{y}_0\right). \tag{3.21} $$

In the similar way, forward scattered fields for right- and left-handed helical resonators and taking into account their orientations in the unit cell were summarized in Table 3.2. Total backward or forward scattering fields are a sum of all components of scattered fields in backward and forward directions, respectively. Therefore, total backward scattered field ${}_{+\text{z}}E^{total}_{\text{sc}}$ from the unit cell consisting of right-handed and left-handed helical resonators with balanced polarizabilities which are oriented vertically and horizontally can be expressed as follows:

$$ {}_{+\text{z}}E^{total}_{\text{sc}} = \zeta\left(-\mathbf{x}_0 + j\mathbf{y}_0 + \mathbf{x}_0 - j\mathbf{y}_0 + \mathbf{x}_0 + j\mathbf{y}_0 - \mathbf{x}_0 - j\mathbf{y}_0\right) = 0, \tag{3.22} $$

and in the forward direction

$$ {}_{-\text{z}}E^{total}_{\text{sc}} = \zeta\left(\mathbf{x}_0 - j\mathbf{y}_0 + \mathbf{x}_0 - j\mathbf{y}_0 - \mathbf{x}_0 - j\mathbf{y}_0 - \mathbf{x}_0 - j\mathbf{y}_0\right) = -4j\zeta\mathbf{y}_0. \tag{3.23} $$

On the basis of the foregoing, the reflected and transmitted fields from metasurface can be found in the next way:

$$ \mathbf{E}_{\text{r}} = {}_{+\text{z}}E^{total}_{\text{sc}}, \tag{3.24} $$

$$ \mathbf{E}_{\text{t}} = \mathbf{E}_{\text{inc}} + {}_{-\text{z}}E^{total}_{\text{sc}}, \tag{3.25} $$

or through a total backscattering

$$\mathbf{E}_{\rm r} = {}_{+\rm z}E_{\rm sc}^{total}, \tag{3.26}$$

$$\mathbf{E}_{\rm t} = \mathbf{E}_{\rm inc} - {}_{+\rm z}E_{\rm sc}^{total}. \tag{3.27}$$

Therefore, reflected and transmitted fields from metasurface consists of right- and left-handed helices oriented in xy-plane horizontally and vertically, respectively, expressed as:

$$\mathbf{E}_{\rm r} = 0, \tag{3.28}$$

$$\mathbf{E}_{\rm t} = \mathbf{E}_{\rm inc} - 4j\zeta\mathbf{y}_0 = E_0\mathbf{y}_0\left(1 - 4j\gamma\frac{\alpha}{\eta_0}\right) = -3j\gamma\frac{\alpha}{\eta_0}E_0\mathbf{y}_0. \tag{3.29}$$

As a result, such arrangement of helices in the unit cell of metasurface gives us a zero reflection and co-polarized unit transmission at the resonance. Therefore, we can obtain polarization control in reflection and transmission regimes by choosing the orientation of helices in metasurface. In a similar way, we can define a proper arrangement of helical resonators in the unit cell of metasurface to achieve desired functionalities.

3.2 Linearly polarized rotators for reflected waves

One of the remarkable functionalities that can be realized due to chiral metasurfaces is the rotation by a fixed angle of the polarization plane of reflected or transmitted waves [116]. Some examples of co-polarized rotators based on omega-type bi-anisotropic resonators for the realization of metamirror devices or wavefront shaping metasurfaces in the reflection regime have been reported in references [52, 117, 118]. Also, non-transparent cross-polarized rotators or so-called reflectors based on the three-layer design for THz spectral range [116, 119] and GHz range [120, 121] which might have potential applications in communications as polarizer devices have been reported. Here, due to analytical approach for determination of required arrangement and numerical simulation, we synthesized off-resonance transparent co-polarized and cross-polarized rotators based on double-turn helical resonators with tailoring structural parameter (see Table 2.1) to the balance of their axial polarizabilities which work for reflected waves in the microwave range. In future, these functional helix-based metasurfaces can be used for manipulation of wavefront shaping and anomalous refraction.

3.2.1 Co-polarized reflector

Here, we are aiming to synthesize the helix-based co-polarized rotator for reflected waves or so-called co-polarized reflector in the microwave range. This reflector is a structure that, when illuminated with a linearly polarized incident wave, produces zero transmission and does not rotate the polarization plane in the reflected wave (see Figure 3.1). As well known, when a linearly polarized plane wave is reflected from an ideal mirror, the phase of the reflected wave changes by π while retaining its polarization and amplitude. In this case, the phase of the wave will equal to zero while maintaining the polarization and amplitude of the reflected wave. These properties can be expressed by the following equations:

$$\mathbf{E}_{\rm inc} = E_0\mathbf{x}_0 \Rightarrow \begin{cases} \mathbf{E}_{\rm r} = AE_0\mathbf{x}_0, \\ \mathbf{E}_{\rm t} = 0. \end{cases} \tag{3.30}$$

$$\mathbf{E}_{\rm inc} = E_0\mathbf{y}_0 \Rightarrow \begin{cases} \mathbf{E}_{\rm r} = AE_0\mathbf{y}_0, \\ \mathbf{E}_{\rm t} = 0, \end{cases} \tag{3.31}$$

where A is any complex number (in case of a lossless in metasurface is $|A| = 1$). In accordance with expressions in Table 3.1 and 3.2, we can satisfy the conditions for co-polarized reflection (3.30) and (3.31) in the next combination of helices in the unit cell:

$$\mathbf{E}_{\rm inc} = E_0\mathbf{x}_0 \Rightarrow \begin{cases} \mathbf{E}_{\rm r} = {}_{+z}\mathbf{E}^{\rm x}_{\rm sc_1} + {}_{+z}\mathbf{E}^{\rm x}_{\rm sc_3} = {}_{+z}\mathbf{E}^{\rm y}_{\rm sc_2} + {}_{+z}\mathbf{E}^{\rm y}_{\rm sc_4} = \\ 2j\zeta\mathbf{x}_0 = AE_0\mathbf{x}_0, \\ \mathbf{E}_{\rm t} = \mathbf{E}_{\rm inc} + ({}_{-z}\mathbf{E}^{\rm x}_{\rm sc_1} + {}_{-z}\mathbf{E}^{\rm x}_{\rm sc_3}) = \\ \mathbf{E}_{\rm inc} + ({}_{-z}\mathbf{E}^{\rm y}_{\rm sc_2} + {}_{-z}\mathbf{E}^{\rm y}_{\rm sc_4}) = E_0\mathbf{x}_0 - 2j\zeta\mathbf{x}_0 = 0. \end{cases} \tag{3.32}$$

$$\mathbf{E}_{\rm inc} = E_0\mathbf{y}_0 \Rightarrow \begin{cases} \mathbf{E}_{\rm r} = {}_{+z}\mathbf{E}^{\rm x}_{\rm sc_5} + {}_{+z}\mathbf{E}^{\rm x}_{\rm sc_7} = {}_{+z}\mathbf{E}^{\rm y}_{\rm sc_6} + {}_{+z}\mathbf{E}^{\rm y}_{\rm sc_8} = \\ 2j\zeta\mathbf{y}_0 = AE_0\mathbf{y}_0, \\ \mathbf{E}_{\rm t} = \mathbf{E}_{\rm inc} + ({}_{-z}\mathbf{E}^{\rm x}_{\rm sc_5} + {}_{-z}\mathbf{E}^{\rm x}_{\rm sc_7}) = \\ \mathbf{E}_{\rm inc} + ({}_{-z}\mathbf{E}^{\rm y}_{\rm sc_6} + {}_{-z}\mathbf{E}^{\rm y}_{\rm sc_8}) = E_0\mathbf{y}_0 - 2j\zeta\mathbf{y}_0 = 0, \end{cases} \tag{3.33}$$

where complex number $A = \gamma\cdot\alpha\cdot\eta_0 = \dfrac{k^2}{4\pi\epsilon_0 r}e^{-jkr}\cdot\mu_0\dfrac{SL}{Z_{\rm h}}\cdot\eta_0$ and its module $|A|$ has to be equal one. Therefore, in order to obtain co-polarized reflection with phase equal zero it is necessary to arrange the right-handed and left-handed helices in unit cell only vertically or horizontally respectively in xy-plane of metasurface in accordance with conditions (3.32) or (3.33).

To verify this assumption, we use a numerical simulation based on FEM. In particular case, double-turn helices with balanced polarizabilities and pre-calculated structural parameters (H = 2.3 mm, R = 3.3 mm, and D = 0.5 mm) have been taken from Table 2.1 and used as polarizable resonators. Figures 3.2(a-c) show required arrangements of double-turn helical resonators in the unit cell of metasurfaces to obtain the co-polarized reflection at the resonance in the microwave range of 2.5-3.5 GHz. Metasurfaces are excited by incident linearly polarized waves propagating along the z-axis at normal incidence. Helical resonators consist of copper right-handed (RH) and left-handed (LH) double-turn helices which are embedded halfway into a styrofoam with a thickness of 10 mm. As seen from Figure 3.2(a), unit cell of co-polarized reflector consists of two helices arranged along or parallel x-axis (it means towards along the helix axis) with period of 32 mm. The interelement distance between helices in the x-direction is equal to half of the period. Figure 3.2(b) shows the unit cell of co-polarized reflector where helices are arranged more

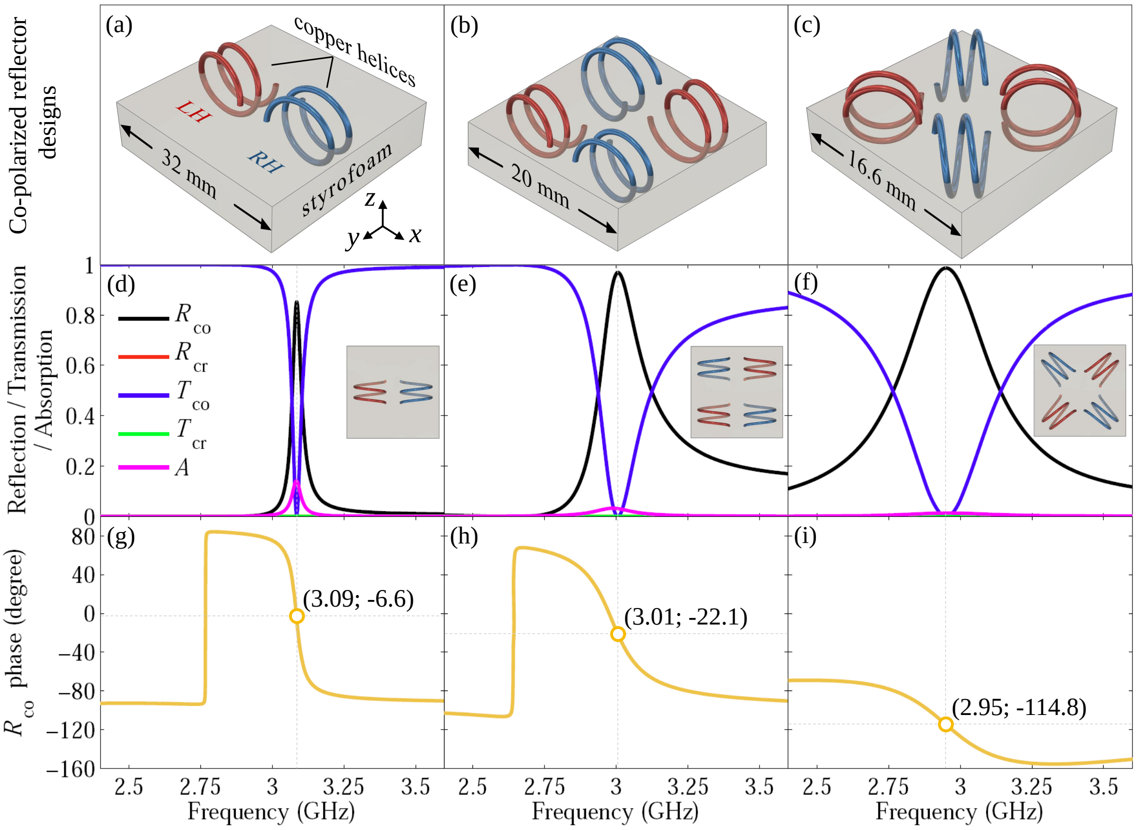

Figure 3.2: (a-c) Unit cell designs of co-polarized reflector based on copper right-handed (blue color) and left-handed (red color) double-turn helical resonators which are halfway embedded into the styrofoam for mechanical support. (d-f) Simulated reflection, transmission, and absorption spectra with respectively polarization states at normal incidence. Top view of the unit cell is depicted in the insert of each figure. (g-i) Phases of co-polarized reflection ($R_{\rm co}$) for the different arrangement of helices in the metasurface.

symmetrically in compare with previous case. The unit cell comprises of two RH and two LH double-turn helices arranged parallel x-axis with a period of 20 mm. In this case, we expect to achieve absolutely independent response from metasurface to the incident linearly polarized waves. In addition, another case of symmetric arrangement of helical resonators in the unit cell to achieve co-polarized reflection is depicted in Figures 3.2(c). Similarly to the previous, the unit cell consists of two RH and two LH helices which are rotated by 45° in the xy-plane relatively to the previous position (see Figure 3.2(b)). The period of metasurface is optimized by numerical simulation and equal of 16.6 mm.

In the process of simulation, the linearly polarized plane wave propagating along $-z$-direction is normally incident onto the unit cell. It should be noted that the result does not depend on the propagation of the wave along the $\pm z$-axis due to consideration of the reciprocal medium. Periodic boundaries are set at x- and y-sides while Floquet modes as source are set at $\pm z$-sides. Fundamentally, Floquet modes are plane waves with propagation direction set by the frequency and geometry of the periodic structure. Numerical simulation is carried out to investigate the polarization transformation behavior. Thus, the co-polarized reflection ($R_{\rm co}$), transmission ($T_{\rm co}$) and cross-polarized reflection ($R_{\rm cr}$), transmission (T_{cr}) coefficients would be studied. In conventional terms, reflection (R), transmission (T) and absorption (A) can be expressed as:

$$\begin{aligned} R &= R_{\mathrm{co}} + R_{\mathrm{cr}}, \\ T &= T_{\mathrm{co}} + T_{\mathrm{cr}}, \\ A &= 1 - R_{\mathrm{co}} - R_{\mathrm{cr}} - T_{\mathrm{co}} - T_{\mathrm{cr}}. \end{aligned} \tag{3.34}$$

As a result, Figures 3.2(d-f) show simulated reflection, transmission and absorption spectra with respectively polarization states in the range of $2.5 - 3.5$ GHz. As seen from Figure 3.2(d), co-polarized reflection peak reaches value of 0.85 at the resonance of 3.09 GHz, while the co-polarized transmission drops to zero. The cross-polarized reflection and transmission are equal to zero. Helix-based co-polarized reflector is fully transparent away from the resonance band as expected. However, relatively high absorption peak ($A = 0.14$) can be seen for resonant copper helices with a low resistance lossy (skin depth is about 1.1903 μm). It comes from the strong electromagnetic coupling between two helices, that leads to increasing of surface current density in each helical conductive wire and, as a consequence, to increasing of the absorption properties in the metasurface. Nevertheless, we obtained the co-polarized reflection at the resonant frequency from helix-based metasurface in the microwave range.

Figure 3.2(e) shows reflectance, transmittance, and absorbance at *co* and *cross* polarizations at normal incidence for symmetric arrangement of double-turn helices. As seen, co-reflectance reaches a peak value of 0.97 at the resonant frequency of 3.01 GHz. The absorption spectrum does not exceed of 0.03 in the entire frequency range. However, metasurface exhibits a low transparency for the higher frequencies what is undesirable for such symmetry arranged helix-based structure. To avoid this drawback, another symmetric arrangement of helical resonators in the unit cell can be used (see Figure 3.2(c)). Simulated R, T, A spectra with relatively polarization state of helix-based co-polarized reflector are shown in Figure 3.2(f). As seen, metasurface exhibits co-polarized reflection of 0.98 at the resonance of 2.95 GHz with absorption about 0.014. As expected, metasurface has the symmetric reflectance, transmittance, and absorption spectra even at higher frequencies. Moreover, highly efficient helix-based co-polarized reflector is fully transparent in the off-resonance band.

As was mentioned before, co-polarized reflector should possess a zero phase of reflection at the operational frequency in comparison with perfect reflector (phase of reflected waves is equal to 180°). This is one of the main difference between our design and perfect reflector. Using numerical simulation, phases of co-polarized reflected waves were calculated as an angle (phase) of a complex amplitude of co-polarized reflection ($cang[E_{\mathrm{co}}]$) with cutting value by ± 180. Figures 3.2(g-i) show simulated phases of co-polarized reflection of designed helix-based metasurfaces in the range of $2.5 - 3.5$ GHz. As seen from Figures 3.2(g) and (h), the phases of a co-polarized reflected waves are equal to $-6.6°$ and $-22.1°$ at the resonances of 3.09 GHz and 3.01 GHz, respectively. The obtained phases do not strictly equal to zero but close to it. Nevertheless, reflected waves do not strongly change the polarization state respects to their incident linearly polarized wave that is satisfied to the conditions of (3.30) or (3.31). Figure 3.2(i) demonstrates R_{co} phase for the last design of co-polarized reflector. In this case, the phase is equal to $-114.8°$ at the resonant frequency of 2.95 GHz. Obtained result is strongly different from the previous two designs and still under investigation. However, this does not disrupt the performance of helix-based co-polarized reflector but the phase should take under consideration carefully.

Thus, all proposed co-polarized reflectors based on copper RH and LH double-turn helices with balanced polarizabilities exhibit off-resonance transparency in the microwave range. In future, this advantage can be used to create a multilayer structure with different resonant frequencies to obtain a broadband response or combine with other functional metasurfaces.

3.2.2 Cross-polarized reflector

Cross-polarizer reflector rotates polarization plane by 90° of reflected wave respect to illuminated linearly polarized plane wave that exhibits zero transmission at the resonance. As was mentioned before, 90° polarization reflectors based on three-layer structures were actively investigated in various spectral ranges [116, 119–123]. Here, we are aiming to synthesize single-layer cross-polarized reflectors consisting of copper double-turn helices for microwave range. Using our approach and numerical simulation, required arrangements of helical resonators in the unit cell of metasurface to achieve pure cross-polarized reflection have been defined. These properties must be satisfied to conditions of cross-polarized transformation for the reflected waves as follows:

$$\mathbf{E}_{\mathrm{inc}} = E_0\mathbf{x}_0 \Rightarrow \begin{cases} \mathbf{E}_{\mathrm{r}} = \pm A E_0 \mathbf{y}_0, \\ \mathbf{E}_{\mathrm{t}} = 0. \end{cases} \tag{3.35}$$

$$\mathbf{E}_{\mathrm{inc}} = E_0\mathbf{y}_0 \Rightarrow \begin{cases} \mathbf{E}_{\mathrm{r}} = \pm A E_0 \mathbf{x}_0, \\ \mathbf{E}_{\mathrm{t}} = 0. \end{cases} \tag{3.36}$$

Following a conventional method, arrangement of helices in unit cell of metasurface can be found from Table 3.1 and 3.2 taking into account requirements (3.35) or (3.36) in the next way:

$$\mathbf{E}_{\mathrm{inc}} = E_0\mathbf{x}_0 \Rightarrow \begin{cases} \mathbf{E}_{\mathrm{r}} = {}_{+z}\mathbf{E}^{\mathrm{x}}_{\mathrm{sc}_1} + {}_{+z}\mathbf{E}^{\mathrm{y}}_{\mathrm{sc}_4} = {}_{+z}\mathbf{E}^{\mathrm{y}}_{\mathrm{sc}_2} + {}_{+z}\mathbf{E}^{\mathrm{x}}_{\mathrm{sc}_3} = \\ \pm 2\zeta \mathbf{y}_0 = \pm A E_0 \mathbf{y}_0, \\ \mathbf{E}_{\mathrm{t}} = \mathbf{E}_{\mathrm{inc}} + ({}_{-z}\mathbf{E}^{\mathrm{x}}_{\mathrm{sc}_1} + {}_{-z}\mathbf{E}^{\mathrm{y}}_{\mathrm{sc}_4}) = \\ \mathbf{E}_{\mathrm{inc}} + ({}_{-z}\mathbf{E}^{\mathrm{y}}_{\mathrm{sc}_2} + {}_{-z}\mathbf{E}^{\mathrm{x}}_{\mathrm{sc}_3}) = E_0\mathbf{x}_0 - 2j\zeta\mathbf{x}_0 = 0. \end{cases} \tag{3.37}$$

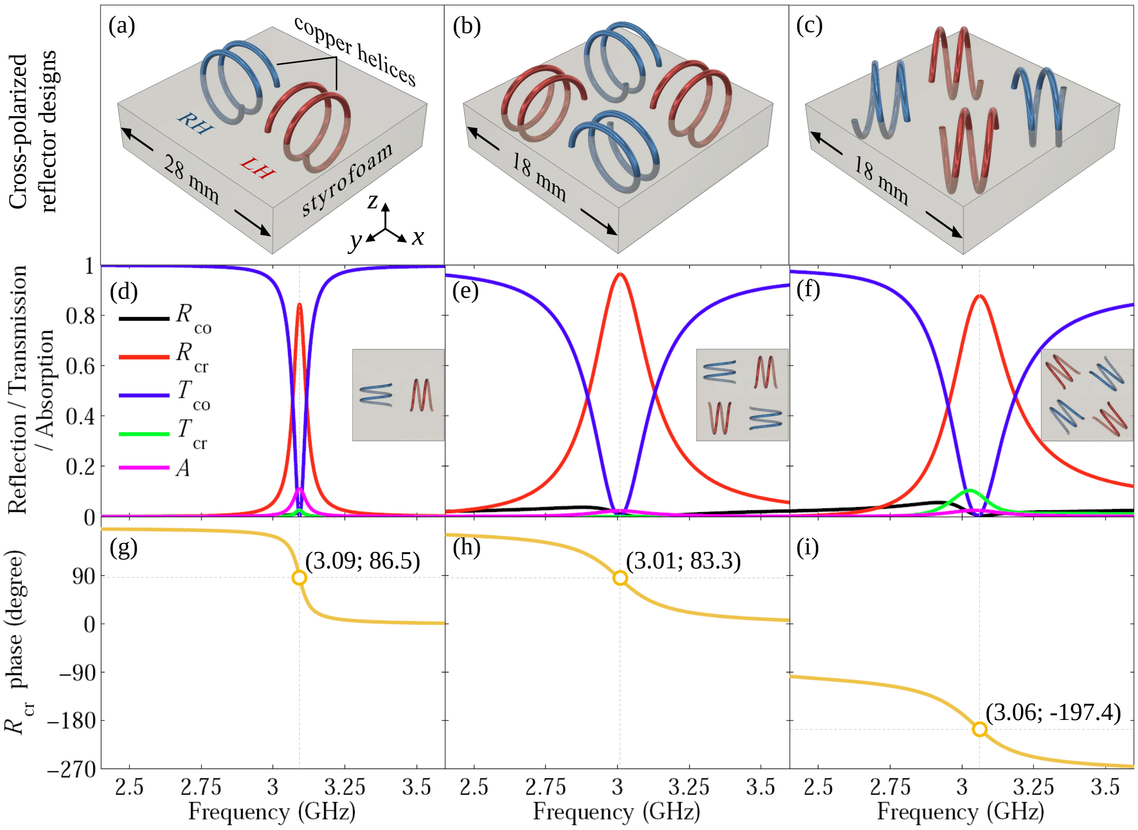

Figure 3.3: (a-c) Unit cell designs of cross-polarized reflector based on copper RH and LH double-turn helical resonators which are halfway embedded into the styrofoam. (d-f) Simulated reflection, transmission, and absorption spectra with respectively polarization states at normal incidence. Top view of the unit cell is depicted in the insert of each figure. (g-i) Phases of cross-polarized reflection (R_{cr}) for the different arrangement of helices in the metasurface.

$$\mathbf{E}_{\text{inc}} = E_0\mathbf{y}_0 \Rightarrow \begin{cases} \mathbf{E}_{\text{r}} = {}_{+z}\mathbf{E}^{\text{x}}_{\text{sc}_5} + {}_{+z}\mathbf{E}^{\text{y}}_{\text{sc}_8} = {}_{+z}\mathbf{E}^{\text{y}}_{\text{sc}_6} + {}_{+z}\mathbf{E}^{\text{x}}_{\text{sc}_7} = \\ \pm 2\zeta\mathbf{x}_0 = \pm AE_0\mathbf{x}_0, \\ \mathbf{E}_{\text{t}} = \mathbf{E}_{\text{inc}} + ({}_{-z}\mathbf{E}^{\text{x}}_{\text{sc}_5} + {}_{-z}\mathbf{E}^{\text{y}}_{\text{sc}_8}) = \\ \mathbf{E}_{\text{inc}} + ({}_{-z}\mathbf{E}^{\text{y}}_{\text{sc}_6} + {}_{-z}\mathbf{E}^{\text{x}}_{\text{sc}_7}) = E_0\mathbf{y}_0 - 2j\zeta\mathbf{y}_0 = 0. \end{cases} \tag{3.38}$$

Figures 3.3(a-c) show required arrangements of double-turn helical resonators in the unit cell of metasurfaces to achieve the cross-polarized reflection at the resonance. Metasurfaces are excited by incident linearly polarized waves propagating along the z-axis at normal incidence. Helical resonators with balanced polarizabilities consist of copper RH and LH double-turn helices which are embedded halfway into a styrofoam with a thickness of 10 mm. Figure 3.3(a) shows the unit cell of cross-polarized reflector design. As follows from equations (3.37) or (3.38), cross-polarized reflection from metasurface can be obtained by arranging of one RH helix vertically and LH another one horizontally in the unit cell. Using numerical simulation, design were found in accordance with the analytical approach where period of structure was optimized and equal to 28 mm. The inter-element distance between helices in the x-direction is equal to half of the period. Figure 3.3(b) shows the unit cell of cross-polarized reflector where helices are arranged more symmetrically in the metasurface in comparison with previous case. The unit cell comprises of two RH and two LH double-turn helices arranged parallel x- and y-axes with a period of 18 mm. In this case, helix-based metasurface have to possess independent EM response to the incident linearly polarized waves. Follows to similar case with co-polarized reflector, another symmetric arrangement of helical resonators in the unit cell was proposed and depicted in Figure 3.3(c). Reciprocally, the unit cell consists of two RH and two LH helices which are rotated by 45° in the xy-plane relatively to the previous position with optimized period of 18 mm.

Figures 3.3(d-f) show simulated reflection, transmission and absorption spectra with respectively polarization states at normal incidence in the range of $2.5 - 3.5$ GHz. As seen from Figure 3.3(d), cross-polarized reflection peak reaches value of 0.84 at the resonance of 3.09 GHz, while the co-polarized transmission drops to zero. The co-polarized reflection and cross-polarized transmission are close to zero in the entire spectrum range. The absorption peak of 0.11 can be seen at the resonance due to the weak lossy in the copper and strong EM coupling between two helices. As expected, helix-based cross-polarized reflector is fully transparent away from the resonance band. Figure 3.3(e) demonstrates R, T, A spectra at *co* and *cross* polarizations of symmetrically arranged double-turn helices in the unit cell, respectively. As can be seen, cross-polarized reflection reaches a peak value of 0.96 at the resonant frequency of 3.01 GHz. The absorption peak is equal to 0.02 at the resonance, while the reflection spectrum at co-polarization does not exceed of 0.04 in the entire range. Figure 3.3(f) shows simulated R_{co}, R_{cr}, T_{co}, T_{cr}, and A spectra of the last design with symmetric arrangement of helices in the cross-polarized reflector. This metasurface exhibits cross-polarized reflection of 0.87 at the resonance of 3.06 GHz and absorption about 0.02 at 3.03 GHz. The absorption peak does not correspond to the main resonance due to increasing of cross-polarized transmission till 0.1 at the same resonant frequency that leads to appear some additional currents in the double turn helices. Also, falling of co-polarized transmission at higher frequencies can be seen (an objectionable behavior).

Helix-based cross-polarized reflector should possess a 90° phase for cross-polarized reflection at the resonance. Figures 3.3(g-i) show simulated phases for cross-polarized reflection of designed helix-based metasurfaces in the range of $2.5 - 3.5$ GHz. As seen from Figures 3.3(g) and (h), the phases of cross-polarized reflected waves are equal to 86.5° and 83.3° at the resonances of 3.09 GHz and 3.01 GHz, respectively. The calculated phases are close the expected value and confirms the effectiveness of cross-reflectors. Figure 3.3(i) demonstrates R_{cr} phase for the last design of cross-polarized reflector. In this case, the phase is equal to $-197.4°$ at the resonant frequency of 2.95 GHz. Obtained result is strongly different from the previous two designs and still under consideration.

In conclusion, using our approach for determination of proper arrangement of helical resonators depending on their functionalities and numerical simulation, off-resonance transparent helix-based cross-polarized reflectors have been designed. These metasurfaces comprising of RH and LH double-turn helices demonstrate good efficiency ($R_{\mathrm{cr}} > 0.84$) at the resonance for 90° rotation of reflected linearly polarized waves in the microwave range.

3.3 Linearly polarized rotators for transmitted waves

The manipulation of polarization state and phase for transmitted waves leads to the novel functionalities. Similar to the previous case described in Section 3.2, it is possible to synthesize helix-based co-polarized and cross-polarized rotators at transmission regime or so-called co-/cross-transmits in the microwave range. Several example of co-polarized rotators have been proposed for realization of transmitarrays with anomalous refractive index [124–126], metalens [51, 127, 128], and wavefront shaping devices for transmitted waves [116, 129, 130]. A brief review of cross-polarized transmits or so called twist polarizers will be described in Section 4.1. Here, using analytical approach for determination of required arrangement and numerical simulation based on FEM, we synthesized off-resonance transparent co-polarized and cross-polarized transmits based on double-turn helical resonators with taken the structural parameter from Table 2.1 and which have the balanced of polarizabilities to achieve co-polarized and cross-polarized transmission properties in the microwave range. In future, these functional helix-based metasurfaces can be used for manipulation of wavefront shaping and anomalous refraction.

3.3.1 Co-polarized transmit

Co-polarized rotator or transmit is a device that allows maintaining the same linear polarization with a unit transmission relative to the polarization of incident waves. Usually, the phase of transmitted waves is equal to 180°. Especially, co-transmits with unit cells tailoring to different phases of transmitted waves can represent as transmitarrays for manipulation of wavefront shaping and anomalous refraction [130]. Here, we consider a simple way to define a proper arrangements of helical resonators with balanced polarizabilities to synthesize co-polarized transmits. Towards to the synthesis of co-polarized transmit designs, it is necessary to satisfy the next conditions:

$$\mathbf{E}_{\mathrm{inc}} = E_0\mathbf{x}_0 \Rightarrow \begin{cases} \mathbf{E}_{\mathrm{r}} = 0, \\ \mathbf{E}_{\mathrm{t}} = -AE_0\mathbf{x}_0. \end{cases} \tag{3.39}$$

$$\mathbf{E}_{\mathrm{inc}} = E_0\mathbf{y}_0 \Rightarrow \begin{cases} \mathbf{E}_{\mathrm{r}} = 0, \\ \mathbf{E}_{\mathrm{t}} = -AE_0\mathbf{y}_0. \end{cases} \tag{3.40}$$

In accordance with data in Table 3.1 and 3.2 and taking into account requirements (3.39) or (3.40), the required arrangement of helical resonators in the unit cell of metasurface can be found. The combination of helical resonators in the unit cell to achieve

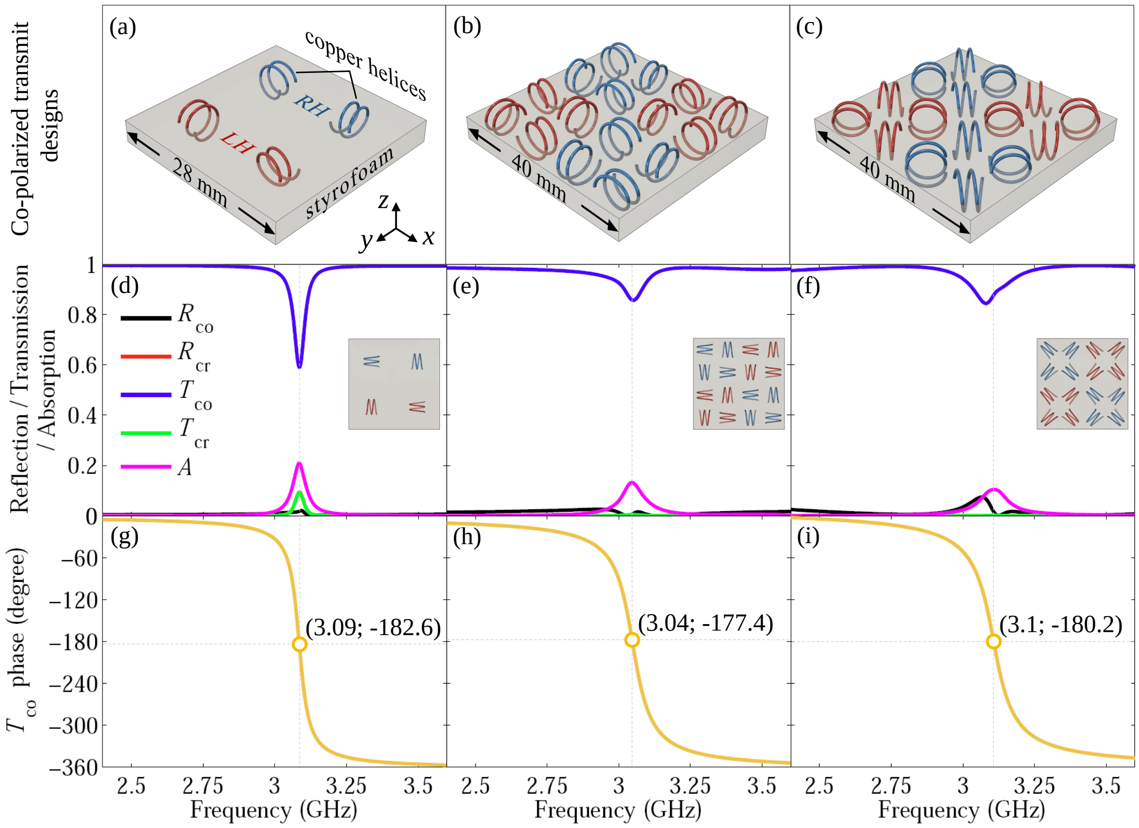

Figure 3.4: (a-c) Unit cell designs of co-polarized transmit based on copper RH and LH double-turn helical resonators which are halfway embedded into the styrofoam. (d-f) Simulated reflection, transmission, and absorption spectra with respectively polarization states at normal incidence. Top view of the unit cell is depicted in the insert of each figure. (g-i) Phases of co-polarized transmission (T_{co}) for the different arrangement of helices in the metasurface.

co-polarized transmission is expressed as follows:

$$\mathbf{E}_{\text{inc}} = E_0\mathbf{x}_0 \Rightarrow \begin{cases} \mathbf{E}_{\text{r}} = {}_{+z}\mathbf{E}^{\text{x}}_{\text{sc}_1} + {}_{+z}\mathbf{E}^{\text{y}}_{\text{sc}_2} + {}_{+z}\mathbf{E}^{\text{x}}_{\text{sc}_3} + {}_{+z}\mathbf{E}^{\text{y}}_{\text{sc}_4} = 0, \\ \mathbf{E}_{\text{t}} = \mathbf{E}_{\text{inc}} + ({}_{-z}\mathbf{E}^{\text{x}}_{\text{sc}_1} + {}_{-z}\mathbf{E}^{\text{y}}_{\text{sc}_2} + {}_{-z}\mathbf{E}^{\text{x}}_{\text{sc}_3} + {}_{-z}\mathbf{E}^{\text{y}}_{\text{sc}_4}) = \\ -3j\zeta\mathbf{x}_0 = -AE_0\mathbf{x}_0. \end{cases} \tag{3.41}$$

$$\mathbf{E}_{\text{inc}} = E_0\mathbf{y}_0 \Rightarrow \begin{cases} \mathbf{E}_{\text{r}} = {}_{+z}\mathbf{E}^{\text{x}}_{\text{sc}_5} + {}_{+z}\mathbf{E}^{\text{y}}_{\text{sc}_6} + {}_{+z}\mathbf{E}^{\text{x}}_{\text{sc}_7} + {}_{+z}\mathbf{E}^{\text{y}}_{\text{sc}_8} = 0, \\ \mathbf{E}_{\text{t}} = \mathbf{E}_{\text{inc}} + ({}_{-z}\mathbf{E}^{\text{x}}_{\text{sc}_5} + {}_{-z}\mathbf{E}^{\text{y}}_{\text{sc}_6} + {}_{-z}\mathbf{E}^{\text{x}}_{\text{sc}_7} + {}_{-z}\mathbf{E}^{\text{y}}_{\text{sc}_8}) = \\ -3j\zeta\mathbf{y}_0 = -AE_0\mathbf{y}_0. \end{cases} \tag{3.42}$$

As follows from equations (3.41) or (3.42), metasurface consists of RH helical resonators arranged in xy-plane vertically and horizontally, and also the similar case for LH helices should produce a co-polarization transmission. Meanwhile, metasurface should possess reflectionless behavior in the entire operational range.

Figures 3.4(a-c) show the unit cells of co-polarized transmit designs with different proper arrangements of helical resonators. Their reflection, transmission, and absorption spectra with relative co-/cross-polarizations at normal incidence are given in Figures 3.4(d-f). The first design of helix-based metasurface represents the co-polarized transmit with unit cell consisting of two RH and two LH copper double-turn helical resonators which are embedded into styrofoam and located vertically and horizontally as is shown in Figure 3.4(a). The period is equal of 28 mm and optimized by numerical simulation to achieve the maximum of amplitude in co-polarized transmission at the resonance. A distance between helical resonators is equal to the half of period. As seen from Figure 3.4(d), helix-based metasurface exhibits co-polarized transmission at all considered frequency range of $2.5 - 3.5$ GHz. However, the resonance in metasurface occurs at the frequency of 3.09 GHz with relatively weak co-transmission of 0.59. Moreover, co-transmit has resonant absorption peak with value of 0.21 and additional peaks in cross-polarized reflection ($R_{\mathrm{cr}} = 0.093$) and transmission ($T_{\mathrm{cr}} = 0.09$), respectively. This indicates a poor quality of co-polarized transmit since it has a low amplitude of transmitted waves and additional unwanted cross-polarized characteristics. To avoid these drawbacks we propose to use four sub-unit cells consisting of RH and LH helices to achieve better performance.

Figures 3.4(b) demonstrates unit cell design of co-polarized transmit consisting of four sub-unit cells with copper double-turn helices that are halfway embedded into the styrofoam. Period of the unit cell is equal 40 mm with an inter-element distance of quarter period. As seen, each sub-unit cells consist of four RH or LH double-turn helices arranged horizontally and vertically in accordance with the analytical approach and Eqns. (3.41) or (3.42). This arrangement of helical resonators in metasurface leads to a balanced EM response between groups of RH and LH helices that subsequently improve the desired properties. As a result, metasurface with balanced EM response exhibits higher co-polarized transmission about 0.86 at the resonant frequency of 3.04 GHz in comparison with the previous design. Meanwhile, the cross-polarized reflection and transmission are equal zero. However, the relatively high absorption peak of 0.13 at the resonance can be seen. Nevertheless, this transparent helix-based co-polarized transmit demonstrates tolerable characteristics in accordance with numerically simulated data.

In addition, we have investigated a case when helical resonators have been shifted by $45°$ respect to their initial positions as can be seen from Figure 3.4(c). Designed helix-based metasurface has a period of 40 mm with an inter-element distance of quarter period. Reflection, transmission, and absorption spectra with *co* and *cross* polarizations at normal incidence can be seen in Figure 3.4(f). In this case, the resonance occurs at the frequency of 3.1 GHz with co-transmission of 0.87 and absorption peak of 0.11, respectively. As a result, single-layer helix-based co-polarized transmit metasurface exhibits similar performance in comparison with the previous design.

Calculated phases of co-polarized transmitted waves for proposed designs with a different arrangement of helical resonators are shown in Figures 3.4(g-i). As can be seen, all designed metasurfaces exhibit phases of co-polarized transmitted waves at resonance close to $-180°$, while the phase of co-transmission spans nearly full 2π range from 2.5 to 3.5 GHz.

As a result, all proposed helix-based metasurfaces exhibit transparent behavior and broadband low-reflection properties in the operational frequency range. It opens up more freedom in design to achieve new desirable functionalities. For example, our approach was used for realization and experimental verification of novel transmitarray based on double-turn helices [4-A]. This transmitarray represents of similar arrangement of helical resonators in the unit cell that was depicted in Figure 3.4(c). There is shown that helix-based transmitarray exhibits wavefront shaping (with the efficiency more than 80%) of transmitted waves with high transparency beyond the operating frequency range. Thus, helix-based co-polarized transmit can be used for manipulation of transmitted waves to achieve such functionalities as wavefront shaping and anomalous refraction.

3.3.2 Cross-polarized transmit

Here, we are focused on the obtaining of cross-polarized transmit by definition of required arrangement of helical resonators in the unit cell and verified by numerical simulation. The cross-polarized transmit or twist polarizer is a 90° polarization rotator that converts TE polarized incident waves into TM polarized transmitted waves and vice versa with unit transmittance [88, 131]. These properties can be expressed by the following equations:

$$\mathbf{E}_{\mathrm{inc}} = E_0\mathbf{x}_0 \Rightarrow \begin{cases} \mathbf{E}_{\mathrm{r}} = 0, \\ \mathbf{E}_{\mathrm{t}} = \pm A E_0 \mathbf{y}_0. \end{cases} \tag{3.43}$$

$$\mathbf{E}_{\mathrm{inc}} = E_0\mathbf{y}_0 \Rightarrow \begin{cases} \mathbf{E}_{\mathrm{r}} = 0, \\ \mathbf{E}_{\mathrm{t}} = \pm A E_0 \mathbf{x}_0. \end{cases} \tag{3.44}$$

In accordance with expressions for backward and forward scattered fields in Table 3.1 and 3.2, we can find the proper arrangement of helical resonators in the metasurface which have to satisfied the requirements (3.43) or (3.44). Thus, the arrangement of helical resonators in the unit cell are expressed in the following way:

$$\mathbf{E}_{\mathrm{inc}} = E_0\mathbf{x}_0 \Rightarrow \begin{cases} \mathbf{E}_{\mathrm{r}} = {}_{+z}\mathbf{E}^{\mathrm{x}}_{\mathrm{sc}_1} + {}_{+z}\mathbf{E}^{\mathrm{y}}_{\mathrm{sc}_2} = {}_{+z}\mathbf{E}^{\mathrm{x}}_{\mathrm{sc}_3} + {}_{+z}\mathbf{E}^{\mathrm{y}}_{\mathrm{sc}_4} = 0, \\ \mathbf{E}_{\mathrm{t}} = \mathbf{E}_{\mathrm{inc}} + ({}_{-z}\mathbf{E}^{\mathrm{x}}_{\mathrm{sc}_1} + {}_{-z}\mathbf{E}^{\mathrm{y}}_{\mathrm{sc}_2}) = \\ \mathbf{E}_{\mathrm{inc}} + ({}_{-z}\mathbf{E}^{\mathrm{x}}_{\mathrm{sc}_3} + {}_{-z}\mathbf{E}^{\mathrm{y}}_{\mathrm{sc}_4}) = \pm 2\zeta \mathbf{y}_0 = \pm A E_0 \mathbf{y}_0. \end{cases} \tag{3.45}$$

$$\mathbf{E}_{\mathrm{inc}} = E_0\mathbf{y}_0 \Rightarrow \begin{cases} \mathbf{E}_{\mathrm{r}} = {}_{+z}\mathbf{E}^{\mathrm{x}}_{\mathrm{sc}_5} + {}_{+z}\mathbf{E}^{\mathrm{y}}_{\mathrm{sc}_6} = {}_{+z}\mathbf{E}^{\mathrm{x}}_{\mathrm{sc}_7} + {}_{+z}\mathbf{E}^{\mathrm{y}}_{\mathrm{sc}_8} = 0, \\ \mathbf{E}_{\mathrm{t}} = \mathbf{E}_{\mathrm{inc}} + ({}_{-z}\mathbf{E}^{\mathrm{x}}_{\mathrm{sc}_5} + {}_{-z}\mathbf{E}^{\mathrm{y}}_{\mathrm{sc}_6}) = \\ \mathbf{E}_{\mathrm{inc}} + ({}_{-z}\mathbf{E}^{\mathrm{x}}_{\mathrm{sc}_7} + {}_{-z}\mathbf{E}^{\mathrm{y}}_{\mathrm{sc}_8}) = \pm 2\zeta \mathbf{x}_0 = \pm A E_0 \mathbf{x}_0. \end{cases} \tag{3.46}$$

As follows from equations (3.45) or (3.46), in order to obtain the cross-polarization in transmission regime metasurface has to be consists of only RH or LH helical resonators arranged both horizontally and vertically in the unit cell. Using numerical simulation based co-polarized transmit can be designed and tested in accordance with theoretical inference. Figures 3.5(a-c) show unit cell designs of off-resonance transparent cross-polarized transmits with different arrangements of helical resonators. Their reflection, transmission,

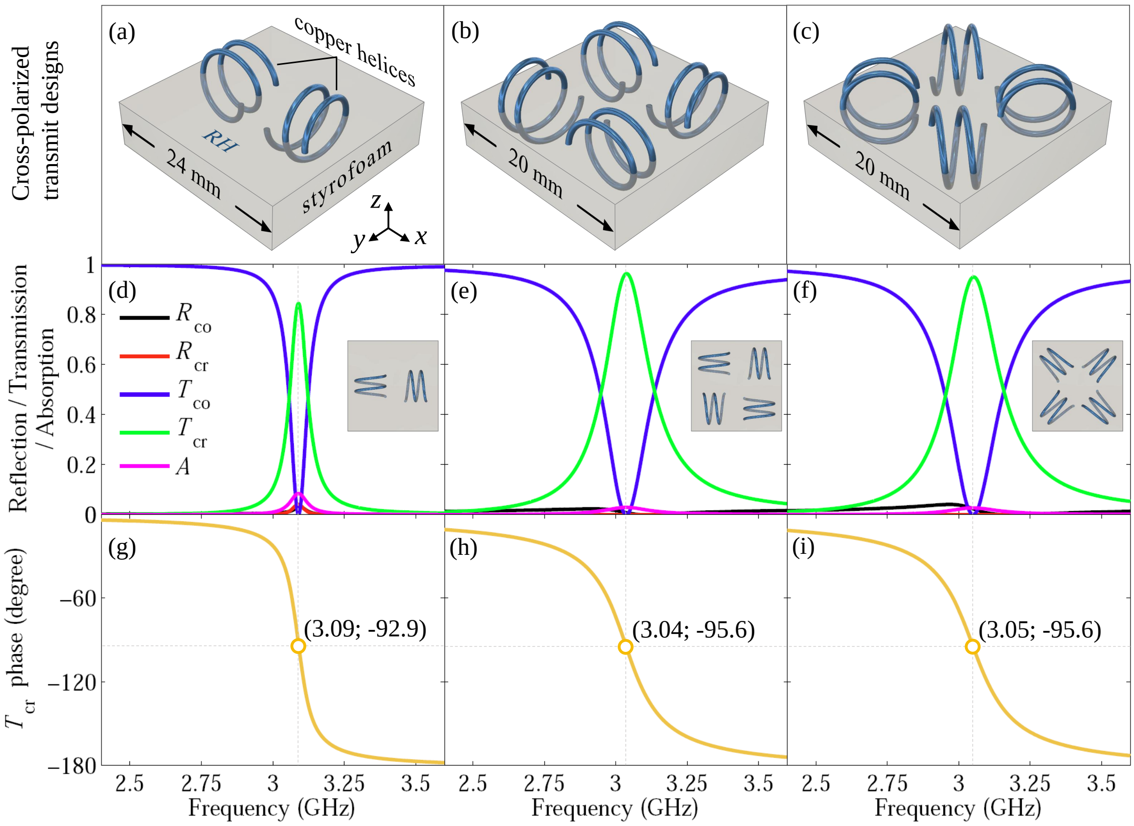

Figure 3.5: (a-c) Unit cell designs of cross-polarized transmit based on copper RH and LH double-turn helical resonators which are halfway embedded into the styrofoam. (d-f) Simulated reflection, transmission, and absorption spectra with respectively polarization states at normal incidence. Top view of the unit cell is depicted in the insert of each figure. (g-i) Phases of cross-polarized transmission (T_{cr}) for the different arrangement of helices in the metasurface.

and absorption spectra with relative co-/cross-polarizations at normal incidence in the microwave range are given in Figures 3.5(d-f). The design of unit cell with defined arrangement of copper RH double-turn helices with tailoring structural parameter to the balance of polarizabilities is shown in Figure 3.5(a). Period of metasurface is equal to 24 mm with half period inter-element distance. Helices are halfway embedded into styrofoam for mechanical support. Helix-based cross-polarized transmit is excited by incident linearly polarized plane wave comes from z direction. As can be seen from Figure 3.5(d), a single-layer helix-based metasurface exhibits cross-polarized transmission peak value of 0.84 at the resonant frequency of 3.09 GHz, while absorbance reaches a maximum of 0.084 at the resonance. Obtained results can be improved using the symmetric arrangement of helices in the unit cell.

Figure 3.5(b) illustrates unit cell of cross-transmit metasurface consisting of four double-turn helices that are located symmetrically in the xy-plane of metasurface. Period of metasurface was optimized and equal to 20 mm and an equivalent distance between helices is equal half of period. Figure 3.5(e) shows R, T, and A spectra with polarization states in the microwave range. As can be seen from simulated data, helix-based metasurface exhibits high cross-transmission value over 0.96 at the resonance of 3.04 GHz, while absorption does not exceed of 0.03 in the wide frequency range from 2.5 to 3.5 GHz. Moreover, reflection spectra with co- and cross-polarizations are close to zero at all considered frequency range. Therefore, high efficient off-resonance transparent cross-polarized helix-based transmit is designed in accordance with the analytical approach and numerical simulation.

In addition, 90° polarization rotator based on copper double-turn helical resonators which are shifted by 45° respect to the previous position is designed and depicted in Figure 3.5(c). A period of unit cell was optimized by numerical simulation and equal to 20 mm. Simulated R_{co}, R_{cr}, T_{co}, T_{cr}, and A spectra at normal incidence are illustrated in Figure 3.5(f). It is clear to see that simulated spectra slightly differ in comparison with the previous design. Cross-polarized transmission reaches a peak value of 0.9, while co-transmission drops to zero at the resonance of 3.05 GHz. Other spectra do not exceed of 0.04 in the entire operational band.

Figures 3.5(g-i) show calculated phases of cross-polarized transmitted waves for proposed designs with a different arrangement of helical resonators in the unit cell. Designed metasurfaces exhibit phases of $-92.9°$, $-95.6°$, and $-95.6°$ for cross-polarized transmitted waves at the resonance, respectively.

It should be noted that we will fabricate and experimentally test the cross-polarized transmit with proper arrangement of the helical resonator in the unit cell which is depicted in Figure 3.5(c). The main experimental results can be found in Section 4.1. However, in order to more improve the obtained result instead of double-turn helices, we will use single-turn helical resonators with balanced polarizabilities. Thus, our approach to finding the proper arrangement in the metasurface works for any helical resonators it will be another evidence of the validity of this method.

3.4 Perfect absorber

Previously, we have synthesized of functional off-resonance transparent helix-based rotators to achieve co- and cross-polarizations for reflected and transmitted waves in the microwave range. Herein, we are aiming to achieve total absorption ($\mathbf{E}_{\mathrm{r}} = 0$, $\mathbf{E}_{\mathrm{t}} = 0$) of incident linearly polarized waves by usage of double-turn helical resonators. In accordance with our approach, any combinations of helical resonators from Table 3.1 and 3.2 directly do not allow to design helix-based perfect absorbers, since we do not take into account lossy in metal. Nevertheless, the finding of the proper arrangement of helical resonators in metasurface to achieve total absorption is still relevant.

As a starting point, we can find the reflected and transmitted electric fields in term of *co* and *cross* effective polarizabilities of bi-anisotropic inclusion that can be expressed as follows [88]:

$$\begin{aligned}\mathbf{E}_{\mathrm{r}} = -\frac{j\omega}{2S}\Bigg\{&\left[\eta_0\widehat{\alpha}_{\mathrm{ee}}^{\mathrm{co}} \pm \widehat{\alpha}_{\mathrm{em}}^{\mathrm{cr}} \pm \widehat{\alpha}_{\mathrm{me}}^{\mathrm{cr}} - \frac{1}{\eta_0}\widehat{\alpha}_{\mathrm{mm}}^{\mathrm{co}}\right]\overline{\overline{I}}_{\mathrm{t}} \\ &+ \left[\eta_0\widehat{\alpha}_{\mathrm{ee}}^{\mathrm{cr}} \mp \widehat{\alpha}_{\mathrm{em}}^{\mathrm{co}} \mp \widehat{\alpha}_{\mathrm{me}}^{\mathrm{co}} - \frac{1}{\eta_0}\widehat{\alpha}_{\mathrm{mm}}^{\mathrm{cr}}\right]\overline{\overline{J}}_{\mathrm{t}}\Bigg\} \cdot \mathbf{E}_{\mathrm{inc}}.\end{aligned} \tag{3.47}$$

$$\begin{aligned}\mathbf{E}_{\mathrm{t}} = \Bigg\{ \Bigg[1 - \frac{j\omega}{2S}\left(\eta_0 \widehat{\alpha}_{\mathrm{ee}}^{\mathrm{co}} \pm \widehat{\alpha}_{\mathrm{em}}^{\mathrm{cr}} \mp \widehat{\alpha}_{\mathrm{me}}^{\mathrm{cr}} + \frac{1}{\eta_0}\widehat{\alpha}_{\mathrm{mm}}^{\mathrm{co}}\right)\Bigg] \overline{\overline{I}}_{\mathrm{t}} \\ -\frac{j\omega}{2S}\left(\eta_0 \widehat{\alpha}_{\mathrm{ee}}^{\mathrm{cr}} \mp \widehat{\alpha}_{\mathrm{em}}^{\mathrm{co}} \pm \widehat{\alpha}_{\mathrm{me}}^{\mathrm{co}} + \frac{1}{\eta_0}\widehat{\alpha}_{\mathrm{mm}}^{\mathrm{cr}}\right) \overline{\overline{J}}_{\mathrm{t}} \Bigg\} \cdot \mathbf{E}_{\mathrm{inc}}.\end{aligned} \tag{3.48}$$

These equations have the same physical interpretation with Eqs. (2.7) and (2.8) from Section 2.1. Next, the requirement of $\mathbf{E}_{\mathrm{r}} = 0$ and $\mathbf{E}_{\mathrm{t}} = 0$ in Eqs. (3.47) and (3.48) means that expressions in square brackets in these equations must be equal zero. Using this argument we can define the conditions for the total absorption under plane-wave irradiation with arbitrary polarization as follows [132]:

$$\eta_0 \widehat{\alpha}_{\mathrm{ee}}^{\mathrm{co}} \pm \widehat{\alpha}_{\mathrm{em}}^{\mathrm{cr}} \pm \widehat{\alpha}_{\mathrm{me}}^{\mathrm{cr}} - \frac{1}{\eta_0}\widehat{\alpha}_{\mathrm{mm}}^{\mathrm{co}} = 0, \tag{3.49}$$

$$\eta_0 \widehat{\alpha}_{\mathrm{ee}}^{\mathrm{cr}} \mp \widehat{\alpha}_{\mathrm{em}}^{\mathrm{co}} \mp \widehat{\alpha}_{\mathrm{me}}^{\mathrm{co}} - \frac{1}{\eta_0}\widehat{\alpha}_{\mathrm{mm}}^{\mathrm{cr}} = 0, \tag{3.50}$$

$$\eta_0 \widehat{\alpha}_{\mathrm{ee}}^{\mathrm{co}} \pm \widehat{\alpha}_{\mathrm{em}}^{\mathrm{cr}} \mp \widehat{\alpha}_{\mathrm{me}}^{\mathrm{cr}} + \frac{1}{\eta_0}\widehat{\alpha}_{\mathrm{mm}}^{\mathrm{co}} = \frac{2S}{j\omega}, \tag{3.51}$$

$$\eta_0 \widehat{\alpha}_{\mathrm{ee}}^{\mathrm{cr}} \mp \widehat{\alpha}_{\mathrm{em}}^{\mathrm{co}} \pm \widehat{\alpha}_{\mathrm{me}}^{\mathrm{co}} + \frac{1}{\eta_0}\widehat{\alpha}_{\mathrm{mm}}^{\mathrm{cr}} = 0. \tag{3.52}$$

As one can see, these conditions involve coupling between co- and cross-polarized effective electric, magnetic, electromagnetic and magnetoelectric polarizabilities. This is an important point, because for arbitrary shaped metal or dielectric inclusions, the cross-polarized magnetoelectric polarizabilities are zero, which limits co-polarized electromagnetic polarizabilities. To achieve zero reflection, it is necessary to satysfied conditions for impedance matching which have the follows form [132]:

$$\eta_0 \widehat{\alpha}_{\mathrm{ee}}^{\mathrm{co}} = \frac{1}{\eta_0}\widehat{\alpha}_{\mathrm{mm}}^{\mathrm{co}} = j\frac{S}{\omega}. \tag{3.53}$$

As seen from Eqn. (3.53), effective electric and magnetic polarizabilities of the unit cell must have equivalent EM response. This means that total absorption in metasurface requires the electric and magnetic response of the same strength, at the same frequency. Consequently, if effective polarizabilities of the unit cell satisfy these conditions, the array has zero reflectivity at all frequencies. As one can see, effective polarizabilities are purely imaginary, that corresponds to the resonance behavior. Conditions for zero transmission can be expressed from (3.50) or (3.52) which require the compensation electromagnetic and magnetoelectric couplings (chiral coupling) in the whole metasurface. Therefore, co- and cross-polarized components of magnetoelectric polarizabilities must be zero [132]. By taking into account the dissipative losses in the inclusions and the compensated chiral coupling in the metasurface, the zero-transmission condition can be expressed as:

$$\widehat{\alpha}_{\mathrm{em}}^{\mathrm{cr}} = \widehat{\alpha}_{\mathrm{me}}^{\mathrm{cr}} = \widehat{\alpha}_{\mathrm{me}}^{\mathrm{co}} = \widehat{\alpha}_{\mathrm{me}}^{\mathrm{co}} = 0. \tag{3.54}$$

Moreover, it is possible to achieve symmetric total absorption from both sides of the negligibly thin metasurface. However, we have to compensate bi-anisotropic coupling in

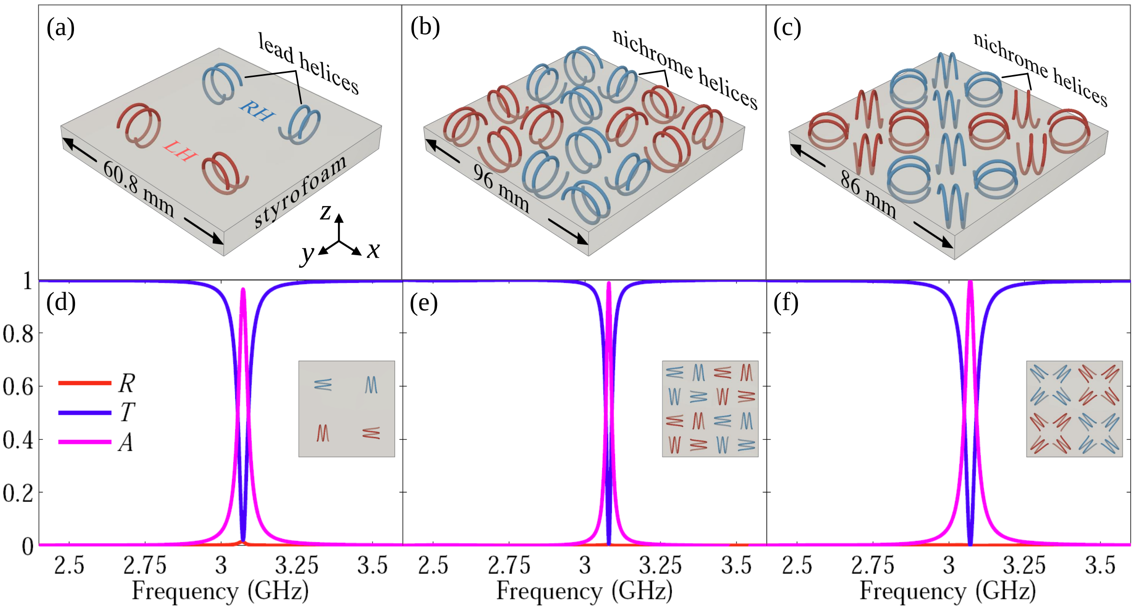

Figure 3.6: (a-c) Unit cell designs of perfect absorber based on metallic RH and LH double-turn helical resonators which are halfway embedded into the styrofoam. (d-f) Simulated reflection, transmission, and absorption spectra at normal incidence. Top view of the unit cell is depicted in the insert of each figure.

the whole metasurface if we are using of bi-anisotropic inclusions as helical or omega resonators. In our case, compensation of chiral coupling in metasurface can be done by usage of RH and LH helical resonators, according to with these requirements, we can use our approach for determination of proper arrangement of helical resonators to achieve total absorption in metasurface. As seen from Table 3.1 and 3.2, only one combination of helical resonators in the unit cell of metasurface can be used to satisfy conditions for total absorption (3.53) and (3.54) taking into account dissipative lossy in helical resonators.

Figures 3.6(a-c) show unit cell designs of off-resonance transparent helix-based perfect absorbers. All designs are excited by the linearly polarized incident wave propagating along the z-axis. Simulated reflection, transmission, and absorption spectra at normal incidence in the microwave range are shown in Figures 3.6(d-f).

Using numerical simulation, helix-based absorption metasurfaces have been designed and tested. Figure 3.6(a) shows unit cell of perfect absorber consisting of metallic RH and LH double-turn helices which are embedded into styrofoam for mechanical support. We utilized nichrome helical wires since they have enough level of resistive loss. Period of helical resonators is equal 60.8 mm, while a distance between helices is equal half of period. As seen from simulated R, T, A spectra, absorption peak reaches a maximum value of 0.96 at the resonant frequency of 3.07 GHz, while reflection does no exceed of 0.015 at the operational frequency range from 2.5 to 3.5 GHz. Thus, metasurface consisting of nichrome helical resonators exhibits near perfect reflectionless behavior and transparency away from the resonant band.

Next, we designed more symmetric arrangement of helical resonators in the unit cell to achieve better resonant absorption properties. Figure 3.6(b) demonstrates unit cell of perfect absorber consists of four sub-unit cells with nichrome four right-handed or left-handed double-turn helices arranged horizontally and vertically that are halfway embedded into the styrofoam. Period of the unit cell is equal 96 mm with an interelement distance of quarter period of absorption metasurface. As seen from Figure 3.6(e), absorption reach peak value of 0.988 at the resonance of 3.08 GHz. In this case, helix-based perfect absorber exhibits perfect zero reflection in the range of $2.5 - 3.5$ GHz and unit transmission in the off-resonance band.

Further, we designed a perfect absorber metasurface comprising of nichrome RH and LH double-turn helices that are shifted by 45° respect to their initial position in the unit cell with a period of 86 mm, which can be seen in Figure 3.6(c). Reflection, transmission, and absorption spectra are given in Figure 3.8(f). Here, helix-based metasurface exhibits perfect absorption $A = 0.999$ at resonance of 3.07 GHz with broadband zero reflection behavior at normal incidence in the microwave range.

Thus, we have outlined the basic mechanisms responsible for the occurrence of perfect absorption resonances in helix-based metasurface, as well as their main design principles with different arrangements of helical resonators in unit cells of metasurfaces. Subsequently, practical fabrication and characteristics of the proposed reflectionless helix-based absorber will be described in Sections 4.2 and 4.3.

3.5 Multifunctional cascaded helix-based metamaterial

Here, we propose a promising way to design multifunctional cascaded metamaterial that provide different operations at different frequencies. We find design solutions for integrated metasurfaces that provide five basic functions such as co- and cross-polarized reflectors and transmits, as well as a perfect absorber. Based on these off-resonant transparent metasurfaces, it can be extended to volumetric metamaterials. Thus, we have combined all previously proposed functional metasurfaces to create 5-layered multifunctional multi-frequency cascaded metamaterial.

First of all, we have chosen single-layer helix-based polarization rotators and perfect absorber with a good efficiency and high transparency away from the resonance. Then, by proportionally changing of structural parameters of helical resonators to keep them to the balance of polarizabilities we have tuned helix-based metasurfaces to different operational frequencies with "symmetric" functionalities respects to the position of the perfect absorber in the cascaded metamaterial. Moreover, we expect that each functional metasurface will not interact with each other in the broadband microwave range. Such flexibility and functionality of metasurfaces are significant advantages in comparison with natural materials.

Figure 3.7 illustrates unit cell design of 5-layered cascaded metamaterial consisting of co-/cross-polarized reflectors, co-/cross-polarized transmits, and perfect absorber based on double-turn helical resonators with balanced polarizabilities. Using numerical simulation, structural parameters were proportionally scaling up and down in accordance to tailoring their resonant frequencies. The period of the multifunctional metamaterial is equal

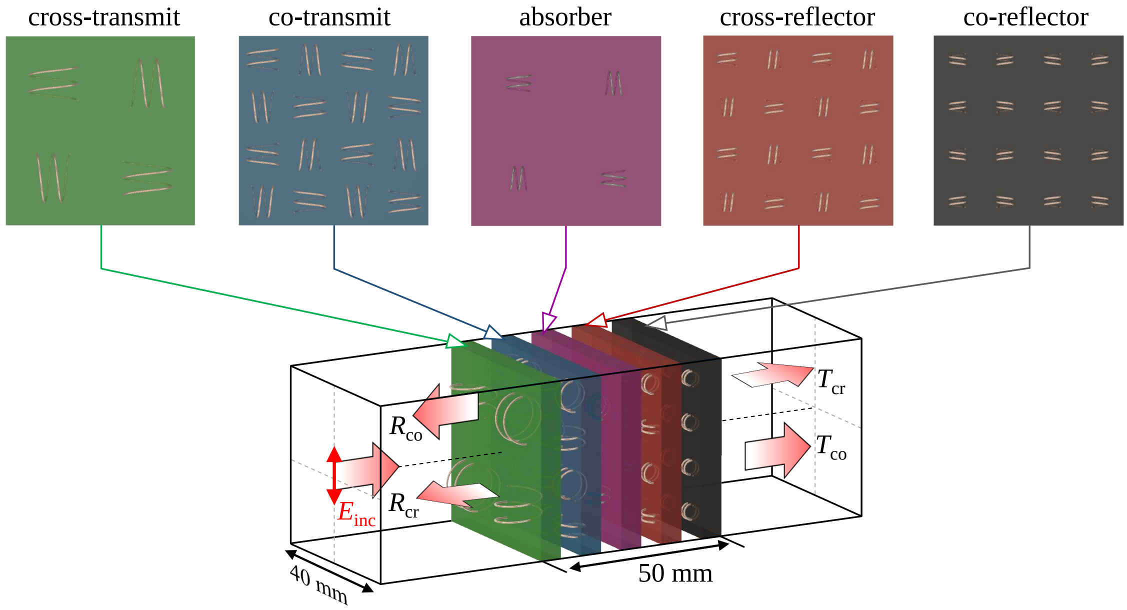

Figure 3.7: Unit cell of multifunctional multifrequency cascaded metamaterial

40 mm and remains to be the same for all metasurfaces. This greatly simplifies numerical calculation of spectra in such complex structure and significantly reduces the computation time. The distance between each metasurface is equal 10 mm which gives a total thickness of cascaded metamaterial is about 50 mm. Thus, the thickness of cascaded metamaterial even with five layers is still small with respects to the operational wavelengths of the incident waves. Double-turn helices comprising of cascaded metamaterial have the same diameter of the wire ($d = 0.2$ mm) and equivalent EM response (polarization-insensitive) to the incident waves. The remaining structural parameters of double-turn helices and the main spectral characterizations are given in Table 3.3.

Figure 3.8(a) shows reflection, transmission, and absorption spectra respect to their polarization states of 5-layered multifunctional cascaded helix-based metamaterial at normal incidence. It is clear to see that helix-based metamaterial exhibits frequency-selective multifunctional properties in the microwave range of $1-7$ GHz. The efficiency of each helix-based metasurface is over 85% in the broadband range, that is a great result for this amount of layers and such complex architecture. Figure 3.8(b) shows total reflection, transmission and absorption spectra of metamaterial at normal incidence. It can

No.	Design	Arrangement	H, mm	R, mm	f_{res}, GHz	Amplitude
1)	Cross-transmit	Fig. 3.5(b)	3.57	5.12	2	$T_{cr} = 0.92$
2)	Co-transmit	Fig. 3.4(b)	2.30	3.30	3	$T_{co} = 0.85$
3)	Absorber	Fig. 3.6(b)	1.75	2.52	4	$A = 0.92$
4)	Cross-reflector	Fig. 3.3(b)	1.38	1.98	5	$R_{cr} = 0.85$
5)	Co-reflector	Fig. 3.2(b)	1.15	1.65	6	$R_{co} = 0.85$

Table 3.3: Structural parameters of double-turn helix of each functional metasurfaces with their spectral characterizations.

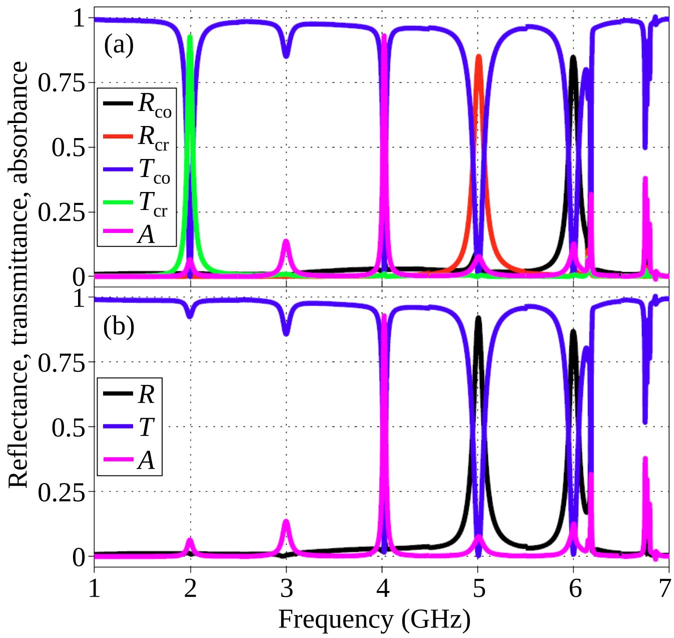

Figure 3.8: (a) Simulated R_{co}, R_{cr}, T_{co}, T_{cr}, and A spectra of cascaded metamaterial based on double-turn helical resonators. (b) Total reflection, transmission, and absorption spectra of helix-based cascaded metamaterial at normal incidence.

be seen that each helix-based metasurface exhibits high transmission behavior and low reflection spectra away from resonances as it was expected with our predictions. Thus, due to the off-resonance transparent properties of functional helix-based metasurfaces, we designed multifunctional multifrequency cascaded metamaterial for microwave range. It was shown that helix-based metasurfaces can be tuned to the desired resonant frequencies by proportional up and down scaling of structural parameters in the range of $1-7$ GHz.

Nevertheless, there are some difficulties for the realization with the good efficiency of cascaded metamaterial, for example, in the more wider microwave range. These difficulties occur due to the undesired secondary resonance in helical resonators at higher frequencies. For example, it can be seen from Figure 3.8(a) that the secondary resonant peak occurs at the frequency of 6.25 GHz for the first helix-based layer of cross-polarized transmit operating at the frequency of 2 GHz. This imposes certain limitations for using of the amount of off-resonance transparent helix-based functional metasurfaces. Nevertheless, some ways to extend the operational range can be found. For example, it is possible to use triple-turn helical resonators instead of double-turn helices which have more broadband off-resonance transparent properties, however, it is difficult to realize in a practice. Also, it is possible to use only one type of functionality which have the most broadband off-resonance transparent behavior such as perfect absorbers based on nichrome double-turn helices. The secondary peak occurs at the 8 GHz for helix-based perfect absorber operating at 2 GHz. Moreover, perfect absorbers exhibit narrow band resonance behavior that allows creating over thirteen helix-based layers (resonance step is 0.5 GHz) in cascaded metamaterial operating in the range of $1-9$ GHz.

It is worth noting that multifunctional cascaded metamaterial based on omega and helical resonators was designed and experimentally verified in accordance with literature [4-A]. In this work, authors have been proposed the approach for designing of 3-layered multi-functional cascades of metamaterial consists of metamirror using omega resonators, perfect absorber based on nichrome double-turn helices and low-lossy helix-based transmitarray for wavefront shaping and anomalous refraction. Depending on the frequency of incident radiation, this cascade exhibits different responses at different frequencies that were carefully adjusted. Authors pay attention that, going to the limiting case of cascading metasurfaces, one can design a single metasheet that incorporates different kinds of inclusions performing a multifunctional response, where is cascade of metasurfaces can be also extended to volumetric metamaterials [4-A]. Such advanced capabilities of off-resonance transparent metasurfaces for the creation of cascaded metamaterials with various functionalities demonstrate great opportunities for applications in the microwave range.

3.6 Conclusions

- Simple method for determination of required arrangement of helical resonators in metasurface depending on desired functionalities was proposed. This method is based on the definition of forward and backward scattering fields in the far-zone taking into account orientation and handedness of helical resonators in the plane of metasurfaces. Moreover, there is not necessary to calculate amplitudes of scattering fields from helix-based metasurfaces. Total scattered fields are determined only through orientation and handedness of helical resonators leading to the previously known results depending on the desired functionalities. As a result, forward and backward scattering electric fields from helix-based metasurface were summarized in Tables 3.1 and 3.2, respectively.

- Based on our approach, proper arrangements of helical resonators in the unit cell of metasurfaces for the synthesis of off-resonance transparent co-polarized rotators for reflected waves in the microwave frequency range have been proposed. Using numerical simulation based on FEM, co-polarized reflectors based on copper RH and LH double-turn helices with balanced polarizabilities were designed. All helix-based metasurfaces exhibit co-polarized reflection peak over 85% in the vicinity of the resonant frequency of 3 GHz, while they are transparent away from the resonance. Thus, off-resonance transparent co-polarized reflectors based on helical resonators might have potential application for the realization of multifrequency-selective cascaded metasurfaces and wavefront shaping in the microwave range.

- Helix-based cross-polarized rotators for transmitted waves have been synthesized by definition of required arrangement of copper double-turn helices in the unit cell of metasurface. Using numerical simulation, three versions with proper arrangement of helical resonators in metasurface have been designed. Simulated spectra of all helix-based metasurfaces were carried out to produce the cross-polarized reflection, where the normalized to the unit amplitude of cross-reflection exhibits over of 0.84

and total low reflection behavior in the outside of resonance band.

- Using our approach and numerical simulation, off-resonance transparent helix-based co-polarized rotators for transmitted waves have been synthesized for microwave range. For all proposed metasurfaces, co-polarized transmittance reaches peak value over 59% in vicinity of the resonant frequency band of $3.05 - 3.11$ GHz and exhibits low reflection in the operational frequencies of $2.5 - 3.5$ GHz, respectively. Thus, helix-based co-polarized transmits can be used for manipulation of wavefront shaping and anomalous refraction in the microwave range.

- Cross-polarized helix-based rotators for transmitted waves have been designed with taking into account the proper arrangement of helical resonators in the cell and numerical simulation. As a result, all cross-transmits exhibit resonant behavior near of 3.07 GHz with a maximum of cross-transmittance peaks over 84%. Meanwhile, total reflection from helix-based metasurfaces does not exceed of 4% in the entire frequency range.

- Towards to synthesis of helix-based perfect absorbers, conditions for total absorption ($\eta_0\widehat{\alpha}_{ee}^{co} = \frac{1}{\eta_0}\widehat{\alpha}_{mm}^{co} = j\frac{S}{\omega}$, $\widehat{\alpha}_{em}^{co} = -\widehat{\alpha}_{me}^{co} = 0$) through effective polarizabilities of unit cell in the chiral metasurfaces have been reported. In addition, taking into account required arrangement of helical resonators and conditions for total absorption, off-resonance helix-based perfect absorbers have been designed and tested by numerical simulation. All absorbing helix-based metasurfaces consist of high lossy nichrome wires. As a result, metasurfaces exhibit high absorption over 98% in the vicinity of resonant frequency 3.08 GHz. Meanwhile, helix-based absorbers exhibit near-zero reflection ($R < 0.015$) in the considered frequency range. Thus, off-resonance transparent helix-based perfect absorbers demonstrate high efficiency in the microwave range of $2.5 - 3.5$ GHz.

- For the realization of cascaded metamaterial, a combination of designed off-resonance transparent co-/cross-polarized helix-based rotators for reflected and transmitted waves and perfect absorber has been proposed. Using numerical simulation, multifunctional multifrequency 5-layered cascaded metamaterial based on functional off-resonance transparent helix-based metasurfaces for microwave range has been designed. Proposed cascaded metamaterial exhibits ultrabroad resonant frequency-selective (2, 3, 4, 5, and 6 GHz) behavior with desired functionalities in the microwave range. The main spectral characterizations were summarized in Table 3.3.

Chapter 4

Fabrication of helix-based metasurfaces for microwave range

The fabrication of functional off-resonance transparent helix-based metasurfaces in the microwave frequency range is presented. Numerical study and practical realization of 90° polarization rotator for transmitted waves or so-called twist polarizer using single-turn copper helical resonators which tailored to the balance of their polarizabilities is carried out (Section 4.1). To achieve a total absorption in metasurfaces, numerical simulation and fabrication process of perfect absorber based on nichrome single-turn helices were performed (Section 4.2). Afterward, simulated and measured data of perfect absorber using nichrome double-turn helical resonators were reported (Section 4.3).

4.1 Twist polarizer

Usage conventional materials it is possible to rotate the polarization plane of a linearly polarized electromagnetic wave by a fixed angle with unit transmittance. It is well known such as levorotatory and twisted nematic liquid crystals, the Faraday Effect, and anisotropic media [133]. One of the devices that it rotates the polarization of a linearly polarized input wave by 90° upon transmission is a twist polarizer (polarization rotator). This device converts the polarization, in which transverse electric (TE) polarized light is converted into transverse magnetic (TM) polarized light and vice versa and it represents a half-wave plate. Typically, these structures have the thickness comparable to the operating wavelength, which is an important drawback for their applications for the microwave frequencies. This drawback possible to overcome using typical chiral three-layered metasurfaces that have an electrically thin thickness (much smaller than the operating wavelength) and possess strong optical activity in microwave spectral range [134–136]. However, some deficiencies are still presented in three-layered designs such as polarization angle dependence, non-unit transmission performance, splitting of the resonance band, and non-transparency outside of the resonance [137–139]. Afterward, several other metasurfaces overcoming some drawbacks have been proposed in the literature [47,140]. However, these structures do not show a low reflectivity (transparency) away from resonance, which is one of the advantages for the realization of multifunctional metasurfaces [4-A].

In one of the works [98], a proposed twist polarizer possesses low reflectivity properties that present as a single-layer chiral metasurface comprising crossed canonical helices. Nevertheless, a practical implementation of this promising polarizer is a very difficult task since it requires a soldering of a huge amount of the canonical helical wires. Subsequently, this design has been changed to three-layered architecture but it has a relatively weak cross-polarization transmission in the resonance band [88]. In our work, we have improved this design using smooth single-turn helical resonators that can be easily fabricated for radio frequency range. Here, we report numerical study and fabrication process of electrically thin off-resonance transparent helix-based twist polarizer that rotates the polarization plane of transmitted waves by 90° relatively to the incident linearly polarized waves. Twist polarizer exhibits an equivalent EM response to the external excitation that leads to the low reflectivity behavior over a wide frequency range from 0.1 GHz to 5.8 GHz. As a result, fabricated helix-based twist polarizer may be applicable for the design of cascade multifunctional devices in the microwave frequency range.

4.1.1 Design and simulation results

As mentioned earlier, for the synthesis of functional off-resonance transparent metasurfaces it is necessary to achieve impedance matching of metasurfaces with free space in the considered range. This can be achieved by usage of bi-anisotropic chiral inclusions with balanced polarizabilities comprising of metasurface [71,98,106]. As we have already determined earlier, smooth helical resonators with individually balanced polarizabilities [97, 106] is the most suitable inclusions for practical realization of twist polarizer metasurface. Taking into account our approach for determination of required arrangement of helical resonators in the unit cell of metasurface and already designed and tested by numerical simulation twist polarizer based on double-turn helices, we are aiming to fabricate the off-resonance transparent helix-based twist polarizer for microwave range.

Figure 4.1(a) shows a design of helix-based twist polarizer with a schematically illustrated rotation of polarization plane for transmitted waves. Top and front views of the unit cell consisting of four copper single-turn RH helical resonators arranged in a periodic 2D lattice in xy-plane which is embedded halfway into styrofoam are given in Figures 4.1(b,c). A low-permittivity ($\epsilon = 1.03$) styrofoam material with thickness t serves as mechanical support for helical resonators since this material is transparent in the microwave range. Tailoring structural parameters of single-turn helices (helix radius $R = 7.2$ mm, pitch $H = 11.3$ mm, and helix arm diameter $D = 1$ mm) to the balance of their polarizabilities were taken from Table 2.1. Using numerical simulation based on FEM, intercell distance $s = 20.5$ and period $p = 50$ mm of unit cell were optimized. The thickness of single-layer helix-based metasurface is about $t = 14.4$ mm which is equal to $\lambda_{\text{res}}/7$ operational wavelength.

In the process of simulation, a linearly polarized plane wave propagating along -z-direction is normally incident onto the unit cell. Periodic boundaries are set at x- and y-sides while Floquet modes as a source are set at $\pm z$-sides. Fundamentally, Floquet modes are plane waves with propagation direction set by the frequency and geometry of the periodic structure. Numerical simulation is carried out to investigate the polarization transformation behavior. Thus, the co-polarized reflection (R_{co}), transmission (T_{co}) and cross-polarized reflection (R_{cr}), transmission (T_{cr}) coefficients would be studied.

Figure 4.2(a) shows the reflection, transmission, and absorption spectra respect to polarization state in the microwave range. Numerical results show that in the vicinity

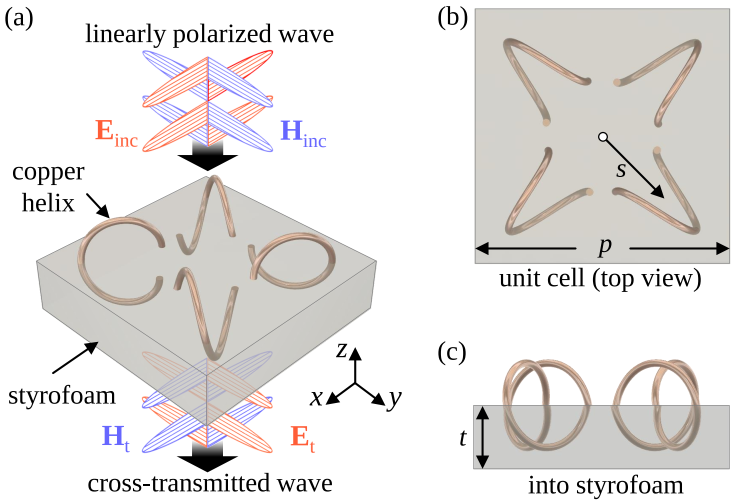

Figure 4.1: (a) Unit cell design of off-resonance transparent helix-based twist polarizer for microwave frequency range. The rotation of polarization plane of the transmitted wave by 90° relatively to linearly polarized incident wave is illustrated. (b) Unit cell of twist polarizer (top view) with indicated parameters of $s = 20.5$ mm and $p = 50$ mm, respectively. (c) Unit cell (front view) of twist polarized based on copper single-turn helices embedded halfway into styrofoam with thickness of $t = 14.4$ mm.

of 3.1 GHz, the cross-polarized transmittance reaches a peak value of 0.98, while the co-polarized transmittance is equal to zero at the same resonant frequency. As seen from simulated data, total reflection (R) does not exceed of 6% in the wide frequency band from 2 to 4 GHz. It should be mentioned that the secondary resonance occurs at the frequency of 5.8 GHz, where a circumference of one turn of the helix becomes comparable to the wavelength. Thus, helix-based twist polarizer exhibits broadband low reflectivity behavior with high efficient cross-polarized transmission at the resonance.

The efficiency of polarization rotation can be characterized by a polarization rotating angle (θ) and an ellipticity (η) of transmitted waves. These parameters can be expressed as follows [25]:

$$\theta = \frac{1}{2}\left[\arg(T_+) - \arg(T_-)\right] \tag{4.1}$$

$$\eta = \frac{1}{2}\arcsin\left(\frac{|T_+|^2 - |T_-|^2}{|T_+|^2 + |T_-|^2}\right), \tag{4.2}$$

where $T_+ = T_{\rm co} + iT_{\rm cr}$ and $T_+ = T_{\rm co} - iT_{\rm cr}$ are transmission coefficients of the right- and left-circular polarized waves, respectively. The polarization rotation angle θ represents the angle between the polarization planes of the incident and transmitted waves, while the ellipticity η denotes the polarization state of the transmitted wave. Pure transformation to the cross-polarized transmitted wave corresponds to case when an ellipticity is equal zero ($\eta = 0°$) while the polarization plane has rotation angle of $\theta = 90°$ with respect to the normal incidence. If the ellipticity is equal to $\pm 45°$ then the transmitted wave has circular polarization.

The simulated polarization rotation angle, θ, and ellipticity, η, are given in Figure 4.2(b). The polarization angle and ellipticity reach their maximum values of $\theta = 90.05°$

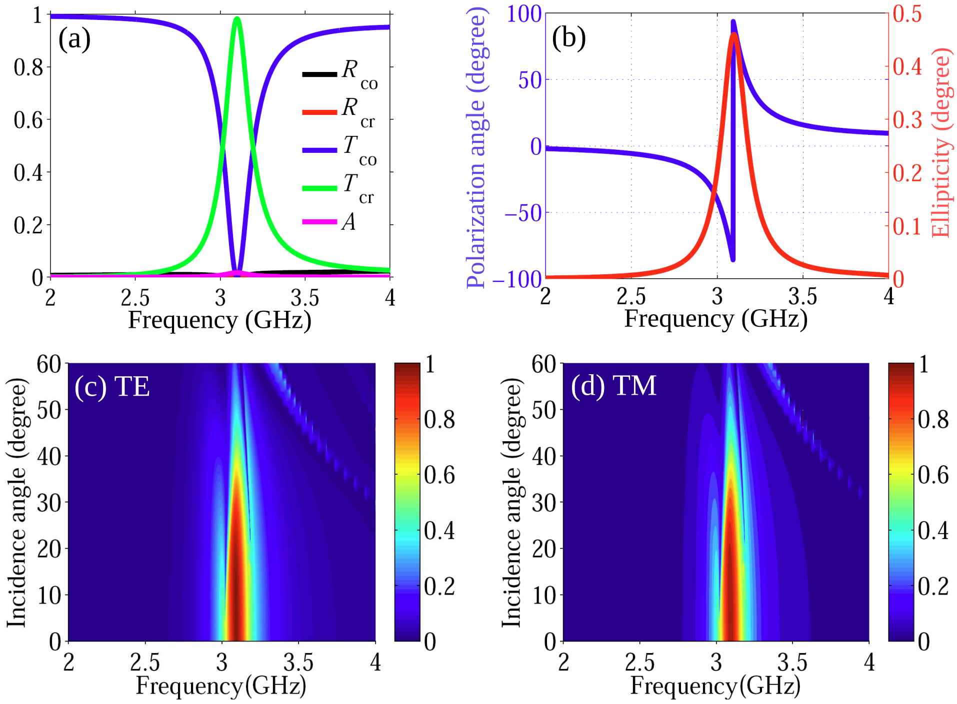

Figure 4.2: (a) Simulated reflection, transmission, and absorption spectra with respect polarization state at normal incidence in the microwave range. (b) Polarization angle (θ) and ellipticity (η) responses of transmitted waves at normal incidence. Simulated cross-transmission spectra as a function of incidence angle for (c) TE and (d) TM polarization, respectively.

and $\eta = 0.46°$ at the resonance frequencies of 3.1 GHz, respectively. Optical isolation between co- and cross-polarized transmitted waves (i.e., the optical isolation between TE and TM polarizations at the input and output waves) is around 99.9% at the resonance. This represents a high degree of spectral purity of twist polarizer. Figures 4.2(c) and (d) show simulated cross-polarized transmission spectra of the proposed helix-based structure as a function of incidence angle for TE and TM linearly polarized waves, respectively. One can see that resonance with the invariant central frequency of 3.1 GHz and cross-transmittance $T > 90\%$ is retained for up to 35° for TE and TM polarizations, respectively. Such identical wave propagation for both polarizations respects to oblique incidence up to 35° characterizes a balanced electromagnetic response from single-turn helices comprising of twist polarizer metasurface.

Thus, according to numerically simulated data, designed single-layer twist polarizer based on single-turn copper helical resonators with balanced polarizabilities exhibits polarization-invariant, wideband low-reflection behavior and near-unit cross-polarized transmission with conversion efficiency is about 99.9% at resonance of 3.1 GHz. The transmitted wave is linearly polarized where polarization plane is rotated by 90° with near-unit transmission respect to the incident wave at the resonance frequency.

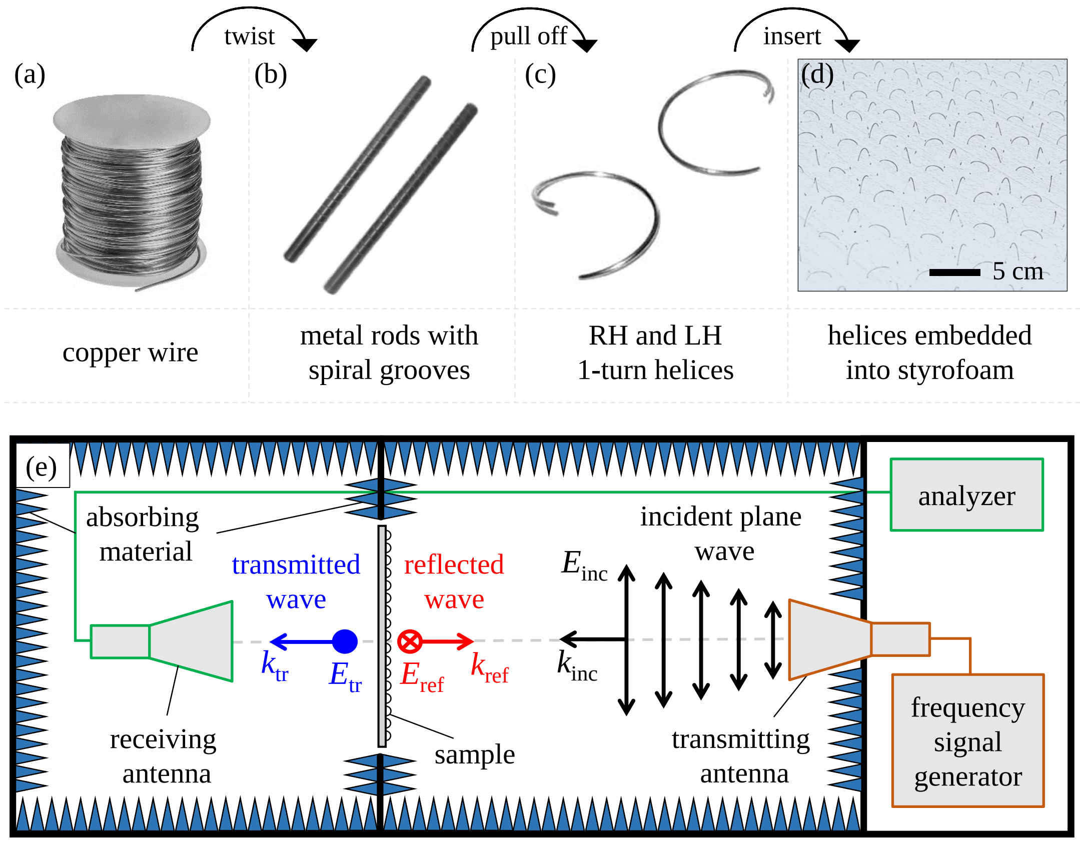

Figure 4.3: (a-d) The fabrication process of helix-based twist polarizer for microwave frequency range. (e) A schematic illustration of measurement setup.

4.1.2 Experimental verification

Using smooth single-turn helical resonators, off-resonance transparent twist polarizer can be easily fabricated. The fabrication process of helix-based metasurfaces was developed in Refs. [72, 97] and depicted in Figures 4.3(a-d). Nevertheless, some features were applied in the fabrication process of the sample. Specifically, the copper wire was wound on a metal rod with spiral grooves that ensures mutual identity and precise compliance with the specified dimensions of helices. In order to remove the wire from the template while maintaining the parameters, the wire is curled from the template along the longitudinal groove. In further, the long helical wire has cut with corresponding to numbers of helical turns. Subsequently, helical resonators were embedded halfway into styrofoam in accordance with required arrangement in the unit cell of metasurface. As mentioned before, styrofoam is a transparent material in the operating frequency band that provides mechanical support of copper helical resonators.

The operation of the twist polarizer metasurface was verified by conducting measurements in an anechoic chamber based on the free-space method [141]. A schematic illustration of measurement setup is shown in Figure 4.3(e). A microwave frequency signal generator (high-frequency signal generator, G4-80) was connected to a transmitting horn antenna (horn antenna, P6-23A) radiates linearly polarized radio waves, while the signal at the receiving linearly polarized horn antenna (P6-23A) was analyzed with a microwave an-

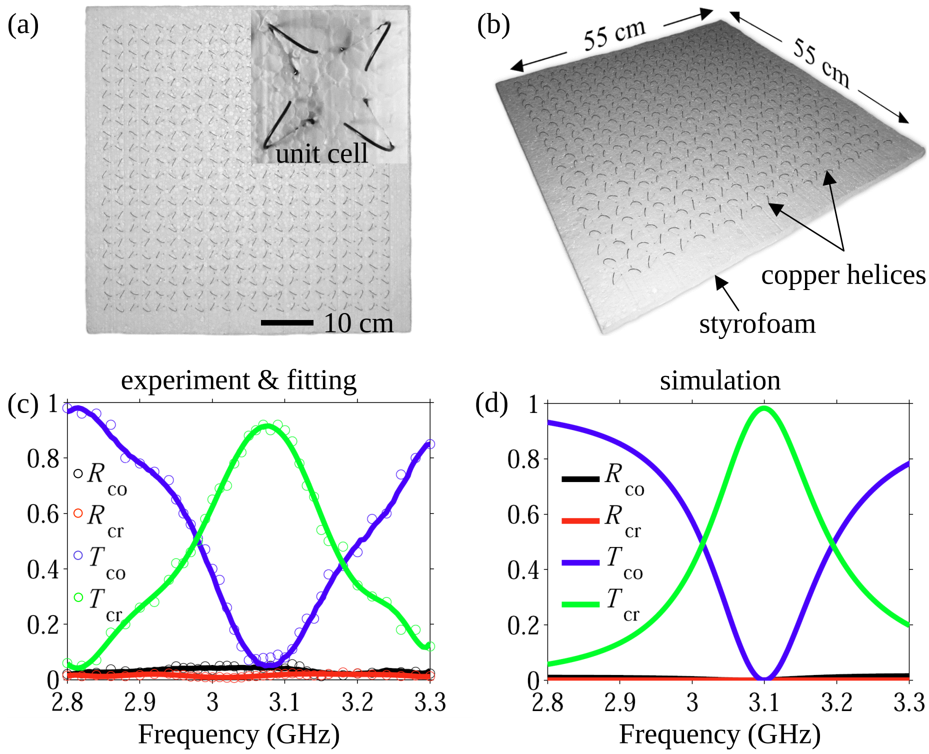

Figure 4.4: (a) Photo of fabricated off-resonance transparent helix-based twist polarizer. The unit cell of the sample is depicted in the inset. (b) Perspective view of the sample where copper single-turn helices are embedded into the styrofoam. (c) Measured and analytical fitting (solid line) co-/cross-polarized reflection and transmission spectra at normal incidence. The measured values are indicated by dots (◦) in the experiment. (d) Represented simulated results for comparison with measured data.

alyzer (measuring receiver, P5-5B). The horn antennas had the apertures of (35×27) cm^2. Fabricated sample was mounted in the hole of a wall made of microwave absorbing material and located at the distance of four meters from the transmitting antenna, which approximately secures plane-wave excitation of the samples. The receiving horn antenna was positioned at the distance of one meter behind a sample.

Sample with a total area of (55×55) cm^2 consisting of copper single-turn helical resonators which are halfway embedded into low-permittivity styrofoam material was fabricated. As a result, photographs of twist polarizer sample comprising of 11×11 unit cells is presented in Figures 4.4(a,b). Amplitudes of co-polarized and cross-polarized transmitted waves were measured in accordance with orientation (vertical or horizontal) of receiving horn antenna relatively to transmitting one in the frequency range of $2.8 - 3.3$ GHz. Amplitudes of co-polarized and cross-polarized reflected waves from the sample were found using the same approach. Transmission measurements were calibrated to the transmission between the horn antennas in the absence of the sample. The reflection measurements were calibrated by using a copper plate with the area equal to that of the sample. The measurement was carried out at normal incidence of linearly polarized electromagnetic waves.

Measured reflection and transmission coefficients with respect to the polarization state are shown in Figure 4.4(c). The fitting curves quantitatively demonstrate spectra behavior in accordance with measured data in the microwave range. As seen, the cross-polarized transmission reaches a peak value of 0.92 at the resonance frequency of 3.07 GHz while the co-transmission coefficient tends to zero. The measured total reflection does not exceed of 6% in the operating frequency band from 2.8 GHz to 3.3 GHz (R = 5.4% at the resonance). As expected, realized twist polarizer based on single-turn helices exhibits a low-reflection behavior and a relatively high cross-transmittance ($T_{\mathrm{cr}} = 0.92$) in the operating frequency range. Figure 4.4(d) shows the results of numerical simulation for qualitative comparison with measured data in considered frequency range. As seen, both numerical and experimental results qualitatively represent the spectral characteristics of proposed polarizer. Nevertheless, some inaccuracies in manual fabrication led to some performances degradation due to slightly varying geometrical dimensions as a loop radius r and a height h of single-turn helices. As a result, helices resonate at slightly different frequencies that lead increasing the resonant bandwidth of the metasurface but decreasing of the cross-transmittance peak values. Another reason might be a diffuse scattering on metasurface inhomogeneities (slightly varying period, etc.). Nevertheless, all these possible shortcomings critically do not impair the efficiency of fabricated off-resonance transparent helix-based twist polarizer in the microwave range. Measured and simulated data are in a good agreement, that manifestly confirm the effective operation of the proposed metasurface as a wideband low-reflection 90° polarization rotator based on helical resonators with balanced polarizabilities.

To conclude, we have demonstrated a single-layer off-resonance transparent twist polarizer metasurface comprising of copper single-turn helical resonators which have the equivalent EM response to external excitation by linearly polarized incident waves. Both simulation and experiment results demonstrate 90° polarization rotation with a high cross-transmission coefficient at the resonance. Cross-polarization conversion of helix-based twist polarizer is performed with almost 100% efficiency. The major advantages of the proposed polarization rotator are an electrically thin thickness ($\lambda_{\mathrm{res}}/7$), polarization-invariant to oblique incidence up to 35°, low reflectivity (less 6%) in a wideband frequency range (0.1 − 5.5 GHz), and easy fabrication process. Low-reflection features allow to easily extend the functionalities of rotation metasurface to multiple-frequency ranges for control of the polarization state using a cascade metamaterials [4-A]. The designed "invisible" helix-based polarization rotator could be developed to explore more potential applications in radio antennas and communication systems.

4.2 Absorber based on single-turn helices

The incident electromagnetic energy can be nearly fully absorbed in thin layers but only in a narrow frequency band [142–145]. The absorption bandwidth of any passive layer obeys a fundamental limitation, as follows from the causality principle [46, 146, 147]. The limitations on periodical arrays concern only the transmission properties [147]. Obviously, exploitation of the opportunity to design a resonant absorber, which is transparent outside of the absorption band, could open up a number of novel possibilities in applications, for example, in ultra-thin filters for wave trapping, selective multi-frequency bolometers, and sensors. Such an all-frequencies-matched resonant absorber would be "invisible" from the illuminated sides, still acting as a band-stop filter in transmission. To the best of our knowledge, such wideband matched thin resonant absorbers are not known.

In fact, most of the known designs of thin absorbers contain a continuous metal ground plane (a mirror) behind the absorbing layer [142–145]. The mirror obviously produces nearly full reflection outside of the absorption band. Although this feature is crucial for some applications, it forbids designing resonant absorbers which are transparent outside of the absorption band. The use of a mirror reflector can be avoided in absorbers based on arrays of subwavelength Huygens sources (so-called Huygens metasurfaces) that possess the appropriate level of dissipative loss. Such Huygens sources scatter secondary waves only in the forward direction (without reflection) which destructively interfere with the incident wave, yielding zero transmission. Pioneering topologies of Huygens inclusions were introduced in Refs. [72, 97, 106, 148]. Subsequently, Huygens inclusions of different topologies have been used as structural elements in sheets to control transmission wavefronts [124, 130, 149].

Recently, several topologies of absorbers based on cut wire arrays separated by a dielectric layer have been proposed [150–154]. However, in all these structures the Huygens balance between the electric and magnetic responses (which is necessary for cancellation of the reflected waves) holds only inside a narrow-frequency band for which the dimensions have been optimized. Outside of this band, reflections appear due to prevailing excitation of either electric or magnetic modes. The physical reason for this is that the different resonant modes exhibit different frequency dispersions. The same conclusion is valid for the idea of using a resistive sheet placed in a close proximity of resonating magnetic inclusions to realize absorbing layers [155].

The analysis of these solutions reveals another feature of the known designs: absorbers have multi-layered architectures. Typically, they comprise at least three layers (metal–dielectric–metal). Although manufacturing of such structures is simple and inexpensive, electric and magnetic responses in such compound architectures inevitably resonate as different electric and magnetic modes. Thus, within that scenario, it is impossible to realize a resonant absorber which is reflectionless over an ultra-wide frequency range.

Here, a possibility to create a thin resonant polarization-insensitive absorber which produces negligible reflections in an ultra-wide frequency range is explored and experimentally demonstrated. We examine the physical requirements for full and symmetric (from either of the sides) absorption of incident waves and show that the ideal performance can be accomplished in a single-layer array of specifically designed helical inclusions. We show, both theoretically and experimentally, that an array of these inclusions truly operates as a Huygens surface in a very wide frequency range, exhibiting zero reflectivity even far from the absorption band.

The symmetric absorption regime in a metasurface is possible only if there is no bi-anisotropic coupling in the structure [132]. Taking into account conditions for total ab-

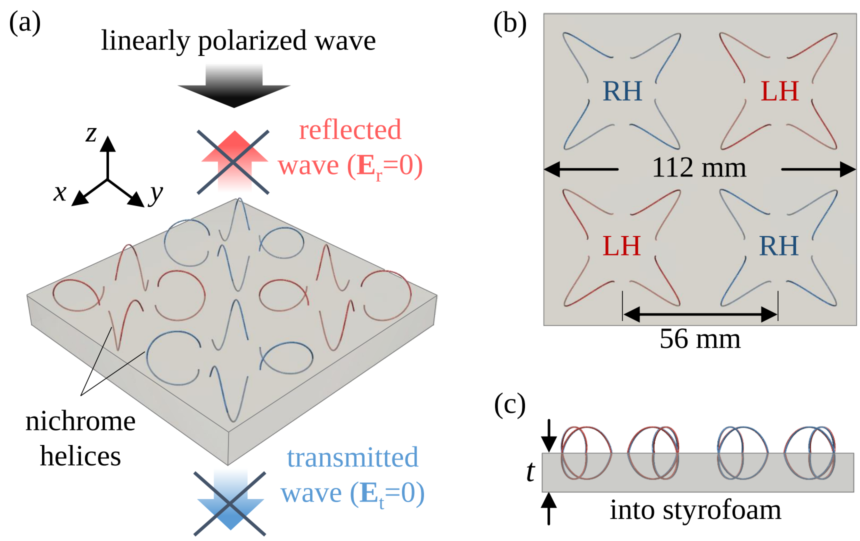

Figure 4.5: (a) Unit cell design of off-resonance transparent perfect absorber based on LH (red color) and RH (blue color) nichrome single-turn helices. Waves interaction with helix-based absorber at the resonance at normal incidence is illustrated. (b) Top view of the unit cell with structural parameters. (c) Front view of unit cell where helices are embedded halfway into styrofoam with thickness of $t = 14.4$ mm.

sorption (3.53) and (3.54) and already proposed the design of perfect absorber based on double-turn helices (see Figure 3.6(c)), we fabricated off-resonance transparent helix-based absorber that ideally operates for incident waves impinging on either or both of its sides and shows how the bi-anisotropy can be suppressed.

It should be mentioned one more time that second part of the condition for total absorption (3.54) ($\alpha_{\rm em}^{\rm co} = -\alpha_{\rm me}^{\rm co} = 0$) means when using bi-anisotropic inclusions built-in a unit cell the bi-anisotropy must be compensated on the level of the entire array. This is possible to achieve by alternating bi-anisotropic inclusions of two sorts in the array. These two sorts differ only by the sign of the electromagnetic coupling parameter, therefore, the combination of them yields bi-anisotropy compensation. Thus, keeping zero electromagnetic coupling within the array, at the same time we create coupled electric and magnetic dipole moments in each unit cell resonating exactly at the same frequency and having the same loss factors. Since the inclusions of the two sorts possess identical dipole moments, no splitting of the resonance frequency of the structure occurs. As a result, it is possible to realize a lossy and resonant array of inclusions so that the condition of full absorption (3.54) is satisfied at one frequency, but the condition for impedance matching or zero reflection ($\eta_0\alpha_{\rm ee}^{\rm co} = \alpha_{\rm mm}^{\rm co}/\eta_0$) holds in an ultra-wide frequency range, although both polarizabilities are frequency dispersive.

Figure 4.5(a) shows a design of off-resonance transparent perfect absorber based on nichrome single-turn helices embedded halfway into a styrofoam. We position the helices in the xy-plane in accordance with the analytical approach for determination of proper arrangement of helical resonators in the unit-cell of metasurface depending on their desired functionalities. The sub-unit cell of the metasurface consists of four blocks of helices as shown in Figure 4.5(b). The blocks comprising four helices of specific handedness are

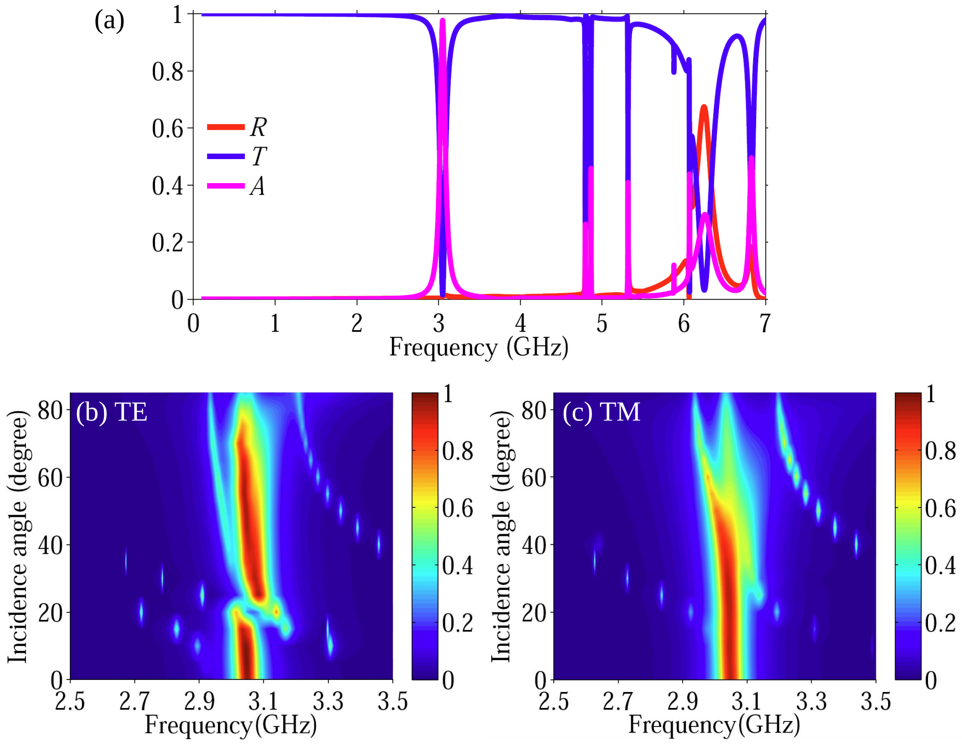

Figure 4.6: (a) Reflectance, transmittance, and absorbance of helix-based PA versus frequencies at normal incidence. Simulated absorbance spectra as a function of incidence angle of the proposed absorber for TE (b) and TM (c) polarizations, respectively.

staggered in the unit cell. The size of such a structural block of single-turn helices is equal of $0.6\lambda_{\text{res}} = 56$ mm and period of the unit cell is $1.1\lambda_{\text{res}} = 112$ mm. As seen, the periodicity is not truly sub-wavelength, the arrays are in fact metasurfaces since they can be homogenized. Numerical simulations show that the amplitudes of the Floquet modes which become propagating for oblique illumination of the arrays are negligible compared with that of the fundamental harmonic. Therefore, these arrays can be modeled as sheets of homogeneous surface electric and magnetic currents. Structural parameters of single-turn helices were taken from Table 2.1. In our design, we utilize helices made of nichrome NiCr60/15 with the conductivity of 10^6 S/m, which approximately ensures the required level of dissipation loss. A wire diameter was chosen as 0.2 mm in accordance with the requirement of a proper level of dissipative loss in the helical resonators. As seen from Figure 4.5(c), helical resonators are embedded in styrofoam plate for mechanical support with a thickness of 14.4 mm.

Figure 4.6 shows reflection, transmission, and absorption frequency spectra of helix-based absorber that were calculated using numerical simulation based on FEM. One can see that designed metasurface based on single-turn helices absorb 96.5% of the incident power at the resonance frequency of 3.05 GHz. Due to their symmetrical geometry, absorber identically operates with waves impinging on either of their sides. Also, it can be seen that reflection coefficient is practically zero in the absorption band of $0.1 - 4.8$ GHz. Nevertheless, when the circumference of single-turn helix becomes comparable with the

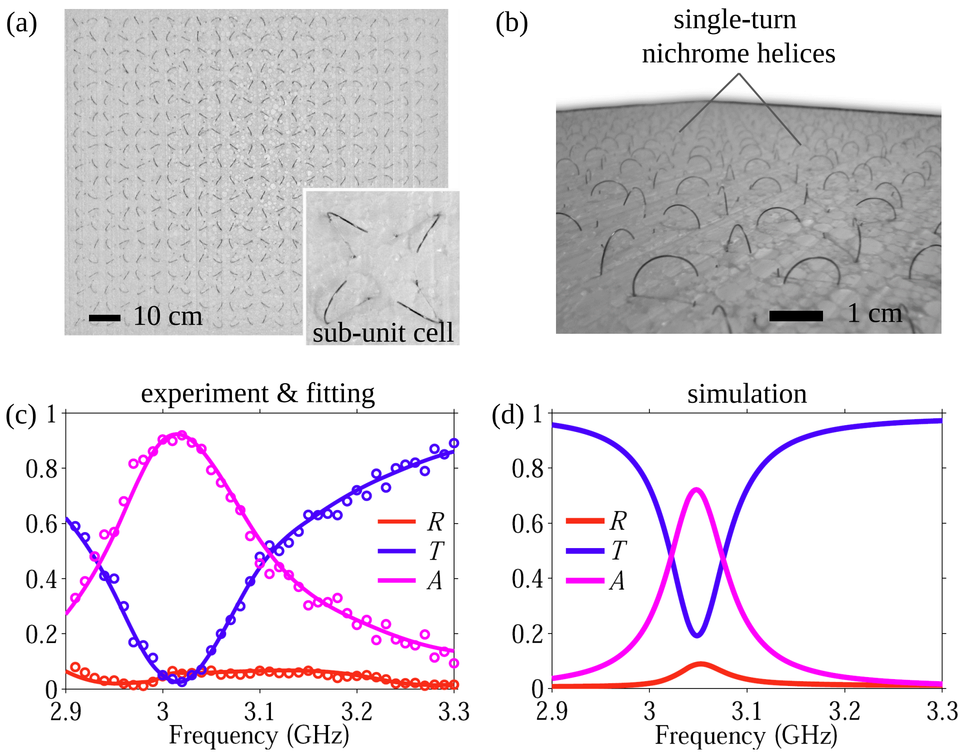

Figure 4.7: (a) Photo of fabricated metasurfaces comprising of 480 nichrome helical resonators. Sub-unit cell of the sample is depicted in the inset. (b) An enlarged view of the sample based on single-turn helices embedded into a styrofoam. (c) Measured and analytical fitting (solid line) reflection, transmission, and absorption spectra at normal incidence. The measured values are indicated by dots ($\circ$) in the experiment. (d) Represented simulated results for comparison with measured data.

wavelength and the first higher-order resonance appears.

For many applications of absorbers, it is of particular importance to absorb normally incident radiation as well as radiation impinging on the structure at oblique angles. The angular stability of the proposed absorber for TE and TM polarizations is shown in Figures 4.6(b,c). It is seen that whereas the metasurface based on single-turn helices absorbs nearly perfectly only at the incidence angles close to normal. Nevertheless, for both TE and TM polarizations the absorber operates with efficiency over 95% at angles of $0° - 15°$ and $23° - 44°$, respectively.

Figures 4.7(a,b) shows photos of fabricated low-reflection absorber comprising of 480 single-turn helical resonators embedded into the styrofoam. The sample preparation and measurement details were described in the previous section (see Figures 4.3). Manufacturing single-turn helices with a small wire diameter of 0.2 mm optimized in simulations imply practical difficulties associated with very flexible and unstable wire forming the helix. Therefore, for our measurements, we fabricated an array of single-turn helices with the wire diameter of 0.5 mm. The sample with single-turn helices has dimensions of $6\lambda_{\text{res}} \times 7.2\lambda_{\text{res}}$. It would be stressed that we used single-turn nichrome helices with respectively low conductivity which differs from the case of realization of twist polarizer metasurface based on copper single-turn helices (see Section 4.1).

The measured reflection R, transmission T and absorption A spectra of fabricated sample are depicted in Figure 4.7(c). The fitting curves quantitatively demonstrate the spectral behavior in accordance with measured data in the microwave range. Sample exhibits peak absorption amounts to 92% at the resonant frequency of 3.02 GHz, while reflectance does not exceed of 7% in the entire frequency range. Simulated results of the helix-based absorber with a diameter of the wire 0.5 mm for comparison with measured data are presented in Figure 4.7(d). As seen from simulated spectra, absorption peak reaches a value of 72% at the resonance of 3.05 GHz, while reflectance and transmittance are equal to 8.8% and 19.2%, respectively. The absorption level difference in 20% between simulation and experiment can be related to diffuse scattering on array inhomogeneities and without taking into account some dissipative losses in the conductor. Nevertheless, the simulated and measured spectra have similar shapes and nearly the same resonance frequencies.

Summarizing, we have fabricated off-resonance transparent perfect absorber based on nichrome single-turn helical resonators with balance polarizabilities. Absorber demonstrates high efficiency ($A = 90\%$) at the resonance, being totally transparent for radiation of other frequencies. Also, the helix-based absorber is polarization-insensitive and symmetrically operating from both sides. This regime implies that the helices of the absorber are equally strongly polarized electrically and magnetically, in the wide frequency range as possible. From the theoretical point of view, the proposed absorber is probably the first microwave realization of a dispersive and lossy structure which does not reveal its dispersive and lossy nature when observed in reflections at any frequency. In view of simplicity of the design and realization, we utilize smooth single-turn helices, since similar resonant inclusions operating even at infrared frequencies can be manufactured based on fabrication technologies reported in Ref. [75, 156].

4.3 Absorber based on double-turn helices

Here, we are aiming to improve the obtained results described in the previous section by the realization of perfect absorber based on double-turn helical resonators with balanced polarizabilities. As mentioned early, absorbing metasurfaces based on double-turn helices exhibit more broadband impedance matching leading to zero reflection and more strong resonance behavior in comparison with single-turn helical resonators. Moreover, symmetric current density distribution in double-turn helices might lead more stable absorption angular dependence at the resonance.

Figure 4.8(a) shows unit cell design of off-resonance transparent helix-based absorber for microwave range. The unit cell of metasurface consists of four blocks RH and LH double-turn helices (similar case with absorber based on single-turn helical resonators) that are embedded halfway into the styrofoam. Structural parameters of helices tailored to the balance of their individual polarizabilities were taken from Table 2.1. The size of each structural block of double-turn helices is equal of $0.4\lambda_{\mathrm{res}} = 43$ mm and period of $0.9\lambda_{\mathrm{res}} = 86$ mm, respectively. Helix-based metasurface is excited by the normally incident

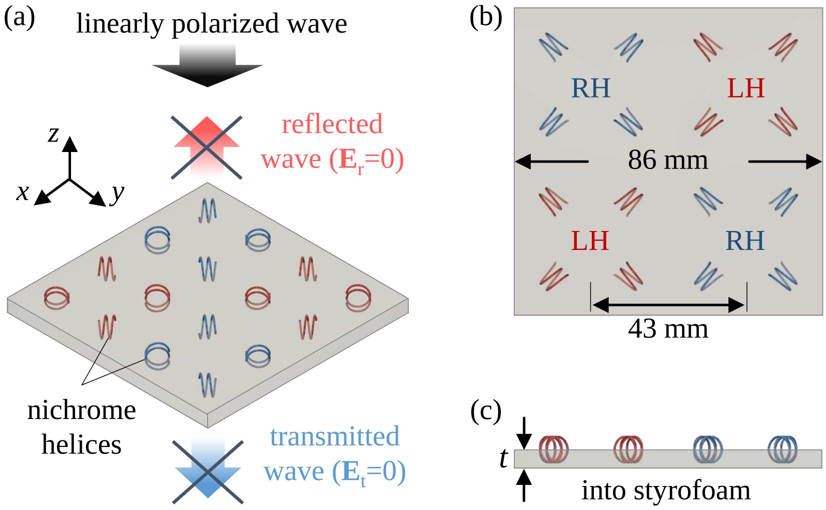

Figure 4.8: (a) Unit cell design of off-resonance transparent perfect absorber based on LH (red color) and RH (blue color) nichrome double-turn helices. Waves interaction with helix-based absorber at the resonance at normal incidence is illustrated. (b) Top view of the unit cell with indicated structural parameters. (c) Front view of the unit cell where helices are embedded halfway into styrofoam with thickness of $t = 14.4$ mm.

plane wave. Figures 4.8(b,c) show top and front views of unit cell double-turn helix-based absorber. In accordance with numerical optimization, we utilize the nichrome helical resonators with a conductivity of 10^6 S/m, which approximately ensures the required level of dissipation loss.

Figure 4.9(a) shows simulated reflection, transmission, and absorption spectra at normal incidence in the frequency range of $0.1-10$ GHz. Helix-based absorber exhibits narrow resonant peak centered near of 3.07 GHz frequency with peak absorptivity in excess of 99.99%. Meanwhile, absorber exhibits a low-reflection ability in the broad frequency range from 0.1 GHz to 9.7 GHz. Thus, absorbing metasurface based on double-turn helices is a better candidate for the realization of perfect off-resonance transparent absorbing metasurface in comparison with proposed absorber based on single-turn helices. Figures 4.9(b,c) show simulated absorption coefficient as a function of incidence angle for TE and TM polarizations, respectively. The incident angle is varied in 5° steps from 0° to 85°. It can be seen that helix-based absorber exhibits stable absorption behavior for TM incident waves remains nearly angle-invariant up to 60°, while absorption for TE polarization shows a sharp dip near 50°. Nevertheless, the off-resonance transparent helix-based absorber can be regarded as polarization and incidence angle-invariant up till 40° incidence. Moreover, this absorber demonstrates wider angular stability at oblique incidence in comparison with the single-turn helix-based absorber (till 15 degrees) for both polarizations.

Figure 4.10(a,b) shows photos of a sample based on nichrome double turn helical resonators. The sample comprising of 324 double-turn helices embedded halfway into styrofoam is realized follows to fabrication approach described in Figures 4.3(a-d). The nichrome wire with a diameter of 0.2 mm was utilized for fabrication of off-resonance transparent helix-based absorber. As a result, the sample has dimensions of $3.6\lambda_{\mathrm{res}} \times$

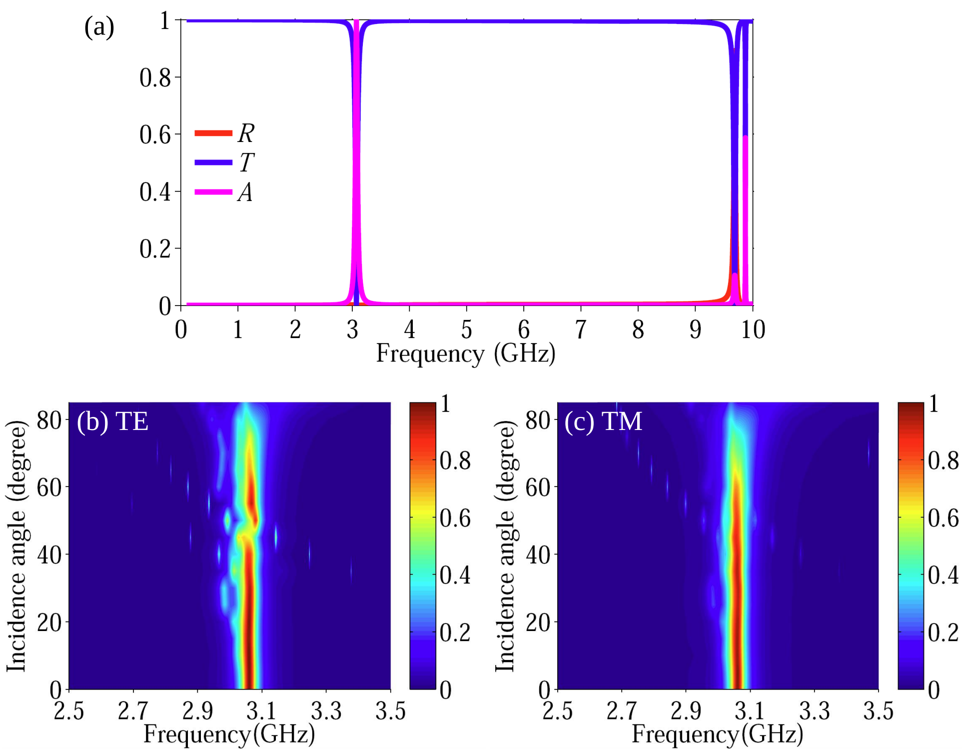

Figure 4.9: (a) Simulated reflection, transmission, and absorption spectra of the absorber at normal incidence. Dependencies of the absorption with angle of incidences for (b) TE polarization and (c) TM polarization, respectively.

$3.6\lambda_{\text{res}}$.

The simulated and measured reflection, transmission, and absorption spectra are shown in Figure 4.10(c). In the experiment, resonant absorption band centered near of 3.08 GHz with the absorption peak of 81%, while reflectivity does not exceed of 12% in the considered frequency range. Numerically simulated results for qualitative comparison with measured data are depicted in Figure 4.10(d). As can be seen, simulated and measured results are in good agreement. Nevertheless, resonance in the experiment exhibits broader behavior than it was predicted. This is most likely due to inhomogeneous broadening resulting from random variations of the helical parameters in the characterized area. Also, double-turn helical resonators are difficult to fabricate using a hand-made approach since the size of each helix is very small ($\lambda_{\text{res}}/15$) and structural parameters can be easily changed leading to undesirable disbalance of polarizabilities. Nevertheless, these deficiencies do not diminish our main achievement such as realization of the off-resonance transparent perfect absorber for microwave range. It should be mentioned that more detail about the theoretical background and practical realization of reflectionless absorbers based on single-turn and double-turn helices can be found in our article [5-A].

It can be concluded that unique property of low reflectivity in an ultra-wide frequency range combined with frequency-selective absorption offers exciting possibilities in applications, allowing the creation of perfect electrically thin band-stop filters for radiation of an arbitrary frequency. The off-resonance transparency of the absorbers allows one to construct various complex multi-frequency filters, combining in a parallel stack metasurfaces

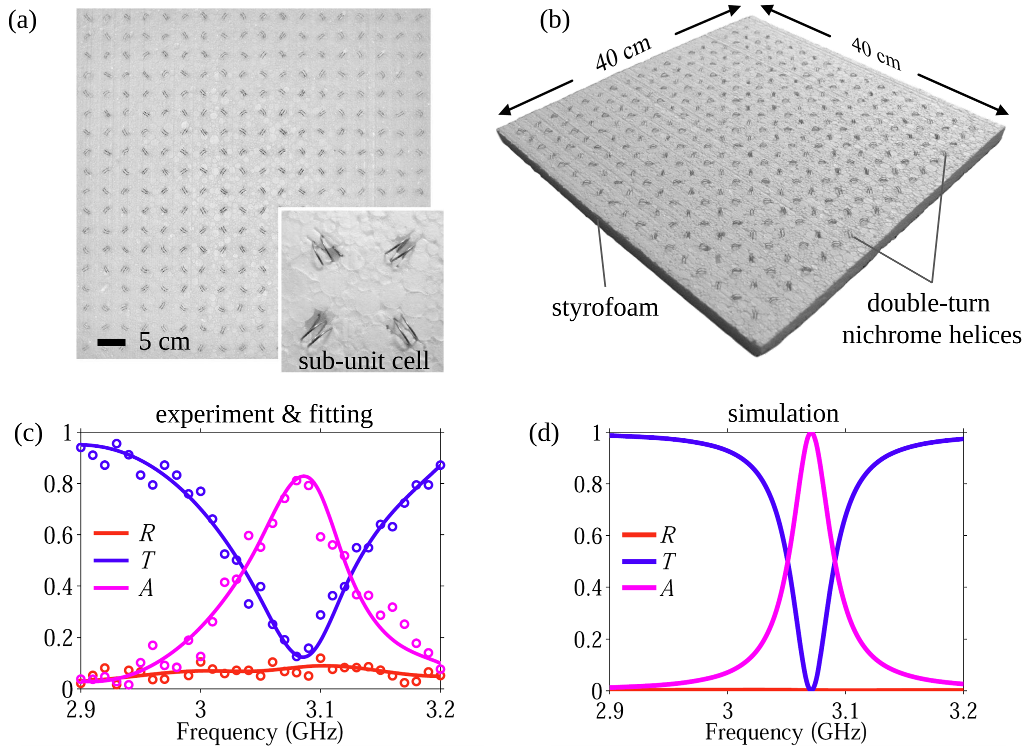

Figure 4.10: (a) Photo of fabricated metasurfaces comprising of 324 nichrome double-turn helical resonators. Sub-unit cell of the sample is depicted in the inset. (b) Perspective view of the sample based on helical resonators embedded into styrofoam for mechanical support. (c) Measured and analytical fitting (solid line) reflection, transmission, and absorption spectra at normal incidence. The measured values are indicated by dots (○) in the experiment. (d) Represented simulated results for comparison with measured data.

resonating at different frequencies. The neighboring metasurfaces would not disturb the performance of one another, and the overall thickness of such multi-layer structure would be still of the order of one wavelength or less. Another exciting possibility of implementation of the proposed absorbers lies in designing new types of "invisible" bolometers and sensors. Using the multi-layer metasurface absorber, it becomes possible to design a single bolometer that measures the power of incident radiation of different spectral lines at the same time. Moreover, the narrow-band response of the proposed absorbers makes them ideal candidates for implementation in bolometer arrays in astronomy at millimeter wavelengths. Due to the reflectionless operation, the proposed absorbers can be successfully used for stealth applications, especially for non-metallic objects. In contrast to conventional metal-backed absorbers, they do not increase the radar cross section of the hidden object outside of the absorption band.

4.4 Conclusions

- Off-resonance transparent twist polarizer based on copper single-turn helical resonator has been realized. We utilized hand-made approach for fabrication of helix-based metasurfaces for microwave range. The experiment was carried out in an anechoic chamber in the frequency range of $2.8 - 3.3$ GHz. Simulated and measured data demonstrate 90° polarization rotation with a high cross-transmission coefficient over of 0.92 at the resonance with up to 35° at oblique incidence. Meanwhile, helix-based twist polarizer exhibits low reflectivity ($R < 6\%$) in the wideband frequency range from 2 to 4 GHz in accordance with numerical simulation.

- Using numerical simulation and experimental verification, perfect absorber based on nichrome single-turn helical resonators with balanced polarizabilities was studied in the microwave range. Helix-based sample absorbs more than 90% incident radiation at the resonance frequency of 3.05 GHz, being totally transparent for radiation in the range of $0.1 - 4.8$ GHz. Both simulation and experimental results are in a good agreement.

- To extend the transparency properties of perfect absorber based on single-turn helices, ultra broadband absorptive metasurface using nichrome double-turn helical resonators has been tested numerically and experimentally, respectively. In accordance with simulation data, the proposed helix-based absorber exhibits near-unity reflection in the range of $0.1 - 10$ GHz with resonant absorption peak over of 99.99%, respectively. In the experiment, resonant absorption band centered near of 3.08 GHz with peak absorbance of 81%, while the reflectivity of the sample does not exceed of 12% in the entire microwave range.

- In addition, the realized off-resonance transparent twist polarizer can found potential applications in radio antennas and communication systems. Helix-based absorption metasurfaces allowing the creation of perfect electrically thin band-stop filters for radiation of an arbitrary frequency and in order to construct various complex multifrequency filters. Another exciting possibility in the application is a designing of new types of “invisible” bolometers and sensors.

Chapter 5

Direct laser write lithography

Towards to realization of functional off-resonance transparent metasurfaces helical resonators for infrared spectral range, the problem of practical downscaling helix-based metasurfaces using direct laser write lithography was solved. This chapter is devoted to the fabrication of 3D dielectric architectures with micro/nanoscale size by usage of direct laser writing lithography based on the principle of two-photon absorption in the photosensitive material. This method makes it possible to produce 3D near-arbitrary shaped micro/nanostructures with a spatial resolution of the order of 100 nm. The mechanism of two-photon absorption in a photosensitive material is described in details (Section 5.1). Experimental setups which used in the process of fabrication 3D architectures are described (Section 5.2). 3D dielectric volumetric and planar microstructures using femtosecond pulsed direct laser writing technique were fabricated (Section 5.3). Moreover, determination of optimal exposure condition to achieve the minimum feature size of exposed voxel in microstructure using laser fabrication was carried out.

5.1 Direct laser writing

In the first attempts for the creation of metamaterials with micro or even nanoscale dimensions, standard lithographic methods were used (EBL, FIB, inkjet printing and etc.). However, these tools were not intended for realization of 3D composites comprising subwavelength meta-atoms with nanoscale sizes. Thus, in order to realize the metamaterial with their advantageous properties, the scientific community has spent a lot of effort to expand and develop the 3D fabrication approaches giving several remarkable solutions. One of them is a direct laser writing technique that allows us to fabricate the 3D metamaterial architecture with subwavelength microscale inclusions.

5.1.1 Micro and nanofabrication methods

Currently, methods and technologies for the manufacture of nano- and microscale devices that play a dominant role in information and communication technologies are actively developing. A variety of methods has been developed to create the complex models with a micrometer resolution or much lower. The dimensions and geometry of the desired pattern determine the real choice for a particular technique. As a rule, the fabrication of nano- and micro-patterns is realized owing of photolithography, electron-beam lithography, X-ray lithography, microprocessing, direct writing or holography.

All manufacturing methods can be divided into two types: “top-down”or “bottom-up” approaches. In general, the “top-down” approach starts with a mass substance and proceeds to reduce the size, removing unwanted substances or simply working in areas of interest. On the other hand, the “bottom-up” approach starts with the smallest particles and leaves as a whole, up to intramolecular force and dynamics at the molecular level, to reach a low-energy point where the individual particles self-organize and settle. Respect to these approaches the most common 3D fabrication techniques are self-assembly method, glancing angle deposition technique, multiple-beam interference, and direct laser writing.

Self-assembly method is a general bottom-up growth approach using colloidal crystals [157]. Colloids refer to structures containing fine particles suspended in a liquid. By immersing the substrate in colloidal crystals, the particles will be deposited in a periodic matrix on the surface of the substrate layer by layer after removal of the solvent at a temperature close to the boiling point [158, 159]. Self-assembly is very suitable for inexpensive and large 3D architectures [160].

Another popular “bottom-up” approach is glancing angle deposition (GLAD) that allows producing 3D metallic and dielectric templates. During the GLAD process, the vapor flux arrives at the substrate with an oblique angle from the normal to the substrate and structures grow to a vapor source [161, 162].

Multi-beam interference is a method of “top-down” large-scale production that widely used for manufacturing 2D and 3D polymer microstructures [163, 164]. Interference occurs when several beams are added together provided that the phase differences between them remain constant over the observation time. It leads to exposing of photosensitive transparent materials well-known as photoresist and after the development procedure, the unexposed photoresist can be stored or deleted depending on negative or positive-type photoresist was used. However, this technique does not give enough degrees of freedom to fabricate metamaterials with arbitrarily shaped inclusions.

The direct laser writing (DLW) is an innovative and promising “top-down” approach with truly 3D fabrication capabilities [165–167]. Three-dimensional nanostructures with a particle size of less than 100 nm [168–170] were fabricated by overcoming the diffraction limit. A minimum particle size of up to 40 nm was achieved by single-color initiation and deactivation of polymerization [171]. Of all the above, laser direct writing is the only method capable of arbitrarily producing various structures, such as spirals [170, 172] woodpile structures [173, 174], “slanted pore” structures [175] and others.

Similar to standard methods of photolithography, structuring is carried out by illuminating photoresists with negative or positive tone via light with a well-defined wavelength. Due to two-photon absorption process, the photoresist will be exposed. The mechanism of two-photon photopolymerization will be described below.

5.1.2 Two-photon absorption

Two-photon absorption (TPA) is the simultaneous absorption of two photons of identical or different frequencies in order to excite a molecule from one state (usually the ground state) to a higher energy electronic state. The energy difference between the involved lower and upper states of the molecule is equal to the sum of the photon energies of the two photons. Two-photon absorption is a third-order process several orders of magnitude

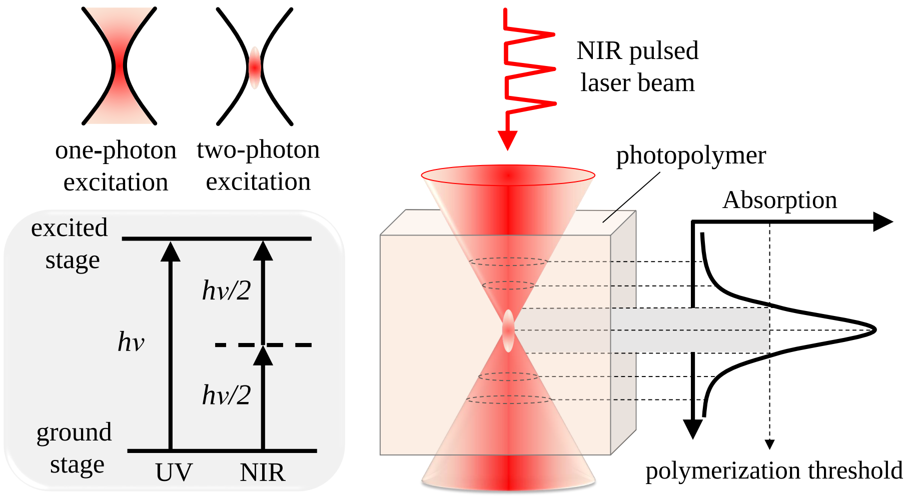

Figure 5.1: Fundamentals of two-photon absorption generated by a focused laser beam [178].

weaker than linear absorption at low light intensities. It differs from linear absorption in that the atomic transition rate due to TPA depends on the square of the light intensity, thus it is a nonlinear optical process, and can dominate over linear absorption at high intensities [176].

Two-photon absorption (TPA) was predicted theoretically as early as 1931 and was confirmed experimentally only in 1961 by Kaiser and Garrett [165]. Subsequently, TPA was used only for spectroscopic purposes, but after published work [166] in 1965, it was starting to use for induction of polymerization. Further development was updated for lithographic microfabrication well-known as direct laser writing by Kawata's group in 1997 [167]. To these days, the direct laser write technologies actively are used to manufacture various photonic, micro-optical, microchemical and metamaterials devices [177–179]. The principle of TPA is based on a nonlinear response of a two-photon transition rate to optical intensity [178].

Photoresist simultaneously absorbs two near infrared (IR) photons, the collective energy of which is equal to the ultraviolet photon, as shown in Figure 5.1. If the energies of two photons are exactly the same number, this process is called a degenerate TPA, otherwise, it is non-degenerate. The speed of the TPA is proportional to the square of the light intensity, which causes the TPA to mainly occur around the laser focal point. The linear relationship between the TPA and the quadratic light intensity leads to the fact that the size of the TPA region exceeds the diffraction limit of the wavelength of the incident light.

As it was mentioned before, the TPA process occurs at a focal point that leads to induce a dramatic change in the solubility of the photoresist for appropriate developers. The advantage of TPA is that the excitation process is a heat insulating process where the deposition of photon energy occurs so quickly that electrons do not have time to absorb it for the phonon emission. This feature is useful for photochemical reactions since the thermal effects are undesirable. Moreover, polymers typically exhibit negligible linear absorption in the near-IR spectral range that allows the laser beam to penetrate deeply into the sample and directly induce polymerization inside the material without disturbing the external focal volume. All these functions of TPA are very useful tools in various applications that are given in the following section.

5.1.3 Applications

Many new applications require 3D patterns and one of them is the emerging field of metamaterials. To manipulate visible and infrared radiation, it is required nanostructures consist of subwavelength inclusions with dimensions on the order of 0.03–5 μm. Researchers relied heavily on EBL and UV photolithography in combination with the deposition stages of the material to create metamaterials. EBL is used when a very high resolution is required, and UV photolithography is used when the resolution requirements are on a micron scale. However, to create a truly 3D metastructures, these technologies were not suitable, except for the creation of multilayered planar metamaterials. The fabrication process is quite cumbersome time-consuming and is limited in a design freedom. The usage of laser lithography gave us to create 3D dielectric micro- and nanostructures with a 100 nm spatial resolution for the subwavelength inclusions. Subsequently, the realization of metallic nanostructures can be performed by using various metallization methods. It should be noted that the method of laser lithography goes far beyond the construction of only 3D structures since it is widely used in nanophotonics, microelectromechanical systems (MEMS), microelectronics and microfluidics. Several examples of DLW lithography applications are given bellow:

- using femtosecond pulsed laser, it was demonstrated a 3D microfabrication with proteins, such as bovine serum albumin and collagen [180,181]. As a result, artificial protein architectures are porous and demonstrate promise for use as drug delivery devices or sustained-release devices that can be useful for biological applications;
- for biochip applications, it was recently developed a lobed micropump driven by light [182];
- for photonic applications, using photosensitive materials and laser lithography it can be applied to produce gratings and photonic crystals [168, 175];
- it can be used to create high-quality waveguides, either in free space or on substrates. For instance, unsupported waveguide structures, such as couplers, splitters and Mach-Zehnder interferometers, between the ends of optical fibers have been fabricated [183, 184]. Further metallization of waveguide structures can be highly conductive that opens up the door for electrical applications such as the microinductor [185];
- the combination of stimulated emission depletion (STED) with DLW technique gives huge opportunities and application for 3D manufacturing with extremely high spatial resolution to produce the photonic crystals, waveguides, metamaterials and etc [75, 179];

- laser technologies are widely used for coding consumer products with bar codes and indicators of the last use date on food packaging;
- special polymers or additives are used to transmit laser radiation in written information. Moreover, the products have been written in more complex templates, full-color templates, and images, as well as DLW, can be used even for personalized security features.

It should be mentioned that commercial applications are on the horizon in the creation of high-performance, photonic crystals and microinductors, and functional 3D components for microfluidic systems [178].

5.2 Experimental setup

In this section, we describe the main experimental setup, principle of work and their functionalities that were used in this study. The experimental setup of DLW, a principle of critical point drying procedure and the optical characterizations measured by IR spectroscopy is described in details.

5.2.1 DLW setup

In the 1990s, the commercialization of femtosecond lasers, in addition to recognizing high-performance photosensitive materials, significantly accelerated micro/nanofabrication in solid and even liquid media. Properties such as the duration of an ultrashort pulse (less than 5 fs), high beam quality, coherence, significant nonlinearity, power, frequency stability, strong localization, and others allow us to control various materials by laser lithography.

Figure 5.2 shows a schematic illustration of DLW setup for fast prototyping of 3D dielectric patterns. The laser source is a Ti: Sapphire femtosecond oscillator (Mai Tai, Spectra-Physics). The Spectra-Physics Mai Tai oscillator is used for a wide variety of applications: from general spectroscopy to multiphoton microscopy. Due to its leading technical characteristics and the largest installed base characteristics of any laser of this type, Mai Tai is truly an advanced tool for basic research and biological imaging. The reliability of the Mai Tai series is supported using a ultra-stable regenerative mode-locking. Using this method, the Mai Tai oscillator is capable of hands-free supporting, that allows you to quickly collect excitation profiles with just one click.

The system has a central wavelength (λ) at 800 nm with a temporal pulse length (τ_{pulse}) of about 120 fs. The laser beam is passed through a computer-controlled variable attenuator and mechanical shutter. Variable metallic attenuators are used to reduce and adjust pulse energy to the order of several nanojoules for fabrication purposes. In order to correspond to the scan speed during the translation stage during actual production, a repetition rate frequency f = 80 Hz is usually used. The repetition rate and the speed of scanning of the stage determine the distance between the exposed voxels produced by a series of laser pulses. The collimated laser beam is fed into an inverted optical

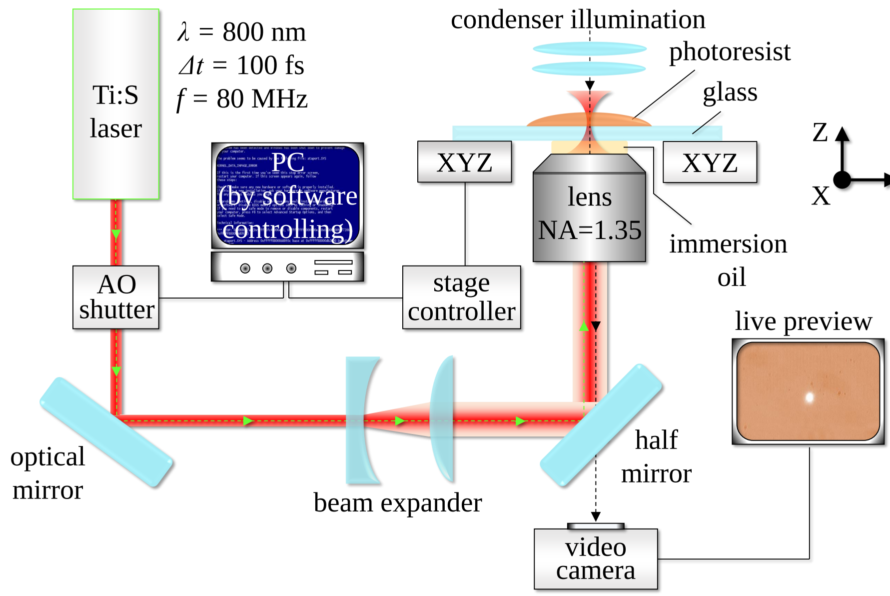

Figure 5.2: Experimental setup for DLW process.

microscope and tightly focused owing a microscope objective with an oil immersion (magnification 60×, NA =1.35) in the photoresist sample. The sample is attached to a piezoelectric transducer (PZT) via controlling of a high-precision 3D translation stage (Physik Instrumente P-563.3CL) which provides nanoscale positioning accuracy within the range of (300 × 300 × 300) μm in XYZ axes, as well as the resolution of 3 nm and 1.5 nm, respectively. In actual production, an accuracy of about 1% of the degree of shear with continuous scanning is observed at the stage.

The position scanning of the sample and the intensity of the laser beam are controlled by a personal computer (PC) by software program 3DPoliCompiler. The software mainly uses for translation commands, for example, to move at a certain distance in certain directions (in the X, Y or Z directions) and is a subset for the digital stage controller. The controller has provisions for performing real-time probing to get the current stage positions. The overall monitoring of the fabrication was achieved when the halogen lamp was illuminated (condenser illumination) using video camera attached to the microscope. In photoresist samples, the image of modification is usually hidden, but the exposed resist along the transfer lines can still be seen due to a small modification (10^{-6}) of the refractive index, therefore, it is possible to monitor the manufacturing process in the real-time. In addition, it is necessary to pass the light from condenser lens through a red filter before shining it on the sample. As a result, spatial resolution approaching 100 nm can be obtained by carefully adjusting average laser power slightly above the photopolymerization threshold.

5.2.2 Critical point drying process

Figure 5.3(a) shows the photo of critical point drying (CPD) machine (JCPD-5, Jeol) with the indicated notations. Critical point drying is a process to remove liquids in such a way

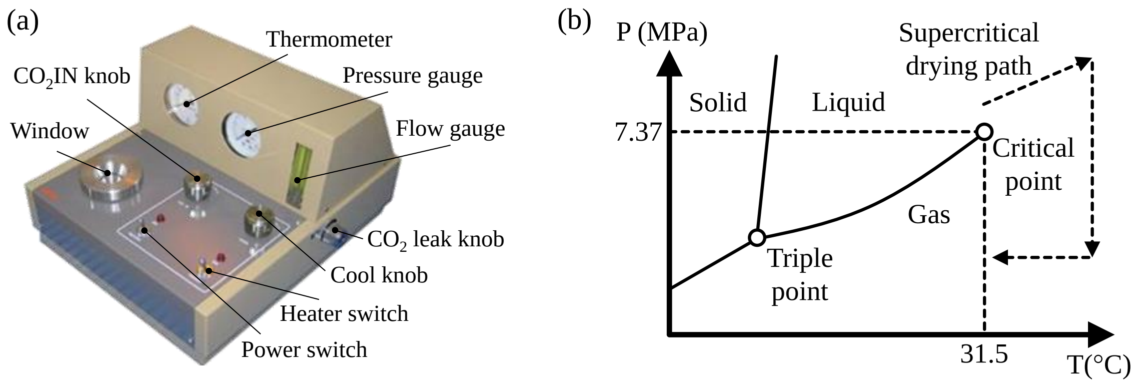

Figure 5.3: (a) Photo of the supercritical point drying apparatus (JCPD-5, Jeol) with indicated notations. (b) Phase diagram of the pressure versus temperature. The data in critical point are indicated for CO_2 liquid.

that the entire structure is not damaged during the drying process. Applications for critical point drying are the preparation of biological samples for scanning electron microscopy (SEM), production of aerogel, decaffeinating of coffee, production of micromechanical systems, micro/nanostructures and others.

In the development process, the fabricated samples by DLW are usually put in the liquid (usually alcohol) to remove unexposed photoresist. If after that the samples are dried in air, the liquid passes at a certain rate into the gas (evaporates), while a number of liquid decreases at the same rate. When this occurs in the samples, the surface tension in the liquid body pulls against any structures with which the liquid contacts. Therefore, the delicate structures (especially with nanoscale size) are easily destroyed and can not be studied. To avoid this, the sample must be dried above the critical point through the supercritical region. The supercritical fluid has no difference between gas and liquid (equal densities) and, therefore, does not border on liquid and gas.

Figure 5.3(b) shows the phase diagram of the pressure versus temperature ranges where solid, liquid and vapor exist. The boundaries between the phases intersect at a point on a graph called a triple point. Along the boundary between the liquid and vapor phases, one can choose a certain temperature and the corresponding pressure at which liquid and vapor can co-exist and, therefore, have the same density. This is the critical temperature and pressure. Drying in critical condition is based on this physical principle. The liquid in the sample is replaced with a suitable inert liquid, the critical temperature of which for the realized pressure is slightly higher than the surrounding medium.

The carbon dioxide (CO_2) liquid is ideal for the CPD process due to the low temperature of the critical point, easily miscible with alcohol, non-flammable, non-toxic, and low costs. To replace alcohol, a high-pressure liquid CO_2 is used, and after that, the sample is completely immersed in supercritical CO_2. Then it is heated until the temperature is the critical point. After this, the pressure can be gradually reduced, allowing the gaseous CO_2 to escape and leave a clean dry sample. A critical point can be used at 35°C and a pressure of 7.37 MPa. Thus, the temperature is raised to the critical temperature and the liquid CO_2 passes into the vapor without changing the density and surface tension effects with saving the sample architecture.

5.2.3 FTIR setup

Fourier transform infrared spectroscopy (FTIR) is a common technique to measure reflectance, transmittance or absorbance spectra of the fabricated samples. An FTIR spectrometer simultaneously collects high spectral resolution data over a wide spectral range. This confers a significant advantage over a dispersive spectrometer which measures intensity over a narrow range of wavelengths at a time [186].

In this study, we used two FTIR spectrometers: spectrometer MFT-2000, JASCO and FT/IR-6300, JASCO with microscope attachment of IRT-7000, JASCO. The first one, we used to measure the reflection spectra and the second one (more advance) was used for measurement of 2D mapping reflection. Setup for optical characterization of two FTIR spectrometers is pretty similar that is not require description for both ones.

The main components and optical reflection and transmission pathways for FTIR setup are given in Figure 5.4. The $M1$ mirror provides a switch for measuring the reflection or transmission of a laser source from an FTIR spectrometer. Mirrors $R1$ and $R2$ serve to guide the transmitted light through the sample to the detector, and for the same purposes, $R1$ and $R2$ mirrors are designed to direct light into the detector. The Cassegrainian objectives (marked in blue) with magnification $16\times$, $NA = 0.5$, the minimum and maximum convergence angle is about $16.5°$ and $31.7°$, respectively, collect light for reflection or transmission, which is routed to the detector through $M2$. The mercury cadmium tellurium (MCT-M) detector is used in combination with a beam splitter with germanium covered with potassium bromide (Ge/KBr) and a highly sensitive ceramic light source. The measurement is carried out in the range of $2 - 15.4$ μm. The sample is installed on the stage platform, which has freedom of translation in XYZ directions. The personal computer performs data processing and analysis of the measured spectra.

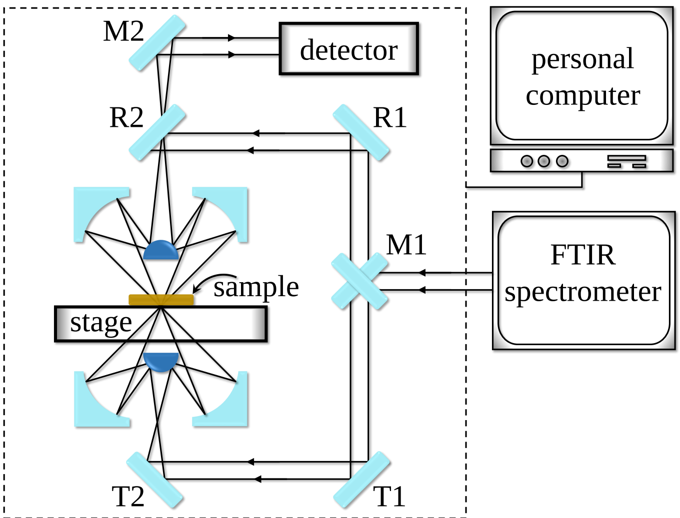

Figure 5.4: FTIR spectrometer used for optical characterization of the fabricated samples.

5.3 Prototyping of 3D dielectric microstructures

Here, we are focused on the realization of 3D dielectric micro/nanostructures using DLW technique. We have performed a simple test for determination of minimum feature size by finding the best exposure conditions of DLW to achieve a high spatial resolution of about 100 nm. Further, to demonstrate the capabilities of DLW fabrication, we realized several 3D dielectric samples.

5.3.1 Fabrication details

At first, it is necessary to find or synthesize the photoresist that uses as the initial material of two-photon absorption for DLW technique. As well known, SU-8 is often photoresist that used in conventional MEMS photolithography [187]. However, for the photopolymerization of epoxy resins such as SU-8, cationic polymerization occurs that generates a catalytic photo acid under illumination and therefore, each photoacid generator can produce multiple polymerizations. It can easily be converted into thick films to produce structures with a high aspect ratio. However, the added complexity resulting from the required stages of spin-coating and post-baking makes SU-8 less favorable than SZ2080 [188] or acrylic resins for the rapid prototyping of micro/nanostructures.

In this study, we use negative-tone 20:80 mixture of zirconium-silicon with methacrylate sol-gel hybrid organic-inorganic photoresist SZ2080 with 0.4% 4,4'-bis(diethylamino) benzophenone added as photo initiator for DLW process. Details on synthesis, parameters and applications of SZ2080 can be found in the available literature [189]. Figure 5.5 shows the workflow steps of fast prototyping of 3D dielectric micro/nanostructures. All steps for realization some dielectric sample are described in the follows:

1. The sample was prepared by drop-casting the SZ2080 solution onto 170 μm-thick microscope cover glass substrates (Matsunami), and subsequently dried on a hot plate using temperature ramp (for 5 min) between 40°, 60°, and 80°C (for 20 min) and with a smooth cooling of the samples to room temperature. The refractive index of the dried samples is about 1.50.

2. Next, one dried sample is fixed at XYZ stage control for the femtosecond laser exposure. Using optomechanical setup (see Fig. 5.2) with the same exposure conditions the arbitrarily-shaped pattern was writing in the photoresist SZ2080 by pulsed femtosecond laser illumination. By carefully adjusting the parameters of laser exposure we can achieve the sub-micrometric spatial resolution in the used photoresist.

3. After DLW process, the sample was developed in 4-methyl-2-pentanone or in 1-propanol: isopropanol (50:50) solution for 5 min and rinsed in ethanol.

4. In order to gently remove the ethanol from the sample and minimize the destructive action of capillary forces on the finely-patterned photoresist, we have dried the sample in a supercritical point drying machine using a high-pressure liquid CO_2.

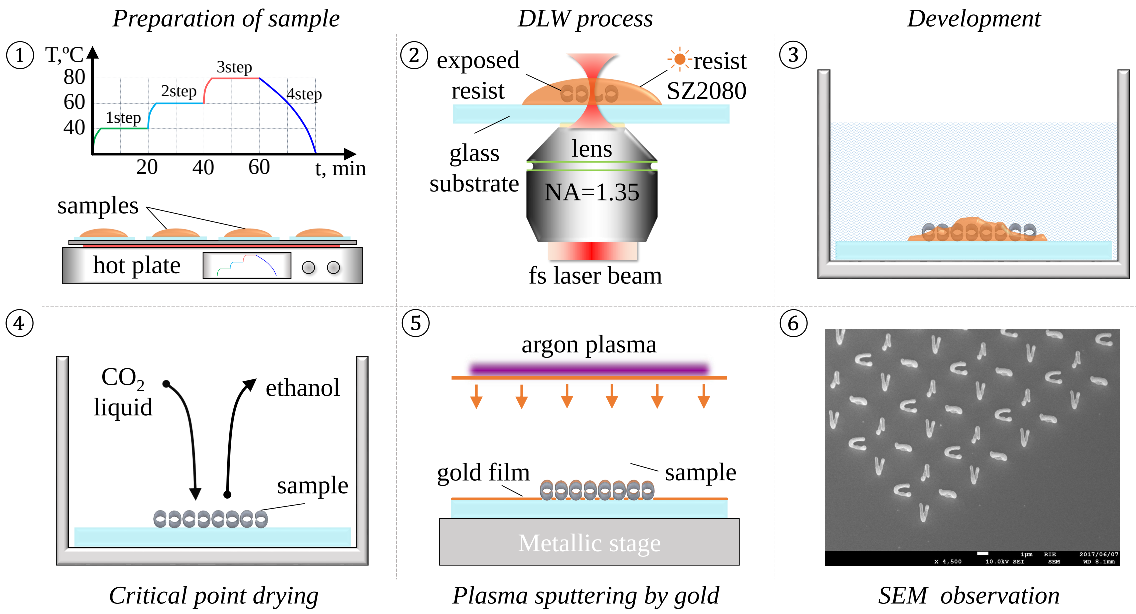

Figure 5.5: Workflow steps for fast 3D prototyping of dielectric micro/nanostructures.

(5) Before to see the fabricated sample using Scanning Electron Microscopy (SEM), the sample needs to be coated with thin layer of metal to make it conductive. Therefore, an initially dielectric sample was coated with gold using plasma sputtering (Quick coater SC-701 MkII). Since sputtering is not spatially selective, it coats both the photoresist sample and the glass substrate.

(6) Finally, observation of samples using SEM.

It should be mentioned that all fabrication process takes about 5 hours. Usually, time is highly dependent on the DLW process due to the complexity of the geometry, the amount and area of the pattern, the scanning speed and the intensity of the laser beam. In some special cases, the fabrication time of the samples can reach several days or even weeks depending on the task.

Some examples of 3D dielectric volumetric and planar structures realized by DLW technique can be seen in Figure 5.6. It is clear to see the difference between volumetric (upper row) and planar (lower row) structures. Here, we did not focus on any functionality of volumetric structures or obtaining a high resolution. However, the realized dielectric structures demonstrate the capabilities of the DLW fabrication for the realization of 3D complex structures as well for planar periodic structures that resemble metasurfaces. In future, this will allow us to create the functional metasurfaces based on helical or other inclusions to obtain desired optical properties.

5.3.2 Determination of the minimum feature size

As well known, one laser pulse creates a single photomodified volumetric region known as a voxel (see Figure 5.7(a)), an ellipsoidal shape is obtained from the light intensity distribution in the focal volume of the laser beam. So called a “series of pulse trains”

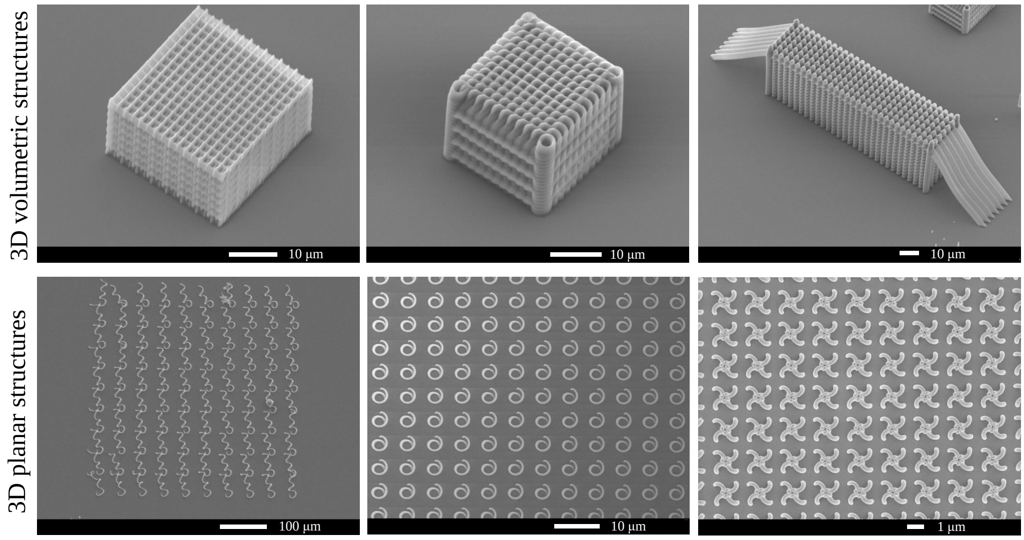

Figure 5.6: SEM images of 3D volumetric (upper row) and planar (lower row) dielectric microstructures realized by DLW lithography.

creates a continuous chain of voxels, which is associated with the formation of lines or continuous structures by choosing the appropriate laser repetition frequency and scan speed. One can imagine that it works like when you are drawing by a sharp tip of a pen on the paper the same a focal spot of a femtosecond laser is drawing in the volumetric photosensitive material. However, laser beam remains fixed, but the photoresist itself is moving in all XYZ-directions, so the drawing process is carried out. The inter-distance between Δ (in nanometer units) adjacent voxel or laser pulses (for example in the x-direction) is given by the next expression:

$$\Delta = \frac{\upsilon_{\mathrm{x}} \cdot 10^6}{f}, \tag{5.1}$$

where υ_{x} is the scanning speed along the x-axis, and f is the laser repetition frequency. The scanning speed and laser repetition rate determine the fabrication time, while the pulse energy is drastically affected by the size of the voxels, that is determined the final size of the elements in the structure. By manipulation of these parameters, the optimal exposure condition for laser writing can be found, where the structural strength and filling factor of periodic structures influence to the quality of fabricated structures.

Moreover, the voxel is the basic structural element from which various 2D and 3D architectures are subsequently built, therefore, knowing the dimensions of the voxel, you can determine the spatial resolution obtained by DLW process. Each voxel takes the form of an ellipsoid and has a lateral d_{xy} and axial d_{z} sizes, respectively. It should be mentioned that it is possible to achieve the near-spherical form of voxels by adding auxiliary elements to the optical system and careful control of the exposure conditions [77]. In this study, we use unmodified DLW technique with typical setup (see Figure 5.5) that allows obtaining the only ellipsoid shape of the voxel. With various exposure conditions, such as laser pulse energy, the overlap between the adjacent voxel and voxel size itself, the final dimension

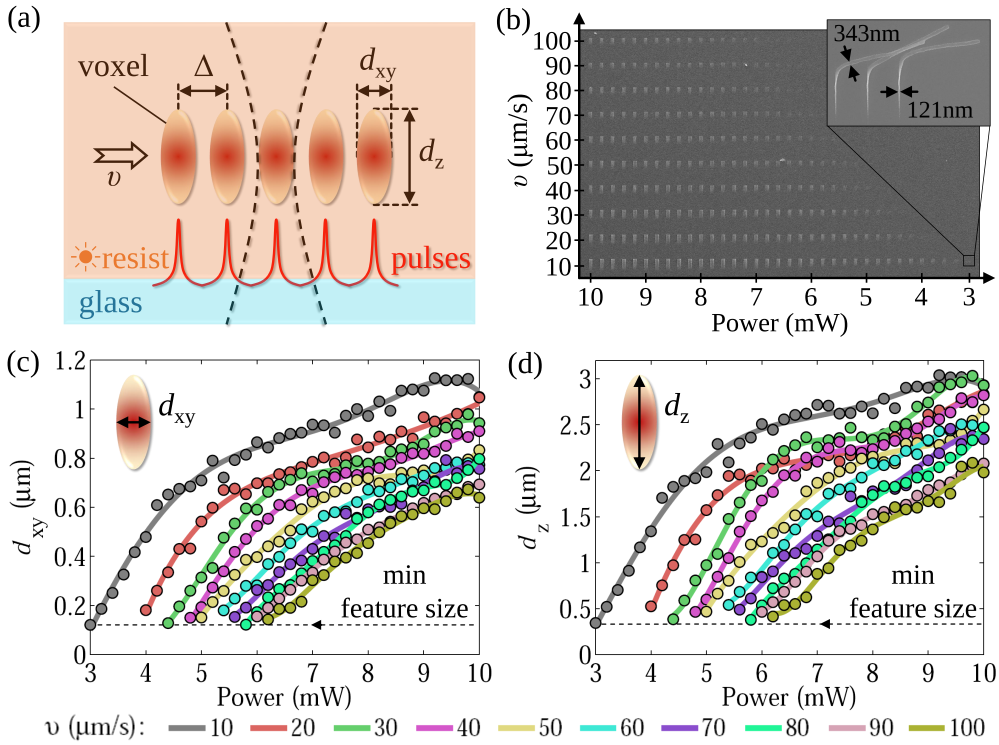

Figure 5.7: (a) Schematic illustration of laser pulse trains creating the volumetric voxels with denoted inter-distance Δ, lateral d_{xy} and axial d_z sizes. (b) SEM image of sample for determination of minimum feature size using exposure matrix with different structural parameters depending on the laser power and scanning speed, respectively. The minimum feature size can be seen in the inset, where lateral $d_{xy} = 112$ nm and axial $d_z = 325$ nm parameters are indicated. Dependence of lateral size (c) and axial size (d) on the scanning speed, respectively.

of the structure is determined. Here, we use a photoresist SZ2080 that has a threshold response, which means that a constant photomodification occurs when the fluency or intensity increases above a certain threshold value. From theory, the threshold value can be found knowing the maxima of the two-photon irradiation dose that have a full width at half maximum (FWHM) and can be expressed in the following way [179]

$$FWHM = \frac{\lambda}{5.5 \cdot NA}. \tag{5.2}$$

For example, at $NA = 1.35$ FWHM is seven times smaller than the free-space wavelength. Theoretically, the exposure profile will be even smaller for processes of higher order FWHM. In actual fabrication, it is difficult to control and maintain the laser intensity to such an optimum limit above the threshold due to fluctuations in the energy of the laser pulses. In the case of TPA, the irradiated region has a quadratic dependence on the intensity of the laser pulse, which means that it is even more sensitive to energy fluctuations. Therefore, the photopolymerization threshold can be found only from the direct experimental measurements of the later and axial dimensions of the voxels. Thus, it is necessary to carry out a simple test for determination of minimum feature size using exposure matrix with different energy pulses and scanning speed to define the structural parameters of the voxel, d_{xy} and d_{z}, respectively. The SEM image of the exposure matrix is shown in the Figure 5.7(b).

We chose different power of laser pulses P_{p} in the range of $6-3$ mW with step of 0.1 mW and scanning speed (υ_{x} in the range of $10-100$ μm/s) to determine the lateral (d_{xy}) and axial (d_{xy}) width of the twisted rod by usage of the SEM. Directly measuring the width of the rods (average of three measurements), the truncation or torsion errors unlike might be arisen. Figures 5.7(c,d) show the dependence of the lateral and axial width of the twisted rod (particular, the size of the voxel) on the power of laser pulses and the scanning speed, respectively.

It can be seen that a multiplicity of combinations of laser power pulses and scanning speed lead to a dynamic range of linewidths (from 100 to 660 nm). The smallest later sizes of voxel d_{xy} and d_{z} are about 120 nm and 600 nm, respectively, and an elongation factor ($d_{\mathrm{z}}/d_{\mathrm{xy}} = 2.8$) can be inferred. The best parameters for laser fabrication of 3D microstructures are chosen such as $\upsilon = 10$ μm/s and $P_{laser} = 3$ mW, respectively. These values provide an idea to the resolution achievable by DLW, using a high focusing optical system for recording in a polymerizable photoresist SZ2080 by nonlinear TPA. The width of these lines is less than the length of the used recording wavelength, it is verified that the resolution of the sub-diffraction limit has been obtained. Subsequently, it is useful and important to know the exposure conditions to realize the architecture consisting the elements with high spatial resolution, for example, helix-based metasurfaces.

5.4 Conclusions

- Towards to realization of helix-based metasurfaces for infrared spectral range, DLW technique was chosen as one of the modern approaches for the realization of 3D dielectric micro/ nanostructures in the photosensitive material with a high spatial resolution close to 100 nm based on TPA process.
- Capabilities of DLW technique for realization of 3D volumetric and planar microstructures has been demonstrated.
- By producing the straight twisted rods in the exposure matrix, the sought-for parameters of exposure conditions of $\upsilon = 10$ μm/s and $P_{laser} = 3$ mW for fabrication with 120 nm feature size were found. Thus, the 3D dielectric microstructure can be realized with high spatial resolution using DLW approach.

Chapter 6

Entire metal absorbing metasurfaces fabricated by DLW technique

Using DLW maskless technique, entire metal absorbing metasurfaces for mid-infrared spectral range have been fabricated. Designs and fabrication of all-metal absorbers based on 3D vertically standing split-ring resonators operating in the wavelength range of $4.5-9.2$ μm has been reported (Section 6.1). Entire metal chiral-plate helix-based absorbers in the spectral range of $6-11$ μm using a combination of high-resolution DLW lithography and simple metallization process have been designed and successfully fabricated (Section 6.2). Towards to realization of the off-resonance transparent absorbing metasurfaces for infrared spectral range, all-metal compensated absorbers based on RH and LH single-turn helical resonators have been realized (Section 6.3). All realized absorbing metasurfaces exhibit non-transparent behavior in the mid-infrared spectral range.

6.1 VSRR-based absorber

Optical metamaterials allow the realization of extraordinary optical properties, such as a negative refraction index [1] and a near-zero [190] via the subwavelength artificial structuring of inclusions. In this respect, vertical split-ring resonators (VSRRs) are especially interesting as building blocks for metamaterials at optical frequencies, since they exhibit a direct interaction with the magnetic field of incident waves and enable a broad range of optical functionalities [191]. For example, a perfect resonant absorption in structures composed of weakly absorbing metals and dielectrics can be achieved. Perfect absorber (PA) metamaterials based on VSRRs are attractive for sensitivity enhancement in optical detectors and as thermal emitters, radiative coolers, and so forth [142, 192]. However, the realization of three-dimensional (3D) VSRRs at optical frequencies is a challenge, since it requires the 3D structuring of inclusions with a submicron spatial resolution. High-resolution planar structuring based on electron-beam lithography and thin-film deposition, etching, and lift-off are poorly suited for 3D geometries; therefore, simpler architectures consisting of a patterned metallic film separated from a metallic ground plane by a thin dielectric film [193, 194], have been mostly explored. Although planar architectures may also enable an artificial magnetism at optical frequencies [68], their magnetic response is mainly driven by the electric field of incident waves, whereas the direct interaction with an optical magnetic field is weak. Also, planar PAs exhibit poor heat dissipation [195, 196], which may lead to thermal damage to intense absorption. An all-metallic architecture consisting of VSRRs placed above the ground plane would be free of these disadvantages [197, 198], but its realization by planar fabrication methods, such as electron-beam

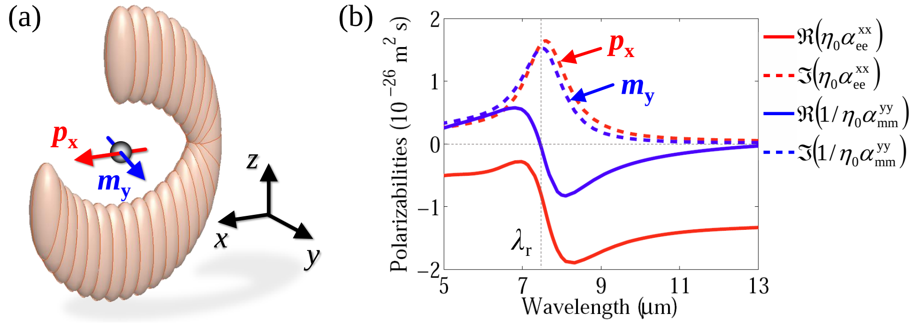

Figure 6.1: (a) Schematic image of a VSRR with radius $r = 0.5$ μm of built from multiple overlapping ellipsoidal voxels (volume elements) with minor and major diameters denoted by $w_{\mathrm{xy}} = 0.25$ μm and $w_{\mathrm{z}} = 0.7$ μm. (b) Normalized individual polarisabilities of an VSRR made of Au at the resonance wavelength of $\lambda_{\mathrm{r}} = 7.5$ μm.

double exposure [199], multilayer electroplating [200], stress-driven assembly [201], and others [202] is difficult and not widely accessible.

Using numerical simulation based on finite element method (FEM) VSRR-based structures were designed taking into account fabrication the features of laser lithography. Figure 6.1(a) shows a single vertically standing split-ring resonator with non-uniformly elongated elliptical cross-sectional shape in accordance with fabrication by DLW technique. Since the focal region of the writing laser beam is elongated along the z-axis direction, the shape of resonator fabricated by translating the focus also has an elongated elliptical cross section. VSRR induces at the resonance a magnetic ($\mathbf{m}$) and perpendicular to it an electric ($\mathbf{p}$) dipole moments by excitation of incident electric ($\mathbf{E}_{\mathrm{inc}}$) or magnetic ($\mathbf{H}_{\mathrm{inc}}$) fields, respectively. Therefore, the induced dipole moments can be described in the following form

$$\begin{aligned} \mathbf{p}_{\mathrm{x}} = \alpha_{\mathrm{ee}}^{\mathrm{xx}} \cdot \mathbf{E}_{\mathrm{inc}}, \qquad \mathbf{m}_{\mathrm{x}} = 0, \\ \mathbf{p}_{\mathrm{y}} = 0, \qquad \mathbf{m}_{\mathrm{y}} = \alpha_{\mathrm{mm}}^{\mathrm{yy}} \cdot \mathbf{H}_{\mathrm{inc}}, \end{aligned} \tag{6.1}$$

Figure 6.1(b) shows individual polarizabilities of VSRR normalized to the impedance of free-space η_0. As one can see, the resonance is similar to the plasmonic resonance at an interface of metal (negative real part of the polarizability), although in this case there is no surface-wave excitation. A number of losses in the VSRR-based layer are chosen so that the value of the total input impedance is equal to η_0 at the resonance. Therefore, only oscillation of magnetic moment gives the response at such configuration of VSRRs in the array.

We have performed the fast prototyping of functional VSRR-based PA structures for an IR wavelength range, using direct laser writing (DLW) [169, 203] and plasma sputtering techniques. DLW is a maskless, high-resolution laser lithography exploiting the nonlinear exposure of a photoresist by tightly focused ultrashort laser pulses that can deliver nearly arbitrary 3D self-supporting structures with a submicron spatial resolution [204]. Dielectric templates prepared by DLW can be metallized to produce metallic optical elements, such as broadband polarization converters [75, 77], PA structures [1-B, 2-B, 2-A]

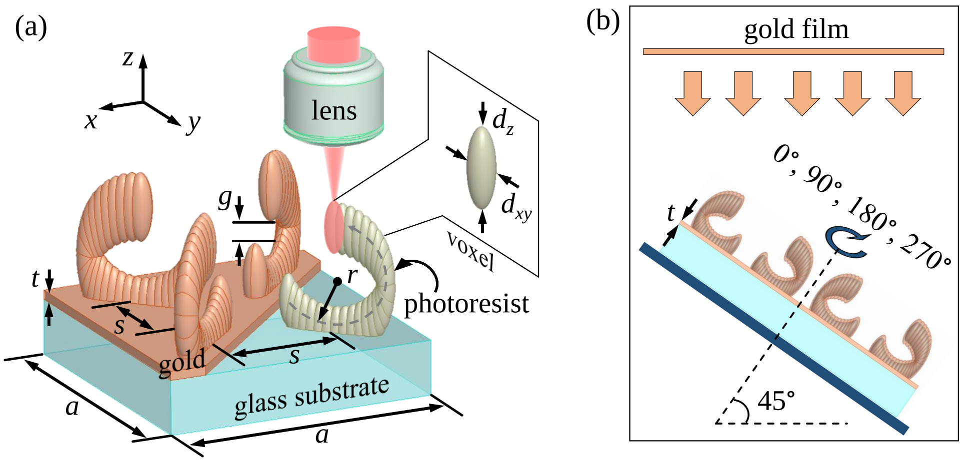

Figure 6.2: (a) Structural parameters and schematic image of VSRR unit cell before and after metallization, inset illustrates size and shape of single exposed voxel. (b) Metalization by plasma sputtering using tilted sample mounting and four-step deposition at several azimuthal rotation angles.

and photonic crystals [205, 206]. Although realization of VSRR structures using this approach was reported earlier [207] to demonstrate the 3D structuring capability, no optical characterization was performed. Here, we report the theoretical optimization, fabrication, and optical characteristics of all metallic PA structures based on the VSRR geometry. The structures were theoretically optimized for an IR wavelength range of $7-9\,\mu$m, fabricated using DLW and gold sputtering techniques and characterized optically by reflectance spectroscopy. In accordance with expectations, resonant absorbance bands with peak absorbances of $A \geq 0.85$ were confirmed experimentally.

Various VSRR-based metamaterial architectures are known from the literature [200–202]. The unit cell of our VSRR structure intended for DLW-assisted fabrication is shown schematically in Figure 6.2(a). Four identical split rings having a radius r and a gap width g are arranged on the corners of a square with a side length s, with gaps oriented towards the center of a square unit cell with a side length a. Four split rings form two crossed pairs of antiparallel magnetic resonators, ensuring a polarization-invariant optical response dominated by coupling between the VSRRs and the magnetic field of incident waves at normal incidence.

The fabrication of dielectric rings by DLW is most convenient using a laser beam focused along the z-axis. The exposed volume elements (voxels) in the photoresist are ellipsoids elongated in the z-axis direction, with the minor and major diameters d_{xy} and d_z shown in the inset of Figure 6.2(a). VSRRs are drawn by the elongated focus arms with a cross-sectional shape varying between a circle (radius r_{xy}) and an ellipse (radii r_{xy} and r_z). During DLW, an oil immersion lens with the numerical aperture (NA) of 1.35 was used, and the writing beam was focused in the photoresist through the glass substrate (opposite focusing direction is indicated in Figure 6.2(a) for the sake of clarity). The beam was derived from a Ti: Sapphire oscillator (MaiTai, Spectra Physics, pulse length 120 fs, central wavelength 800 nm, repetition rate 80 MHz). Drawing was facilitated by

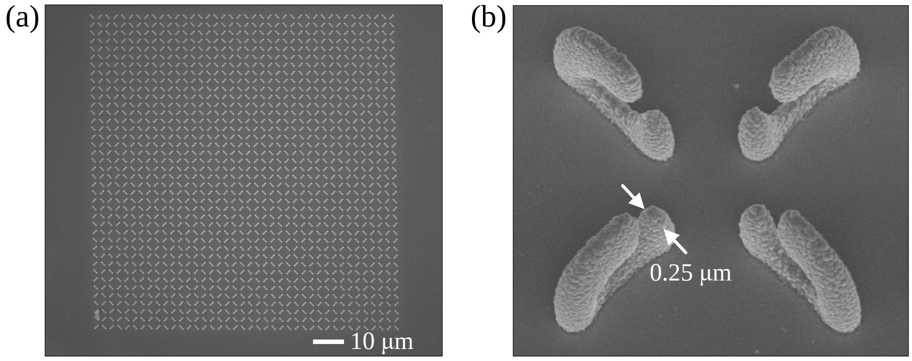

Figure 6.3: (a) SEM image of sample and (b) SEM images of unit cell for PA VSRR-based structure with minimum feature size of 0.25 μm, respectively.

translating the sample using a high-precision three-axis piezo-stage (Physik Instrumente P-563.3CD). Under these conditions, the resulting voxel elongation is $d_z/d_{xy} \approx 2.8$ [206]. The high spatial resolution of DLW was controlled by maintaining the optical exposure dose slightly above the photopolymerization threshold in the photoresist. Typically, an average power 3 mW at a translation speed of $10-50$ μm/s was sufficient for obtaining the lateral resolution $d_{xy} \approx 100$ nm. The initial material for DLW was the negative-tone Zr-containing hybrid organic-inorganic photoresist SZ2080 with 0.4% 4,4'-Bis(diethylamino) benzophenone added as photo initiator [188]. The samples were prepared by drop-casting the photoresist on microscope cover glass substrates (Matsunami) and subsequently drying them on a hot plate. The exposed samples were developed in 1-propanol: isopropanol (50:50) solution, rinsed with ethanol and dried in a critical point drying apparatus (JEOL JCPD-5) to minimize the destructive action of surface tension forces.

Dielectric and metalized features are emphasized in Figure 6.2(b). Metalization by gold was performed using a plasma sputtering machine (Quick Coater SC-701 MkII). To achieve conformal coating and minimize shadowing, the substrates were mounted on a tilted stage and sputtering was repeated four times at different angles of rotation about their normal (0, 90, 180, and 270°) as illustrated schematically in Figure 6.1(b). The thickness of the metal film was controlled by adjusting the sputtering time and was typical $t = 30-50$ nm, which is larger than the skin depth in Au, $t_s \approx 12\,\mathrm{nm}$ at $\lambda \approx 5-10\,\mu$m.

In order to optimize the PA performance, suitable combinations of the parameters r, g, s, a, d_{xy} and d_z were found using numerical simulations based on the electromagnetic finite element method (FEM). Optical properties of the metal used were also taken into account. Our DLW technique enables a spatial resolution corresponding to the voxel diameters $d_{xy} \approx 100$ nm and $d_z \approx 280$ nm. Using these parameters as the lowest limit for the thickness of the split-ring arms, the approximate resonance wavelength infeasible PA structures made of various noble metals was estimated to be in the range of $5-10$ μm. Further optimization for this spectral range was performed using optical properties of gold because gold was found to perform well during the simulations, and metalization by gold sputtering was readily induced.

The samples were inspected by Scanning Electron Microscope (SEM) (JSM-7800F,

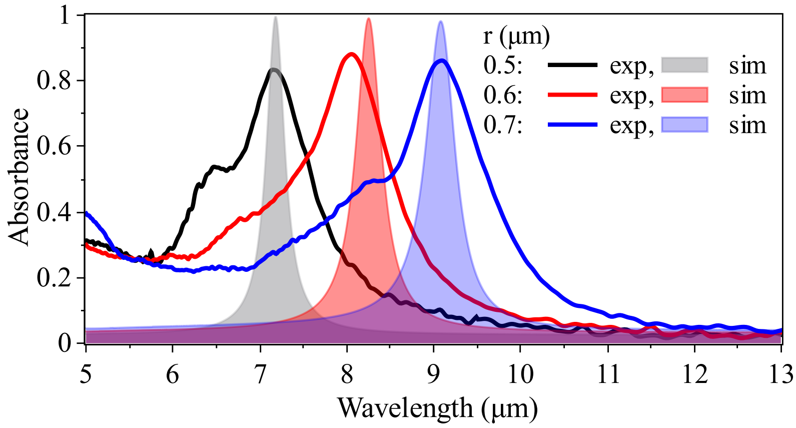

Figure 6.4: A comparison between simulated (shaded area) and measured (solid lines) absorbance spectra of three VSRR structures having different split-ring radius of $r = 0.5, 0.6$, and $0.7\,\mu$m but identical parameters $a = 3\,\mu$m, $s = 1.5\,\mu$m, $g = 0.3\,\mu$m, $d_{\mathrm{xy}} = 0.25\ \mu$m, $d_{\mathrm{z}} = 0.7\ \mu$m, $t = 0.1\ \mu$m.

JEOL). SEM images in Figures 6.3(a) and (b) show large-scale and detailed images of the VSRR structure having $r = 0.5\,\mu$m, respectively. Typically, the samples had an area of $50 \times 50\ \mu\mathrm{m}^2$, which is sufficient for optical characterization. Good long-range order and relatively uniform shapes of individual split rings can be seen. Arms of the metalized rings have the lateral diameter $d_{\mathrm{xy}} = 0.25\,\mu$m. Assuming that approximate thickness of gold film is 50 nm, uncoated features had diameter $d_{\mathrm{xy}} \approx 150\,$nm, which indicates the high resolution of DLW structuring. Slight irregularities, such as the lateral deformation of the rings and their grainy surface can also be observed. Deformations usually occur owing to the loss of rinse liquid (ethanol) and the accompanying photoresist shrinkage during drying and become more pronounced with decreasing thickness or photoresist features. Because of this circumstance, we did not attempt to increase the spatial resolution of DLW even further during this study. The nanoscale surface roughness of the gold film originates from sputtering. These irregularities lead to random scatterings and nonabsorptive losses that cannot be easily incorporated into the simulations.

Numerically simulated absorbance spectra of three optimized VSRR structures having different radius r values of split rings are shown in Figure 6.4(a). Other geometrical parameters are given in the caption. All structures exhibit the perfect absorption $A = 1$ at resonance, which can be tuned in the wavelength range of $\lambda_{\mathrm{res}} = 7.2 - 9.2\,\mu$m by increasing the radii of the split rings from $r = 0.5\,\mu$m to $0.7\,\mu$m. From the well-known relationship between the resonance wavelength λ_{res} and geometrical length of the resonator $L = \lambda_{\mathrm{res}}/2 = 2\pi r - g$, their effective radii $r \approx 0.5, 0.6$ and $0.7\,\mu$m, which are close to the design values, can be estimated. Hence, the nonuniformity of the split rings due to voxel elongation does not affect the resonance wavelength significantly. We have also performed the analysis of the simulated current density distribution at resonance, which confirmed that surface current predominantly flows and absorptive losses occur in the split rings.

Experimental absorbance spectra were estimated from reflectance spectra measured using a Fourier-Transform Infrared (FT-IR) spectrometer coupled with an IR microscope

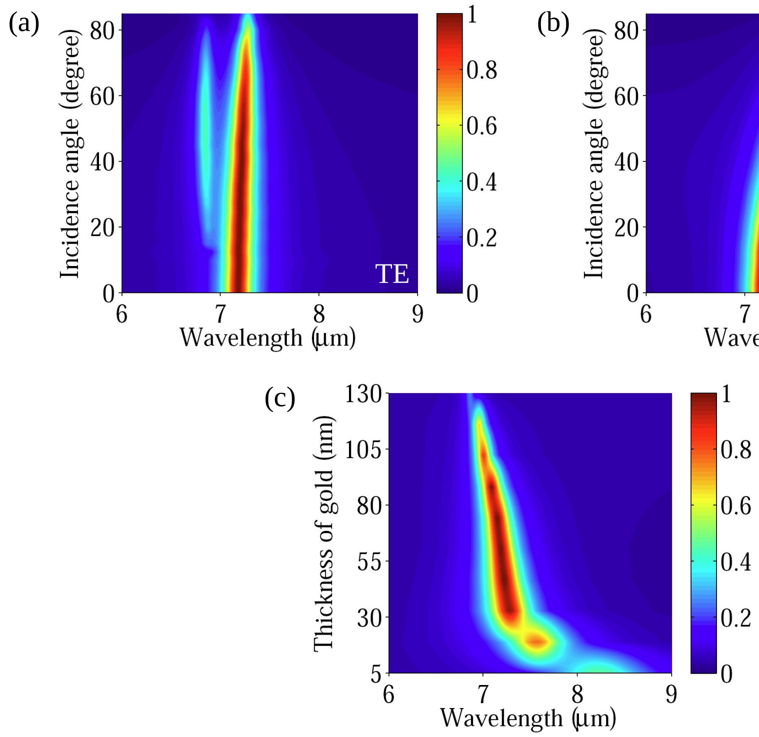

Figure 6.5: Simulated absorbance spectra as a function of incidence angle for (a) TE, (b) TM polarizations, and (c) the thickness of gold for a VSRR-based architecture.

(JASCO FT=IR-6300, IRT-7000). Since the transmittance of the ground plane is $T = 0$ at all wavelengths, the absorbance $A(\lambda) = 1 - R(\lambda)$, where $R(\lambda)$ is the reflectance. The experimental absorbances of three samples, whose design parameters are close to those of the three simulated samples discussed earlier, are presented in Figure 6.4 for a direct comparison with simulations. As can be seen, the simulated peaks spectrally match the measured peaks, but are spectrally narrower and exhibit higher peak absorbances. The spectral broadening of experimental peaks most likely represents an inhomogeneous broadening due to structural irregularities pointed out earlier. Another potential reason for the observed differences is the construction of the reflective Cassegrainian objective lens in the IR microscope. The Cassegrainian lens blocks normally incident rays but transmits oblique rays with incidence angles distributed around the average 30° value corresponding to NA=0.5 of the objective.

PA resonance is relatively insensitive to the incidence angle. This is illustrated in Figures 6.5(a,b), which shows calculated absorbance in the structure with $r = 0.5\,\mu$m as a function of incidence angle for transverse electric (TE) and transverse magnetic (TM) linear polarizations. TE resonance retains its spectral position and magnitude $A > 0.9$ for incidence angles up to 50°. In the range of $20 - 80°$, an additional weaker peak develops at shorter wavelengths due to excitation of parasitic dipoles in the structure at oblique incidence. For TM resonance, nearly stable spectral position and absorbance $A > 0.8$ are retained for up to 30°. These results allow expecting polarization and incidence angle-averaged performance with absorbance $A \geq 0.8$ for incidence angles up to 30°.

The calculated absorption spectra as a function of sputtered gold thickness dependence

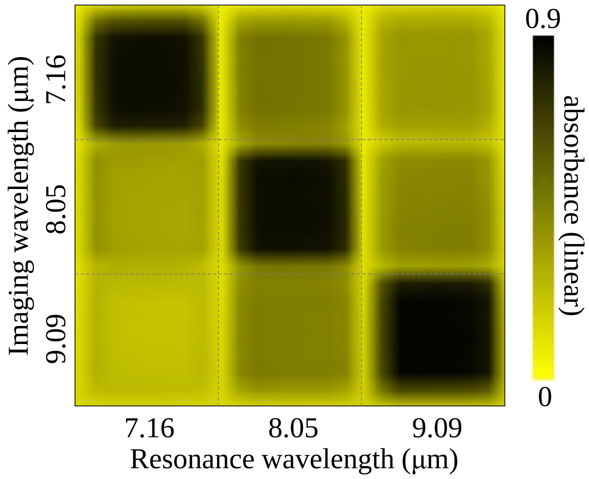

Figure 6.6: 2D spatial absorbance maps of three VSRR samples with different resonance wavelengths $\lambda_\mathrm{r} = 7.16, 8.05$, and $9.09\,\mu$m (left to right columns) scanned at their corresponding resonance wavelengths (top to bottom rows).

of VSRR-based architecture are illustrated in Figure 6.5(c). As one can see, absorbance peaks reach maximum values in the range of thickness gold about $30 - 90$ nm. A further increase in the thickness leads to a significant decrease in the radius in the resonator, thereby destroying the magnetic dipole moment and all electromagnetic response in the whole structure.

According to simulated data from Figure 6.5(a,b), the oblique incidence leads to spectral shifts and the appearance of a weaker secondary resonance at shorter wavelengths (for TE polarization). Indeed, such peaks can be seen emerging in the experimental data shown in Figure 6.4. Despite the broadening, experimental absorbance peaks exhibit a high magnitude of $A \geq 0.85$ in all investigated structures. Hence, the qualitative agreement between the experimental and simulation data is good.

The flexibility of the DLW-based approach allows one to combine multiple structures having different resonant wavelengths into a spectrally selective absorber matrix. Figure 6.6 illustrates spectral and spatial selectivities obtained by comparing 2D absorbance maps of a row of VSRR samples having the resonant wavelengths λ_res = 7.16, 8.05, and $9.09\,\mu$m. At each resonance spatial map of reflectance was measured by scanning narrow spatial window of $(5 \times 5)\,\mu\mathrm{m}^2$ over the samples. The resulting absorbance images are shown in the figure. Dark areas correspond to high-absorbance regions. As can be seen, the absorbing region systematically shifts with resonance wavelength. In each row, off-resonant regions are somewhat brighter, which indicates their higher reflectance due to the ground plane. Nevertheless, reflectance is still lower than that of a bare gold film owing to scattering by the split rings.

6.1.1 Mesh-type VSRR-based absorber

The above data suggest that increasing r and L produces red-shift of PA resonance. However, this trend continues only to the point when neighboring split rings begin to be in

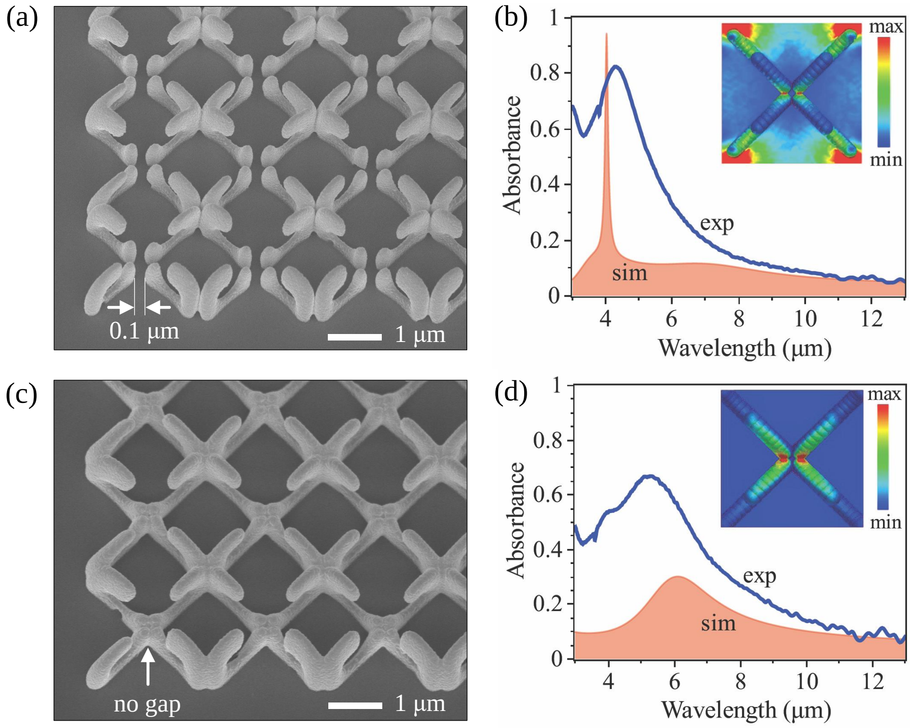

Figure 6.7: (a) SEM image of a closely-packed VSRR sample. (b) Comparison between experimental and simulated absorbance spectra. (c) SEM image of a merged VSRR sample. (d) Comparison between its experimental and simulated absorbance spectra. In (b,d), simulations are performed for normally-incident plane waves, insets show top-view of 3D surface current distribution in the unit cell at resonance.

contact with each other. The accompanying marked change in the metamaterial architecture and its optical response are illustrated in Figures 6.7(a) and (b), respectively. When split rings come into contact with each other, but their gap regions are still isolated from the nearest neighbors, four-ring clusters are formed. In our case, this condition was achieved by increasing the split-ring radius to $r = 0.8\,\mu$m, while other parameters (s, a, t, and g) were the same as in Figure 6.2(a). As can be seen from Figure 6.7(a), inter-cluster gaps are about 100 nm. Experimental absorbance shown in Figure 6.7(b) exhibits a strong peak with $A > 0.8$ at $\lambda_{\text{res}} = 4.3\,\mu$m, i.e., blue-shift by approximately 40% was achieved by increasing the split-ring radius.

The numerically simulated spectrum shown in the same plot qualitatively reproduces the observed resonance wavelength and peak absorbance. The main peak is somewhat narrower than the experimental one, most likely due to inhomogeneous broadening not accounted for by the simulations, and rides on a wider peak centered near the $6 - 7\,\mu$m wavelength, which cannot be resolved in the experimental spectrum owing to the broadening.

The physical origin of both peaks can be understood by considering the corresponding spatial modes. The simulated distribution of the induced surface current in the unit cell at resonance is shown in the inset of Figure 6.7(b). The detailed analysis of the calculated 3D current distribution did not reveal physically significant circular currents in the split rings, which indicates a low magnetic coupling in the structure and allows us to describe the modes in a top-view representation. Hence, clustering achievable via the increase in the split-ring radius r markedly transforms the perfect absorption resonance from predominantly magnetic to predominantly electric, simultaneously producing a strong blue shift without the loss of absorbance. At the main resonance ($\lambda_{\text{res}} = 4.3\ \mu\text{m}$), the strongest current flow occurs on the ground plane in the gaps between clusters (corresponding to the corners of the calculated maps). A weaker spatial peak can also be seen at the center of the map where a deep corrugation (pit) is formed by the surfaces of four split rings.

To gain further insight, we have also examined a merged structure (Figure 6.7(c)) in which gaps between clusters were completely eliminated by increasing the split-ring radius to $r = 0.9$. The experimental absorbance spectrum of the merged 3D meshlike structure shown in Figure 6.7(d) exhibits only the broad peak with amplitude $A > 0.65$ centered at $\lambda_{\text{res}} = 6\,\mu\text{m}$. Surface current distribution of this mode, shown in the inset, exhibits only the weaker spatial peak in the vicinity of the pit. Hence, in the clustered structures dominant resonant modes are concentrated in the gaps between the clusters on the ground plane, whereas in the merged structures they are concentrated in the pits between split-rings $\approx r$ above the ground plane. These observations suggest that clustering achievable via increasing the split-ring radius r drastically transforms the perfect absorption resonance from predominantly magnetic to predominantly electric nature, simultaneously producing a strong blue-shift without loss of absorbance. Transition from clustered to merged structure transforms lateral position and height at which electric field modes are localized.

The considerable absorbance, albeit at longer wavelengths, is retained in the merged VSRR structures, with experimental absorbance (Figure 6.7(d)) being even higher than predicted by simulations. This difference is most likely caused by non-absorptive losses, such as randomness and diffraction in densely-packed structures, which scatter reflected signal away from the angular acceptance the range of microscope lens used for sample imaging during spectral measurements.

In conclusion, we have fabricated functional all-metallic metamaterial absorbers based on VSRR architecture for IR spectral range using DLW technique as the main structuring tool. Our PAs operate in the wavelength range of $4.5 - 9.2\,\mu\text{m}$, can be spectrally tuned by changing their geometric parameters, and exhibit polarization and incidence angle-invariant absorbance $A \geq 0.85$ for incidence angles up to 30°. Practical advantages of VSRR-based PAs, such as tunable magnetic or electric resonances and good heat dissipation may be exploited in IR optical detectors, thermal emitters and radiative coolers. DLW-based fabrication method can be regarded as a facile tool enabling exploration and applications of optical metamaterials having geometries more complex than would be achievable via traditional planar fabrication.

6.2 Chiral-plate helix-based absorber

Chiral optical metamaterials attract strong interest due to their giant circular dichroism controllable via artificial structuring [208]. Most straightforward way to realize them is by assembling periodic 2D or 3D arrays of chiral particles, such as helices, but in practice, this is difficult, especially at optical frequencies, where 3D fabrication with high spatial resolution is required in order to properly downscale unit cell of the structure.

Although helical metamaterials also exhibit other exotic optical properties, such as optical activity, polarization transformations, and perfect absorption phenomenon, their deeper experimental exploration at optical frequencies is impeded by difficult fabrication. Thin resonant PAs with structurally-tunable optical properties can be realized using electromagnetic metamaterials [197]. Helix-based metasurface PAs operating at infra-red (IR) or near-infrared (NIR) frequencies would be attractive candidates for use in narrow-band thermal absorbers, emitters, energy converters, and applications relying on enhanced IR absorption [143, 209]. Unlike planar metamaterial PAs consisting of densely packed patterned metallic and dielectric films [142, 192, 196, 210], helix-based PAs have sparse all-metallic 3D architecture, which is permeable to liquid or gaseous substances and is more stable against thermal damage due to better heat dissipation [68]. Moreover, helix-based PAs do not require a metallic substrate for their operation and thus in principle may enable PAs which are transparent at off-resonant frequencies.

Helix-based PA structure consisting of macroscopic periodically arranged single-turn helices was proposed and successfully realized for radio-frequency (RF) spectral range [5-A] by mechanical machining. Tuning the PA resonance towards IR or NIR frequencies would require scaling the unit cell down to micrometers or by $\sim 10^4$ times, which is a challenging task. Therefore helix-based PAs for optical frequencies have been mainly explored via numerical simulations [211, 212]. In this study, we address tunability of the helix-based PA architecture to IR frequencies experimentally, via the use of DLW technique and simple metallization process. We demonstrate that IR spectral range is indeed accessible using this relatively simple and accessible route.

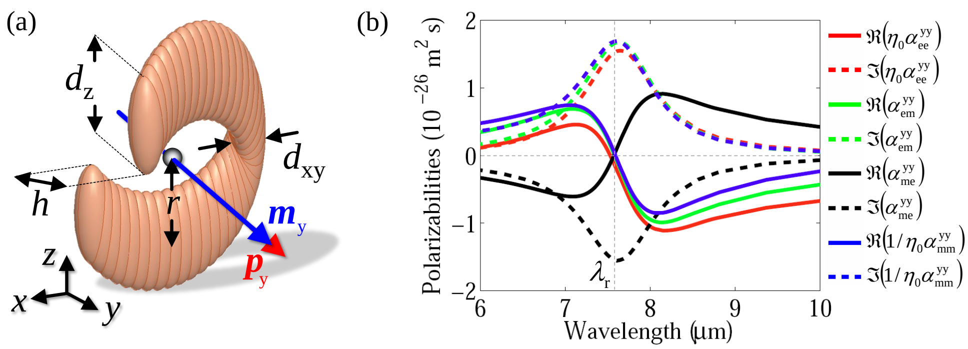

Figure 6.8: (a) A schematic image and parameters of a single-turn helix built from multiple overlapping ellipsoidal voxels (volume elements) with minor and major diameters denoted by d_{xy} and d_z, respectively. (b) Normalized axial individual polarizabilities of an single-turn helix made of Au, with optimized structural parameters $r = 0.6$ μm, $h = 0.72$ μm, $d_{xy} = 0.24$ μm, and $d_z = 0.67$ μm in the vicinity of the resonance.

6.2.1 Numerical simulation

Figure 6.8(a) depicts the typical shape of the down-scaled helical resonator to fabrication by DLW technique. Similar to VSSR design, single-turn helix was built from multiple overlapping ellipsoidal voxels where the features of laser fabrication were taken into account. Therefore, realistic shape of the helix was included, and coating by Au film with thickness $t = 80$ nm exceeding the skin-depth at IR wavelengths was assumed. Figure 6.8(b) shows axial components of polarizability tensors for the single-turn metallic helix. By optimization of structural parameters the axial components of polarizability tensors were balanced ($\alpha_{\rm ee}^{yy} = 1/\eta_0^2 \alpha_{\rm mm}^{yy}$) in accordance with conditions of free-space impedance matching. As seen, polarizabilities become purely imaginary (zero real part) at the resonance wavelength of 7.8 μm.

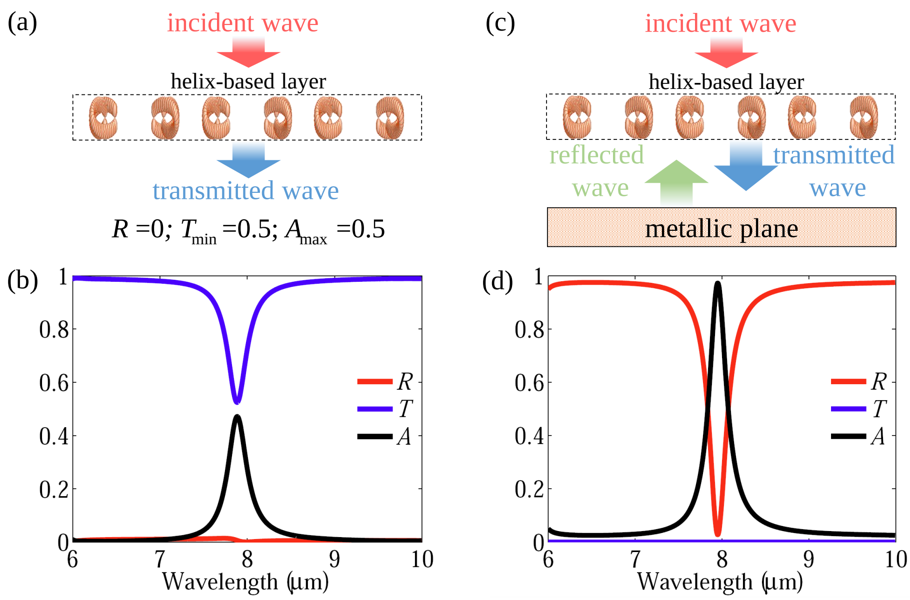

Figure 6.9: (a) A schematic image of working principle of chiral metasurface based on balanced single-turn helices without a ground plane. (b) Simulated reflection, transmission, and absorption spectra under the linearly polarized excitation. (c) Working principle of chiral metasurface with ground plane. (d) Simulated spectra of chiral-plate PA at normal incidence.

Figure 6.9 shows a schematic image of working principle chiral metasurface based on balanced single-turn helices without a ground plane. Simulated reflection, transmission, and absorption spectra under the linearly polarized excitation were shown in Figure 6.9(b). As one can see, low reflectivity $R < 0.02$ is obtained in the broad spectral range $6-10\,\mu$m. Nevertheless, this structure can absorb only half of the incident energy $A \approx 0.5$ at the resonance wavelength of $7.9\,\mu$m, since an electromagnetic coupling of helices must be compensated ($\alpha_{\rm em}^{\rm yy} = -\alpha_{\rm me}^{\rm yy} = 0$) as there are no ground plane [132]. On the other hand, such architecture with the ground plane (see Figure 6.9(a)) and essentially non-compensated electromagnetic coupling exhibit high absorbance $A = 0.97$ at the resonance $7.9\,\mu$m as shown in Figure 6.9(d). Adding ground plane in helix-based metasurface would result in $T = 0$, but $R = 0$ (leading to $A = 1$) would be retained despite high reflectivity of the substrate, since half of the transmitted energy lost through structure and due to the presence of ground plane is reflected, leading to their absorption in the helix-based metasurface. Further, the architecture can be referred to as a "chiral-plate" PA [213] due to dominant chirality in metasurface.

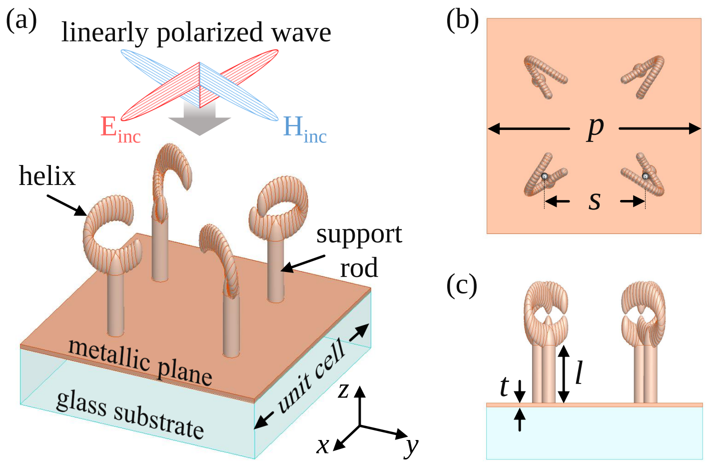

Figure 6.10: Unit cell of helix-based chiral-plate PA metasurface at perspective (a), top (b) and front (c) views, respectively. Metasurface is excited by linearly polarized incident wave.

In order to mechanically support helices above glass substrate on which photoresist is deposited prior to DLW, vertical rods of length l were added between the helices separated by a distance $s = 4\,\mu$m with array period of $p = 6\,\mu$m and the substrate as shown in Figure 6.10. Furthermore, non-uniformly elongated elliptical cross-sectional shape of helix arms fabricated by DLW has to be taken into account during design and numerical simulations. Figure 6.11(a) shows the simulated distribution of Poynting vector of a helix-based PA unit cell. The fields are shown on a cross-sectional plane parallel to the incident light direction, at the resonant wavelength of 7 μm. As can be seen, power is predominantly localized in the helix layer, thus illustrating that excitation of the helical resonators is dominant, while ground plane plays a role only a mirror.

Figures 6.11(b) and (c) show current density distribution at resonance for excitation by normally incident TE and TM polarized waves. Strictly speaking, the distinction between TE and TM polarizations is lost at normal incidence, but here we use these definitions to define two mutually orthogonal linear polarization states. Figure 6.11(b,c) illustrates selective excitation of different helix pairs by TE and TM excitation. For intermediate polarization orientation contribution from both pairs leads to polarization-invariant response. We emphasize, that current density is highest in the inner circumference of the helices, which therefore defines length and resonance frequency of individual resonators in the structure.

Figures 6.12(a) and (b) show simulated absorbance of the PA structure as a function of incidence angle for transverse electric (TE) and transverse magnetic (TM) linearly polarized waves, respectively. One can see that resonance with nearly-invariant central wavelength and absorbance $A > 0.8$ is retained for up to 30° for TE polarization. For

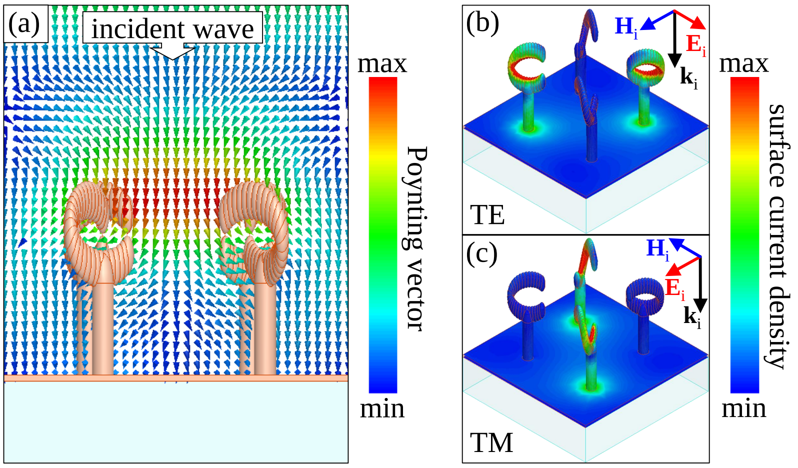

Figure 6.11: (a) Numerically simulated field distribution of Poynting vector in the unit cell at the resonance wavelength of 7 μm (side view). Distribution of surface current density at TE (b) and TM (c) polarizations of incident light at the resonance, respectively.

TM polarization, $A > 0.95$ is retained for up to 45°, except for $\approx 10°$, where sudden drop is observed. Anisotropic and non-monotonous angular dependence of absorbance can be tentatively ascribed to parasitic dipole moments which evolve at the slanted incidence and violate the conditions of perfect absorption. Nevertheless, one can estimate polarization and incidence angle-averaged absorbance $A \geq 0.7$ for incidence angles up to 30°. Notice, that high-absorbance can be still also obtained at certain wavelengths for incidence angles as high as 80° for both polarizations.

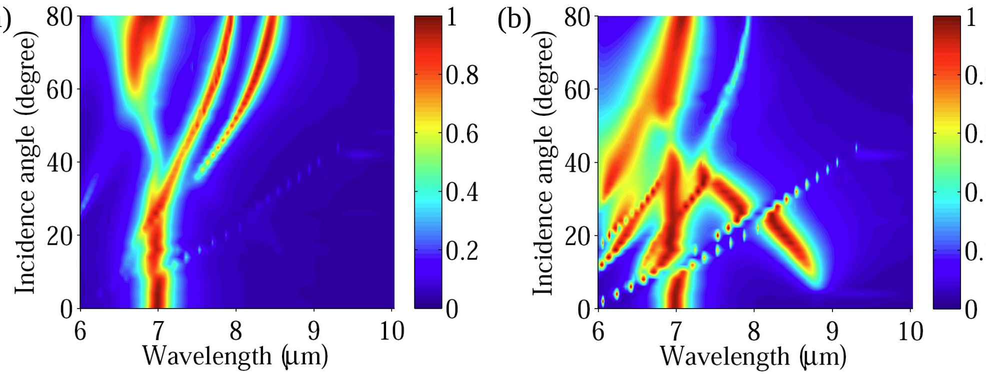

Figure 6.12: Simulated absorbance spectra as a function of incidence angle of a chiral-plate PA structure for TE (a) and TM (b) polarizations, respectively.

6.2.2 Experimental verification

Experimental details regarding sample fabrication, processing and characterization are described previously. Implementation of DLW lithography technique was used to fabricate dielectric templates of PA structures with subsequent metallization by gold sputtering. Figures 6.13(a) shows SEM images of the chiral-plate PA architectures. The square of the sample is about (60×60) μm^2 with a total time of fabrication process about five hours. SEM image of unit cell chiral-plate structure can be seen in Figure 6.13(b). An

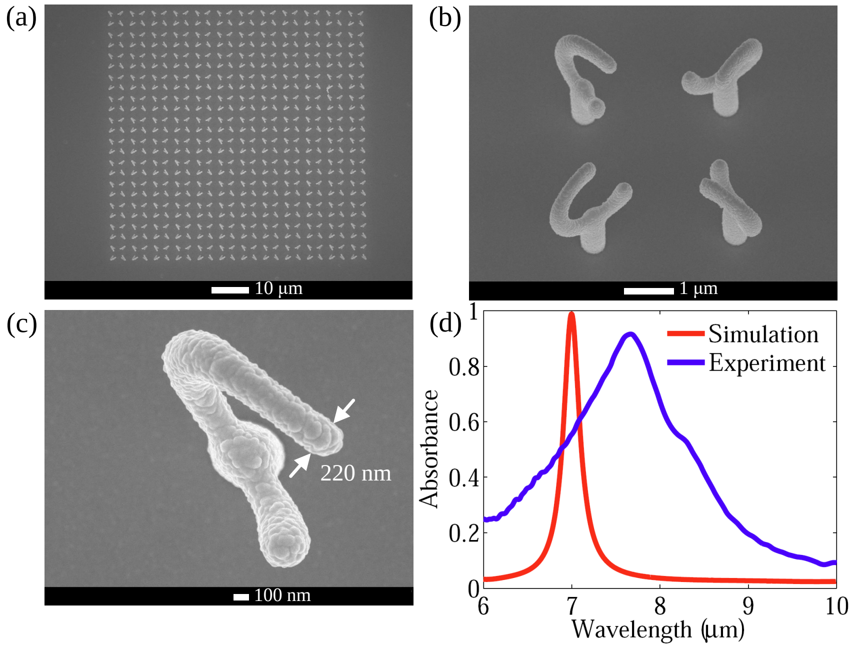

Figure 6.13: SEM images of helix-based PA architecture (a) and its unit cell (b), and (c) enlarged view of single-turn helix, respectively. (d) Simulated and measured reflection spectra at nominally normal incidence.

enlarged view of the single-turn helix are presented in Figure 6.13(c). Design parameters of these structures were obtained and optimized using numerical simulations. Their actual parameters estimated from SEM are slightly different due to shrinkage and deformation of photoresist templates. It should be noted that lateral width of the helix arms is about 220 nm, while a thickness of the metallic film is about $70 - 90$ nm, which shows that photoresist templates were fabricated with sub-150 nm spatial resolution. Obviously, the samples exhibit high uniformity, although some disorder and nanoscale surface roughness can be seen. Thus, the design of 3D metallic PA architecture with optimized structural parameters was successfully realized using DLW technique.

Optical properties of the samples were characterized using reflectance measurement by FT-IR spectrometer. Reflectivity spectrum of the bare metallic surface was used as a reference, and the sample reflectivity was normalized to the reference. Figure 6.13(d) shows simulated and measured absorption spectra of helix-based PA architecture in IR spectral range. A resonant absorption band centered near the 7.7 μm wavelength with peak absorbance of 90% can be clearly seen in the spectra. It can be concluded that our theoretical predictions described before demonstration of a good qualitative agreement with measured data. The resonance band is broader than predicted, most likely due to inhomogeneous broadening resulting from random variations of the spiral parameters in the characterized area. Also, homogeneous broadening due to a higher than expected loss in the sputtered gold film may contribute to these observations. Nevertheless, these deficiencies do not diminish our main achievement, namely realization of helix-based nearly perfect absorber structures for IR spectral range.

The spectral tunability of PA structures is illustrated by the data shown in Figure 6.14.

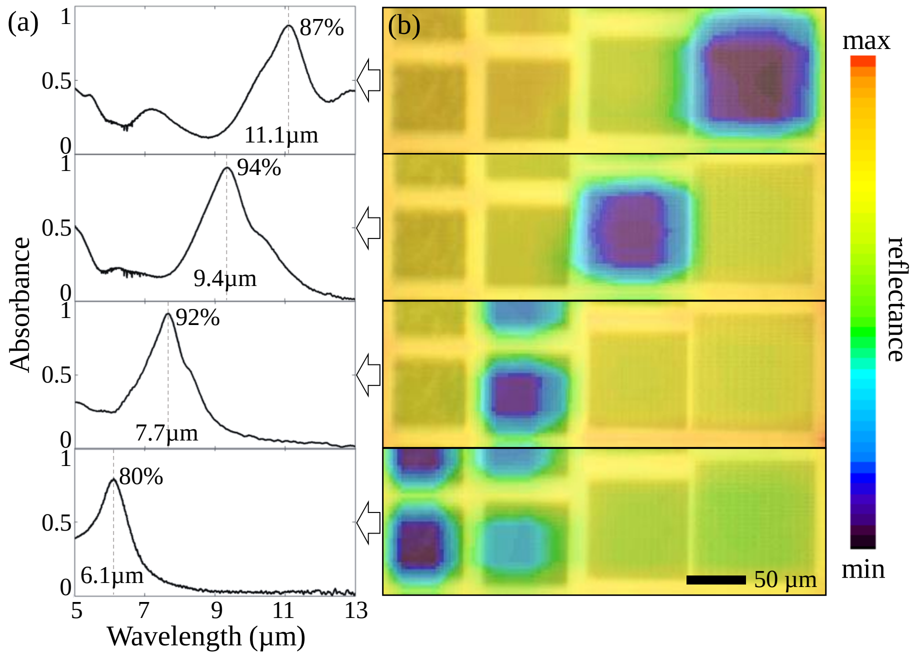

Figure 6.14: Spectral tunability of chiral-plate PA structures: (a) Reflectance spectra of several samples with unit cell size proportionally downscaled by the factor of 1.2 (from top to bottom), (b) 2D reflectivity maps of the samples measured at their respective resonance wavelengths of $\lambda_{\text{res}} = 11.1, 9.4, 7.7$, and $6.1\,\mu$m.

For these studies, chiral-plate PA structures with unit cell parameters proportionally scaled down by the factor of 1.2 were fabricated on the same substrate. The substrate was subsequently investigated by an imaging FTIR spectrometer. Experimental absorbance spectra of the structures shown in Figure 6.14(a) illustrate tunability of PA resonance in the $6 - 11\,\mu$m wavelength range. 2D reflectivity maps taken at the resonant wavelength of each structure are shown in Figure 6.14(b). In the images, blue, low-brightness areas correspond to low reflectivity and a high absorbance at the resonance. On the other hand, yellow, high brightness areas indicate high off-resonance reflectance and low absorbance, since helix layer is nearly transparent to radiation, and does not block the radiation incident on the sample or reflected from the metallic substrate. Reflectance in the gaps separating different PA structures does not increase to the reflectivity of the gold film because size of the imaged area during the scanning, $(5 \times 5)\,\mu\text{m}^2$, is comparable to the gap width, and scanning in the gaps areas always integrates some loss due to residual scattering from the neighboring PA areas. Scanning further away from the PA (not shown) results in a high reflectivity of the bare gold film. The overall correlation between spectra and images shown in Figures 6.14(a,b) is good. PA structures may be regarded as spectrally-sensitive pixels, from which larger arrays can be composed of imaging-related applications. Such arrays can be relatively easily prepared using DLW-assisted fabrication.

Interestingly, spectral tuning of PA resonance can be also achieved without scaling the helices, but by changing length l of the vertical rods instead. This possibility is illustrated in Figures 6.15(a,b). According to simulations, the resonance wavelength of chiral-plate PA structures increases linearly with l as is demonstrated in Figure 6.15(a).

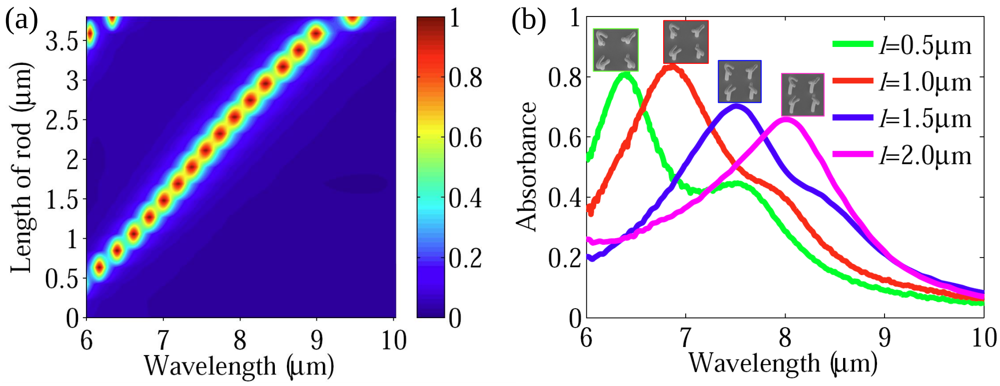

Figure 6.15: (a) Simulated PA absorbance spectra versus the length of supporting vertical rods l. (b) Experimental absorbance spectra of samples with different l.

Notice that available tuning range in this case ($\lambda \approx 6 - 9\,\mu$m) is nearly as broad as that achievable by scaling the unit cell. At shortest wavelengths examined ($\lambda_{\text{res}} \approx 6\,\mu$m), the second line of peaks can be seen emerging in the top-left corner of the plot when l is increased by an amount of $\Delta l \approx \lambda_{\text{res}}/2$. This behavior suggests the formation of planar waveguide modes confined between the helix layer and the substrate. By changing the rod length l, the thickness of the waveguide (or size of an extended 3D unit cell) is scaled, leading to proportional spectral shifts. Hence, in this case interactions between the metallic substrate and the helix layer are important. Numerical simulations represent qualitatively the experimental data shown in Figure 6.15(b), where absorbance spectra of several PA samples having different rod lengths are shown. As one can see, practical tuning of PA resonance within the $6-8\,\mu$m wavelength range is possible. Since fabrication of vertical rods involves simple single-axis translation, adjusting the rod length provides a highly practical alternative way to fine-tune the PA structures.

Summarizing, in our samples, polarization-invariant absorption $A \geq 0.8$ within IR wavelength range of $6 - 11\,\mu$m at normal incidence, and $A \geq 0.7$ at incidence angles up to 30° was estimated. These results clearly illustrate the possibility to the downscale unit cell of helix-based absorbers thus tuning the PA resonance to IR spectral range.

6.3 Compensated helix-based absorber

As was mentioned previously, helix-based PA metasurface can operate without a metallic substrate, thus enabling high off-resonance optical transparency and low reflectivity. However, in our structures, where the metallic substrate is always present we can test the PA architecture that design closely similar to the low-reflection PA metasurface described and tested for RF band (see Chapter 4.2). Here, the design with the ground plane will be called as "compensated PA" architecture comprised of both LH and RH helices can be simplified to a single 4-helix group. Chirality of the helices and condition of total absorption require an equal number of inclusion with LH and RH helices, which is done by alternating four-helix groups as shown in Figure 6.16. Hence, the unit cell of compensated helix-based PA structure, in general, comprises four groups separated by a distance p. It

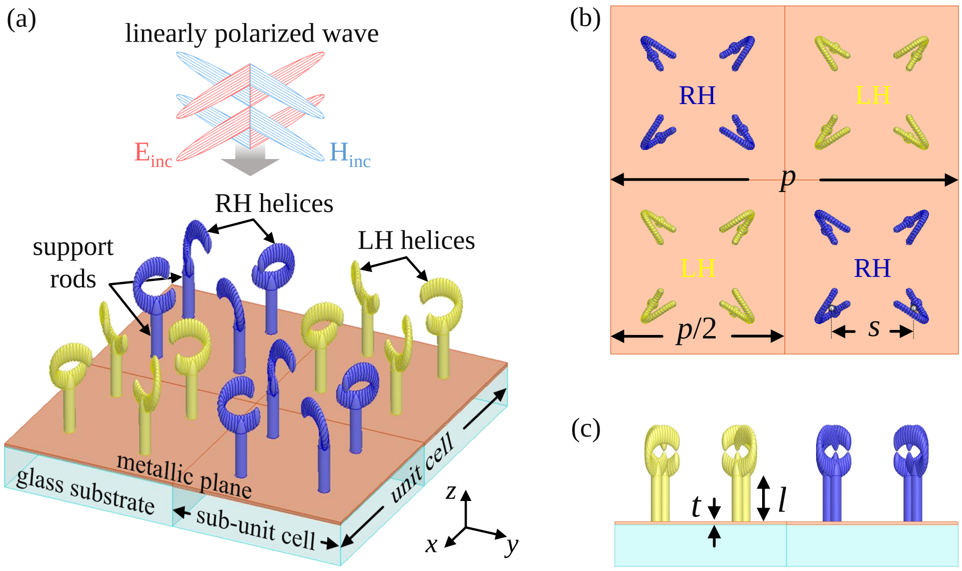

Figure 6.16: Unit cell of helix-based chiral-plate PA metasurface at perspective (a), top (b) and front (c) views, respectively. Structural parameters are $p = 12$ μm, $s = 4$ μm, $l = 1.6$ μm, and $t = 0.1$ μm.

worth notice, that resonators comprising the unit cell must exhibit a moderate amount of dissipative loss without drastic reduction of their quality factor.

The DLW fabrication was performed with exposing conditions described in Section 5.3. An oil-immersion objective with numerical aperture $NA = 1.35$ was used to achieve tight focusing and ensure maximum possible spatial resolution of DLW, while exposure conditions were controlled by adjusting the DLW speed and laser beam intensity of 10 μm/s and 5 mW, respectively. The initial material for DLW was a negative-tone Zr-containing hybrid organic-inorganic photoresist SZ2080. The fabricated samples were subsequently coated with a thin gold film and thus converted from a dielectric to a metallic substrate.

Figure 6.17(a) shows SEM image of all-metal compensated PA architecture with the square of a sample of (60×60) μm^2. SEM image of the unit cell consists of helices with different handedness can be seen in Figure 6.17(b). An enlarged view of the single-turn helix with a wire thickness of the Au-coated helices is about 240 nm, which suggests that minimum feature size of the original dielectric helices was close to 150 nm. Structural parameters of samples are close to the optimized parameters that were calculated using numerical simulation.

Figure 6.17(d) shows absorption spectra obtained by numerical simulation and in the experiment for the mid-IR spectral range. A resonant absorption band centered near the 7.7 μm wavelength with peak absorbance of 90% can be clearly seen in the spectra. As can be seen, the absorbance of the compensated PA exhibits an additional weaker peak near $\lambda_{\mathrm{res}} = 9.2\,\mu$m. This peak was also observed in other compensated PA samples and is qualitatively reproduced by simulations (a narrow spike near $\lambda_{\mathrm{res}} = 7.8\,\mu$m in simulation). Detailed analysis of the simulated field patterns associated with this peak has revealed that its physical origin can be associated with electromagnetic coupling between groups of four helices of different handedness, in contrast to the main resonance which can be

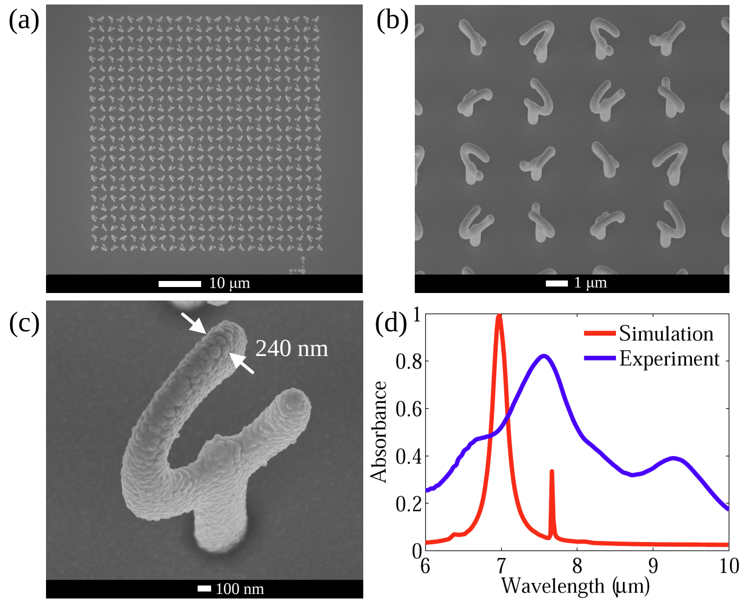

Figure 6.17: SEM images of helix-based PA architecture (a), its unit cell (b) consisting of 4 sub-unit cells, and enlarged view (c) of single-turn helix. (d) Simulated and measured reflection spectra at nominally normal incidence.

associated with coupling between helices within groups of the same handedness. Therefore, the secondary peak can be also associated with compensated chirality of the PA structure. This data also allows expecting that performance of a compensated PA structure would be nearly the same (except for off-resonance transparency) once the metallic substrate is removed.

The angular stability of compensated PA architecture at 25°, 50°, and 75° incidence angles for TE and TM polarizations of incident waves is shown in Figure 6.18. Shading area marked in gray means the range of the main resonance. It is seen that for TE and TM polarized waves illuminating helix-based architecture it absorbs above 95% nearly to the main resonance at 7 μm only at the incidence angles of 25° and 50°, respectively. However, the resonant shift can be seen clearly for TE and TM polarizations. Such not stable angular dependence of absorption level can be explained by the 3D complex geometry of structure where it might appear additional parasitic dipole moments that do not correspond to analytical statements and conditions of total absorption.

Strictly speaking, a simple metallization process used in this study has inadvertently created reflecting metallic plane behind the helices, thus preventing a demonstration of genuinely transparent PA, this circumstance prevents the realization of transparent PA metasurface in this study. Nevertheless, our data suggest that dominant contribution to absorption in our structures comes from helical resonators, with substrate playing a minor role. Also, other attractive characteristics related to the sparse all-metallic architecture of the helix layer (e.g., environmental permeability, heat exchange capability) are retained. Thus, transparent PAs can be realized in future via the use of more advanced, spatially selective metallization methods.

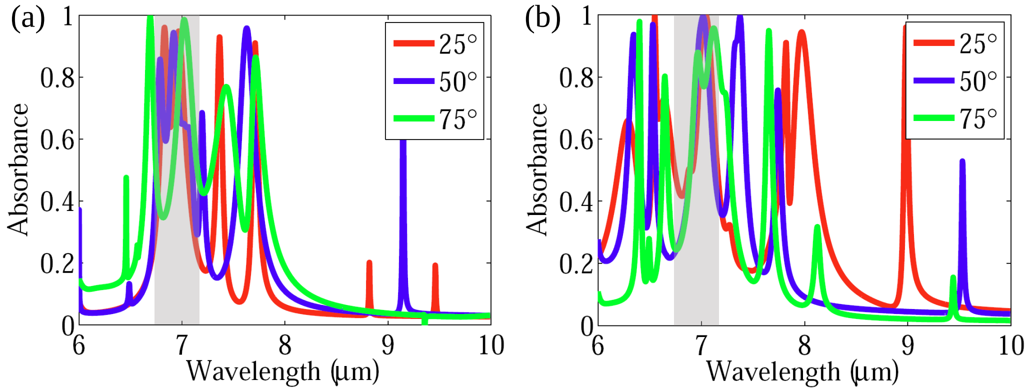

Figure 6.18: Simulated absorbance spectra of a compensated PA structure at oblique incidence of 25°, 50°, and 75° for TE (a) and TM (b) polarizations, respectively. The main resonant band at normal incidence is marked by the shading area.

6.4 Conclusions

- Design and fabrication of entire metal absorbing metasurfaces based on VSRR for IR wavelength range of $7-9\,\mu$m have been reported. Using numerical simulation based on FEM and DLW technique with subsequent gold sputtering process, fabricated samples exhibit peak absorbances of $A \geq 0.85$ at the resonances in accordance. Moreover, VSRR-based absorbers exhibit polarization and incidence angle-invariant operation for incidence angles up to 30°. Thus, maskless DLW approach was successfully used for the realization of functional 3D absorbing metasurfaces with high spatial resolution for IR spectral range.

- Using DLW technique with subsequent non-selective metallization, chiral plate helix-based PA architectures for IR spectral range were fabricated. Samples were found to exhibit polarization-invariant resonant absorption over 90% at the IR wavelengths of $6-11$ μm in qualitative agreement with numerical simulation. Moreover, the possibility of tunability the resonant absorption to different wavelengths by usage of two simple way: by proportional scalability all structural parameters and by variation of supporting rods was experimentally demonstrated. This result illustrates the possibility to use a DLW-assisted fast prototyping for the fabrication of PA structures and can be easily extended to other metasurfaces operating similar frequencies.

- Towards to the realization of the off-resonance transparent helix-based metasurfaces compensated absorbing metasurfaces based on RH and LH helical resonators in the IR spectral range have been realized. The designed absorber is very similar to the off-resonance transparent helix-based absorbers based on single-turn metallic helices for microwave range (see Section 4.2). However, compensated helix-based PA has a metallic substrate that makes its non-transparent for radiation. Nevertheless, compensated helix-based structures exhibit polarization-invariant absorption peak of 90% near the resonant wavelength of 7.8 μm. As a result, both numerically simulated and experimental data are in a good agreement.

Chapter 7

Off-resonance transparent helix-based metasurfaces for IR range

Using numerical simulation, functional off-resonance transparent helix-based metasurfaces for IR spectral range has been designed. Also, laser ablation process for removing a metallic substrate from entire metal architectures to make them off-resonance transparent was carried out (Section 7.1). Conventional and our designs of helix-based twist polarizer metasurfaces have been reported as well as some experimental performance for the conventional design was carried out (Section 7.2). High efficient (over 89%) off-resonance transparent cross-polarized reflector based on silver single-turn helical resonators in the IR spectral range has been designed (Section 7.3). In accordance with numerical simulation, frequency-selective helix-based absorber has been designed for practical realization by DLW technique, where selective metallization is required (Section 7.4). All proposed functional off-resonance transparent helix-based designs can be fabricated using DLW technique.

7.1 Laser ablation process

Previously, we have realized entire metal helix-based PA metasurfaces that have a non-transparent metallic substrate the IR spectral range. Here we are focused on the realization of off-resonance transparent metasurfaces based on the helical resonators using DLW technique. However, our approach for the implementation of helix-based metasurfaces does not allow us to reach this goal since we have used a non-selective metallization (plasma sputtering) of the dielectric templates. To solve this issue, it requires either a selective metallization of the helices or the removal of the metallic substrate from the metasurface after the sputtering. Here, we will try to perform the second way by usage of the laser ablation process.

Laser ablation is the process of removing material from a solid (or occasionally liquid) surface by irradiating it with a laser beam. With a small laser beam, the material is heated by the absorbed laser energy and evaporates or sublimes. With a high laser flux, the material, as a rule, is converted to plasma. Usually, laser ablation refers to the removal of material by a pulsed laser, but it is possible to smooth the material with a laser beam of a continuous wave if the laser intensity is sufficiently high. The depth at which the laser energy is absorbed and, consequently, the amount of material removed by a single laser pulse depends on the optical properties of the material, the laser wavelength, and the pulse duration. The total mass removed from the target by the laser pulse is usually called the ablation rate. Such features of laser radiation as laser beam scanning speed and

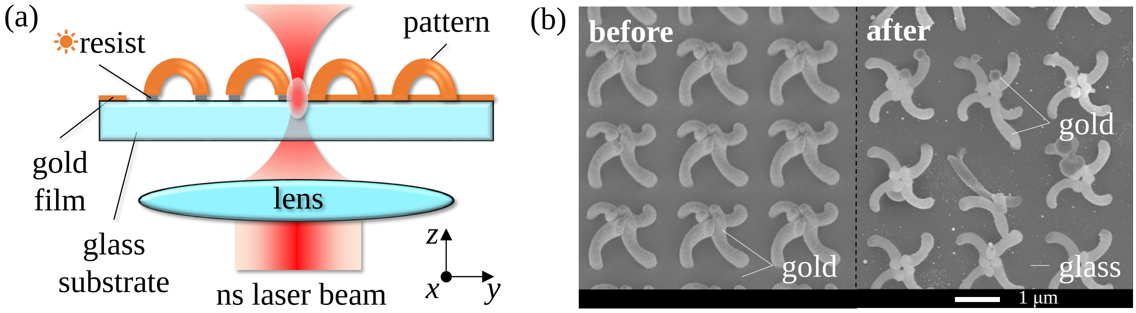

Figure 7.1: (a) A schematic illustration of removing metallic thin substrate by laser ablation process. (b) SEM images of 3D metallic pattern before and after laser ablation process.

scanning line coverage can significantly affect the ablation process [214].

The Nanosecond Pulsed Laser Ablation (PLA) has been extensively studied as an effective method for the complete mask-less direct patterning due to precisely localized ablation for a variety of materials. However, for materials with a high thermal diffusivity, such as metals, a pattern without damage can only be achieved by femtosecond pulses [215]. It was done due to the precisely localized ablation for a wide variety of materials and the completely controllable data and the maskless nature of the PLA process. Laser pulses can vary over a very wide range of duration (milliseconds to femtoseconds) and fluxes and can be precisely controlled. Therefore, this makes laser ablation very valuable for this research as well as it has become an accessible technique in applications such as circuit patterning and trimming, mask repair, and so on.

Figure 7.1(a) illustrates the ablation process by usage of a nanosecond pulsed laser (Nd:YAG) with an excited wavelength of $\lambda = 1.03$ μm, a temporal pulse length of 0.6 ns, repetition rate of 1 kHz and average power 10 mW, respectively. Using the DLW lithography, we fabricated a dielectric template consists of periodically arranged elements with arbitrary shape with a resolution of about 200 nm. Next, we metalized the dielectric template by gold using the plasma sputtering, where the thickness of gold film was about 100 nm. Thus, a full metallic periodic microstructure was fabricated, which in principle is similar to a metasurface based on helical inclusions. In order to carefully remove the metallic film from the structure while keeping the inclusions metallic, we have focused on 100 nm gold film and sublimates it by controlling the irradiative laser power, scanning speed and position of the focused beam along z-axis.

Figure 7.1(b) shows the obtained results where SEM images have been presented for comparison of the periodic pattern before and after laser ablation by nanosecond pulsed laser. It can be seen that the gold film was successfully removed from the entire metallic pattern. However, the presence of deformations and even destructions of inclusions is obvious, as well as spherical nanoparticles formation by melting gold are noticeable. In general, the laser ablation process can be used as a method for removing a metallic film from a microstructure, but this requires more careful control of the laser beam and the choice of the optimal exposure conditions during the laser ablation.

7.2 Twist polarizers

Optical metamaterials based on 3D helical inclusions have been actively investigated in the IR spectral range to obtain circular polarization [75, 77, 208, 216, 217], perfect absorption [78, 211, 212], and an wavefront manipulation [218]. Usually, helix-based architectures consist of vertically standing helices (the helix axis is perpendicular to the plane of architecture) and the incident wave propagates along the helix axis. Such design consisting of vertically standing helices we will call "conventional design" since it was already used in many studies with this arrangement of helices in the metamaterial. Before we have investigated only the helix-based metasurfaces in which the axes of the helices were directed only in the plane of the metasurface, we can say that the helices lie on the plane, as it were. In this section, we will demonstrate two types of twist polarizers (conventional and our designs) for obtaining a cross-polarized transmission in the MIR spectral range.

7.2.1 Conventional design

Here we report a conventional design for the realization of twist polarizer (TP) based on 3D vertically standing helical resonators that relatively easy to fabricate using laser lithography for IR spectral range. It is worth mentioning once again that TP is a device that rotates the polarization of a linearly polarized input wave by 90° upon transmission, can be realized using chiral metamaterials. Physical insight into the working principle of helix-based TP can be gained from Sections 3.3 and 4.1, where we have demonstrated a realization of TP metasurfaces based on single- and double-turn helical resonators in microwave frequency range.

Figure 7.2(a) shows the design of conventional TP structure consists of vertically standing metallic helices that are located on CaF_2 substrate (transparent in the considered range). The unit cell of polarizer consists of four right-handed single-turn helices that are rotated by 90° respectively to their initial positions that they have a phase shift. One aspect of this spiral structure is an elliptic cross-section of helices (voxel) corresponds to laser fabrication features that will be described below. We consider the case when electromagnetic plane waves with TE or TM polarizations are normally incident along z-axis on helix-based architecture. Figures 7.2(b) and (c) show the unit cell of TP with indicated structural parameters at the top and front views, respectively. All structural parameters were optimized owing to simulation based on FEM. Notice, that thickness of TP structure does not exceed $\lambda_{\mathrm{res}}/3$ and period of $p = 2$ μm, therefore, in fact, it is a helix-based metasurface.

The main optical characteristics of TP are the co-polarized transmission (T_{co}) and cross-polarized transmission (T_{cr}), respectively. Cross-polarized transmittance indicates that the polarization of the transmitted waves has changed exactly by $\pi/2$ with respect to the initial polarization of the incident waves. It was computed by exciting the two lowest cut-off modes of the Floquet port, which have TE and TM polarization respectively. Figure 7.3(a) demonstrates the simulated cross-transmittance of investigated TP structure in IR spectral range. The helices were assumed to consist of different noble metals by

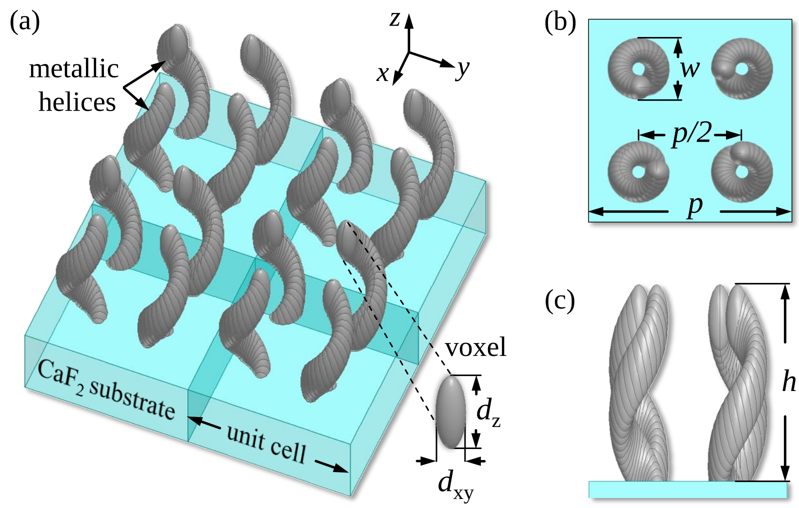

Figure 7.2: (a) Conventional design of helix-based twist polarizer consisting of metallic single-turn helices. Top (b) and front (c) views of the unit cell of the polarizer, respectively. Structural parameters are follows: $d_{xy} = 0.25$ μm, $d_z = 0.7$ μm, $w = 0.6$ μm, $h = 1.8$ μm, $p = 2$ μm.

taking into account dielectric properties and their dispersion [219, 220]. As one can see, silver helix-based metasurface demonstrates more high resonant cross-transmittance of light over 85% at the resonance of $\lambda_{res} = 5.6$ μm in comparison with other metals, therefore, this structure is preferable to obtain high-efficient TP device.

For completeness, optical properties of TP metasurface based on silver helices in the comparable range are shown in Figure 7.3(b). As one can see that maximum value of absorbance does not exceed of 12% in the IR spectral range of $4 - 7$ μm. Meanwhile, TP structure exhibits low reflectance (less than 7%) in the comparable wavelength range. This offers the advantage to create a multifrequency resonant multilayer design that allows operating in the broadband wavelengths range (see Section 3.5).

The efficiency of the polarization transformation can be characterized by the angle of rotation of the polarization and the ellipticity of the transmitted waves. It is worth mentioning once again that a pure transformation into a cross-polarized transmitted wave corresponds to the case when the ellipticity is zero, while the polarization plane has a rotation angle of 90°. When the ellipticity is equal 45°, the transmitted wave has a circular polarization. Figure 7.3(c) demonstrates the simulated polarization angle and ellipticity of cross-polarized transmitted waves, respectively. At the resonant wavelength of 5.6 μm, the polarization angle and ellipticity reach values about 89.9° and 3.5°, respectively. Optical isolation between co- and cross-polarized transmitted waves is about 99.8% at the resonance. This represents a high degree of spectral purity of the helix-based metasurface in mid-IR spectral range.

Figure 7.3(d) shows the cross-polarized transmission versus the oblique incident angles for TE and TM polarizations of incident light, respectively. Due the to the symmetric arrangement of helices in metasurface, cross-transmittance does not depend on the polarization of incident light till 20°. In addition, the optical properties only slightly change at

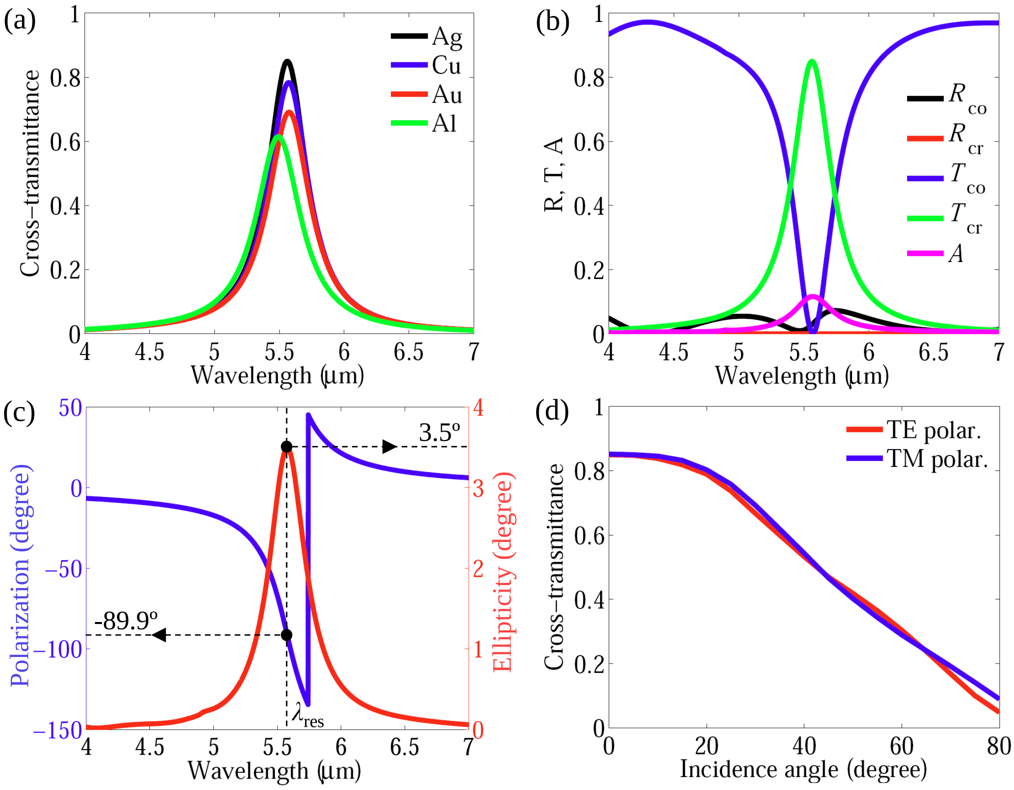

Figure 7.3: (a) Simulated spectrum of cross-polarization transmission coefficient for different metals. (b) Reflectance, transmittance and absorbance respect to the polarization state versus the wavelength at normal incidence. (c) Polarization angle and ellipticity responses of cross-transmitted waves for the proposed TP design. (d) Cross-polarized transmission at oblique incidence for TE and TM polarizations, respectively.

oblique incidence for both polarizations. The distribution of electric field, surface current density, and vector Poynting in the unit cell at the resonant wavelength of 5.6 μm can be seen from Figure 7.4. As seen from the distribution of electric field, helix-based TP rotates the polarization of transmitted waves by 90° respects to the polarization of incident waves. As in a case with balanced helices, the vertically standing helices has a maximum of the surface current density at the middle part of the helical curve that corresponds to the excitation of the main resonant mode ($\lambda_{res}/2$). The distribution of vector Poynting shows us that energy almost concentrates in the helical layer, especially, at the middle where the maximum of extinction field occurs. Therefore, helical layer rotates the polarization of transmitted waves by 90° at the main resonant mode.

Aiming to fabricate proposed TP design we used DLW technique that capable of fabricating 3D spiral-based architecture with sub-micrometer spatial resolution in the underlying material. However, fabrication of conventional helix-based TP metasurface with high spatial resolution presents a significant practical challenge on the path towards realization of off-resonance transparent devices for optical spectral range, since it requires selective metallization of helix-based dielectric pattern fabricated by pulsed femtosecond laser writing.

At first, we have fabricated full-metal helix-based TP metasurface using DLW and all

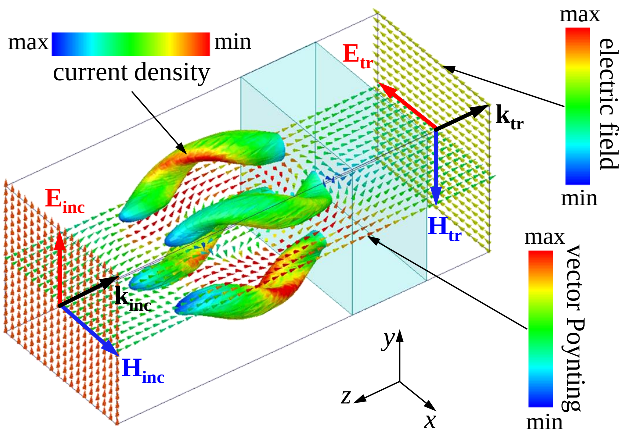

Figure 7.4: Distribution of electric field, surface current density, and vector Poynting in the unit cell of conventional TP at the resonance wavelength of 5.6 μm.

steps of post-processing that are described in Sections 5.3 and 6.1. It should be mentioned that we have used gold sputtering to metalize the dielectric template, since as for the first trial of realization using in additional laser ablation process described in above. The fabricated structure by DLW technique before laser ablation can be seen in Figure 7.5(a). The helices have a slightly different size and phase shift respectively to each other because of difficulties in controlling PZT stage in z-positions and the shrinkage effects too. Nevertheless, the helix-based structure with a high spatial resolution about 150 nm was fabricated. The structural parameters of samples are close to optimized by numerical simulation in accordance with expectations.

Next, we have applied the pulsed nanosecond laser ablation to carefully remove a metallic film from helix-based TP metasurface. Figure 7.5(b) shows SEM image of TP after laser ablation process. As can be seen, by carefully controlling of laser energy and focus point position, the metallic film about 100 nm was successfully removed from the helix-based structure. However, the gold particles still can be seen and some scratches that might influence for the operation of TP design. Moreover, during the measuring process by FTIR spectrometer, we have not found any resonance response from the structure. Probably, it comes from some inconsistencies during the fabrication process or laser ablation. Therefore, such issue is still under consideration.

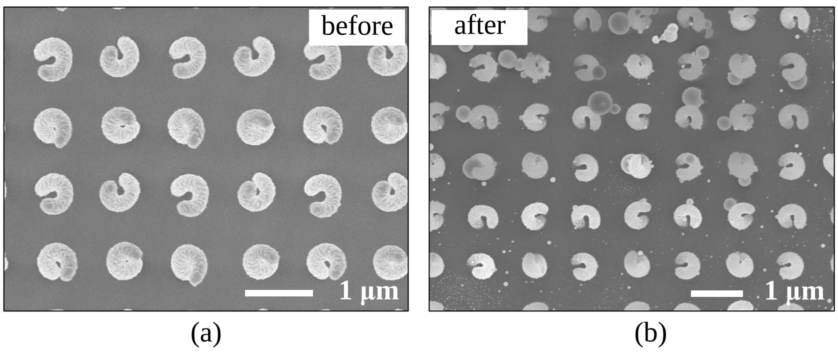

Figure 7.5: SEM images of helix-based TP samples before (a) and after (b) laser ablation process, respectively.

Unfortunately, to achieve truly TP design need to apply better approach for the realization that is still in the development process or a new design of TP metasurface. Nevertheless, the obtained results demonstrate potential efficiency and possibilities realization by femtosecond laser lithography of 3D spiral-based metamaterial TP in IR spectral range.

To conclude, using FEM numerical simulations the design of TP structure and their optical properties were proposed and tested, respectively. Worth noting that conventional helix-based architecture exhibits polarization-insensitive transformation electromagnetic waves from TE to TM polarizations and vise verse within a considerable range. The amplitude of transmitted light with cross polarization over 85% at the resonant wavelength of 5.6 μm has been obtained. Such high performance and broadband low reflectance may be advantageous in some applications.

7.2.2 Our design

Herein, we report another design of the off-resonance transparent helix-based twist polarizer. Previously, the helix-based design of TP metasurface has been proposed and successfully tested in the microwave frequency range (see Section 4.1). However, the realization of such TP in optical range is a non-trivial task since it requires not only downscaling of the size of the structure and takes into account the properties of materials but even other design with structural elements are suitable for manufacturing technology. However, tuning such structures towards optical range by straightforward scaling down of their structural elements into micro or nanoscale leads to drastic loss of conversion efficiency and increases ellipticity of the converted waves. Thus, practical realization of efficient TPs for optical spectral range requires taking into consideration many aspects during the capable fabrication technique. DLW approach and laser ablation are capable of the realization of the metallic off-resonance transparent helix-based microstructure. Thus, we designed off-resonance transparent TP metasurface based on single-turn helices similar to a case considered in Section 4.1.

First of all, we designed a helix-based TP metasurface using numerical simulation and taking into account the features of laser fabrication. Figure 7.6(a) illustrates the design of TP metasurface based on metallic helical resonators with optimized structural parameters. The unit cell consists four silver single-turn helices with a period of $p = 3.47$ μm and half of period inter-element distance. To be realistic in the simulation design, metallic helices contact with CaF_2 substrate through a photoresistive stem with length of $l = 0.2$ μm (the initial form and cross-section $d_{\mathrm{xy}} = 0.25$ μm of helices according to DLW results), which is obtained by removing the metallic film from the sample by laser ablation process. Consequently, metallic helices are over a transparent substrate, since the photoresist does not contribute to the performance of the TP metasurface. The thickness of the structure is about $\lambda_{\mathrm{res}}/5$ and unit cell size of $\lambda_{\mathrm{res}}/3$. The structural parameters of helical resonators such as pitch ($h = 0.72$ μm), radius ($r = 0.6$ μm), and cross section of voxel ($d_{\mathrm{xy}} = 0.25$ μm and $d_{\mathrm{z}} = 0.7$ μm) are the same as in Figure 6.8 with balanced polarizabilities, respectively. The TP metasurface is excited by an incident plane wave propagating along z-axis.

Figure 7.6(b) shows simulated co- and cross-polarized reflection, transmission, and

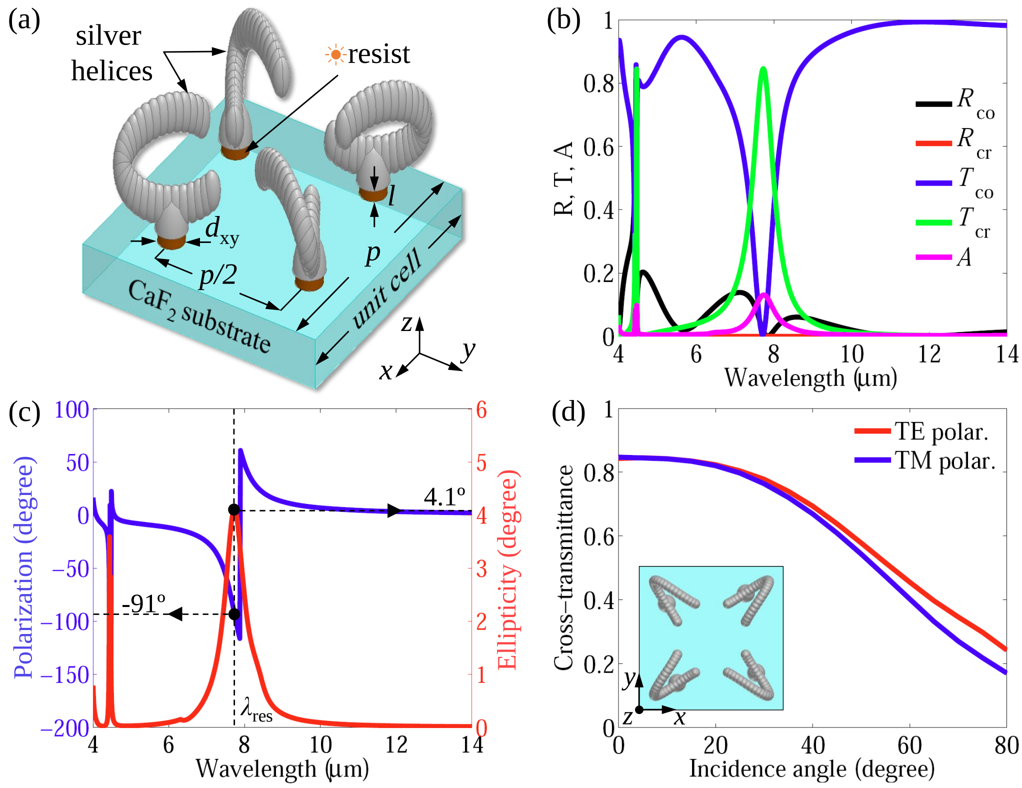

Figure 7.6: (a) Design of helix-based TP metasurface consisting of silver single-turn helices with optimized by simulation structural parameters. (b) Co- and cross-polarized reflection, transmission, and absorption spectra at normal incidence. (c) Polarization angle and ellipticity of cross-transmitted waves versus wavelengths. (d) Cross-polarized transmission at oblique incidence for TE and TM polarizations, respectively.

absorption spectra at normal incidence. As can see, the cross-transmission peak occurs at the resonant wavelength of 7.7 μm with normalized to the unit amplitude of 0.85. We also emphasize relatively low reflectivity of about 13%, and low absorption 13% in the 4.6 – 14 μm wavelength range. The secondary peak (the high order resonance mode in helices) occurs at the 4.4 μm wavelength. As one can see from Figure 7.6(c), polarization rotation angle is $-91°$ at the resonance wavelength, whereas ellipticity is less than 4.1°. It is noteworthy that optical isolation between co- and cross-polarized wave transmission is high around 98.8% at the resonance. In addition, we have investigated a polarization dependents versus oblique incidence of TP metasurface for TE and TM polarizations, respectively. It can be seen in Figure 7.6(d). The cross-transmission is stable at oblique incident angles from 0° to 27°. The obtained result is a little better than in the case of conventional TP metasurface. Thus, our helix-based TP design demonstrates a good performance and operation in the considered IR spectral range. In future, we are planning to fabricate this helix-based TP metasurface by usage of DLW technique, non-selective metallization process, and laser ablation. The fabrication process of designed TP helix-based metasurface is under consideration.

7.3 Cross-polarized reflector

Another kind of cross-polarized rotator for reflected waves or we called "twist-reflector" can be designed for IR spectral range. As it was mentioned previously, twist reflector (TR) is a device that allows rotating the polarization plane of the reflected wave by 90° relative to the polarization plane of the incident electromagnetic wave. Several works have been reported at radio frequencies [120, 121, 123] and THz range [116, 119], respectively. However, there is still no implementation of TR for the IR spectral range. Thus, the realization of such polarizer for IR wavelengths is under investigation.

We are aiming to realize TR by usage of helical resonators that have balanced polarizabilities in the microwave region that it was reported in Section 3.2. Here, we will demonstrate the results of numerical simulation for helix-based TR metasurface for the mid-IR spectral range. In the designed structure all peculiarities were taking into account in accordance with the formation of microarchitectures by DLW process.

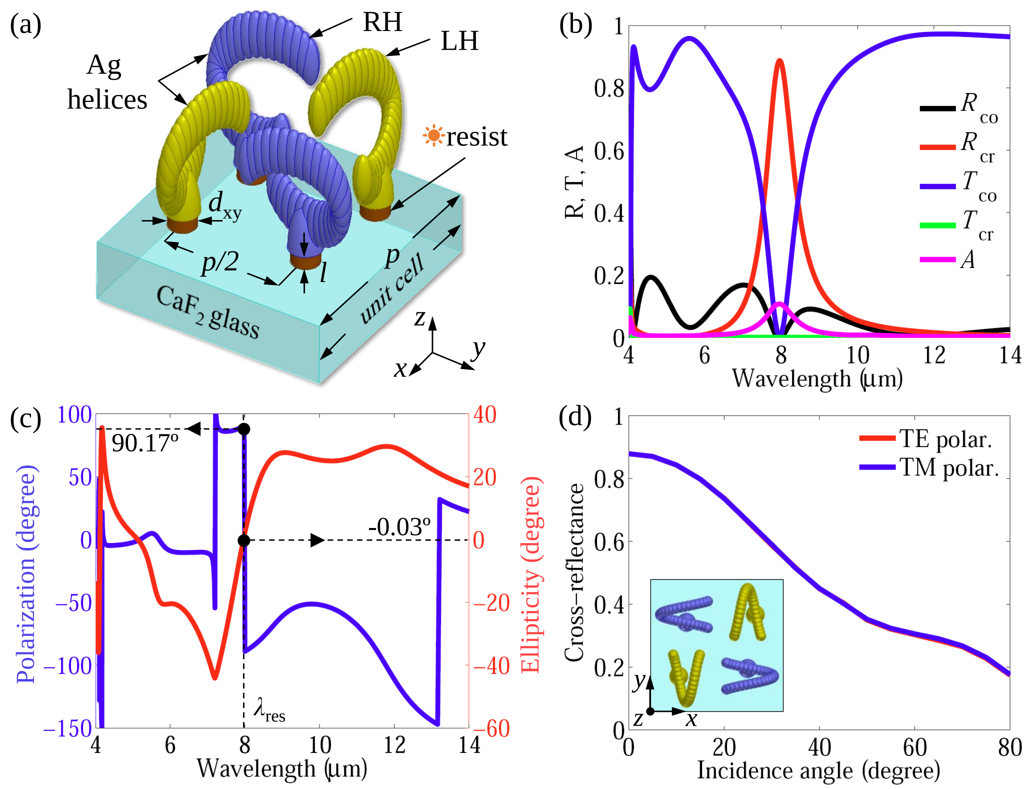

Figure 7.7: (a) Design of helix-based twist reflector with indicated parameters. (b) Reflection, transmission, and absorption spectra respect to the polarization state at normal incidence. (c) Polarization angle and ellipticity of cross-polarized reflected waves versus wavelengths. (d) Cross-reflectance of TR at oblique incidence for TE and TM polarizations, respectively.

Figure 7.7(a) shows the design of TR metasurface consisting of silver single-turn helical resonators arranged into a periodic lattice with indicated optimized structural parameters. The unit cell comprising of RH (blue color) and LH (red color) metallic helical resonators is depicted in Figure 7.7(a). Similar to helix-based twist-polarizer design, all helices are supported by photoresistive stems, therefore, helices are located a little above of CaF_2 glass that is transparent in the considered range. The TP metasurface is illuminated by a normally incident plane wave propagating along the $-z$-direction.

The simulated spectra of co- and cross-polarized reflection, transmission, and absorption coefficients at normal incidence can be seen in Figure 7.7(b). Cross-polarized reflectance has a peak value of 0.89 at the resonant wavelength of 7.95 μm. Co-polarized reflectivity does not exceed of 17%, with the low absorption peak of 11% in the wavelength range of $4.1 - 14$ μm. As seen, designed helix-based TR exhibits several peaks in the vicinity of the resonance for the co-reflectance spectra that might be corresponded to the disbalance polarizabilities of helices as well as some additional undesired coupling effects occur between RH and LR helices. The high order resonance peak can be seen at the wavelength of 4 μm.

Figure 7.7(c) shows the polarization rotation angle and ellipticity for a cross-polarized reflected wave in the considered spectral range. It can be seen that polarization rotation angle is equal 90.17° at the resonance wavelength, while the ellipticity is about $-0.03°$. Therefore, optical isolation between TE and TM polarizations at the input and output waves is around 99.8% at the resonance. This corresponds to a high degree of spectral purity of the helix-based TR metasurface.

Figure 7.7(d) shows simulated cross-reflection at the resonance ($\lambda_{\text{res}} = 7.95$ μm) of the proposed helix-based structure as a function of incidence angle for TE and TM linearly polarized waves, respectively. One can see that TR metasurface is strongly depended for the oblique incidence for both polarizations. The cross-reflectance properties are invariant only till 7° of incidence angles. However, the spectra behavior at TE and TM polarizations are absolutely the same in all considered range of oblique incidence angles.

Thereby, TR metasurface based on helical resonators exhibits normally incident polarization-insensitive transformation electromagnetic waves for reflection regime from TE to TM polarizations and vise verse within a considerable range. The amplitude of reflected light with cross polarization about 89% at the resonant wavelength of 7.95 μm has been obtained. Further, this design can be possible to realized owing to DLW technique, where the selective metallization of helical resonators is required.

7.4 Absorber

In this Section, we propose a low-reflection absorptive metasurface based on helical resonators using DLW technique for the MIR spectral range. Previously, we have studied the similar design of helix-based perfect absorber (compensated PA) in MIR spectral range, numerically and experimentally (see Section 6.3). The compensated PA architecture was comprised of metallic single-turn RH and LH helices located on a metallic substrate. Here, we demonstrate the results of numerical simulations for the off-resonance transparent helix-based absorber. Therefore, this absorber does not have a metallic substrate that allows making transparent away from resonance. This property was already demonstrated for microwave frequency band theoretically and experimentally (see Section 4.2) but still

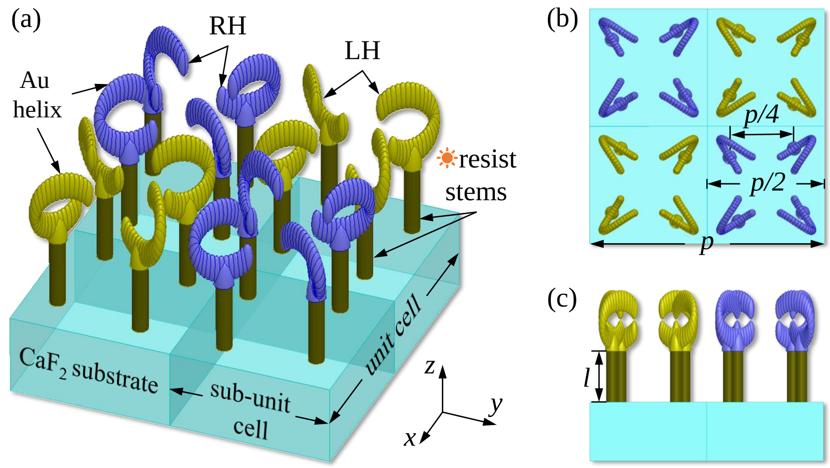

Figure 7.8: (a) A schematic Illustration of the off-resonance transparent helix-based absorber for IR spectral range. (b) Top view of a unit cell with a period of the structure $p = 7.3$ μm. (c) Front view of the helix-based absorber with selected length of photoresistive stems ($l = 1.6$ μm).

does not for optical spectrum. At this moment we have performed only the simulation results, but hopefully, we will soon fabricate a low-reflection absorber using DLW technique with subsequent applying of laser ablation to achieve transparent properties in the optical range.

Using numerical simulation based on FEM the low-reflection absorptive metasurface based on helical resonators was designed and tested in the MIR spectral range. Figure 7.8(a) shows the design of low-reflection absorber at a perspective view. The unit cell of absorber consists of four sub-unit cell based on four gold RH(blue color) or LH (yellow color) single-turn helices that are connected to transparent CaF_2 substrate by dielectric stems (photoresist) for mechanical supporting. The helix-based absorber is illuminated by a normally incident plane wave propagating along the z-direction. Figures 7.8(b) and (c) show the unit cell of architecture with indicated structural parameters at the top and front views, respectively. All structural parameters were optimized owing to numerical simulation. As can be seen, the length of dielectric stems is much longer in comparison with previous design of polarization rotators for reflected and transmitted waves (see Figs. 7.6 and 7.7). This feature in the design will be described below.

Using numerical simulation, the optical properties of helix-based absorber were obtained. Reflection, transmission, and absorption spectra at normal incidence can be seen in Figure 7.9(a). The absorption peak reaches maximum value of 0.79 at the resonant wavelength of 7.7 μm, while the transmission is reduced to a value of 0.14. As can be seen, the reflectance does not exceed of 27% in the range of $4.1 - 14$ μm that is a rather high value for low reflection performance. Away from the resonance, the transmission spectra exhibit transparency of helix-based absorber more than 70% in the considered range. Nevertheless, transmission exceeds of 85% for the longer wavelength range of $8.3 - 14$ μm.

Figure 7.9(b) shows the dependence of absorption spectra at normal incidence for the different length of dielectric stems. As can be seen, the absorption peak slightly increases

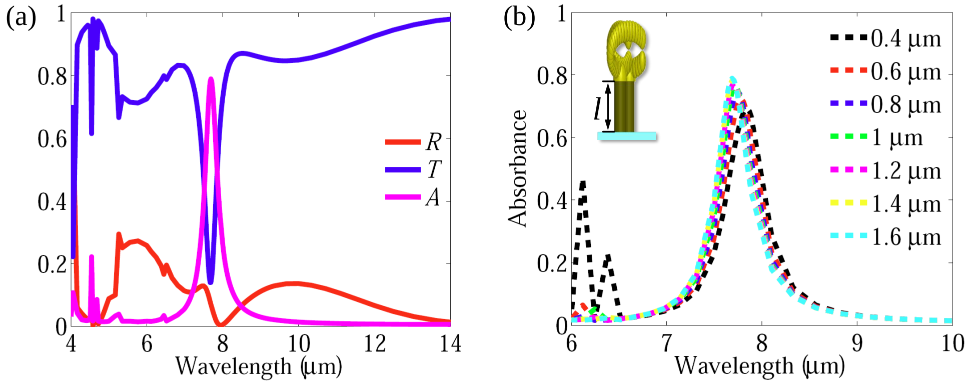

Figure 7.9: (a) R, T, A spectra of helix-based absorber at normal incidence. (b) Absorption spectra at different length of dielectric stems.

with proportional elongation length of stems. The stem length ranges from 0.4 μm to 1.6 μm with a step of 0.2 μm, respectively. Therefore, we have chosen the length of supporting stems is about 1.6 μm that it has relatively good absorption ($A = 0.85$). However, the further increase of length is not suitable since it will be difficult to remove the metallic covering from the helix-based structure using laser ablation. It requires a very precise focusing position of nanosecond pulsed laser and controlling of laser power since it can be easily broken due to the loss of the mechanical strength of the stems. In our opinion, this length of the stem is optimal for fixing helices on the transparent substrate during the laser ablation process.

Thus, we have designed a low reflection absorber based on Au single-turn helical resonators for MIR spectral range. Unfortunately, the obtained helix-based absorber demonstrates a rather high reflection outside of the resonance and as a consequence, a weak transparency, that makes this design not very promising for the implementation of a multilayer cascade metamaterial in the future. Nevertheless, the proposed helix-based architecture absorbs the incident power of over 79% and exhibits some properties of the off-band transparency away from the resonance band.

7.5 Conclusions

- A simple way for selective metallization of 3D microscale inclusions in the metasurface from a full metallic architecture after the usage of the conventional non-selective metallization process by gold sputtering has been reported. For removing the undesired metallic substrate in micro/nanostructures, nanosecond pulsed laser ablation has been used.

- Conventional design of TP metasurface based on vertically standing single-turn helices was tested using numerical simulation based on FEM. In accordance with theoretical expectations, the helix-based TP metasurface exhibits cross-polarization efficiency over of 85% at the resonant wavelength of 5.6 μm, while the total reflection does not exceed of 12% in the considered spectral range. Optical isolation between co- and cross-polarized transmitted waves is about 99.8% at the resonance. The designed polarizer was realized by usage of DLW technique, non-selective gold sputtering, and laser ablation process. By carefully controlling the exposure conditions of laser ablation process gold film with a thickness about 100 nm was removed from the helix-based architecture. Further optical characterization and better fabrication are under investigation.

- Using numerical simulation, another design of helix-based TP metasurface was proposed. This TP consists of the usual single-turn metallic helices with optimized structural parameters and arrangement of inclusions in the unit cell. Our design demonstrates resonant cross-transmittance peak of 0.85 at the wavelength of 7.7 μm, while reflectance does not exceed of 13% in the operational spectral range. However, the realization of the proposed TP metasurface is still under fabrication.

- Cross-polarized reflector (twist reflector) based on single-turn helices were designed for mid-IR spectral range by usage of numerical simulation based on FEM. Helix-based TR metasurface exhibits 90° rotation of polarization plane for reflected waves with an amplitude of 0.89 respects to the unit at the resonant wavelength of 7.95 μm, while a transmission reaches a value of 0.83 in the outside of the resonance band. This design was adapted for realization by DLW technique with subsequent selective metallization.

- Off-resonance transparent helix-based perfect absorber has been designed by numerical simulation. PA structure possesses relatively low reflectivity properties ($R \leq 27\%$) in the range of $4.1 - 14$ μm with the absorption peak of 0.79 at the resonance of 7.7 μm. Unfortunately, the obtained helix-based absorber does not good operate as off-resonance transparent metasurface even in the simulation model and further optimization in design is still required. Nevertheless, the absorption properties with transparency away from resonance can be seen in the IR spectral range.

Chapter 8

Summary and outlook

8.1 Summary

Summarizing, we have designed and fabricated functional off-resonance transparent 3D helix-based metasurfaces in the microwave range. In particular, perfect absorbers and co-/cross-polarized rotators for reflected and transmitted waves have been reported. Our goals have been to enhance the operation, tunability, and fabrication of off-resonance transparent metasurfaces based on helical resonators with balanced polarizabilities. Here, we briefly summarize these findings:

1) One of the most important theoretical results is the determination of all components of polarizability tensors of electrically small polarizable scatterers with arbitrary shape. As a result, we can define the EM response and behavior of any small scatterers to the incident radiation. Consequently, it allows synthesizing of absolutely any material consisting of these polarizable scatterers in order to obtain the desired electromagnetic properties in the wide frequency range [8-A]. Moreover, conditions for impedance matching and balance of polarizabilities of chiral metasurfaces to achieve zero reflection has been reported. As a result, off-resonance transparent polarization-insensitive helix-based metasurfaces using numerical simulation has been designed.

2) An analytical approach for determination of proper arrangement of helical resonators in the unit cell of metasurfaces depending on the desired electromagnetic properties was proposed. Since even if we know the individual polarizabilities of helical resonators, the knowledge of the necessary arrangement in the metasurface is still required because of the strong impact of the electromagnetic coupling between the inclusions in the entire metasurface. As a result, functional reflectionless helix-based metasurfaces can be designed taking into account proposed an analytical approach and numerical simulation.

3) Using numerical simulation, we have demonstrated several off-resonance transparent linearly polarized rotators based on copper double-turn helical resonators with balanced polarizabilities which rotate the polarization plane of transmitted or reflected linearly polarized waves by 90 degrees at the resonance in the microwave range. In other words, transverse electric polarized waves are converted into transverse magnetic polarized waves and vice verse [6-A, 2-B, 4-B, 4-C, 9-C]. In addition, we have shown several metasurfaces based on double-turn helices that allow us to keep the polarization state of transmitted or reflected waves respect to the incidence with controlling of the phase of these waves. It opens up new opportunities for realization of wavefront shaping and anomalous refraction of reflected and transmitted waves using helix-based metasurfaces [4-A, 3-B].

4) Off-resonance transparent helix-based twist polarizer in the microwave range has been verified both numerically and experimentally. Several off-resonance transparent absorbers based on single-turn and double-turn helical resonators in the microwave range have designed [4-A, 5-A, 7-A, 3-B, 8-B, 3-C]. In our opinion, we achieved the excellent results, since the proposed helix-based absorbers are probably the first realization of dispersive and lossy structure which does not reveal its dispersive and lossy in nature when observed in reflections at any frequency [5-A]. As a result, all functional metasurfaces exhibit low-reflection behavior in the operation microwave range.

5) Towards to realization of the off-resonance transparent functional 3D helix-based metasurfaces for IR spectral range, DLW technique has been proposed. However, practical development of 3D helix-based metasurfaces is impeded by their difficult fabrication, since it requires 3D structuring of metallic helical resonators with sub-micrometric size. To solve this problem, we emphasized on practical realization of functional metasurface structures for infrared spectral range using Direct Laser Write lithography that enables us to fabricate of 3D dielectric pattern in a photosensitive material with subsequent simple metallization by sputtering of gold [2-C].

6) Practical implementation and optical characterization of helix-based PA metasurfaces in the infrared spectral range were carried out. As a result, we have fabricated several entire metal absorbing metasurfaces comprising of single-turn gold helical resonators using the DLW approach with subsequent non-selective metallization [2-A, 1-B, 5-B, 1-C, 6-C, 8-C]. In addition, we have fabricated several entire metallic PA metasurfaces based on vertical split-ring resonators in the mid-IR wavelengths [1-A, 5-C].

7) Using numerical simulation, functional off-resonance transparent helix-based metasurfaces in the mid-IR spectral range have been designed. In addition, laser ablation process for removing a metallic substrate from entire metal architectures to make them off-resonance transparent was carried out. However, preliminary experimental results have not shown good performance and still fabrication process is under investigation. Nevertheless, due to DLW technique, non-selective metallization, and laser ablation process, it is possible to fabricate truly off-resonance transparent helix-based metasurfaces in the IR spectral range.

All designed metasurfaces with the best and the main optical characteristics for microwave and IF spectral range reported in this doctoral thesis are summarized in Tables 8.1 and 8.2. To conclude, we hope that our results will form the basis for the future work of researchers and scientists who are interested in continuing research on the above topics and will further expand the functionalities and understanding of electromagnetic interactions with helix-based metasurfaces. We hope, it gives evolutionary advances in technology.

Microwave frequency range					
No.	Design	Value, % (simulation)	Value, % (experiment)	f_{res}, GHz	Range, GHz
1)	Co-reflector [Figure 3.2(c)]	$R_{\mathrm{co}} = 98$ $R_{\mathrm{cr}} = 0.1$ $T_{\mathrm{co}} = 0.4$ $T_{\mathrm{cr}} = 0.1$ $A = 1.4$	–	2.95	$2 - 4$
2)	Cross-reflector [Figure 3.3(b)]	$R_{\mathrm{co}} = 1.2$ $R_{\mathrm{cr}} = 96$ $T_{\mathrm{co}} = 0.1$ $T_{\mathrm{cr}} = 0.1$ $A = 2.4$	–	3.01	$2.5 - 3.5$
3)	Co-transmit [Figure 3.4(b)]	$R_{\mathrm{co}} = 1.2$ $R_{\mathrm{cr}} = 0.1$ $T_{\mathrm{co}} = 86$ $T_{\mathrm{cr}} = 0.3$ $A = 12.3$	–	3.06	$2.5 - 3.5$
4)	Cross-transmit [Figure 3.2(b)]	$R_{\mathrm{co}} = 0.8$ $R_{\mathrm{cr}} = 0.1$ $T_{\mathrm{co}} = 0.1$ $T_{\mathrm{cr}} = 96.2$ $A = 2.9$	–	3.04	$2.5 - 3.5$
5)	Cascaded metamaterial [Figures 3.7]	$R_{\mathrm{co}} = 85$ $R_{\mathrm{cr}} = 85$ $T_{\mathrm{co}} = 85$ $T_{\mathrm{cr}} = 92$ $A = 92$	–	6 5 3 2 4	$1 - 7$
6)	Twist-polarizer sim:[Figure 4.1] exp:[Figure 4.4]	$R_{\mathrm{co}} = 0.1$ $R_{\mathrm{cr}} = 0.1$ $T_{\mathrm{co}} = 0.1$ $T_{\mathrm{cr}} = 98$ $A = 1.7$	$R_{\mathrm{co}} = 4$ $R_{\mathrm{cr}} = 1$ $T_{\mathrm{co}} = 6$ $T_{\mathrm{cr}} = 92$ $A = 1$	sim: 3.1 exp: 3.07	$0.1 - 6$ $2.8 - 3.3$
7)	Absorber sim:[Figure 4.5] exp:[Figure 4.7]	$R = 1.4$ $T = 0.9$ $A = 97.6$	$R = 5.8$ $T = 2.6$ $A = 92$	sim: 3.05 exp: 3.02	$0.1 - 7$ $2.9 - 3.3$
8)	Absorber sim:[Figure 4.8] exp:[Figure 4.10]	$R = 0.1$ $T = 0.0$ $A = 99.9$	$R = 6.3$ $T = 12.6$ $A = 81.7$	sim: 3.07 exp: 3.08	$0.1 - 10$ $2.9 - 3.2$

Table 8.1: The main optical characteristics of functional off-resonance transparent helix-based metasurfaces in the microwave range.

Infrared spectral range					
No.	Design	Value, % (simulation)	Value, % (experiment)	λ_{res}, μm	Range, μm
1)	Twist-polarizer [Figure 7.2]	$R_{\mathrm{co}} = 3.14$ $R_{\mathrm{cr}} = 0.01$ $T_{\mathrm{co}} = 0.3$ $T_{\mathrm{cr}} = 84.9$ $A = 11.7$	–	5.56	$4-7$
2)	Twist-polarizer [Figure 7.6]	$R_{\mathrm{co}} = 2.35$ $R_{\mathrm{cr}} = 0.01$ $T_{\mathrm{co}} = 0.45$ $T_{\mathrm{cr}} = 84.6$ $A = 13.1$	–	7.73	$4-14$
3)	Cross-reflector [Figure 7.7]	$R_{\mathrm{co}} = 0.3$ $R_{\mathrm{cr}} = 88.7$ $T_{\mathrm{co}} = 0.3$ $T_{\mathrm{cr}} = 0.01$ $A = 10.8$	–	7.95	$4-14$
4)	Low-reflection absorber [Figure 6.16]	$R = 7.06$ $T = 14.1$ $A = 78.9$	–	7.69	$4-14$
5)	Chiral-plate absorber sim:[Figure 6.10] exp:[Figure 6.13]	$R = 0.2$ $T = 0$ $A = 98.8$	$R = 8.5$ $T = 0$ $A = 91.5$	sim: 7 exp: 7.7	$5-13$
6)	Compensated absorber sim:[Figure 6.16] exp:[Figure 6.17]	$R = 0.8$ $T = 0$ $A = 99.2$	$R = 17.9$ $T = 0$ $A = 82.1$	sim: 6.97 exp: 7.6	$6-10$
7)	VSRR-based absorber sim:[Figure 6.2] exp:[Figure 6.3]	$R = 0.4$ $T = 0$ $A = 99.6$	$R = 11.9$ $T = 0$ $A = 88.1$	sim: 7.18 exp: 8.05	$5-13$
8)	Mesh-type VSRR-based absorber [Figure 6.7]	$R = 5.7$ $T = 0$ $A = 94.3$	$R = 17.6$ $T = 0$ $A = 82.4$	sim: 4.03 exp: 4.3	$3-13$

Table 8.2: The main optical characteristics of functional metasurfaces in the IR spectral range.

8.2 Outlook and future work

Here, proposed electromagnetic metasurfaces with helix-based architecture can be applied for spectral filtering, polarization transformation, and absorption enhancement of radio and optical waves. Absorption metasurfaces allow to harvesting radiation and absorption enhancement in infra-red detectors, as well as a realization of narrow-band infrared thermal emitters and radiation uncooled arrays are especially attractive. Since that, the available broadband uncooled arrays of microbolometers are generally not sensitive enough for low-concentration chemical detection. Perfect absorber metasurfaces based on the resonant inclusions can be used to improve the performance of microbolometer arrays to hold the potential for a significant improvement in thermal imaging, night vision, chemical and biological probing capabilities.

Based on the huge number of obtained results, several suggestions can be singled out for future work:

1) Fabrication of off-resonance transparent helix-based PA architectures in the near-IR or even visible range (further downscaling of unit cell).

2) Fabrication of efficient transparent twist polarizers for reflected and transmitted light using our approach described in Section 7.1.

3) Since there are still some difficulties in the fabrication process of 3D helical microarchitecture using DLW lithography, it might be possible to modify the helix-based design to multilayered flat nanostructures that are for more suitable for fabrication by standard highly accurate nanoimprint techniques (electron beam lithography, self-assembly method, multibeam interference technique and others).

4) To improve the fabrication approach for realization of functional helix-based metasurfaces in the microwave range, it is possible to adjust the design for printed circuit board (PCB) technology. This opens up new opportunities for the design of multifunctional multifrequency devices. Moreover, cheap mass-production manufacturing technologies can be used.

Author's Publications

Articles

1-A I. Faniayeu, S. Khakhomov, I. Semchenko, and V. Mizeikis, Highly transparent twist polarizer metasurface, *Applied Physics Letters* (accepted).

2-A I. Faniayeu, V. Mizeikis, Vertical split-ring resonator perfect absorber metamaterial for IR frequencies realized via femtosecond direct laser writing, *Applied Physics Express*, Vol. 10, 062001 (2017).

3-A I. Faniayeu, V. Mizeikis, Realization of a helix-based perfect absorber for IR spectral range using the direct laser write technique, *Optical Materials Express*, Vol. 7, Issue 5, pp. 1453-1462 (2017).

4-A S.D. Barsukov, A.S. Pobiyaha, A.P. Balmakov, I.A. Faniayeu, T.A. Derzhavskaya, I.V. Semchenko, S.A. Khakhomov, A.L. Samofalov, S.B. Glybovskij, and P.A. Belov, All-directional bifilar helical antenna of circular polarization, *Antennas*, Vol. 3, pp. 43-48 (2017). [in Russian].

5-A A.A. Elsakka, V.S. Asadchy, I.A. Faniayeu, S.N. Tcvetkova, and S.A. Tretyakov, Multifunctional cascaded metamaterials: integrated transmitarrays, *IEEE Transactions on Antennas and Propagation*, Vol. 64, No. 10, pp. 4266-4276 (2016).

6-A V.S. Asadchy, I.A. Faniayeu, Y. Radi, S.A. Khakhomov, I.V. Semchenko, and S.A. Tretyakov, Broadband reflectionless metasheets: frequency-selective transmission and perfect absorption, *Physical Review X*, Vol. 5, 031005 (2015).

7-A I.A. Faniayeu, I.V. Semchenko, S.A. Khakhomov, and A.L. Samofalov, Uniaxial electrically thin rotator of polarization of electromagnetic waves, *Problems of Physics, Mathematics and Technics*, Vol. 1, pp. 32-37 (2015). [in Russian].

8-A I.A. Faniayeu, I.V. Semchenko, S.A. Khakhomov, and T.A. Dziarzhauskaya, Total absorption based on smooth double-turn helices, *Advanced Materials Research*, Vol. 1117, pp. 39-43 (2015).

9-A V.S. Asadchy, I.A. Faniayeu, Y. Ra'di, and S.A. Tretyakov, Determining polarizability tensors for an arbitrary small electromagnetic scatterer, *Photonics and Nanostructures Fundamentals and Applications*, Vol. 12, No. 4, pp. 298-304 (2014).

Conference proceedings

1-B I.A. Faniayeu, V. Mizeikis, Realisation of 3D metamaterial perfect absorber structures by direct laser writing, Proc. SPIE 10115, Advanced Fabrication Technologies for Micro/Nano Optics and Photonics X, 101150X (February 20, 2017).

2-B I.A. Faniayeu, V. Mizeikis, Realization of twist polarizer design using femtosecond direct laser write technique in infra-red spectral range, The 18th Takayanagi Kenjiro Memorial Symposium, Hamamatsu, Japan, pp. 111-113 (15-16 November 2016).

3-B V.S. Asadchy, A.A. Elsakka, I.A. Faniayeu, S.N. Tcvetkova, and S.A. Tretyakov, Multifunctional cascaded metasurfaces, 10th International Congress on Advanced Electromagnetic Materials in Microwaves and Optics, Chania Crete, Greece, pp. 729731 (17-22 September 2016).

4-B I.A. Faniayeu, V.S. Asadchy, and V. Mizeikis, Mid-infrared twist polarizer metasurface based on spiral architecture, 10th International Congress on Advanced Electromagnetic Materials in Microwaves and Optics, Chania Crete, Greece, pp. 437-439 (17-22 September 2016).

5-B I.A. Faniayeu, V. Mizeikis, Fabrication of metasurface-based infrared absorber structures using direct laser write lithography, Proc. SPIE 9759, Advanced Fabrication Technologies for Micro/Nano Optics and Photonics IX, 975917, (14 March 2016).

6-B I.A. Faniayeu, I.V. Semchenko, and V. Mizeikis, Nearly perfect plasmonic absorber based on heavily-doped semiconductor, 9th International Congress on Advanced Electromagnetic Materials in Microwaves and Optics, Oxford, United Kingdom, pp. 739-741 (7-12 September 2015).

7-B I.V. Semchenko, S.A. Khakhomov, I.A. Faniayeu, and A.P. Balmakov, DNA-type helix with optimal shape in soft X-ray range, 9th International Congress on Advanced Electromagnetic Materials in Microwaves and Optics, Oxford, United Kingdom, pp. 621-623 (7-12 September 2015).

8-B I.A. Faniayeu, V.S. Asadchy, T.A. Dzerzhauskaya, I.V. Semchenko, and S.A. Khakhomov, A single-layer meta-atom absorber, 8th International Congress on Advanced Electromagnetic Materials in Microwaves and Optics (IEEE), pp. 112-114 (25-28 August 2014).

Abstracts

1-C I.A. Faniayeu, V. Mizeikis, Laser microfabrication and optical properties of metallic spiral based perfect absorber metamaterial for mid-infrared frequencies, The 14th International Conference on Near-field Optics, Nanophotonics, and Related Techniques (NFO-14), Hamamatsu, Japan, p. 357 (4-8 September 2016).

2-C I.A. Faniayeu, V. Mizeikis, Fabrication of bi-anisotropic optical metamaterials for infra-red spectral range by direct laser write technique, The Second Smart Laser Processing Conference (SLPC), Yokohama, Japan, p. 48 (17-19 May 2016).

3-C V.S. Asadchy, I.A. Faniayeu, and S.A. Tretyakov, Large-area ground-free terahertz absorbers, In Millimeter Waves (GSMM) & 2016 Global Symposium on ESA Workshop on Millimetre-Wave Technology and Applications (IEEE), pp. 1-2 (6-8 June 2016).

4-C I.A. Faniayeu, and V. Mizeikis, Twist Polarizer Metamaterial for Mid-Infrared Spectral Range, The 63nd Spring Meeting of The Japan Society of Applied Physics, Tokyo, Japan, p. 03-007 (19-22 March 2016).

5-C I.A. Faniayeu, V. Mizeikis, Photonic metamaterial absorber for infrared spectral range based on 3D split-ring resonators, 14th International Conference on Global Research and Education, Hamamatsu, Japan, pp. 94-95 (28-30 September 2015).

6-C I.A. Faniayeu, V. Mizeikis, Chiral plate perfect absorber metamaterial for infra-red spectral range based on 3D spiral architecture, The 76th JSAP Autumn Meeting of The Japan Society of Applied Physics, JSAP-OSA Joint Symposia, Nagoya, Japan, p. 212-1 (13-16 September 2015).

7-C I.A. Faniayeu, I.V. Semchenko, V. Mizeikis, Design of perfect absorber based on spiral architecture metamaterial for near-infrared spectral range, The 62nd Spring Meeting of The Japan Society of Applied Physics, Hiratsuka, Japan, p. 04-407 (11-14 March 2015).

8-C I.A. Faniayeu, V. Mizeikis, Ultrathin absorber based on bifilar helix for NIR, International Symposium toward the future of advanced researches in Shizuoka University, Hamamatsu, Japan, p. 42 (27-28 January 2015).

9-C I.A. Faniayeu, V.S. Asadchy, I.V. Semchenko, S.A. Khakhomov, Wave transformations in thin metamaterial layers, International scientific conference "Optics of Crystals", Mozyr, Belarus, pp. 112-113 (23-26 September 2014).

Bibliography

[1] J. B. Pendry, "Negative refraction makes a perfect lens," *Physical Review Letters*, vol. 85, no. 18, p. 3966, 2000.

[2] D. R. Smith, W. J. Padilla, D. Vier, S. C. Nemat-Nasser, and S. Schultz, "Composite medium with simultaneously negative permeability and permittivity," *Physical Review Letters*, vol. 84, no. 18, p. 4184,2000.

[3] V. G. Veselago, "The electrodynamics of substances with simultaneously negative values of ϵ and μ," *Soviet Physics Uspekhi*, vol. 10, no. 4, p. 509, 1968.

[4] S. Linden, C. Enkrich, M. Wegener, J. Zhou, T. Koschny, and C. M. Soukoulis, "Magnetic response of metamaterials at 100 terahertz," *Science*, vol. 306, no. 5700, pp. 1351–1353, 2004.

[5] V. M. Shalaev, W. Cai, U. K. Chettiar, H.-K. Yuan, A. K. Sarychev, V. P. Drachev, and A. V. Kildishev, "Negative index of refraction in optical metamaterials," *Optics Letters*, vol. 30, no. 24, pp. 3356–3358, 2005.

[6] S. Zhang, W. Fan, B. Minhas, A. Frauenglass, K. Malloy, and S. Brueck, "Midinfrared resonant magnetic nanostructures exhibiting a negative permeability," *Physical Review Letters*, vol. 94, no. 3, p. 037402, 2005.

[7] S. Zhang, W. Fan, N. Panoiu, K. Malloy, R. Osgood, and S. Brueck, "Experimental demonstration of near-infrared negative-index metamaterials," *Physical Review Letters*, vol. 95, no. 13, p. 137404, 2005.

[8] D. Stavenga, "Invertebrate superposition eyes-structures that behave like metamaterial with negative refractive index," *Journal of the European Optical Society-Rapid Publications*, vol. 1, 2006.

[9] S. Kinoshita, S. Yoshioka, and K. Kawagoe, "Mechanisms of structural colour in the morpho butterfly: cooperation of regularity and irregularity in an iridescent scale," *Proceedings of the Royal Society of London B: Biological Sciences*, vol. 269, no. 1499, pp. 1417–1421, 2002.

[10] D. Barber and I. C. Freestone, "An investigation of the origin of the colour of the lycurgus cup by analytical transmission electron microscopy," *Archaeometry*, vol. 32, no. 1, pp. 33–45, 1990.

[11] F. E. Wagner, S. Haslbeck, L. Stievano, S. Calogero, Q. Pankhurst, and K.-P. Martinek, "Before striking gold in gold-ruby glass," *Nature*, vol. 407, no. 6805, pp. 691–692, 2000.

[12] U. Leonhardt, "Optical metamaterials: Invisibility cup," *Nature Photonics*, vol. 1, no. 4, pp. 207–208, 2007.

[13] J. C. Bose, "On the rotation of plane of polarisation of electric waves by a twisted structure," *Proceedings of the Royal Society of London*, vol. 63, no. 389-400, pp. 146–152, 1898.

[14] W. E. Kock, "Metal-lens antennas," *Proceedings of the IRE*, vol. 34, no. 11, pp. 828–836, 1946.

[15] J. Brown, "Artificial dielectrics having refractive indices less than unity," *Proceedings of the IEE-Part IV: Institution Monographs*, vol. 100, no. 5, pp. 51–62, 1953.

[16] W. Rotman, "Plasma simulation by artificial dielectrics and parallel-plate media," *IRE Transactions on Antennas and Propagation*, vol. 10, no. 1, pp. 82–95, 1962.

[17] W. Hardy and L. Whitehead, "Split-ring resonator for use in magnetic resonance from 200–2000 mhz," *Review of Scientific Instruments*, vol. 52, no. 2, pp. 213–216, 1981.

[18] W. Froncisz and J. S. Hyde, "The loop-gap resonator: a new microwave lumped circuit ESR sample structure," *Journal of Magnetic Resonance (1969)*, vol. 47, no. 3, pp. 515–521, 1982.

[19] J.-S. Hong and M. J. Lancaster, "Couplings of microstrip square open-loop resonators for cross-coupled planar microwave filters," *IEEE Transactions on Microwave Theory and Techniques*, vol. 44, no. 11, pp. 2099–2109, 1996.

[20] M. M. Saadoun and N. Engheta, "A reciprocal phase shifter using novel pseudochiral or ω medium," *Microwave and Optical Technology Letters*, vol. 5, no. 4, pp. 184–188, 1992.

[21] F. Capolino, *Theory and phenomena of metamaterials*, CRC Press, 2009.

[22] N. Engheta and R. W. Ziolkowski, *Metamaterials: physics and engineering explorations*, John Wiley and Sons, 2006.

[23] G. V. Eleftheriades and K. G. Balmain, *Negative-refraction metamaterials: fundamental principles and applications*, John Wiley and Sons, 2005.

[24] A. K. Sarychev and V. M. Shalaev, *Electrodynamics of metamaterials*, World Scientific, 2007.

[25] J. D. Jackson, *Electrodynamics*, Wiley Online Library, 1975.

[26] I. S. Grigoriev, E. Z. Melikhov, and A. A. Radzig, *Handbook of physical quantities*, CRC, 1997.

[27] I. V. Lindell, A. Sihvola, S. Tretyakov, and A. Viitanen, "Electromagnetic waves in chiral and bi-isotropic media," Artech House, 1994.

[28] L. Novotny and B. Hecht, *Principles of nano-optics*, Cambridge University Press, 2012.

[29] J. Kästel and M. Fleischhauer, "Quantum electrodynamics in media with negative refraction," *Laser Physics*, vol. 15, no. 1, pp. 1–11, 2005.

[30] D. R. Smith, J. B. Pendry, and M. C. Wiltshire, "Metamaterials and negative refractive index," *Science*, vol. 305, no. 5685, pp. 788–792, 2004.

[31] A. V. Kildishev, A. Boltasseva, and V. M. Shalaev, "Planar photonics with metasurfaces," *Science*, vol. 339, no. 6125, p. 1232009, 2013.

[32] N. Yu, P. Genevet, M. A. Kats, F. Aieta, J.-P. Tetienne, F. Capasso, and Z. Gaburro, "Light propagation with phase discontinuities: generalized laws of reflection and refraction," *Science*, vol. 334, no. 6054, pp. 333–337, 2011.

[33] P. Genevet, N. Yu, F. Aieta, J. Lin, M. A. Kats, R. Blanchard, M. O. Scully, Z. Gaburro, and F. Capasso, "Ultra-thin plasmonic optical vortex plate based on phase discontinuities," *Applied Physics Letters*, vol. 100, no. 1, p. 013101, 2012.

[34] E. H. Khoo, E. P. Li, and K. B. Crozier, "Plasmonic wave plate based on subwavelength nanoslits," *Optics Letters*, vol. 36, no. 13, pp. 2498–2500, 2011.

[35] Y. Zhao and A. Alu, "Manipulating light polarization with ultrathin plasmonic metasurfaces," *Physical Review B*, vol. 84, no. 20, p. 205428, 2011.

[36] C. R. Simovski, P. A. Belov, A. V. Atrashchenko, and Y. S. Kivshar, "Wire metamaterials: physics and applications," *Advanced Materials*, vol. 24, no. 31, pp. 4229–4248, 2012.

[37] H. Lamb, "On the reflection and transmission of electric waves by a metallic grating," *Proceedings of the London Mathematical Society*, vol. 1, no. 1, pp. 523–546, 1897.

[38] G. MacFarlane, "Surface impedance of an infinite parallel-wire grid at oblique angles of incidence," *Journal of the Institution of Electrical Engineers-Part IIIA: Radiolocation*, vol. 93, no. 10, pp. 1523–1527, 1946.

[39] M. Kontorovich, V. Y. Petrunkin, N. Yesepkina, and M. Astrakhan, "The coefficient of reflection of a plane electromagnetic wave from a plane wire mesh," *Radio Engineering and Electronic Physics*, vol. 7, no. 2, pp. 222–231, 1962.

[40] A. Pors, M. G. Nielsen, R. L. Eriksen, and S. I. Bozhevolnyi, "Broadband focusing flat mirrors based on plasmonic gradient metasurfaces," *Nano Letters*, vol. 13, no. 2, pp. 829–834, 2013.

[41] S. Zouhdi, A. Sihvola, and A. P. Vinogradov, *Metamaterials and plasmonics: fundamentals, modelling, applications*, Springer Science and Business Media, 2008.

[42] S. B. Glybovski, S. A. Tretyakov, P. A. Belov, Y. S. Kivshar, and C. R. Simovski, "Metasurfaces: From microwaves to visible," *Physics Reports*, vol. 634, pp. 1–72, 2016.

[43] C.-N. Chiu and W.-Y. Wang, "A dual-frequency miniaturized-element FSS with closely located resonances," *IEEE Antennas and Wireless Propagation Letters*, vol. 12, pp. 163–165, 2013.

[44] N. Behdad, "Miniaturized-element frequency selective surfaces (MEFSS) using subwavelength periodic structures," in *Radio and Wireless Symposium*, pp. 347–350, IEEE, 2008.

[45] D. Sievenpiper, L. Zhang, R. F. Broas, N. G. Alexopolous, and E. Yablonovitch, "High-impedance electromagnetic surfaces with a forbidden frequency band," *IEEE Transactions on Microwave Theory and Techniques*, vol. 47, no. 11, pp. 2059–2074, 1999.

[46] K. N. Rozanov, "Ultimate thickness to bandwidth ratio of radar absorbers," *IEEE Transactions on Antennas and Propagation*, vol. 48, no. 8, pp. 1230–1234, 2000.

[47] Y. Ye and S. He, "90° polarization rotator using a bilayered chiral metamaterial with giant optical activity," *Applied Physics Letters*, vol. 96, no. 20, p. 203501, 2010.

[48] J. E. Roy, "New analysis of a reciprocal left hand circular polarization selective surface (LHCPSS)," in *Antennas and Propagation Society International Symposium, APSURSI'09*, pp. 1–4, IEEE, 2009.

[49] P. Alitalo, A. Karilainen, T. Niemi, C. Simovski, and S. Tretyakov, "Design and realisation of an electrically small Huygen's source for circular polarisation," *IET Microwaves, Antennas and Propagation*, vol. 5, no. 7, pp. 783–789, 2011.

[50] C. Caloz, T. Itoh, and A. Rennings, "CRLH metamaterial leaky-wave and resonant antennas," *IEEE Antennas and Propagation Magazine*, vol. 50, no. 5, 2008.

[51] X. Ni, S. Ishii, A. V. Kildishev, and V. M. Shalaev, "Ultra-thin, planar, babinet-inverted plasmonic metalenses," *Light: Science and Applications*, vol. 2, no. 4, p. e72, 2013.

[52] Y. Ra'di, V. S. Asadchy, and S. A. Tretyakov, "Tailoring reflections from thin composite metamirrors," *IEEE Transactions on Antennas and Propagation*, vol. 62, no. 7, pp. 3749–3760, 2014.

[53] M. F. Volk, B. Reinhard, J. Neu, R. Beigang, and M. Rahm, "In-plane focusing of terahertz surface waves on a gradient index metamaterial film," *Optics Letters*, vol. 38, no. 12, pp. 2156–2158, 2013.

[54] X. Ni, A. V. Kildishev, and V. M. Shalaev, "Metasurface holograms for visible light," *Nature Communications*, vol. 4, 2013.

[55] C. L. Holloway, E. F. Kuester, J. A. Gordon, J. O'Hara, J. Booth, and D. R. Smith, "An overview of the theory and applications of metasurfaces: The two-dimensional equivalents of metamaterials," *IEEE Antennas and Propagation Magazine*, vol. 54, no. 2, pp. 10–35, 2012.

[56] N. Yu and F. Capasso, "Flat optics with designer metasurfaces," *Nature Materials*, vol. 13, no. 2, pp. 139–150, 2014.

[57] Y. Ra'di, C. Simovski, and S. Tretyakov, "Thin perfect absorbers for electromagnetic waves: theory, design, and realizations," *Physical Review Applied*, vol. 3, no. 3, p. 037001, 2015.

[58] E. Hendry, R. Mikhaylovskiy, L. Barron, M. Kadodwala, and T. Davis, "Chiral electromagnetic fields generated by arrays of nanoslits," *Nano Letters*, vol. 12, no. 7, pp. 3640–3644, 2012.

[59] A. Papakostas, A. Potts, D. Bagnall, S. Prosvirnin, H. Coles, and N. Zheludev, "Optical manifestations of planar chirality," *Physical Review Letters*, vol. 90, no. 10, p. 107404, 2003.

[60] V. Fedotov, P. Mladyonov, S. Prosvirnin, A. Rogacheva, Y. Chen, and N. Zheludev, "Asymmetric propagation of electromagnetic waves through a planar chiral structure," *Physical Review Letters*, vol. 97, no. 16, p. 167401, 2006.

[61] K. Aydin, Z. Li, M. Hudlička, S. Tretyakov, and E. Ozbay, "Transmission characteristics of bianisotropic metamaterials based on omega shaped metallic inclusions," *New Journal of Physics*, vol. 9, no. 9, p. 326, 2007.

[62] M. Albooyeh and C. Simovski, "Substrate-induced bianisotropy in plasmonic grids," *Journal of Optics*, vol. 13, no. 10, p. 105102, 2011.

[63] M. Albooyeh and C. Simovski, "Huge local field enhancement in perfect plasmonic absorbers," *Optics Express*, vol. 20, no. 20, pp. 21888–21895, 2012.

[64] J. Arnaud and F. Pelow, "Resonant-grid quasi-optical diplexers," *The Bell System Technical Journal*, vol. 54, no. 2, pp. 263–283, 1975.

[65] S.-W. Lee, "Scattering by dielectric-loaded screen," *IEEE Transactions on Antennas and Propagation*, vol. 19, no. 5, pp. 656–665, 1971.

[66] R. Baggen, M. Martínez-Vázquez, J. Leiss, S. Holzwarth, L. S. Drioli, and P. de Maagt, "Low profile Galileo antenna using EBG technology," *IEEE Transactions on Antennas and Propagation*, vol. 56, no. 3, pp. 667–674, 2008.

[67] F. Bayatpur and K. Sarabandi, "Single-layer high-order miniaturized-element frequency-selective surfaces," *IEEE Transactions on Microwave Theory and Techniques*, vol. 56, no. 4, pp. 774–781, 2008.

[68] J. Hao, J. Wang, X. Liu, W. J. Padilla, L. Zhou, and M. Qiu, "High performance optical absorber based on a plasmonic metamaterial," *Applied Physics Letters*, vol. 96, no. 25, p. 251104, 2010.

[69] T.-J. Yen, W. Padilla, N. Fang, D. Vier, D. Smith, J. Pendry, D. Basov, and X. Zhang, "Terahertz magnetic response from artificial materials," *Science*, vol. 303, no. 5663, pp. 1494–1496, 2004.

[70] C. Enkrich, F. Pérez-Willard, D. Gerthsen, J. Zhou, T. Koschny, C. M. Soukoulis, M. Wegener, and S. Linden, "Focused-ion-beam nanofabrication of near-infrared magnetic metamaterials," *Advanced Materials*, vol. 17, no. 21, pp. 2547–2549, 2005.

[71] I. Semchenko, S. Khakhomov, and A. Samofalov, "Transformation of the polarization of electromagnetic waves by helical radiators," *Journal of Communications Technology and Electronics*, vol. 52, no. 8, pp. 850–855, 2007.

[72] I. Semchenko, S. Khakhomov, and A. Samofalov, "Helices of optimal shape for nonreflecting covering," *The European Physical Journal Applied Physics*, vol. 49, no. 3, p. 33002, 2010.

[73] T. A. Morgado, S. I. Maslovski, and M. G. Silveirinha, "Uniaxial indefinite material formed by helical-shaped wires," *New Journal of Physics*, vol. 14, no. 6, p. 063002, 2012.

[74] X. Xiong, S.-C. Jiang, Y.-H. Hu, J.-M. Zhao, Y.-J. Feng, R.-W. Peng, and M. Wang, "Assembling optically active and nonactive metamaterials with chiral units," *AIP Advances*, vol. 2, no. 4, pp. 075119–R, 2012.

[75] J. K. Gansel, M. Thiel, M. S. Rill, M. Decker, K. Bade, V. Saile, G. von Freymann, S. Linden, and M. Wegener, "Gold helix photonic metamaterial as broadband circular polarizer," *Science*, vol. 325, no. 5947, pp. 1513–1515, 2009.

[76] M. Esposito, V. Tasco, F. Todisco, A. Benedetti, D. Sanvitto, and A. Passaseo, "Three dimensional chiral metamaterial nanospirals in the visible range by vertically compensated focused ion beam induced-deposition," *Advanced Optical Materials*, vol. 2, no. 2, pp. 154–161, 2014.

[77] J. Kaschke, L. Blume, L. Wu, M. Thiel, K. Bade, Z. Yang, and M. Wegener, "A helical metamaterial for broadband circular polarization conversion," *Advanced Optical Materials*, vol. 3, no. 10, pp. 1411–1417, 2015.

[78] Y.-J. Jen, Y.-J. Huang, W.-C. Liu, and Y. W. Lin, "Densely packed aluminum-silver nanohelices as an ultra-thin perfect light absorber," *Scientific Reports*, vol. 7, 2017.

[79] S. Maci, "Metasurfing: Addressing waves on metasurfaces for realizing antennas and microwave devices," in *Microwave, Antenna, Propagation, and EMC Technologies for Wireless Communications (MAPE), 2011 IEEE 4th International Symposium on*, pp. K1–K4, IEEE, 2011.

[80] R. W. Ziolkowski, "Metamaterial-based antennas: research and developments," *IEICE Transactions on Electronics*, vol. 89, no. 9, pp. 1267–1275, 2006.

[81] R. W. Ziolkowski, P. Jin, and C.-C. Lin, "Metamaterial-inspired engineering of antennas," *Proceedings of the IEEE*, vol. 99, no. 10, pp. 1720–1731, 2011.

[82] N. Engheta, "Antenna-guided light," *Science*, vol. 334, no. 6054, pp. 317–318, 2011.

[83] R. Stevenson, M. Sazegar, A. Bily, M. Johnson, and N. Kundtz, "Metamaterial surface antenna technology: commercialization through diffractive metamaterials and liquid crystal display manufacturing," 10^{th} *International Congress in Advanced Electromagnetic Materials in Microwaves and Optics*, pp. 349–351, IEEE, 2016.

[84] J. Bonache, G. Zamora, F. Paredes, S. Zuffanelli, P. Aguilà, and F. Martin, "Application of metamaterials in near field UHF-RFID readers,"10^{th} *International Congress in Advanced Electromagnetic Materials in Microwaves and Optics*, pp. 64–66, IEEE, 2016.

[85] D. Jaggard, A. Mickelson, and C. Papas, "On electromagnetic waves in chiral media," *Applied Physics*, vol. 18, no. 2, pp. 211–216, 1979.

[86] W. Weiglhofer, "Dipole radiation in uniaxial bianisotropic medium," *Electronics Letters*, vol. 29, no. 10, pp. 844–845, 1993.

[87] A. Serdyukov, I. Semchenko, S. Tertyakov, and A. Sihvola, *Electromagnetics of bi-anisotropic materials–Theory and Application*, Gordon and Breach Science Publishers, 2001.

[88] T. Niemi, A. O. Karilainen, and S. A. Tretyakov, "Synthesis of polarization transformers," *IEEE Transactions on Antennas and Propagation*, vol. 61, no. 6, pp. 3102–3111, 2013.

[89] V. Asadchy and I. Fanyaev, "Simulation of the electromagnetic properties of helices with optimal shape, which provides radiation of a circularly polarized wave," *Journal of Advanced Research in Physics*, vol. 2, no. 1, 2011.

[90] J. Jackson, "Radiating systems, multipole fields and radiation," *Classical Electrodynamics*, pp. 407–455, 1999.

[91] S. Mühlig, C. Menzel, C. Rockstuhl, and F. Lederer, "Multipole analysis of meta-atoms," *Metamaterials*, vol. 5, no. 2, pp. 64–73, 2011.

[92] F. B. Arango and A. F. Koenderink, "Polarizability tensor retrieval for magnetic and plasmonic antenna design," *New Journal of Physics*, vol. 15, no. 7, p. 073023, 2013.

[93] S. A. Tretyakov, "Thin pseudochiral layers: approximate boundary conditions and potential applications," *Microwave and Optical Technology Letters*, vol. 6, no. 2, pp. 112–115, 1993.

[94] S. Zouhdi, A. Fourrier-Lamer, and F. Mariotte, "On the relationships between constitutive parameters of chiral materials and dimensions of chiral objects (helices)," *Journal de Physique III*, vol. 2, no. 3, pp. 337–342, 1992.

[95] S. A. Tretyakov, F. Mariotte, C. R. Simovski, T. G. Kharina, and J.-P. Heliot, "Analytical antenna model for chiral scatterers: comparison with numerical and experimental data," *IEEE Transactions on Antennas and Propagation*, vol. 44, no. 7, pp. 1006–1014, 1996.

[96] I. Semchenko, S. Khakhomov, M. Podalov, and S. Tretyakov, "Radiation of circularly polarized microwaves by a plane periodic structure of ω elements," *Journal of Communications Technology and Electronics*, vol. 52, no. 9, pp. 1002–1005, 2007.

[97] I. Semchenko, S. Khakhomov, and A. Samofalov, "Optimal helix shape: equality of dielectric, magnetic, and chiral susceptibilities," *Russian Physics Journal*, vol. 52, no. 5, pp. 472–479, 2009.

[98] T. Niemi, A. O. Karilainen, and S. A. Tretyakov, "Synthesizing a twist polarizer," in *Antennas and Propagation Society International Symposium, APSURSI*, pp. 1–2, IEEE, 2012.

[99] A. O. Karilainen and S. A. Tretyakov, "Isotropic chiral objects with zero backscattering," *IEEE Transactions on Antennas and Propagation*, vol. 60, no. 9, pp. 4449–4452, 2012.

[100] Y. Ra'di and S. Tretyakov, "Optimizing small particles for strong interactions with electromagnetic fields," in *Electromagnetic Theory (EMTS), Proceedings of 2013 URSI International Symposium on*, pp. 348–349, IEEE, 2013.

[101] S. Tretyakov, S. Maslovski, I. Nefedov, A. Viitanen, P. Belov, and A. Sanmartin, "Artificial tellegen particle," *Electromagnetics*, vol. 23, no. 8, pp. 665–680, 2003.

[102] Y. Ra'di and S. A. Tretyakov, "Balanced and optimal bianisotropic particles: maximizing power extracted from electromagnetic fields," *New Journal of Physics*, vol. 15, no. 5, p. 053008, 2013.

[103] M. Mirmoosa, Y. Ra'di, V. Asadchy, C. Simovski, and S. Tretyakov, "Polarizabilities of nonreciprocal bianisotropic particles," *Physical Review Applied*, vol. 1, no. 3, p. 034005, 2014.

[104] S. Tretyakov, A. Sihvola, A. Sochava, and C. Simovski, "Magnetoelectric interactions in bi-anisotropic media," *Journal of Electromagnetic Waves and Applications*, vol. 12, no. 4, pp. 481–497, 1998.

[105] S. Tretyakov, A. Sihvola, and B. Jancewicz, "Onsager-casimir principle in the theory of bi-anisotropic media," Tech. Rep., DTIC Document, 2000.

[106] E. Saenz, I. Semchenko, S. Khakhomov, K. Guven, R. Gonzalo, E. Ozbay, and S. Tretyakov, "Modeling of spirals with equal dielectric, magnetic, and chiral susceptibilities," *Electromagnetics*, vol. 28, no. 7, pp. 476–493, 2008.

[107] T. Li, H. Liu, F. Wang, Z. Dong, S. Zhu, and X. Zhang, "Coupling effect of magnetic polariton in perforated metal/dielectric layered metamaterials and its influence on negative refraction transmission," *Optics Express*, vol. 14, no. 23, pp. 11155–11163, 2006.

[108] H. Guo, N. Liu, L. Fu, T. P. Meyrath, T. Zentgraf, H. Schweizer, and H. Giessen, "Resonance hybridization in double split-ring resonator metamaterials," *Optics Express*, vol. 15, no. 19, pp. 12095–12101, 2007.

[109] N. Liu and H. Giessen, "Coupling effects in optical metamaterials," *Angewandte Chemie International Edition*, vol. 49, no. 51, pp. 9838–9852, 2010.

[110] C. Rockstuhl, T. Zentgraf, H. Guo, N. Liu, C. Etrich, I. Loa, K. Syassen, J. Kuhl, F. Lederer, and H. Giessen, "Resonances of split-ring resonator metamaterials in the near infrared," *Applied Physics B: Lasers and Optics*, vol. 84, no. 1, pp. 219–227, 2006.

[111] N. Liu, H. Guo, L. Fu, S. Kaiser, H. Schweizer, and H. Giessen, "Plasmon hybridization in stacked cut-wire metamaterials," *Advanced Materials*, vol. 19, no. 21, pp. 3628–3632, 2007.

[112] N. Liu, H. Guo, L. Fu, S. Kaiser, H. Schweizer, and H. Giessen, "Three-dimensional photonic metamaterials at optical frequencies," *Nature Materials*, vol. 7, no. 1, pp. 31–37, 2008.

[113] J. Zhou, J. Dong, B. Wang, T. Koschny, M. Kafesaki, and C. M. Soukoulis, "Negative refractive index due to chirality," *Physical Review B*, vol. 79, no. 12, p. 121104, 2009.

[114] N. W. Ashcroft, N. D. Mermin, and S. Rodriguez, "Solid state physics," AAPT, 1978.

[115] I. V. Lindell, "Methods for electromagnetic field analysis," New York, NY (United States); Oxford Univ. Press, 1992.

[116] N. K. Grady, J. E. Heyes, D. R. Chowdhury, Y. Zeng, M. T. Reiten, A. K. Azad, A. J. Taylor, D. A. Dalvit, and H.-T. Chen, "Terahertz metamaterials for linear polarization conversion and anomalous refraction," *Science*, vol. 340, no. 6138, pp. 1304–1307, 2013.

[117] V. Asadchy, Y. Ra'di, J. Vehmas, and S. Tretyakov, "Functional metamirrors using bianisotropic elements," *Physical Review Letters*, vol. 114, no. 9, p. 095503, 2015.

[118] V. Asadchy, M. Albooyeh, and S. Tretyakov, "Optical metamirror: all-dielectric frequency-selective mirror with fully controllable reflection phase," *Journal of the Optical Society of America B*, vol. 33, no. 2, pp. A16–A20, 2016.

[119] Y. Z. Cheng, W. Withayachumnankul, A. Upadhyay, D. Headland, Y. Nie, R. Z. Gong, M. Bhaskaran, S. Sriram, and D. Abbott, "Ultrabroadband reflective polarization convertor for terahertz waves," *Applied Physics Letters*, vol. 105, no. 18, p. 181111, 2014.

[120] H. F. Ma, G. Z. Wang, G. S. Kong, and T. J. Cui, "Broadband circular and linear polarization conversions realized by thin birefringent reflective metasurfaces," *Optical Materials Express*, vol. 4, no. 8, pp. 1717–1724, 2014.

[121] P. Tuong, J. Park, Y. Kim, Y. Yoo, Y. Lee, J. Rhee, K. Kim, S. Nikitov, and N. Anh, "Broadband reflection of polarization conversion by 90° in metamaterial," *Journal of the Korean Physical Society*, vol. 64, no. 8, pp. 1116–1119, 2014.

[122] J. Hanfling, G. Jerinic, and L. Lewis, "Twist reflector design using e-type and h-type modes," *IEEE Transactions on Antennas and Propagation*, vol. 29, no. 4, pp. 622–629, 1981.

[123] S. S. H. Naqvi and N. C. Gallagher, "Analysis of a strip-grating twist reflector," *Journal of the Optical Society of America A*, vol. 7, no. 9, pp. 1723–1729, 1990.

[124] F. Monticone, N. M. Estakhri, and A. Alù, "Full control of nanoscale optical transmission with a composite metascreen," *Physical Review Letters*, vol. 110, no. 20, p. 203903, 2013.

[125] C. Pfeiffer and A. Grbic, "Millimeter-wave transmitarrays for wavefront and polarization control," *IEEE Transactions on Microwave Theory and Techniques*, vol. 61, no. 12, pp. 4407–4417, 2013.

[126] K. Achouri, B. A. Khan, S. Gupta, G. Lavigne, M. A. Salem, and C. Caloz, "Synthesis of electromagnetic metasurfaces: principles and illustrations," *arXiv preprint arXiv:1510.05997*, 2015.

[127] F. Lemoult, G. Lerosey, J. de Rosny, and M. Fink, "Resonant metalenses for breaking the diffraction barrier," *Physical Review Letters*, vol. 104, no. 20, p. 203901, 2010.

[128] C. Ma and Z. Liu, "A super resolution metalens with phase compensation mechanism," *Applied Physics Letters*, vol. 96, no. 18, p. 183103, 2010.

[129] B. Walther, C. Helgert, C. Rockstuhl, F. Setzpfandt, F. Eilenberger, E.-B. Kley, F. Lederer, A. Tünnermann, and T. Pertsch, "Spatial and spectral light shaping with metamaterials," *Advanced Materials*, vol. 24, no. 47, pp. 6300–6304, 2012.

[130] C. Pfeiffer and A. Grbic, "Metamaterial huygens surfaces: tailoring wave fronts with reflectionless sheets," *Physical Review Letters*, vol. 110, no. 19, p. 197401, 2013.

[131] M. Euler and V. Fusco, "RCS control using cascaded circularly polarized frequency selective surfaces and an AMC structure as a switchable twist polarizer," *Microwave and Optical Technology Letters*, vol. 52, no. 3, pp. 577–580, 2010.

[132] Y. Ra'di, V. S. Asadchy, and S. A. Tretyakov, "Total absorption of electromagnetic waves in ultimately thin layers," *IEEE Transactions on Antennas and Propagation*, vol. 61, no. 9, pp. 4606–4614, 2013.

[133] B. E. Saleh, M. C. Teich, and B. E. Saleh, *Fundamentals of photonics*, vol. 22, Wiley New York, 1991.

[134] T. Li, H. Liu, T. Li, S. Wang, F. Wang, R. Wu, P. Chen, S. Zhu, and X. Zhang, "Magnetic resonance hybridization and optical activity of microwaves in a chiral metamaterial," *Applied Physics Letters*, vol. 92, no. 13, p. 131111, 2008.

[135] E. Plum, V. Fedotov, and N. Zheludev, "Optical activity in extrinsically chiral metamaterial," *Applied Physics Letters*, vol. 93, no. 19, p. 191911, 2008.

[136] E. Plum, J. Zhou, J. Dong, V. Fedotov, T. Koschny, C. Soukoulis, and N. Zheludev, "Metamaterial with negative index due to chirality," *Physical Review B*, vol. 79, no. 3, p. 035407, 2009.

[137] M. Liu, Y. Zhang, X. Wang, and C. Jin, "Incident-angle-insensitive and polarization independent polarization rotator," *Optics Express*, vol. 18, no. 11, pp. 11990–12001, 2010.

[138] R. Zhao, L. Zhang, J. Zhou, T. Koschny, and C. Soukoulis, "Conjugated gammadion chiral metamaterial with uniaxial optical activity and negative refractive index," *Physical Review B*, vol. 83, no. 3, p. 035105, 2011.

[139] K. Song, Y. Liu, Q. Fu, X. Zhao, C. Luo, and W. Zhu, "90° polarization rotator with rotation angle independent of substrate permittivity and incident angles using a composite chiral metamaterial," *Optics Express*, vol. 21, no. 6, pp. 7439–7446, 2013.

[140] M. Mutlu and E. Ozbay, "A transparent 90° polarization rotator by combining chirality and electromagnetic wave tunneling," *Applied Physics Letters*, vol. 100, no. 5, p. 051909, 2012.

[141] D. K. Ghodgaonkar, V. V. Varadan, and V. K. Varadan, "A free-space method for measurement of dielectric constants and loss tangents at microwave frequencies," *IEEE Transactions on Instrumentation and Measurement*, vol. 38, no. 3, pp. 789–793, 1989.

[142] N. Landy, S. Sajuyigbe, J. Mock, D. Smith, and W. Padilla, "Perfect metamaterial absorber," *Physical Review Letters*, vol. 100, no. 20, p. 207402, 2008.

[143] N. Liu, M. Mesch, T. Weiss, M. Hentschel, and H. Giessen, "Infrared perfect absorber and its application as plasmonic sensor," *Nano letters*, vol. 10, no. 7, pp. 2342–2348, 2010.

[144] M. Diem, T. Koschny, and C. M. Soukoulis, "Wide-angle perfect absorber/thermal emitter in the terahertz regime," *Physical Review B*, vol. 79, no. 3, p. 033101, 2009.

[145] B. A. Munk, P. Munk, and J. Pryor, "On designing jaumann and circuit analog absorbers (ca absorbers) for oblique angle of incidence," *IEEE Transactions on Antennas and Propagation*, vol. 55, no. 1, pp. 186–193, 2007.

[146] M. Gustafsson, C. Sohl, C. Larsson, and D. Sjöberg, "Physical bounds on the all-spectrum transmission through periodic arrays," *EPL (Europhysics Letters)*, vol. 87, no. 3, p. 34002, 2009.

[147] M. Gustafsson, I. Vakili, S. E. B. Keskin, D. Sjoberg, and C. Larsson, "Optical theorem and forward scattering sum rule for periodic structures," *IEEE Transactions on Antennas and Propagation*, vol. 60, no. 8, pp. 3818–3826, 2012.

[148] M. Kerker, D.-S. Wang, and C. Giles, "Electromagnetic scattering by magnetic spheres," *Journal of the Optical Society of America B*, vol. 73, no. 6, pp. 765–767, 1983.

[149] M. Decker, I. Staude, M. Falkner, J. Dominguez, D. N. Neshev, I. Brener, T. Pertsch, and Y. S. Kivshar, "High-efficiency dielectric huygens' surfaces," *Advanced Optical Materials*, vol. 3, no. 6, pp. 813–820, 2015.

[150] C. Hu, X. Li, Q. Feng, X. Chen, and X. Luo, "Introducing dipole-like resonance into magnetic resonance to realize simultaneous drop in transmission and reflection at terahertz frequency," *Journal of Applied Physics*, vol. 108, no. 5, p. 053103, 2010.

[151] H. Tao, N. I. Landy, C. M. Bingham, X. Zhang, R. D. Averitt, and W. J. Padilla, "A metamaterial absorber for the terahertz regime: Design, fabrication and characterization," *Optics Express*, vol. 16, no. 10, pp. 7181–7188, 2008.

[152] G. R. Keiser, A. C. Strikwerda, K. Fan, V. Young, X. Zhang, and R. D. Averitt, "Decoupling crossover in asymmetric broadside coupled split-ring resonators at terahertz frequencies," *Physical Review B*, vol. 88, no. 2, p. 024101, 2013.

[153] Y. Cheng, H. Yang, Z. Cheng, and B. Xiao, "A planar polarization-insensitive metamaterial absorber," *Photonics and Nanostructures-Fundamentals and Applications*, vol. 9, no. 1, pp. 8–14, 2011.

[154] N. Landy, C. Bingham, T. Tyler, N. Jokerst, D. Smith, and W. Padilla, "Design, theory, and measurement of a polarization-insensitive absorber for terahertz imaging," *Physical Review B*, vol. 79, no. 12, p. 125104, 2009.

[155] F. Bilotti, A. Toscano, K. B. Alici, E. Ozbay, and L. Vegni, "Design of miniaturized narrowband absorbers based on resonant-magnetic inclusions," *IEEE Transactions on Electromagnetic Compatibility*, vol. 53, no. 1, pp. 63–72, 2011.

[156] A. Radke, T. Gissibl, T. Klotzbücher, P. V. Braun, and H. Giessen, "Three-dimensional bichiral plasmonic crystals fabricated by direct laser writing and electroless silver plating," *Advanced Materials*, vol. 23, no. 27, pp. 3018–3021, 2011.

[157] Y. Xia, B. Gates, Y. Yin, and Y. Lu, "Monodispersed colloidal spheres: old materials with new applications," *Advanced Materials*, vol. 12, no. 10, pp. 693–713, 2000.

[158] Y. Xia, B. Gates, and Z.-Y. Li, "Self-assembly approaches to three-dimensional photonic crystals," *Advanced Materials*, vol. 13, no. 6, pp. 409–413, 2001.

[159] D. J. Norris, E. G. Arlinghaus, L. Meng, R. Heiny, and L. Scriven, "Opaline photonic crystals: How does self-assembly work?," *Advanced Materials*, vol. 16, no. 16, pp. 1393–1399, 2004.

[160] Y. Zhu, Y. Cao, J. Ding, Z. Li, J. Liu, and Y. Chi, "Three-dimensional photonic bandgap crystals of titania hollow spheres at visible wavelengths," *Applied Physics A: Materials Science and Processing*, vol. 94, no. 4, pp. 731–734, 2009.

[161] M. Summers, K. Tabunshchyk, A. Kovalenko, and M. Brett, "Fabrication of 2D–3D photonic crystal heterostructures by glancing angle deposition," *Photonics and Nanostructures–Fundamentals and Applications*, vol. 7, no. 2, pp. 76–84, 2009.

[162] M. Summers and M. Brett, "Optimization of periodic column growth in glancing angle deposition for photonic crystal fabrication," *Nanotechnology*, vol. 19, no. 41, p. 415203, 2008.

[163] M. Campbell, D. Sharp, M. Harrison, R. Denning, and A. Turberfield, "Fabrication of photonic crystals for the visible spectrum by holographic lithography," *Nature*, vol. 404, no. 6773, pp. 53–56, 2000.

[164] C. K. Ullal, M. Maldovan, E. L. Thomas, G. Chen, Y.-J. Han, and S. Yang, "Photonic crystals through holographic lithography: simple cubic, diamond-like, and gyroid-like structures," *Applied Physics Letters*, vol. 84, no. 26, pp. 5434–5436, 2004.

[165] W. Kaiser and C. Garrett, "Two-photon excitation in CaF_2: Eu_{2+}," *Physical Review Letters*, vol. 7, no. 6, p. 229, 1961.

[166] Y.-H. Pao and P. Rentzepis, "Laser-induced production of free radicals in organic compounds," *Applied Physics Letters*, vol. 6, no. 5, pp. 93–95, 1965.

[167] S. Maruo, O. Nakamura, and S. Kawata, "Three-dimensional microfabrication with two-photon-absorbed photopolymerization," *Optics Letters*, vol. 22, no. 2, pp. 132–134, 1997.

[168] V. Mizeikis, K. K. Seet, S. Juodkazis, and H. Misawa, "Three-dimensional woodpile photonic crystal templates for the infrared spectral range," *Optics Letters*, vol. 29, no. 17, pp. 2061–2063, 2004.

[169] S. Juodkazis, V. Mizeikis, K. K. Seet, M. Miwa, and H. Misawa, "Two-photon lithography of nanorods in SU-8 photoresist," *Nanotechnology*, vol. 16, no. 6, p. 846, 2005.

[170] K. K. Seet, V. Mizeikis, S. Juodkazis, and H. Misawa, "Three-dimensional horizontal circular spiral photonic crystals with stop gaps below 1 μm," *Applied Physics Letters*, vol. 88, no. 22, p. 221101, 2006.

[171] L. Li, R. R. Gattass, E. Gershgoren, H. Hwang, and J. T. Fourkas, "Achieving $\lambda/20$ resolution by one-color initiation and deactivation of polymerization," *Science*, vol. 324, no. 5929, pp. 910–913, 2009.

[172] K. K. Seet, V. Mizeikis, S. Matsuo, S. Juodkazis, and H. Misawa, "Three-dimensional spiral-architecture photonic crystals obtained by direct laser writing," *Advanced Materials*, vol. 17, no. 5, pp. 541–545, 2005.

[173] H.-B. Sun, S. Matsuo, and H. Misawa, "Three-dimensional photonic crystal structures achieved with two-photon-absorption photopolymerization of resin," *Applied Physics Letters*, vol. 74, no. 6, pp. 786–788, 1999.

[174] M. Straub and M. Gu, "Near-infrared photonic crystals with higher-order bandgaps generated by two-photon photopolymerization," *Optics Letters*, vol. 27, no. 20, pp. 1824–1826, 2002.

[175] M. Deubel, G. Von Freymann, M. Wegener, S. Pereira, K. Busch, and C. M. Soukoulis, "Direct laser writing of three-dimensional photonic-crystal templates for telecommunications," *Nature Materials*, vol. 3, no. 7, pp. 444–447, 2004.

[176] N. V. Tkachenko, *Optical spectroscopy: methods and instrumentations*, Elsevier, 2006.

[177] H.-B. Sun and S. Kawata, "Two-photon photopolymerization and 3D lithographic microfabrication," in *NMR 3D Analysis Photopolymerization*, pp. 169–273, Springer, 2004.

[178] S. Maruo and J. T. Fourkas, "Recent progress in multiphoton microfabrication," *Laser and Photonics Reviews*, vol. 2, no. 1-2, pp. 100–111, 2008.

[179] J. Fischer and M. Wegener, "Three-dimensional optical laser lithography beyond the diffraction limit," *Laser and Photonics Reviews*, vol. 7, no. 1, pp. 22–44, 2013.

[180] S. Basu, L. P. Cunningham, G. D. Pins, K. A. Bush, R. Taboada, A. R. Howell, J. Wang, and P. J. Campagnola, "Multiphoton excited fabrication of collagen matrixes cross-linked by a modified benzophenone dimer: bioactivity and enzymatic degradation," *Biomacromolecules*, vol. 6, no. 3, pp. 1465–1474, 2005.

[181] L. P. Cunningham, M. P. Veilleux, and P. J. Campagnola, "Freeform multiphoton excited microfabrication for biological applications using a rapid prototyping cad-based approach," *Optics Express*, vol. 14, no. 19, pp. 8613–8621, 2006.

[182] S. Maruo and H. Inoue, "Optically driven micropump produced by three-dimensional two-photon microfabrication," *Applied Physics Letters*, vol. 89, no. 14, p. 144101, 2006.

[183] S. Klein, A. Barsella, H. Leblond, H. Bulou, A. Fort, C. Andraud, G. Lemercier, J. Mulatier, and K. Dorkenoo, "One-step waveguide and optical circuit writing in photopolymerizable materials processed by two-photon absorption," *Applied Physics Letters*, vol. 86, no. 21, p. 211118, 2005.

[184] S. Klein, A. Barsella, G. Taupier, V. Stortz, A. Fort, and K. Dorkenoo, "Optical components based on two-photon absorption process in functionalized polymers," *Applied Surface Science*, vol. 252, no. 13, pp. 4919–4922, 2006.

[185] K. Jolic, M. Ghantasala, J. Hayes, and H. Jin, "Fabrication of three-dimensional inductor coil using excimer laser micromachining," *Journal of Micromechanics and Microengineering*, vol. 13, no. 5, p. 782, 2003.

[186] P. R. Griffiths and J. A. De Haseth, *Fourier transform infrared spectrometry*, John Wiley and Sons, 2007.

[187] J. M. Shaw, J. D. Gelorme, N. C. LaBianca, W. E. Conley, and S. J. Holmes, "Negative photoresists for optical lithography," *IBM Journal of Research and Development*, vol. 41, no. 1.2, pp. 81–94, 1997.

[188] A. Ovsianikov, X. Shizhou, M. Farsari, M. Vamvakaki, C. Fotakis, and B. N. Chichkov, "Shrinkage of microstructures produced by two-photon polymerization of zr-based hybrid photosensitive materials," *Optics Express*, vol. 17, no. 4, pp. 2143–2148, 2009.

[189] A. Ovsianikov, A. Gaidukeviciute, B. Chichkov, M. Oubaha, B. MacCraith, I. Sakellari, A. Giakoumaki, D. Gray, M. Vamvakaki, M. Farsari, *et al.*, "Two-photon polymerization of hybrid sol-gel materials for photonics applications," *Laser Chemistry*, vol. 2008, 2008.

[190] A. Alù, M. G. Silveirinha, A. Salandrino, and N. Engheta, "Epsilon-near-zero metamaterials and electromagnetic sources: tailoring the radiation phase pattern," *Physical Review B*, vol. 75, no. 15, p. 155410, 2007.

[191] W. Cai and V. M. Shalaev, *Optical metamaterials*, Springer, 2010.

[192] M. Pu, C. Hu, M. Wang, C. Huang, Z. Zhao, C. Wang, Q. Feng, and X. Luo, "Design principles for infrared wide-angle perfect absorber based on plasmonic structure," *Optics Express*, vol. 19, no. 18, pp. 17413–17420, 2011.

[193] A. A. Tseng, K. Chen, C. D. Chen, and K. J. Ma, "Electron beam lithography in nanoscale fabrication: recent development," *IEEE Transactions on Electronics Packaging Manufacturing*, vol. 26, no. 2, pp. 141–149, 2003.

[194] Y. Chen, "Nanofabrication by electron beam lithography and its applications: a review," *Microelectronic Engineering*, vol. 135, pp. 57–72, 2015.

[195] H.-B. Sun, T. Tanaka, K. Takada, and S. Kawata, "Two-photon photopolymerization and diagnosis of three-dimensional microstructures containing fluorescent dyes," *Applied Physics Letters*, vol. 79, no. 10, pp. 1411–1413, 2001.

[196] J. Wang, Y. Chen, J. Hao, M. Yan, and M. Qiu, "Shape-dependent absorption characteristics of three-layered metamaterial absorbers at near-infrared," *Journal of Applied Physics*, vol. 109, no. 7, p. 074510, 2011.

[197] X. Xiong, S.-C. Jiang, Y.-H. Hu, R.-W. Peng, and M. Wang, "Structured metal film as a perfect absorber," *Advanced Materials*, vol. 25, no. 29, pp. 3994–4000, 2013.

[198] S. Ogawa, D. Fujisawa, H. Hata, and M. Kimata, "Absorption properties of simply fabricated all-metal mushroom plasmonic metamaterials incorporating tube-shaped posts for multi-color uncooled infrared image sensor applications," *Photonics*, vol. 3, no. 1, p. 9, 2016.

[199] W. T. Chen, C. J. Chen, P. C. Wu, S. Sun, L. Zhou, G.-Y. Guo, C. T. Hsiao, K.-Y. Yang, N. I. Zheludev, and D. P. Tsai, "Optical magnetic response in three-dimensional metamaterial of upright plasmonic meta-molecules," *Optics Express*, vol. 19, no. 13, pp. 12837–12842, 2011.

[200] K. Fan, A. C. Strikwerda, H. Tao, X. Zhang, and R. D. Averitt, "Stand-up magnetic metamaterials at terahertz frequencies," *Optics Express*, vol. 19, no. 13, pp. 12619–12627, 2011.

[201] C. C. Chen, C. T. Hsiao, S. Sun, K.-Y. Yang, P. C. Wu, W. T. Chen, Y. H. Tang, Y.-F. Chau, E. Plum, G.-Y. Guo, *et al.*, "Fabrication of three dimensional split ring resonators by stress-driven assembly method," *Optics Express*, vol. 20, no. 9, pp. 9415–9420, 2012.

[202] J. Wendt, D. Burckel, G. Ten Eyck, A. Ellis, I. Brener, and M. Sinclair, "Fabrication techniques for three-dimensional metamaterials in the mid-infrared," *Journal of Vacuum Science & Technology B, Nanotechnology and Microelectronics: Materials, Processing, Measurement, and Phenomena*, vol. 28, no. 6, pp. C6O30–C6O33, 2010.

[203] S. Kawata, H.-B. Sun, T. Tanaka, and K. Takada, "Finer features for functional microdevices," *Nature*, vol. 412, no. 6848, pp. 697–698, 2001.

[204] M. Malinauskas, H. Gilbergs, A. Žukauskas, V. Purlys, D. Paipulas, and R. Gadonas, "A femtosecond laser-induced two-photon photopolymerization technique for structuring microlenses," *Journal of Optics*, vol. 12, no. 3, p. 035204, 2010.

[205] F. Formanek, N. Takeyasu, T. Tanaka, K. Chiyoda, A. Ishikawa, and S. Kawata, "Three-dimensional fabrication of metallic nanostructures over large areas by two-photon polymerization," *Optics Express*, vol. 14, no. 2, pp. 800–809, 2006.

[206] V. Mizeikis, S. Juodkazis, R. Tarozaite, J. Juodkazyte, K. Juodkazis, and H. Misawa, "Fabrication and properties of metalo-dielectric photonic crystal structures for infrared spectral region," *Optics Express*, vol. 15, no. 13, pp. 8454–8464, 2007.

[207] M. Farsari and B. N. Chichkov, "Materials processing: Two-photon fabrication," *Nature photonics*, vol. 3, no. 8, p. 450, 2009.

[208] H.-H. Huang and Y.-C. Hung, "Designs of helix metamaterials for broadband and high-transmission polarization rotation," *IEEE Photonics Journal*, vol. 6, no. 5, pp. 1–7, 2014.

[209] D. Shrekenhamer, W. Xu, S. Venkatesh, D. Schurig, S. Sonkusale, and W. J. Padilla, "Experimental realization of a metamaterial detector focal plane array," *Physical Review Letters*, vol. 109, no. 17, p. 177401, 2012.

[210] C. Wu, I. Burton Neuner, G. Shvets, J. John, A. Milder, B. Zollars, and S. Savoy, "Large-area wide-angle spectrally selective plasmonic absorber," *Physical Review B*, vol. 84, no. 7, p. 075102, 2011.

[211] Z. Lu, M. Zhao, Z. Yang, L. Wu, and P. Zhang, "Helical metamaterial absorbers: broadband and polarization-independent in optical region," *Journal of Lightwave Technology*, vol. 31, no. 16, pp. 2762–2768, 2013.

[212] Z. Lu, M. Zhao, Z. Yang, L. Wu, P. Zhang, Y. Zheng, and J. Duan, "Broadband polarization-insensitive absorbers in 0.3–2.5 μm using helical metamaterials," *Journal of the Optical Society of America B*, vol. 30, no. 5, pp. 1368–1372, 2013.

[213] S. Liao and G. Yin, "Reflectance of a chiral plate absorber," *Applied Physics Letters*, vol. 62, no. 20, pp. 2480–2482, 1993.

[214] V. Veiko, A. Skvortsov, T. H. Cong, and A. Petrov, "Laser ablation of monocrystalline silicon under pulsed-frequency fiber laser," *Scientific and Technical Journal of Information Technologies*, vol. 15, p. 426, 2015.

[215] D. Baeuerle, "Laser processing and chemistry springer verlag," Heidelberg, Berlin, 2000.

[216] J. K. Gansel, M. Latzel, A. Frölich, J. Kaschke, M. Thiel, and M. Wegener, "Tapered gold-helix metamaterials as improved circular polarizers," *Applied Physics Letters*, vol. 100, no. 10, p. 101109, 2012.

[217] R. Ji, S.-W. Wang, X. Liu, H. Guo, and W. Lu, "Hybrid helix metamaterials for giant and ultrawide circular dichroism," *ACS Photonics*, vol. 3, no. 12, pp. 2368–2374, 2016.

[218] Z. Yang, Z. Wang, H. Tao, and M. Zhao, "Manipulation of wavefront using helical metamaterials," *Optics Express*, vol. 24, no. 16, pp. 18266–18276, 2016.

[219] S. Babar and J. Weaver, "Optical constants of Cu, Ag, and Au revisited," *Applied Optics*, vol. 54, no. 3, pp. 477–481, 2015.

[220] R. L. Olmon, B. Slovick, T. W. Johnson, D. Shelton, S.-H. Oh, G. D. Boreman, and M. B. Raschke, "Optical dielectric function of gold," *Physical Review B*, vol. 86, no. 23, p. 235147, 2012.